


MATHEMATICAL MODELING AND MULTISCALE SIMULATION  
OF CO<sub>2</sub> STORAGE IN SALINE AQUIFERS

A DISSERTATION  
SUBMITTED TO THE DEPARTMENT OF ENERGY  
RESOURCES ENGINEERING  
AND THE COMMITTEE ON GRADUATE STUDIES  
OF STANFORD UNIVERSITY  
IN PARTIAL FULFILLMENT OF THE REQUIREMENTS  
FOR THE DEGREE OF  
DOCTOR OF PHILOSOPHY

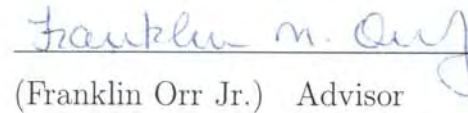
Marc Andre Hesse  
May 2008

© Copyright by Marc Andre Hesse 2008  
All Rights Reserved

I certify that I have read this dissertation and that, in my opinion, it is fully adequate in scope and quality as a dissertation for the degree of Doctor of Philosophy.

  
(Hamdi Tchalepi) Principal Advisor

I certify that I have read this dissertation and that, in my opinion, it is fully adequate in scope and quality as a dissertation for the degree of Doctor of Philosophy.

  
(Franklin Orr Jr.) Advisor

I certify that I have read this dissertation and that, in my opinion, it is fully adequate in scope and quality as a dissertation for the degree of Doctor of Philosophy.

  
(Brian Cantwell)

Approved for the Stanford University Committee on Graduate Studies.

# Abstract

Carbon capture and storage (CCS) is a key technology to reduce  $\text{CO}_2$  emissions from industrial processes, in particular from fossil-fuel based electricity generation. One important aspect of CCS is the safe long-term storage of the captured  $\text{CO}_2$  in geological formations, especially in deep regional saline aquifers. Predicting the long-term evolution of the injected  $\text{CO}_2$  requires an understanding of the basic physical mechanisms and the ability to capture them in field-scale numerical simulations.

Simple mathematical models of trapping processes are developed to allow the identification of the dominant physical processes during  $\text{CO}_2$  storage and their associated length and time scales. First-order estimates of the duration of the active storage period and the migration distance are obtained as a function of the average properties of the aquifer. These estimates support the selection of storage sites, in particular at the early stages when limited data is available. They also show that the length scales associated with the physical processes in regional aquifers can span several orders of magnitude.

Multiscale simulation techniques are necessary to resolve physical processes and geological heterogeneity. In particular, robust multiscale methods of elliptic flow problems, must be developed. The multiscale finite volume method is analyzed in the context of multipoint flux approximations and shown to lose monotonicity for anisotropic problems. Strong anisotropy arises in the simulation of  $\text{CO}_2$  storage, because of the large aspect ratios of regional aquifers. A new compact coarse operator and new local fine-scale problems are introduced to obtain monotone coarse pressure solutions for anisotropic domains. This development presents a major step towards multiscale simulation of  $\text{CO}_2$  storage in large regional saline aquifers.



# Acknowledgements

I would like to thank my PhD advisors Hamdi Tchelepi and Franklin Orr Jr. who have provided the best possible intellectual environment for me. The foundation of this dissertation is their enthusiasm for open enquiry, their appreciation of a good argument, their willingness to question common assumptions, their patience when results were not forthcoming, and their trust in my abilities that has allowed me to explore and develop my own ideas. They have set an example that I hope to emulate in the future. I am also grateful that they have always encouraged me to seek collaborations with other scientists, which has lead to a rich and intellectually diverse graduate experience. Amongst my collaborators I would like to acknowledge Amir Riaz and Brad Mallison, who have shared their knowledge and experience with me and who have made significant intellectual contributions to my dissertation. I would also like to thank Prof. Brian Cantwell for his encouragement and interest in my work, and Prof. Patrick Jenny who hosted me at ETH-Zürich in the summer of 2008 and who has allowed me to participate in the development of iterative multiscale methods.

I want to thank Roland Horne, who carefully assigns students to each office, for my office mates Rami Younis and Felix Kwok. Our office has been a stimulating place to work that has been central to my graduate experience. I thank Felix and Rami for their friendship, and I will miss their company. I hope our paths will cross in the future. I would also like to thank my parents and my family for their support with all my decisions and their love. Finally, I would like to thank Valentina for all her love and the happiness she has brought to my life in the last two years of this dissertation.

# Contents

<b>Abstract</b>	<b>iv</b>
<b>Acknowledgements</b>	<b>v</b>
<b>1 Introduction</b>	<b>1</b>
1.1 Carbon capture and storage . . . . .	1
1.1.1 Clean coal technology . . . . .	2
1.1.2 Geological CO <sub>2</sub> storage . . . . .	3
1.2 Saline aquifer storage . . . . .	5
1.2.1 Storage security . . . . .	6
1.2.2 Leakage mechanisms . . . . .	8
1.2.3 Trapping mechanisms . . . . .	9
1.3 Thesis overview . . . . .	11
1.3.1 Trapping models . . . . .	13
1.3.2 Multiscale simulation . . . . .	14
<b>2 Dissolution Trapping &amp; Convection in the Brine</b>	<b>16</b>
2.1 Introduction . . . . .	16
2.2 Onset of convection . . . . .	17
2.2.1 Model problem . . . . .	17
2.2.2 Previous work . . . . .	19
2.2.3 Linear stability analysis . . . . .	21
2.2.4 Direct numerical simulation . . . . .	33
2.2.5 Discussion . . . . .	44

2.2.6	Conclusions . . . . .	47
2.3	Convective dissolution rates . . . . .	48
2.3.1	Convection in open systems . . . . .	49
2.3.2	Convection in closed systems . . . . .	51
2.3.3	Convective time scales . . . . .	53
2.3.4	Further work . . . . .	55
<b>3</b>	<b>Residual Trapping &amp; CO<sub>2</sub> Gravity Currents</b>	<b>56</b>
3.1	Introduction . . . . .	56
3.1.1	Residual saturations . . . . .	58
3.1.2	Gravity currents . . . . .	58
3.2	Governing equations . . . . .	61
3.2.1	Derivation . . . . .	61
3.2.2	Dimensionless form . . . . .	65
3.2.3	Discretisation . . . . .	66
3.3	Regime transition: confined to unconfined . . . . .	66
3.3.1	Self-similar solution at early times . . . . .	67
3.3.2	Self-similar solution at late times . . . . .	75
3.3.3	Non-self-similar transition . . . . .	78
3.3.4	Regime diagram . . . . .	83
3.4	Gravity currents with residual trapping . . . . .	86
3.4.1	Parabolic limit: horizontal aquifers . . . . .	87
3.4.2	Hyperbolic limit: sloping aquifers . . . . .	92
3.4.3	Numerical results . . . . .	105
3.5	Discussion . . . . .	110
3.5.1	Assumptions . . . . .	110
3.5.2	Implications for CCS . . . . .	112
3.6	Conclusion . . . . .	117
<b>4</b>	<b>Multiscale Simulation</b>	<b>119</b>
4.1	Introduction . . . . .	119
4.1.1	Numerical challenges . . . . .	119

4.1.2	Incompressible two-phase flow in porous media . . . . .	122
4.1.3	Multiscale methods . . . . .	124
4.1.4	Fine-scale problem . . . . .	125
4.1.5	Multipoint flux approximations . . . . .	127
4.2	Multiscale finite volume method . . . . .	129
4.2.1	Coarse operator . . . . .	130
4.2.2	Local problems . . . . .	132
4.2.3	Fine-scale reconstruction . . . . .	134
4.2.4	MSFV properties . . . . .	137
4.3	Anisotropy and monotonicity . . . . .	138
4.3.1	Effective tensor . . . . .	138
4.4	Homogeneous coarse operator . . . . .	141
4.4.1	Original operator . . . . .	141
4.4.2	Compact operator . . . . .	144
4.5	Heterogeneous compact operator . . . . .	146
4.6	Localization . . . . .	148
4.6.1	Transverse equilibrium . . . . .	149
4.6.2	Bilinear local problems . . . . .	150
4.6.3	Linear local problems . . . . .	152
4.7	Numerical results . . . . .	154
4.8	Discussion . . . . .	162
4.9	Conclusion . . . . .	166
<b>5</b>	<b>Conclusions</b>	<b>167</b>
5.1	Results . . . . .	167
5.1.1	Dissolution trapping & convection . . . . .	168
5.1.2	Residual trapping & gravity currents . . . . .	169
5.1.3	Multiscale methods for porous media . . . . .	170
5.2	Future work . . . . .	170

# List of Figures

1.1	(a) Predicted emission scenarios. The line labeled 500 ppm is the emissions scenario necessary to stabilize the CO <sub>2</sub> concentration at approximately twice the preindustrial average. (b) Schematic version of figure <i>a</i> , showing the 7 stabilization wedges. Both graphs are modified from Pacala & Socolow (2004). . . . .	2
1.2	The different states of CO <sub>2</sub> in the underground together with the physical and chemical processes responsible for the transfer between these states. . . . .	7
1.3	A schematic illustration showing the evolution of the fraction of CO <sub>2</sub> in each state as a function of time, modified from Metz <i>et al.</i> (2006). . . . .	9
1.4	Sketches of the limiting cases investigated with simple process models: (a) Dissolution trapping of CO <sub>2</sub> ponded in structural trap. (b) Residual trapping of CO <sub>2</sub> migrating in a horizontal aquifer. (c) Residual trapping of CO <sub>2</sub> migrating in a sloping aquifer. In all cases CO <sub>2</sub> plume is dark gray, residual CO <sub>2</sub> light gray, and dissolved CO <sub>2</sub> shaded. . . . .	13
2.1	Supercritical CO <sub>2</sub> accumulates along the impermeable top boundary. It slowly dissolves into the underlying brine, forming a heavier boundary layer. The resulting gravitational instability leads to the convective transport of CO <sub>2</sub> saturated brine plumes. . . . .	18

2.2	Disturbance concentration profile for $Ra = 500$ and $k = 0$ at different times, obtained from, (a) the IVP in the $\xi$ - $t$ coordinate system with (2.21-2.23) and (b) the IVP in the $z$ - $t$ coordinate system with (2.14-2.18). Random initial conditions are used for both cases. Plot (a) shows that the concentration profile resolves into the correct solution within a very short time, starting from any given set of white noise initial conditions. For the $z$ - $t$ coordinate system on the other hand, plot (b), convergence is much slower and is strongly dependent on initial conditions. . . . .	26
2.3	(a) Growth rate vs. wavenumber curves for $Ra = 500$ computed by the dominant mode method and the IVP. The flow is stable for small times. The growth rate increases with time to become positive at the critical time $t_c$ and the critical wavenumber $k_c$ . Flow instability increases with time beyond $t_c$ with both shortwave and longwave cutoffs. Comparison with the IVP shows exact agreement for small times and small wavenumbers. (b) Comparison of the dominant mode method and the QSSA with the initial value problem for two perturbation wavenumbers at $Ra = 500$ . The dominant mode solution gives exact results for small times but becomes inaccurate for later times particularly for large wavenumbers. The QSSA on the other hand is reasonably accurate for all times. . . . .	29
2.4	(a) Critical time vs. $Ra$ . (b) Critical wavenumber vs. $Ra$ , given by the dominant mode solution. The critical time varies as the $1/Ra$ , while the critical wavenumber scales linearly with $Ra$ . . . . .	31
2.5	(a) Maximum growth rate $\sigma_{\max}$ as a function of time, and (b) The most dangerous wavenumber $k_{\max}$ as a function of time, for different Rayleigh numbers. All the results are obtained using the QSSA. . . .	32
2.6	(a) The longwave cutoff wavenumber $k_L$ as a function of time for different Rayleigh numbers, computed by the dominant mode method. $k_L$ behaves similarly for all $Ra$ and varies approximately linearly with time. (b) The shortwave cutoff $k_S$ computed by the QSSA. . . . .	33

2.7	Comparison of the growth rates obtained from nonlinear direct numerical simulation and the linear initial value problem, for two different initial perturbations with wavenumber, $k$ . . . . .	35
2.8	Concentration contours at different times for $Ra = 4000$ . (a) $t = 1$ , (b) $t = 1.8$ , (c) $t = 2.3$ and (d) $t = 3.8$ A large number of fingers consistent with the linear stability analysis develop initially. Nonlinear interactions rapidly reduce the number of fingers and give rise to large scale structures at later times. The fingers at later times are connected to the top boundary at discrete locations. These connections act as feeding sites of the high density fluid to the convecting fingers below. . . . .	37
2.9	Vorticity contours in the background with overlapping streamlines for $Ra = 4000$ , $t = 2.3$ . Corresponding concentration contours are shown in figure 2.8(c). The vorticity field has a dipole structure that drives the high density fluid through the fingers. The stream lines show how the fluid travels laterally and then descends through the isolated feeding sites for the fingers. The direction of fluid circulation is shown by the arrows. . . . .	38
2.10	The dominant mode of the nonlinear simulations as a function of time for different values of the Rayleigh number. Also shown are the most dangerous modes given by the linear stability analysis. Good agreement is observed between the two for early times. At later times the onset of nonlinear behavior leads to a significant deviation from linear results. . . . .	40
2.11	Concentration contours for (a) $Ra = 1000$ , $t = 2.2$ and (b) $Ra = 8000$ , $t = 1.6$ . The larger Rayleigh number case is marked by intense nonlinear interaction between competing fingers. The small $Ra$ case shows larger fingers with a strong diffusive spreading. . . . .	41

2.12	Concentration contours at time $t_b$ , when the concentration front reaches the bottom. (a) $Ra = 1000$ , $t_b = 8.9$ . (b) $Ra = 2000$ , $t_b = 7$ . (c) $Ra = 4000$ , $t_b = 8.0$ . (d) $Ra = 8000$ , $t_b = 8.5$ . The late time dynamics is governed by large scale fingers. Large Rayleigh number cases continue to display vigorous fingering interactions. . . . .	42
2.13	The position of the most advanced portion of the front as a function of time for different values of the Rayleigh number. The tip moves faster for larger Rayleigh numbers for early times. Fingering interactions significantly influence the rate of front propagation at later times, particularly for large $Ra$ cases. . . . .	43
2.14	(a) Variation with permeability of the critical time, $t_c$ , the critical wavelength, $\lambda_c$ and the penetration depth at the critical time, $\delta_c$ , for $\Delta\rho = 5 \text{ kg/m}^3$ , $\phi = 0.3$ , $\mu = 0.5 \text{ cP}$ and $D = 10^{-9} \text{ m}^2/\text{s}$ . For this range of permeability variation $t_c$ varies between 2000 yrs and 10 days while $\lambda_c$ goes from about 100 m to less than a meter. The penetration depth $\delta_c$ gives information regarding the applicability of our analysis with respect to the layer thickness $H$ , such that $\delta_c \ll H$ . (b) The advance of the fastest finger tip is shown until the bottom of the simulation domain is reached. A diffusive, $t^{0.5}$ , behavior is observed at early times, while the fingers advance proportional to $t$ at later times. . . . .	45
2.15	Evolution of the concentration in an open aquifer for $Ra = 4000$ . . . .	49
2.16	(a) Evolution of the dissolution rate at $Ra = 4000$ . Average dissolution rate over time is shown as dashed line. (b) Time averaged of the dissolution rate for different $Ra$ . . . . .	50
2.17	Evolution of the concentration in a closed aquifer, for $Ra = 1000$ . (a) Plumes of dissolved have not reached the base of the aquifer. Convection similar to an open aquifer. (b-d) Convection in a closed aquifer. . . .	52
2.18	(a) Evolution of the dissolution rate, $dC/d\tau$ , for various $Ra$ in a closed aquifer. (b) Variation of the time scales discussed in the text as a function of $Ra$ . . . . .	53



3.1	(a) Microtomogram of non-wetting CO <sub>2</sub> bubbles (black) and water (white) in the pore space between grains (grey), from Benson <i>et al.</i> (2006). (b) Comparison between non-wetting phase saturation profile after imbibition, inferred from a wire-line log (Koperna & Kuuskraa, 2006), and the simplified step function saturation profile corresponding to the sharp-interface approximation. (c) The geometry of the porous layer and the variables used in the derivation are shown. . . . .	60
3.2	The geometry of the initial condition and the three associated length scales $H$ , $L_d$ , and $L_f$ . A particular initial condition $h_0[x]$ and the corresponding idealized step function initial condition $h_0^*[x]$ are shown. The arrows indicate that the fluid has been injected over the entire thickness of the reservoir. . . . .	63
3.3	The evolution of buoyant CO <sub>2</sub> -vapor (gray) released into a horizontal porous layer saturated by brine (white). The outward propagating tip of the interface is marked by $x_o$ . All figures are exaggerated in the vertical direction, to make the late solution (d) visible. In many situations of interest the width of the invaded region in figure (a) is several times larger than the aquifer thickness. . . . .	68
3.4	Similarity solution is shown for different values of $M$ . The variable $\theta$ is the non-dimensional thickness of the CO <sub>2</sub> , it is measured from the top of the aquifer. . . . .	69
3.5	The numerical values for the outer (a) and inner (b) tip positions are shown as a function of $M$ (solid lines). The scaling laws (3.17) and (3.18) are shown as dashed lines. . . . .	71
3.6	(a) The numerical solution to (3.2) with initial condition (3.22) and $M = 10$ is plotted at various times, $t$ , and compared to the self-similar solution obtained from (3.15) (solid grey line). (b) Numerical solutions to (3.2) with $M = 20$ and initial condition (3.25) is shown for several values of the parameter $a$ in the initial condition and compared to the solution of (3.15) with $a = 0$ (solid grey line). . . . .	73

3.7	The transition of the numerical solution (light lines) from the early to the late similarity solution (both heavy lines) is shown in scaled coordinates. (a) The numerical solution is shown at $\vartheta = \vartheta_b + \{1, 4, 10, 30, 100\}$ , where $\vartheta_b = 0.61$ ; (b) The numerical solution is shown at $\vartheta = \vartheta_b + \{10^1, 10^2, 10^3, 10^4, 10^5\}$ , where $\vartheta_b = 7.1$ . . . . .	79
3.8	The numerical results for the non-dimensional tip position $\xi_o$ are shown as a function of non-dimensional time $\vartheta$ , for different mobility ratios $M$ . In all figures the numerical solution is given by dots ( $\cdots$ ), the tip scaling from the early similarity solution by a dashed line ( $- - -$ ), and the tip scaling from the late similarity solution as a full line ( $—$ ). (a) $\vartheta_t = 2.0$ , $\vartheta_b = 0.1$ ; (b) $\vartheta_t = 2.5$ , $\vartheta_b = 0.24$ ; (c) $\vartheta_t = 29.3$ , $\vartheta_b = 1$ ; (d) $\vartheta_t = 811.3$ , $\vartheta_b = 1$ ; (e) $\vartheta_t = 811.3$ , $\vartheta_b = 7.1$ . . . . .	81
3.9	Regime diagram for a finite release of fluid into a horizontal porous slab, showing the non-dimensional time scales obtained in this study, and the shapes of the gravity current as a function of the mobility ratio $M$ . The shaded region indicates the transition period between the similarity solutions. The characteristic time to dimensionalize all results is $t^d = L_d^2 \kappa^{-1} H^{-1}$ . . . . .	84
3.10	Current evolution in an aquifer with 30 mD permeability, for details of the physical properties see §3.5.2. $\text{CO}_2$ currents (dark grey) and the zone containing residual saturation in their wake. Figures <i>a</i> to <i>d</i> show the evolution in a horizontal aquifer. These figures are equivalent to figure 3.3, but they include the effect of residual trapping. Figures <i>e</i> to <i>h</i> show the evolution in an equivalent aquifer sloping with $5^\circ$ . . . .	86
3.11	(a) Interface shapes for $M = 1$ and $\epsilon$ increasing from 0 to 1 in 0.2 increments. (b) Interface shapes for $M = 10$ and $\epsilon$ increasing from 0 to 1 in 0.2 increments. (c) Contours of the outward propagating tip position, $\zeta_o$ . (d) Contours of the inward propagating tip position, $-\zeta_i$ . . . .	88

3.12	Change of the solution from the early to the late scaling law ( $M = 1$ ). (a) The scaling laws for $\xi_o \propto \vartheta^\beta$ at early and late times as a function of the residual, $\epsilon$ . The symbols at $\epsilon$ of 0, 1/4, 1/2, and 3/4 show the exponents obtained by fitting the numerical data shown in figure <i>b</i> . For the early scaling law the data was fit for $\vartheta$ between 0.1 and 10 and for the late scaling law the data was fit for $\vartheta > 1000$ . (b) The shifted tip position, $\hat{\xi} = \xi_o - \tilde{\xi}$ , is shown as function of $\vartheta$ , for increasing residuals, where $\tilde{\xi} = 1$ . . . . .	91
3.13	(a) The flux function $f$ is shown for $M = 10$ and increasing trapping $\epsilon$ . (b) The corresponding solution profiles given by (3.56) in self-similar coordinates. . . . .	93
3.14	Shock construction for $M = 10$ . (a) In the absence of trapping, $\epsilon = 0$ , the construction for advancing and receding shocks is the same. (b) In the presence of trapping, $\epsilon = 1/2$ , the shock construction for advancing shocks is modified. (c) Shock speed as function of $\eta_L$ , for $\eta_L > \eta_c$ the shock speed depends on the amount of trapping. . . . .	97
3.15	Characteristic portraits of the evolution of initial data (3.71), in the $\xi\tau$ -plane. The current is bounded by the shock, $A$ to $D$ , in the back and the leading characteristic of the rarefaction, $F$ to $D$ , in the front. (a) Analytic solution for $M = 1$ and $\epsilon = 0.4$ . (b) Semi-analytic solution for $M = 5$ and $\epsilon = 0.4$ . (c) Evolution of the current interface (black) and the residual surface (grey). . . . .	100
3.16	(a) Portrait of the shock path and the leading characteristic of the rarefaction, for increasing residual. The locus of the termination points, $\tau_f = \tau_f[\xi_\uparrow]$ , is shown as a dotted line. (b) The corresponding temporal evolution of the shock strength, $\eta_s$ . (c) The corresponding final residual surfaces, $\eta_r = \eta_r[\tau_f]$ . . . . .	102
3.17	Contour plots of the up-dip migration distance, $\log(\xi_\uparrow)$ , on the left and of the total migration time, $\log(\tau_f)$ , on the right. The data for several potential storage aquifers in Alberta, Canada, is shown as circles to indicate typical parameter values (Bachu & Bennion, 2007). . . . .	103

3.18	The effect of the governing parameters on the evolution of the current volume. The passing and final migration times, are shown as circles and triangles. (a) Increasing the residual, $\epsilon$ , from 0.1 to 0.9 at constant $M = 1$ . (b) Increasing the mobility ratio, $M$ , from 1 to 40 at constant $\epsilon = 0.4$ . Circles denote . . . . .	105
3.19	This figure shows several comparisons between the numerical solution ( $\Delta\xi = 0.01$ ) to (3.7a) and the hyperbolic solution for $Pe = 2$ at $\tau = 50$ . (a) Increasing $M$ at constant $\epsilon = 0$ . (b) Increasing $\epsilon$ at constant $M = 10$ .	106
3.20	Evolution of the current volume, $\mathcal{V}$ , as a function of diffusive dimensionless time, $\vartheta$ , for $M = 5$ and increasing $Pe$ . The time axis at the top gives dimensional values corresponding to the parameter choice discussed in §3.5.2, assuming $\cos\theta \approx 1$ . . . . .	107
3.21	Time and length scales obtained from the numerical solution of (3.7) are shown as symbols ( $\Delta\xi = 0.01$ ). All results are for a residual of $\epsilon = 0.4$ . The limiting hyperbolic and self-similar solutions are indicated by full and dashed lines. (a) Down-dip migration distance, $\xi_{\downarrow}$ . (b) Transition time, $\tau_t$ . (c) Up-dip migration time, $\xi_{\uparrow}$ . (d) Final migration time, $\tau_f$ . . . . .	109
3.22	Contour plots of the critical angle, $\theta_c$ , assuming $d_0 = 2$ and the sweep, $\mathcal{S}$ , as function of $M$ and $\epsilon$ . The data for several potential storage aquifers in Alberta, Canada, is shown as circles to indicate typical parameter values (Bachu & Bennion, 2007). . . . .	115
4.1	An example of a typical regional aquifer under consideration for $CO_2$ storage, the Carrizo Formation in east Texas is shown in grey. The figure is vertically exaggerated 16:1, so that the true aspect ratio is much larger than it appears in the figure. The sketch is simplified from Nicot (2008). . . . .	121

4.2	(a) Nine cells of the finite volume grid are shown by dashed lines. The four dual interaction regions, $\tilde{\Omega}^{(1)}$ to $\tilde{\Omega}^{(4)}$ , which connect the shaded finite volume cell in the center to its eight nearest neighbors are shown by solid lines. (b) A dual interaction region is shown with the four coarse cell boundary segments labeled $s_1$ to $s_4$ and the corresponding fluxes $f_1$ to $f_4$ .	127
4.3	The top row shows contour plots of the four standard basis functions of the MSFV method, calculated numerically for a heterogeneous, isotropic fine permeability distribution. The second row shows the underlying dual interaction region with the fine grid and the fine fluxes $\mathbf{t}_{m,k}^*$ along the coarse boundaries (small arrows) and the total coarse fluxes $t_{m,k}$ integrated over each face (big arrows).	133
4.4	The fine-scale solution as well as the reconstructed conservative and the interpolated multiscale solutions are shown for the same problem. The log of the permeability is shown at the base of each figure. A unit pressure gradient is applied in the $x$ -direction, and homogeneous Neumann boundary conditions are applied in the $y$ -directions. (a) The fine-scale solution, $p_h$ . (b) The conservative solution from the flux reconstruction on the fine grid, $\bar{p}_h$ . (c) The coarse solution, $p_H$ , interpolated onto the fine grid using the MSFV basis functions, $\hat{p}_h$ . In (b) and (c) the coarse solution, $p_H$ , is shown as large black dots.	136
4.5	Three solution profiles in the $x$ -direction located at $y = 1/2$ are shown for increasing values of the ratio $a/b$ with $c = 0$ . (a) anisotropy ratio, $a/b = 1 > 1/3$ , corresponding to $A = \Delta x/\Delta y = 1$ . (b) anisotropy ratio, $a/b = 1/100 < 1/3$ , corresponding to $A = 10$ . (c) anisotropy ratio, $a/b = 1/2500 < 1/3$ , corresponding to $A = 50$ .	139
4.6	Numerical results for the stencil components $m_{1,0}$ and $m_{1,1}$ of the MSFV method are compared to the analytic expressions of the MPFA O(1) method. The components are shown as a function of the orientation of the tensor, $\theta$ , for several ratios of the principal components, $\lambda_1/\lambda_2$ .	141

4.7	The monotonicity regions of the original and compact coarse operator are shown in the parameter space $a/b$ vs. $ c /b$ . A gray grid shows the corresponding angle, $\theta$ , and the ratio of principal components, $\lambda_1/\lambda_2$ in the effective permeability tensor given by (4.35). All methods are monotone above the labeled line. (a) The monotonicity regions of both the MPFA O(1) method and the coarse operator of the MSFV method are compared. (b) The monotonicity region of the CMSFV method equals that of the 7-point stencil. . . . .	143
4.8	The triangular domains of dependence of the fluxes in a dual interaction region are shown for both signs of $c$ . The corresponding orientation of the permeability tensor is indicated by the ellipses. . . . .	145
4.9	The approach of the global fine-scale solution to transverse equilibrium, as the effective anisotropy $a/b$ increases. The boundary conditions for this problem are $p(x = 0, y) = 1$ , $p(x = 1, y) = 0$ , and $p_y(x, y = 0, 1) = 0$ and the effective permeability on the fine-scale is diagonal, $c = 0$ . The log of the permeability field is shown at the base. . . . .	148
4.10	Comparison between the fine-scale solution $p_h$ and the interpolated pressure field $\hat{p}_h = \phi_{h_1} + \phi_{h_4}$ in a dual crossing the high permeability channel at $a/b = 1/1000$ . (a) Fine-scale solution, $p_h$ , in the dual, rescaled to a unit pressure gradient, is in transverse equilibrium. (b) Interpolated fine pressure $\hat{p}_h$ with reduced boundary conditions. (c) Interpolated fine pressure $\hat{p}_h$ with linear boundary conditions. (d) Interpolated fine pressure $\hat{p}_h$ with hybrid boundary conditions. . . . .	151
4.11	(a) The unit square domain $\Omega$ , with a $20 \times 20$ coarse grid. The back squares indicate coarse blocks with sources $f_H = \pm 1$ . In these blocks the fine-scale permeability is constant at the mean to give a uniform distribution of the fine-scale flux. (b) A realization of the permeability field with small correlation length. Figures c and d show realizations of the layered permeability fields at angles of $15^\circ$ and $-30^\circ$ respectively. The logarithm of the permeability is shown in all cases. . . . .	154

4.12	Comparison of time of flight maps between multiscale methods and the fine-scale solution for three isotropic but heterogeneous fine-scale permeability fields. All solutions are shown at the same injected volume, corresponding to the breakthrough of the fine-scale solution. The fine-scale solution, $fs$ , is shown in the first row, $a$ to $c$ , the original $MSFV$ -red method in the second row, $d$ to $f$ , the $CMSFV$ -lin method in the third row, $g$ to $i$ , and the $CMSFV$ -hyb method in the fourth row, $j$ to $l$ . The first column shows solutions for a realization of the permeability field shown in figure 4.11b, columns 2 to 3 show solutions for realizations of layered permeability fields at $15^\circ$ and $-30^\circ$ (figure 4.11c and d). . . . .	155
4.13	Comparison of time of flight maps between multiscale methods and the fine-scale solution for three heterogeneous fine-scale permeability fields with grid aligned fine-scale anisotropy, $a/b = 0.01$ . All solutions are shown at the same injected volume, corresponding to the breakthrough of the fine-scale solution. The figure layout is the same as in figure 4.12.	156
4.14	Figures $a$ and $b$ show the mean $L_2$ -errors of the interpolated solution $\hat{p}_h$ and the reconstructed flux field $\bar{\mathbf{u}}_h = -k\nabla\bar{p}_h$ as function of the orientation, $\theta$ , of the fine-scale layering for isotropic fine-scale permeability, $a/b = 1$ . Figures $c$ and $d$ show the same for grid aligned fine-scale anisotropy $a/b = 0.04$ ( $\Delta x/\Delta y = 5$ ). All values shown are means over 20 realizations and the standard deviations are shown as vertical bars, if they are larger than the symbols. . . . .	158
4.15	Figures $a$ and $b$ show the mean $L_2$ -errors of the interpolated solution $\hat{p}_h$ and the reconstructed flux field as function of increasing fine-scale anisotropy $a/b$ . All values shown are means over 20 realizations of the permeability field shown in figure 4.11a. . . . .	160

4.16	Results for the quarter 5-spot shown in figure 4.11a with homogeneous Dirichlet boundary conditions. The first column shows contour maps of $\hat{p}_h$ , the second column shows a horizontal view of $\hat{p}_h$ along the $y$ -axis, and the third column shows streamlines obtained from the conservative reconstruction $\bar{p}_h$ . Figures $a$ to $c$ show the results for MSFV- <i>lin</i> , figures $d$ to $f$ show results for MSFV- <i>hyb</i> , and figures $g$ to $i$ show results for CMSFV- <i>hyb</i> . . . . .	161
4.17	The $L_\infty$ and $L_2$ -norms of $M(\mathbf{L}_H)$ are shown as a function of the angle of the layering. Figures $a$ and $b$ show results for a isotropic fine-scale permeability field ( $a/b = 1$ ), while figures $c$ and $d$ are for a fine-scale anisotropy $a/b = 1/100$ . . . . .	163



# Chapter 1

## Introduction

### 1.1 Carbon capture and storage

Carbon Capture and Storage (CCS) involves capturing the CO<sub>2</sub> arising from industrial processes and transportation to a suitable storage site, where most of it will be sequestered from the atmosphere permanently. CO<sub>2</sub> capture is more easily applied to large point sources, such as fossil fuel power plants, fuel processing plants and plants for the manufacture of iron, steel, cement and bulk chemicals, than to dispersed emission sources. The transport of large quantities of carbon dioxide from the source to the storage site will require a large network of pipelines. Currently carbon dioxide pipelines extend over more than 2500 km in the western US, where they carry 50 MtCO<sub>2</sub>/yr from natural sources to enhanced oil recovery projects in West Texas and elsewhere (Metz *et al.*, 2006). Several geological storage repositories have been suggested, including depleted oil and gas reservoirs, unmineable coal beds, saline aquifers, and deep sea sediments. Gigatonnes of CO<sub>2</sub> per year must be stored in the subsurface to make a significant contribution to the mitigation of climate change (Metz *et al.*, 2006). The capture and storage of carbon dioxide can be implemented at a large scale by applying known technology developed for other purposes, that are is technically feasible today (Metz *et al.*, 2006).

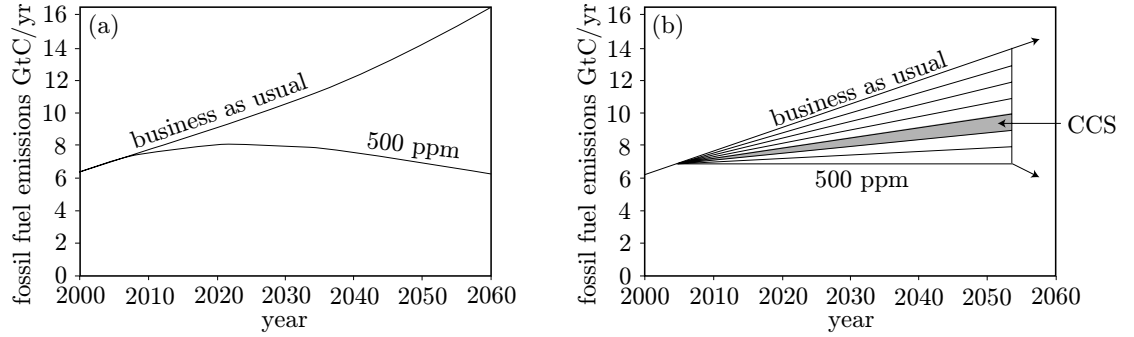


Figure 1.1: (a) Predicted emission scenarios. The line labeled 500 ppm is the emissions scenario necessary to stabilize the  $\text{CO}_2$  concentration at approximately twice the preindustrial average. (b) Schematic version of figure a, showing the 7 stabilization wedges. Both graphs are modified from Pacala & Socolow (2004).

### 1.1.1 Clean coal technology

According to the U.S. Department of Energy, the term clean coal technology describes a new generation of energy processes that sharply reduce air emissions and other pollutants from coal-burning power plants.

Coal is a cheap mainstay of electricity generation in both the developed and developing world, and its use is projected to increase. Coal has the highest carbon content of all fossil fuels, and its increased use will worsen the climate change problem (Katzer, 2007). The large-scale implementation of CCS is therefore an important part of clean coal technology. CCS allows significant reduction in  $\text{CO}_2$  emissions while allowing coal to meet future energy needs. However, critics warn that CCS should not be seen as a silver bullet to reducing emissions, nor should it be researched and developed at the expense of other environmentally sound, technologically feasible, and economically affordable solutions to climate change (Union of Concerned Scientists, 2001).

It is hoped that limiting atmospheric  $\text{CO}_2$  concentrations to less than double the preindustrial concentration of 280 ppm will prevent the most damaging climate change. This requires that emissions are held constant at 7 billion tons of carbon per year (GtC/yr) for the next 50 years, while the current trend will lead to emissions of

approximately 14 GtC/yr in 2060 (figure 1.1*a*). Pacala & Socolow (2004) have introduced the concept of a stabilization wedge (figure 1.1*b*), as an activity that reduces emissions to the atmosphere that starts at zero today and increases linearly until it accounts for 1 GtC/yr of reduced carbon emissions in 50 years. A few examples of such activities are: efficient vehicles and buildings, substitution of gas baseload power for coal baseload power, substitution of nuclear, wind or photovoltaic power for coal power, biomass fuel for fossil fuel, and CO<sub>2</sub> capture at baseload power plants, H<sub>2</sub> plants or coal-to-synfuel plants. Seven stabilization wedges are necessary to avoid a doubling of preindustrial atmospheric CO<sub>2</sub> concentrations. Currently, no single available technology can provide even half of the necessary emission reductions. However, Pacala & Socolow (2004) argue that the necessary reductions in carbon emissions are already possible with a portfolio of options available today. They have identified 15 activities, including those listed above, which can contribute one stabilization wedge each.

Assuming that CCS prevents 90% of the fossil carbon from reaching the atmosphere, a stabilization wedge could be achieved by the installation of 800 GW of baseload coal power plants with carbon capture. The associated geological storage would require that current CO<sub>2</sub> injection, for enhanced oil recovery, be scaled up by a factor of 100 over the next 50 years, or the equivalent of 3500 storage projects comparable to the current CO<sub>2</sub> storage operations at the Sleipner-Vest natural gas field, operated by Statoil (Torp & Gale, 2004).

### 1.1.2 Geological CO<sub>2</sub> storage

Geological storage of anthropogenic CO<sub>2</sub> as a mitigation option for climate change was first proposed by Marchetti (1977). No further published research was done until the Norwegian Parliament decided to stabilize Norway's CO<sub>2</sub> emissions at the 1989 levels by the year 2000 and introduced a carbon tax, approximately equal to 50 \$/ton CO<sub>2</sub>, on CO<sub>2</sub> emissions from burning natural gas offshore. In response to this, Statoil initiated small-scale CO<sub>2</sub>-storage tests in 1989 (Kaarstad, 1992). The options for geological storage were first fully explored during the First International

Conference on Carbon Dioxide Removal in Amsterdam in 1992. Storage in saline aquifers (Kaarstad, 1992; Koide *et al.*, 1992), depleted oil and gas reservoirs (van der Burgt *et al.*, 1992), as well as a combination of enhanced oil recovery with CO<sub>2</sub> storage (Bondor, 1992; Legg, 1992; van der Meer, 1992) were proposed. The storage of CO<sub>2</sub> in deep sea sediments is distinct from aquifer storage on land or on the continental shelf, due to the neutral buoyancy of the injected CO<sub>2</sub> and the potential of a self-sealing CO<sub>2</sub> hydrate cap (Koide *et al.*, 1995, 1997; House *et al.*, 2006). Enhanced coal bed methane recovery from unminable coal seams also provides a possibility for geological CO<sub>2</sub> storage (Stevens *et al.*, 2001). Some have argued that CO<sub>2</sub> can be stored in basaltic rocks in regions where large sedimentary basins are not common, such as the Indian subcontinent (McGrail *et al.*, 2006). However, questions remain about the potential for leakage through fractures that are very common in basalts.

The worldwide storage capacity in depleted oil and gas fields is estimated between 675 and 900 GtCO<sub>2</sub>, the capacity of unminable coal seams is estimated between 3 and 200 GtCO<sub>2</sub>, and the capacity of saline aquifers is at least 1000 GtCO<sub>2</sub> and possibly up to 10000 GtCO<sub>2</sub> (Metz *et al.*, 2006). House *et al.* (2006) initially estimated that the economic zone of the US alone has a storage capacity of more than 10000 GtCO<sub>2</sub>. More recently, Levine *et al.* (2007) showed that the average formation permeability and geomechanical considerations may limit the storage capacity substantially. McGrail *et al.* (2006) estimate that the Columbia River Flood Basalt Province alone has a CO<sub>2</sub> storage potential greater than 100 GtCO<sub>2</sub>. The Deccan Volcanic Province in India has roughly three times the volume of the Columbia River Flood Basalt Province, and it may be an important storage option.

CO<sub>2</sub> storage combined with enhanced oil recovery or enhanced coal bed methane recovery is favorable, because hydrocarbon recovery will offset a part or all of the costs associated with CCS. Unfortunately, the storage capacity of these systems is limited, and CO<sub>2</sub> may have to be transported over long distances from the CO<sub>2</sub> sources in urban areas to the storage locations in hydrocarbon provinces. Carbon storage on a scale large enough to make a significant contribution to the reduction of CO<sub>2</sub> emissions, appears to be viable in saline aquifers. The source-sink matching is easiest for saline aquifers, because many urban areas are located on sedimentary

basins. As of today, there are no economic benefits associated with storage in saline aquifers that can help offset the storage cost. Therefore, other incentives, such as the carbon-emissions tax in Norway, must be in place for the adoption of aquifer storage. Since CO<sub>2</sub> emission regulations, taxes, or both, are expected in the near future, saline aquifer storage is currently the most promising large-scale geological storage option. Therefore, this thesis focuses on accurate mathematical modeling of the complex flow behaviors associated with CO<sub>2</sub> storage in saline aquifers.

## 1.2 Saline aquifer storage

The term saline aquifer or saline formation is used to identify deep sedimentary rocks saturated with formation waters or brines, which contain high concentrations of dissolved salts. Due to their high salinity, these brines are not used as sources of drinking water and cannot be used for irrigation. On the contrary, unsustainable exploitation of shallow groundwater resources may lead to upconing of underlying brines and to a subsequent deterioration of the water quality (Zhou *et al.*, 2003). In some locations deep brines are used for low-temperature geothermal power generation (Lund *et al.*, 2005). In other areas, deep aquifers are used for the injection of drilling slurries (Reed *et al.*, 2002), hazardous chemical waste (Saripalli *et al.*, 2000), and liquid radioactive waste (Rumynin *et al.*, 2005). In comparison with the enormous volumes of saline aquifers available, only a negligible fraction is currently used.

Saline aquifers occur in sedimentary basins throughout the world and are not restricted to coal, oil, or gas provinces. Holloway & Savage (1993) have argued that CO<sub>2</sub> should be injected at depths greater than 800 m. For a geothermal gradient of 25 °C/km, this is the depth required for CO<sub>2</sub> to be in a dense supercritical state, although this depth may vary between 650 and 1200 m in a particular sedimentary basin (Bachu & Stewart, 2002).

Carbon dioxide is injected in the supercritical state to decrease the storage volume, but the long-term storage capacity of an aquifer is determined by the amount of CO<sub>2</sub> that can be dissolved into the brine (Bachu & Adams, 2003). Supercritical CO<sub>2</sub> is less dense than the brine under all continental and shallow marine storage conditions.

An impermeable seal, such as a shale or clay layer, overlying the storage formation is therefore always necessary to prevent upward migration of the injected CO<sub>2</sub> towards the surface. To prevent upward migration of the CO<sub>2</sub> along an inclined seal towards the surface a structural trap, (figure 1.4a), is thought to be necessary for long-term storage security. Based on these and other criteria, Bachu (2003) have proposed a screening and ranking methodology to identify suitable storage aquifers.

CCS projects targeting saline aquifers are under discussion in many countries, including Norway, the US, Japan, Canada, Australia, the UK, France, Germany, Italy, and Poland (Metz *et al.*, 2006). The Sleipner Project, a gas field operated by Statoil on the Norwegian continental shelf, is a good example of CO<sub>2</sub> storage in a saline aquifer. Approximately 1 MtCO<sub>2</sub>/yr is removed from the natural gas stream produced at the Sleipner-Vest platform and injected into the Utsira formation. The operation started in October 1996, and over the lifetime of the project a total of 20 MtCO<sub>2</sub> is expected to be stored. The evolution of the Sleipner CO<sub>2</sub> plume has been successfully monitored by seismic time-lapse surveys. The surveys also show that the caprock prevents migration out of the storage formation (Torp & Gale, 2004).

### 1.2.1 Storage security and CO<sub>2</sub> migration

We expect that some fraction of the injected CO<sub>2</sub> will remain mobile and buoyant in the subsurface for several hundreds or even thousands of years. Therefore, the security of the storage depends strongly on the quality of the geological seal preventing upward migration. The geological seal in oil and gas fields is intact, because they have retained buoyant fluids over millions of years. As long as the integrity of the seal has not been compromised by hydrocarbon extraction, CO<sub>2</sub> stored in depleted oil and gas reservoirs is unlikely leak to the surface. In saline aquifers no such test of the seal integrity exists, and therefore leakage of CO<sub>2</sub> into the shallow subsurface and back into the atmosphere is a major concern that must be evaluated carefully. On the other hand, storage security is increased by physical and chemical processes in the subsurface that either make the CO<sub>2</sub> negatively buoyant or immobile. Such trapping processes progressively reduce the amount of CO<sub>2</sub> available for leakage, and increase

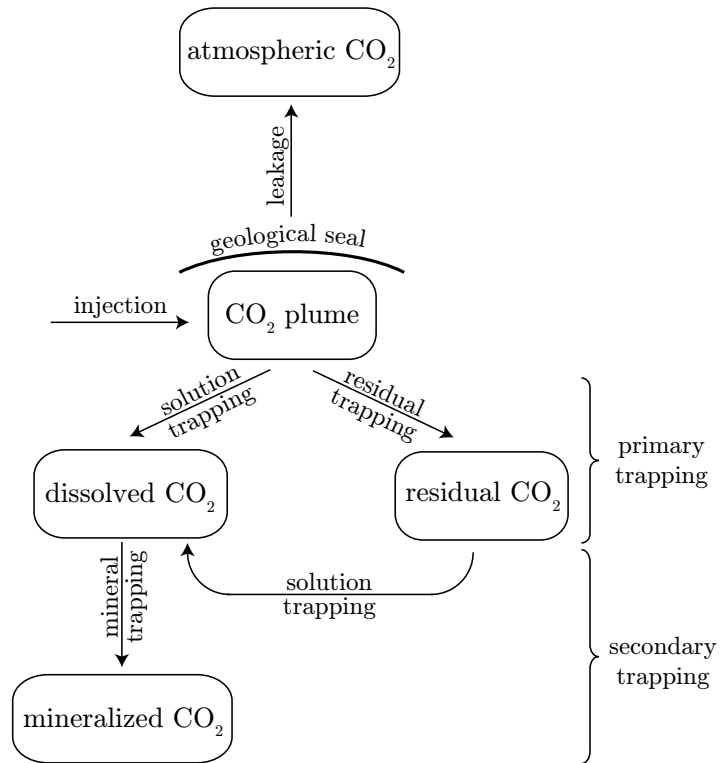


Figure 1.2: The different states of CO<sub>2</sub> in the underground together with the physical and chemical processes responsible for the transfer between these states.

the storage security over time (Metz *et al.*, 2006).

The redistribution of the injected CO<sub>2</sub> between different physical and chemical states is illustrated schematically in figure 1.2. The competition between leakage and trapping processes determines what fraction of CO<sub>2</sub> remains permanently in the subsurface.

### 1.2.2 Leakage mechanisms

Leakage of CO<sub>2</sub> stored in saline aquifers is a major concern, and the research in this field is growing rapidly. Given a laterally continuous seal and a structural trap, Metz *et al.* (2006) identify the following leakage pathways:

1. Through the pore system in low-permeability caprocks, such as shales, if the capillary entry pressure at which CO<sub>2</sub> may enter the caprock is exceeded.
2. Through openings in the caprock, such as lateral discontinuities or fractures and faults.
3. Through anthropogenic pathways, such as poorly completed and/or abandoned pre-existing wells.

Gasda *et al.* (2004) have identified abandoned wells as one of the most probable leakage pathways for CO<sub>2</sub> storage projects, due to their high density in many sedimentary basins, i.e., 350000 wells in the Alberta basin. Nordbotten *et al.* (2004) have used semi-analytic solutions to show that leakage through multiple passive wells is not a simple sum of single well leakage rates, due to leakage induced draw-down around passive wells. They have also identified that multiple aquifers and aquitards mitigate leakage into shallow zones, because of loss of CO<sub>2</sub> into the intervening aquifers. Numerical comparisons under less restrictive assumptions have shown that the inclusion of additional processes leads to reductions in leakage rates (Ebigbo *et al.*, 2006).

Pruess (2005) showed that non-isothermal effects are important during leakage along faults and lead to a self-limiting behavior of the leakage rate. In case CO<sub>2</sub> does leak into the shallow subsurface, CO<sub>2</sub> will displace the lighter resident soil gas. Therefore, CO<sub>2</sub> concentrations may approach 100% in some parts of the vadose zone,



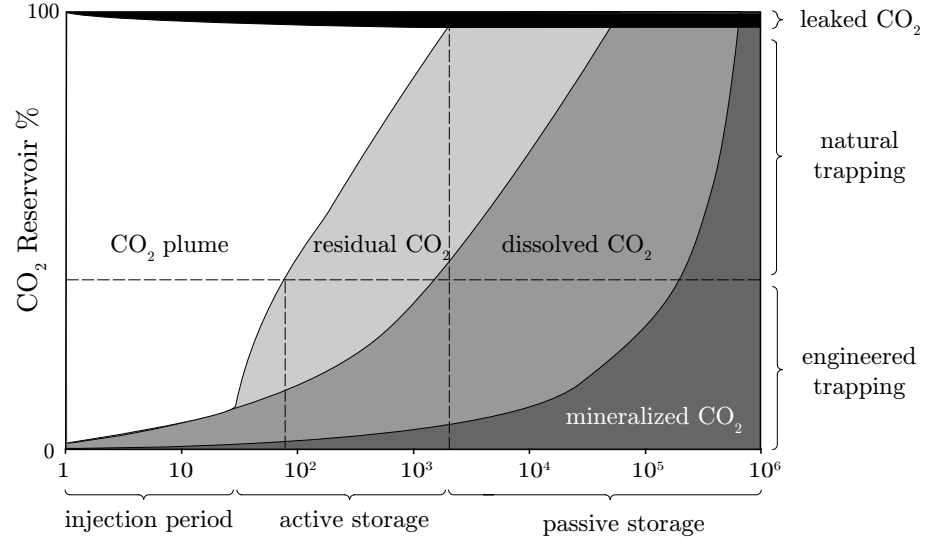


Figure 1.3: A schematic illustration showing the evolution of the fraction of  $\text{CO}_2$  in each state as a function of time, modified from Metz *et al.* (2006).

even for small leakage fluxes (Oldenburg & Unger, 2005). Leakage of  $\text{CO}_2$  plumes is similar to migration of plumes of volatile organic compounds, and similar remediation approaches may be applicable (Zhang *et al.*, 2005).

### 1.2.3 Trapping mechanisms

Carbon dioxide can leak from the geological storage formation back into the atmosphere, because it is mobile and positively buoyant with respect to the brine. Any process that either immobilizes  $\text{CO}_2$ , makes it negatively buoyant, or both, is considered a trapping mechanism. Three dynamic trapping mechanisms have been recognized in saline aquifers:

1. *Residual trapping*, which refers to the formation of residual  $\text{CO}_2$  through capillary snap-off in the wake of a migrating immiscible  $\text{CO}_2$  plume. Residual  $\text{CO}_2$  is still buoyant, but it is immobilized because it is disconnected from the flowing saturation. Holtz (2002) was among the first to point out the potentially large

residual saturations in CO<sub>2</sub>–brine systems. Kumar *et al.* (2005) showed that the formation of residual saturation may be the dominant trapping mechanism in saline aquifer storage, and they highlighted the importance of the magnitude and variation of the residual saturation in the formation as a key petro-physical property.

2. *Dissolution trapping*, which refers to the dissolution of CO<sub>2</sub> into the brine. Dissolved CO<sub>2</sub> is still mobile, through the migration of the CO<sub>2</sub>-rich brine. However, the brine density increases with increasing CO<sub>2</sub> saturation (Yang & Gu, 2006), and the negative buoyancy prevents leakage of dissolved CO<sub>2</sub> (Lindeberg & Wessel-Berg, 1997). Convective motion induced by dense plumes of CO<sub>2</sub>-rich brine may have the potential to increase the overall dissolution rate of the CO<sub>2</sub> significantly (Ennis-King *et al.*, 2005).
3. *Mineral trapping*, which refers to precipitation of dissolved CO<sub>2</sub> as carbonate or calc-silicate minerals. Gunter *et al.* (1997) have shown that the CO<sub>2</sub> trapping reactions are expected to take hundreds of years to complete. Xu *et al.* (2003) showed that the mineral trapping capability of arenaceous formations after 10,000 years is comparable to CO<sub>2</sub> dissolution in pore waters. Johnson & Nitao (2003) and others have argued that the feedback between the dissolution/precipitation and the formation permeability may be important.

Figure 1.2 illustrates the relationship between the different CO<sub>2</sub> trapping processes and the states of CO<sub>2</sub> in the subsurface. Mineralization offers the hope for permanent storage on geological timescales, but CO<sub>2</sub> is effectively trapped by dissolution and residual trapping much earlier. Therefore, we refer to direct dissolution of the mobile CO<sub>2</sub> plume and residual trapping as *primary trapping processes*, and to the dissolution of residual CO<sub>2</sub> and the mineralization of dissolved CO<sub>2</sub> as *secondary trapping processes*. Figure 1.3 is a conceptual sketch of the evolution of the different states of CO<sub>2</sub> over time.

During the injection period, the CO<sub>2</sub> plume contacts fresh brine as it is advancing into the aquifer, leading to some CO<sub>2</sub> dissolution. Residual trapping is expected to be very effective in the period immediately following the end of injection, as the

CO<sub>2</sub> migrates toward the top of the aquifer (Kumar *et al.*, 2005). It is possible to enhance trapping during the injection period and for some period after the end of injection, leading to *engineered trapping*. Examples of engineered trapping include water-alternating-gas injection (Kovscek & Cakici, 2005; Juanes *et al.*, 2006; Ide *et al.*, 2007), and the circulation of brine to increase dissolution (Leonenko & Keith, 2008). However, engineered trapping at large scales will increase the storage cost and is therefore unlikely in aquifers, where economic benefits do not offset the increased cost.

In most situations we have to rely on the trapping of CO<sub>2</sub> by natural processes, in the post-injection period. This reliance on *natural trapping processes* makes the proper selection of the storage site very important. This thesis focusses on *natural trapping processes* in the post-injection period. In situations where the immiscible CO<sub>2</sub> plume has ponded in a structural trap (figure 1.4a) and has come to rest, no further residual saturation forms, and dissolution of CO<sub>2</sub> into the underlying brine is the main process reducing the volume of the stationary CO<sub>2</sub> plume. As long as the immiscible CO<sub>2</sub> plume continues to migrate, CO<sub>2</sub> dissolves into fresh brine and residual CO<sub>2</sub> forms in the wake of the moving CO<sub>2</sub> plume (figures 1.4b-c).

We may also distinguish an *active storage period*, during which mobile buoyant CO<sub>2</sub> is present and leakage is possible, from a *passive storage period*, where CO<sub>2</sub> is only redistributed between trapped phases (figure 1.3). During the active period, leakage and trapping processes compete to reduce the mobile buoyant CO<sub>2</sub> volume. The active period ends when all injected CO<sub>2</sub> has either leaked or been trapped. The time when a CO<sub>2</sub> storage site switches from the active to the passive period is an important time scale that provides an indication of the storage security of a particular site.

### 1.3 Thesis overview

The concern about leakage of CO<sub>2</sub> from a storage site is a dominant theme in the technical literature and also the main concern of the broader public. An important part of the portfolio of measures to avoid leakage is to choose the storage site and

the injection scheme to accelerate trapping processes. Effective trapping reduces the time available for leakage, the active storage period, and is therefore crucial to storage security. Effective trapping also reduces the migration distance of the injected  $\text{CO}_2$ , which reduces the likelihood of encountering a leakage pathway. To estimate the trapping rates, we need to understand the underlying physics of the primary trapping processes, namely dissolution and residual trapping. We also need to ensure that numerical models used to predict storage performance are able to resolve these dynamic flow and transport processes adequately. Therefore, this thesis consists of two parts:

1. Chapters 2 and 3 present simple mathematical models that aim to capture the fundamental dynamics of dissolution and residual trapping.
2. Chapter 4 presents multiscale numerical algorithms for the numerical simulations of  $\text{CO}_2$  storage in large-scale heterogeneous formations.

We develop simple mathematical models of trapping processes to construct a conceptual framework to elucidate the relations among the driving forces, flow characteristics, and the rates of trapping. These models allow us to identify the dominant processes during  $\text{CO}_2$  storage and their associated length and time scales. This gives us first-order estimates of the duration of the active storage period and the migration distance, and how they depend on the average properties of a storage site. These simple estimates support the selection of storage sites, in particular at the beginning when limited data is available. Such a conceptual framework also allows us to understand and evaluate the results of complex numerical models.

The models of  $\text{CO}_2$  plume migration and trapping show the limitations of current numerical simulation tools for large-scale geological systems, and have lead us to the development of new multiscale methods for flow in heterogeneous porous media. In § 4 we present a robust framework for multiscale discretizations of heterogeneous elliptic equations, which lie at the heart of any reservoir simulator. This framework provides the core of a multiscale numerical method for  $\text{CO}_2$  storage; in the near future we hope to be able to simulate  $\text{CO}_2$  storage at the field scale, while resolving important trapping processes appropriately. We believe that such an approach has to

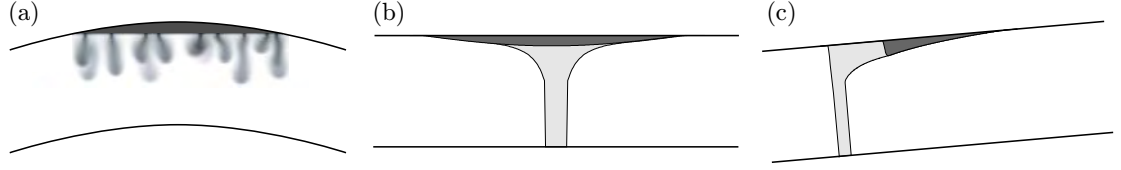


Figure 1.4: Sketches of the limiting cases investigated with simple process models: (a) Dissolution trapping of  $\text{CO}_2$  ponded in structural trap. (b) Residual trapping of  $\text{CO}_2$  migrating in a horizontal aquifer. (c) Residual trapping of  $\text{CO}_2$  migrating in a sloping aquifer. In all cases  $\text{CO}_2$  plume is dark gray, residual  $\text{CO}_2$  light gray, and dissolved  $\text{CO}_2$  shaded.

be adopted to obtain reliable predictions of the long-term evolution of  $\text{CO}_2$  plumes and the duration of the active storage period.

### 1.3.1 Process models for $\text{CO}_2$ trapping

To understand the two primary trapping processes we consider the three limiting cases shown in figure 1.4. In § 2 we assume that the injected  $\text{CO}_2$  has ponded in an anticline. In this scenario, no residual saturation forms and the volume of the plume decreases only by dissolution into the underlying brine (figure 1.4a). If the mass transfer of the dissolved  $\text{CO}_2$  is diffusive, then the dissolved  $\text{CO}_2$  will increase proportional to  $t^{1/2}$ . In this case, the active storage period is very long ( $>100,000$  yrs), and significant leakage may occur even if the leakage rate is small. However, the unstable density gradient in the brine may allow for convective mass transport of dissolved  $\text{CO}_2$ . Assuming the aquifer is large enough, the dissolved  $\text{CO}_2$  increases linearly. Rapid dissolution shortens the active storage period, and the cumulative leakage will be reduced significantly. A criterion that determines the dominant mode of mass transport is therefore very important. In § 2.2 we analyze the linear stability of the diffusive boundary layer, forming below the interface separating supercritical  $\text{CO}_2$  from the underlying brine, and determine the onset of convection as a function of average reservoir parameters. In § 2.3 we present preliminary results on two-dimensional dissolution rates in the fully non-linear regime using direct numerical simulations.

In § 3 we consider the spreading of CO<sub>2</sub> in horizontal and inclined aquifers (figure 1.4*b-c*). In both cases, the continued migration of the CO<sub>2</sub> plume leads to significant residual trapping. We have used a vertical-equilibrium sharp-interface model to study the migration of CO<sub>2</sub> plumes in the post-injection period. In § 3.3 we use similarity solutions to the governing equations to study the effect of vertical confinement on the migration of CO<sub>2</sub> plumes. We show that accounting for the confinement is important to obtain correct scaling laws for the CO<sub>2</sub> plume. In § 3.4 we study the migration of a CO<sub>2</sub> plume in a sloping confined aquifer. We show that the CO<sub>2</sub> migration can be approximated by a hyperbolic conservation law, if the aquifer is confined. This has allowed us to model residual trapping semi-analytically, and we have obtained estimates for the duration of the active storage period and the maximum migration distance. Comparison of our results for the sloping case with the self-similar solutions for horizontal aquifers shows that residual trapping is much more efficient in sloping aquifers.

### 1.3.2 Multiscale simulation of CO<sub>2</sub> storage

In § 3 we show that the CO<sub>2</sub> plume migrates like a traveling wave for tens and up to a few hundred kilometers. Accurate description of the interface separating the gravity current from the brine is necessary for reliable predictions of the transport behavior of CO<sub>2</sub> plumes, and this poses significant challenges for numerical models of the large-scale flow systems of interest.

Gravity currents form a narrow tongue that requires resolution at the sub-meter scale. In addition, we show in § 2 that the convective instability in high-permeability aquifers may require numerical resolution on the decimeter scale. The length scales associated with the physical processes during CO<sub>2</sub> storage may therefore span as much as six orders of magnitude in a sloping high-permeability aquifer. The fraction of the simulation domain that requires these high resolutions is generally small and may be associated with several features, such as multiple supercritical CO<sub>2</sub> plumes and interfaces between brine and potable ground water.

However, adaptive methods for multiphase flow and transport in heterogeneous

porous media are not well developed. This is partly because of upscaling and downscaling problems when the mesh size is changed. Recently, multiscale methods that work on a single coarse grid and incorporate finescale effects through numerical basis functions have been developed. Multiscale methods offer adaptivity through the selective updating of basis functions. In § 4 we discuss the multiscale finite volume (MSFV) method introduced by Jenny *et al.* (2003). The MSFV method is currently the only multiscale method for porous media transport that has been extended to include wells (Lee *et al.*, 2008), compressibility (Lunati & Jenny, 2006; Zhou & Tchelepi, 2008), and gravity (Lunati & Jenny, 2008). However, the original MSFV method is only robust for uniform grids, which prevents the application to saline aquifers that typically have very large aspect ratios. In chapter 4 we analyze the monotonicity of the original MSFV method, and we develop a new Compact Multiscale Finite Volume (CMSFV) discretization that is robust for large aspect ratios. Once these different results have been combined into a single multiscale simulator, the MSFV method should be able to simulate CO<sub>2</sub> storage in saline aquifers at dramatically reduced computational cost.

# Chapter 2

## Dissolution Trapping & Convection in the Brine

### 2.1 Introduction

Dissolution of the supercritical CO<sub>2</sub> into the brine is an important primary trapping process that reduces the volume of the CO<sub>2</sub> plume, and it therefore determines the duration of the active storage period (figure 1.3). Lindeberg & Wessel-Berg (1997) pointed out that the density of the brine increases with increasing CO<sub>2</sub> saturation, and Yang & Gu (2006) verified this for a CO<sub>2</sub>–brine system at reservoir conditions. Dissolved CO<sub>2</sub> is considered trapped, because the CO<sub>2</sub>-rich brine migrates downward and leakage is not likely. The associated reduction in the total volume of the system also allows the pressure in the aquifer to relax.

At an interface where both the supercritical CO<sub>2</sub> and the brine are at rest the dissolution of CO<sub>2</sub> will be slow. In this case, the dissolution rate of the CO<sub>2</sub> across the interface is controlled by molecular diffusion of dissolved CO<sub>2</sub> in the brine, and we expect the dissolution rate of CO<sub>2</sub> to decay as  $t^{-1/2}$ . Much more rapid dissolution of CO<sub>2</sub> occurs across an interface where the supercritical CO<sub>2</sub> continues to contact fresh brine, due to advection in either phase. Both the buoyancy driven migration of the supercritical CO<sub>2</sub> as well as convective motion in the brine can lead to rapid dissolution.



Once the  $\text{CO}_2$  plume has ponded in an anticline, only convective motion in the underlying brine can increase the dissolution rate of the  $\text{CO}_2$  (figure 1.4a). We assume that the supercritical  $\text{CO}_2$  is separated from the brine below by a horizontal interface. Across this horizontal interface,  $\text{CO}_2$  dissolves into the brine to form a diffusive boundary layer that grows with time (Lindeberg & Wessel-Berg, 1997). The  $\text{CO}_2$ -rich brine in this boundary layer is heavier than the underlying fresh brine. Once the boundary layer has grown to a sufficient thickness, it will become unstable, so that fingers of dense  $\text{CO}_2$ -rich brine propagate downward. In this case the dissolution rate is determined by convective mass transport in the brine.

We use both a linear stability analysis and direct numerical simulation to study the onset of this instability. Linear stability analysis is a standard method used to determine the stability of a particular base-state. In 2.2.3 we study the stability of the concentration profile of dissolved  $\text{CO}_2$  in the brine below the interface. If the concentration profile is unstable to small perturbations, convective motion in the brine will develop. The advantage of linear analysis is that it can detect very small unstable wavelengths, because it is not limited by numerical resolution. However, the linear analysis is valid only at early times when the perturbations are small. In §2.2.4 we validate the direct numerical simulations against the linear theory, and we use simulations to investigate the nonlinear evolution of the instability at larger times. These direct numerical simulations are used in §2.3 to study the long-term dissolution rate of  $\text{CO}_2$  in saline aquifers.

## 2.2 Onset of convection in the brine

### 2.2.1 Model problem

Numerical simulations of the full two-phase problem by Lindeberg & Bergmo (2003) have shown that the interface between the supercritical  $\text{CO}_2$  and brine, remains relatively sharp and is not deflected by the density fingering in the underlying brine, as shown schematically in figure 2.1. Both Lindeberg & Bergmo (2003) and Ennis-King & Paterson (2003) showed that local equilibrium between the supercritical  $\text{CO}_2$

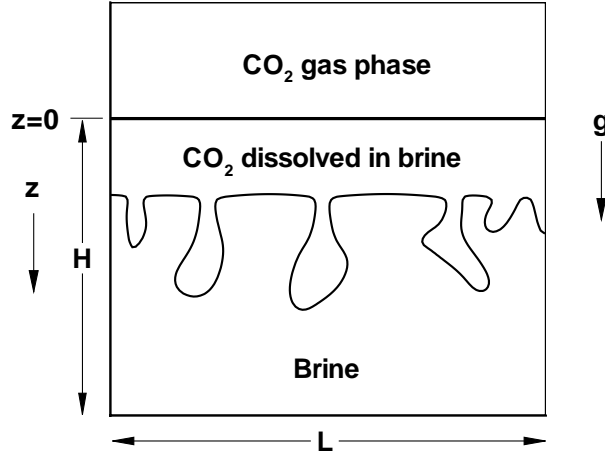


Figure 2.1: Supercritical  $\text{CO}_2$  accumulates along the impermeable top boundary. It slowly dissolves into the underlying brine, forming a heavier boundary layer. The resulting gravitational instability leads to the convective transport of  $\text{CO}_2$  saturated brine plumes.

and the brine can be assumed across the interface. We assume, therefore, that the supercritical  $\text{CO}_2$  layer acts as a horizontal upper boundary, with a constant  $\text{CO}_2$  concentration. These authors propose that the gravitational instability can be studied in the context of a finite domain, bounded at the top by a constant concentration boundary, using the Boussinesq approximation. This problem is analogous to thermal convection in a porous medium with insulated boundaries, that is rapidly heated from below, or cooled from the top, and initially at a fixed temperature. Elder (1967) showed that the diffusive layer at the boundary becomes unstable only after an initial period of decaying perturbations. After this critical time, plumes or fingers of hot fluid rise into the porous medium. This onset time for convection is an important timescale that determines the efficiency of dissolution trapping in saline aquifer storage.

### 2.2.2 Previous work

The stability of a concentration base profile to small perturbations depends on the nature of the base-state. For steady base-states, linear stability theory leads to an algebraic eigenvalue problem (Drazin & Reid, 1981; Nield & Bejan, 1999). The diffusive boundary layer, however, is a time dependent base-state, and linear stability theory leads to a non-autonomous linear system of ordinary differential equations. A common approach to such stability problems is the use of frozen time coefficients, the so-called quasi-steady-state approximation (QSSA). This assumption reduces the system of differential equations to a standard algebraic eigenvalue problem (Lick, 1964; Robinson, 1976). The QSSA is valid if the growth rate of perturbations is large compared to the growth rate of the diffusive boundary layer. Initially, when the boundary layer grows rapidly, the QSSA is not justified, but it becomes valid for large times when the base-state changes relatively slowly (Tan & Homsy, 1987; Riaz & Meiburg, 2003*a,b*). Gresho & Sani (1971) have shown that the QSSA is not valid for the onset of the instability of a thermal boundary layer in a viscous, incompressible fluid.

In order to avoid using the QSSA for small times, several authors have solved the initial value problem (IVP) numerically for a large number of random initial conditions. However, the solution of the initial value problem is sensitive to the particular initial conditions and is therefore not unique (Foster, 1965). Foster (1965, 1968), Gresho & Sani (1971) and Jhaveri & Homsy (1982) solved the IVP for a thermal boundary layer in a viscous, incompressible fluid. Caltagirone (1980) and Kaviany (1984) investigated the IVP for a thermal boundary layer in a porous medium due to a step change in temperature. Ennis-King & Paterson (2003) extended the analysis of Caltagirone (1980) to anisotropic porous media, and they applied it to CO<sub>2</sub> storage. All of these investigations give a wide range of critical times, depending on the particular method of measurement of the growth rate.

The stability of time dependent base-states can be investigated by energy methods (Homsy, 1973; Caltagirone, 1980). Energy methods give a lower bound for the onset of the instability, but give no information about the growth rate and wavenumber of the most dangerous disturbance.

For unbounded domains Pritchard (2004) and Ben *et al.* (2002) argue that a fundamental limitation on the accuracy of the solution at short times is the assumption of decoupled normal modes in the streamwise direction. Since the disturbances are confined within a narrow diffusive zone, the global Fourier eigenfunctions of the diffusion operator do not provide an optimal basis for streamwise perturbations (Pego & Weinstein, 1994). Ben *et al.* (2002) note that the Hermite polynomial based discrete eigenspectrum of the self-similar diffusion operator is the natural basis for streamwise perturbations in an unbounded domain. This eigenspectrum is the solution of the stability problem for the zero wavenumber. The first mode is neutral, it has zero growth rate, while the rest of the modes decay with time. Therefore, the first mode becomes dominant after a relatively short time. For small wavenumbers, the perturbation dynamics can then be projected onto this dominant mode to increase the growth rate from zero to positive values.

A similar approach is adopted here for the stability analysis in the semi-infinite domain. We use the self-similar transform of the diffusion operator in the inhomogeneous direction with localized eigenfunctions. The zero wavenumber solution shows that the first mode of the self-similar diffusion operator decays with time, while the rest of the spectrum decays more rapidly. We use this dominant first mode to capture the perturbation dynamics for larger wavenumbers, which shift the growth rate from negative to positive values at later times. We show that in contrast to the longwave instability in an unbounded domain, a critical time, critical wavenumber, and a long wavelength cutoff characterize the stability problem in the semi-infinite domain.

It is important to note that the dominant mode solution becomes inaccurate for large times and large wavenumbers. For these cases, we use the QSSA in self-similar coordinates, and we show by comparison with solutions to the IVP that the QSSA gives good results. Compared to the poor accuracy in the original coordinates, the success of both QSSA and IVP in self-similar coordinates is due to the localized basis functions in the streamwise direction.

In order to analyze the long-term evolution of the unstable modes predicted by the linear stability theory, we carry out high-accuracy direct numerical simulations (DNS) using a vorticity based formulation (Tan & Homsy, 1988). Voss & Sousa

(1987) have also carried out numerical simulations of density-driven flows. We use the methodology developed by Ruith & Meiburg (2000) using Fourier-Galerkin decomposition in the lateral direction and compact finite differences in the streamwise direction to solve for the velocity field. A 4<sup>th</sup> order Runge-Kutta method is used for time integration. The nonlinear simulations are validated by comparison to the linear stability analysis. Excellent agreement is observed at early times for growth rates associated with individual wavenumbers. The long time behavior, however, is characterized by complex nonlinear interactions that require DNS.

### 2.2.3 Linear stability analysis

#### Governing equations

The equations describing the Boussinesq-flow in a horizontal porous layer, where gravity points in the positive  $z$  direction, are:

$$\mathbf{u} = -\frac{K}{\mu} (\nabla P - \rho g \hat{\mathbf{z}}) , \quad (2.1)$$

$$\phi \frac{\partial C}{\partial t} = -\mathbf{u} \cdot \nabla C + \phi D \nabla^2 C , \quad (2.2)$$

$$\nabla \cdot \mathbf{u} = 0 , \quad (2.3)$$

$$\rho = \rho_0 + \Delta \rho C . \quad (2.4)$$

The normalized concentration  $C$  of the heavier fluid,  $\mathbf{u} = (u, w)$  is the Darcy velocity.  $K$  is the permeability,  $D$  is the diffusion coefficient,  $\phi$  is the porosity, and  $\mu$  is the viscosity. The unit vector in the direction of the gravitational acceleration is  $\hat{\mathbf{z}}$ . Density  $\rho$  is specified as a linear function of concentration, and  $\rho_0$  is the density of the lighter fluid. The initial conditions are  $\mathbf{u}(x, z, t = 0) = 0$  and  $C(x, z, t = 0) = 0$ , and the boundary conditions are given by

$$\begin{aligned} w(x, z = 0, t) &= 0, & w(x, z = H, t) &= 0, \\ C(x, z = 0, t) &= 1, & \left. \frac{\partial C}{\partial z} \right|_{x, z=H, t} &= 0. \end{aligned}$$

We define the following characteristic scales:

$$U = \frac{K \Delta \rho g}{\mu}, \quad (2.5)$$

$$\rho^* = \rho_1 - \rho_0 = \Delta \rho, \quad (2.6)$$

$$P^* = \frac{\mu U H}{K} = \Delta \rho g H, \quad (2.7)$$

$$t^* = \frac{\phi H}{U} = \frac{\phi \mu H}{K \Delta \rho g}. \quad (2.8)$$

where  $H$  is the domain thickness and  $U$  is the buoyancy velocity. The corresponding dimensionless equations are

$$\nabla \cdot \mathbf{u} = 0, \quad (2.9)$$

$$\mathbf{u} = -(\nabla P' - C \hat{\mathbf{z}}), \quad (2.10)$$

$$\frac{\partial C}{\partial t} = -\mathbf{u} \cdot \nabla C + \frac{1}{Ra} \nabla^2 C. \quad (2.11)$$

A modified pressure  $P' = \nabla(P - \rho_0 g \hat{z} / \Delta \rho g H)$  appears in the above equations. The Rayleigh number,  $Ra$ , is the only dimensionless parameter in the problem, which is defined as

$$Ra = \frac{U H}{\phi D} = \frac{K \Delta \rho g H}{\phi D \mu}. \quad (2.12)$$

The boundary conditions are given by

$$\begin{aligned} w(x, z = 0, t) &= 0 & w(x, z = 1, t) &= 0, \\ C(x, z = 0, t) &= 1 & \left. \frac{\partial C}{\partial z} \right|_{x, z=1, t} &= 0. \end{aligned}$$

We eliminate pressure by taking the curl of (2.10) and substitute the transverse velocity from the continuity equation. The streamwise velocity,  $w$ , and concentration are decomposed into the base-state and perturbation components

$$(w, c)(x, z, t) = (w_o, C_o)(z) + (\hat{w}, \hat{c})(z, t)e^{ikx} . \quad (2.13)$$

The base velocity,  $w_o$ , is zero, and the base concentration,  $C_o$ , is assumed constant in the  $x$ -direction and given by the solution of (2.11), with  $u = 0$ . The perturbation variables are decomposed into eigenfunctions, which depend on time and the streamwise coordinate, and normal modes in the transverse  $x$ -direction with wavenumber  $k$ . The linearized perturbation equations can then be expressed as

$$\left( \frac{\partial^2}{\partial z^2} - k^2 \right) \hat{w} = -k^2 \hat{c} , \quad (2.14)$$

$$\frac{\partial \hat{c}}{\partial t} - \frac{1}{Ra} \left( \frac{\partial^2}{\partial z^2} - k^2 \right) \hat{c} = -\frac{\partial C_o}{\partial z} \hat{w} , \quad (2.15)$$

with boundary conditions

$$\hat{c}(z = 0, t) = \hat{w}(z = 0, t) = 0 , \quad (2.16)$$

$$\left. \frac{\partial \hat{c}}{\partial z} \right|_{z=1, t} = \hat{w}(z = 1, t) = 0 . \quad (2.17)$$

Equation 2.11 admits a streamwise 1-D, base-state solution,  $C_o$ , which is

$$C_o(t, z) = 1 - \frac{4}{\pi} \sum_{n=1}^{\infty} \frac{1}{2n-1} \sin((n-1/2)\pi z) e^{-(n-1/2)^2 \pi^2 t / Ra} .$$

The length  $\delta(t)$  over which  $C_o$  is significantly different from zero is the so-called “penetration depth” of the diffusive boundary layer. For  $\delta \propto \sqrt{4t/Ra} \ll 1$ , the domain can be considered semi-infinite in the positive  $z$ -direction, and the base-state is given by

$$C_o(z, t) = 1 - \operatorname{erf} \left( z \sqrt{\frac{Ra}{4t}} \right) \quad \text{on } z \in (0, \infty) \quad (2.18)$$

with the boundary conditions

$$C_o(z = 0, t) = 1, \quad (2.19)$$

$$C_o(z \rightarrow \infty, t) \rightarrow 0. \quad (2.20)$$

The problem has now been redefined as the stability of a diffusive boundary layer in a semi-infinite domain. The parameter range over which the results are valid, for the original layer geometry in a finite domain, is given by  $\delta \propto \sqrt{4t/Ra} \ll 1$ . Note that the semi-infinite domain does not impose any external length scale on the problem. An internal length scale in the problem is the time dependent penetration depth  $\delta(t)$ . A Rayleigh number based on  $\delta(t)$  is itself time dependent, such that a critical Rayleigh number,  $Ra_c = Ra(\delta(t_c))$ , is merely a function of the critical time,  $t_c$ , at which the boundary layer becomes unstable. On the other hand, the Rayleigh number can also be scaled out of the equations by specifying the length scale as a ratio of diffusion to buoyancy velocity,  $H = D/U$ . In this case, the critical time,  $t_c$ , is the only criterion for the onset of instability. For our analysis, we choose to work with the latter. However, we retain the Rayleigh number, with an arbitrary length scale  $H$ , for convenience in comparing the linear stability analysis with the nonlinear results discussed in § 2.2.4. In the discussion of the dimensional results (§ 2.2.5), we show that the imposed length scale cancels out, so that the choice of length scale is arbitrary.

The perturbation equations (2.14-2.17) can be solved in a straight forward manner using the quasi-steady-state approximation (QSSA). Earlier investigations have shown that the QSSA gives accurate results for relatively long times. A fundamental problem with such an approach is that the concentration eigenfunctions are localized in the boundary layer, while the eigenfunctions of the operator  $\partial^2/\partial z^2$ ,  $z \in (0, \infty)$  have global support. Hence, they do not provide an appropriate basis for streamwise perturbations (Chang *et al.*, 1998). Therefore, a finite time is required, in the initial-value-problem (IVP), before the global eigenfunctions can accurately represent the localized structure of the streamwise perturbations. Since the critical time of this problem can relatively short, the QSSA in the original coordinate system may not



able to resolve the early time behavior appropriately.

### Localized eigenmodes of the diffusion operator

In a semi-infinite domain, we transform the perturbation equations such that the eigenfunctions associated with the streamwise diffusion operator are localized around the base-concentration front. The objective is to achieve considerable improvement in accuracy at small times, even with the QSSA. Following a coordinate transformation to the similarity variable of the base-state,  $\xi = z\sqrt{Ra/4t}$ , the base-state and the perturbation equations can be expressed as

$$C_o(\xi) = 1 - \text{erf}(\xi) , \quad (2.21)$$

$$\left( \frac{Ra}{4t} \frac{\partial^2}{\partial \xi^2} - k^2 \right) \hat{w} = -k^2 \hat{c} , \quad (2.22)$$

$$\frac{\partial \hat{c}}{\partial t} - \frac{1}{t} \left( \frac{1}{4} \frac{\partial^2}{\partial \xi^2} + \frac{\xi}{2} \frac{\partial}{\partial \xi} - \frac{k^2 t}{Ra} \right) \hat{c} = \sqrt{\frac{Ra}{\pi t}} e^{-\xi^2} \hat{w} , \quad (2.23)$$

with boundary conditions

$$\hat{c}(\xi = 0, t) = \hat{w}(\xi = 0, t) = 0 , \quad (2.24)$$

$$\hat{c}(\xi = \infty, t) = \hat{w}(\xi = \infty, t) = 0 . \quad (2.25)$$

Note that the self-similarity applies only to the base concentration. The amplitude and the spatial structure of perturbations are time dependent. The streamwise operator of the concentration perturbation in the transformed coordinate,  $\xi$ , is

$$\mathcal{L} = \frac{1}{4} \frac{\partial^2}{\partial \xi^2} + \frac{\xi}{2} \frac{\partial}{\partial \xi} , \quad \xi \in (0, \infty) . \quad (2.26)$$

We expand the perturbation concentration as

$$\hat{c}(\xi, t) = \sum_{n=1}^{\infty} A_n(t) \phi_n(\xi) , \quad (2.27)$$

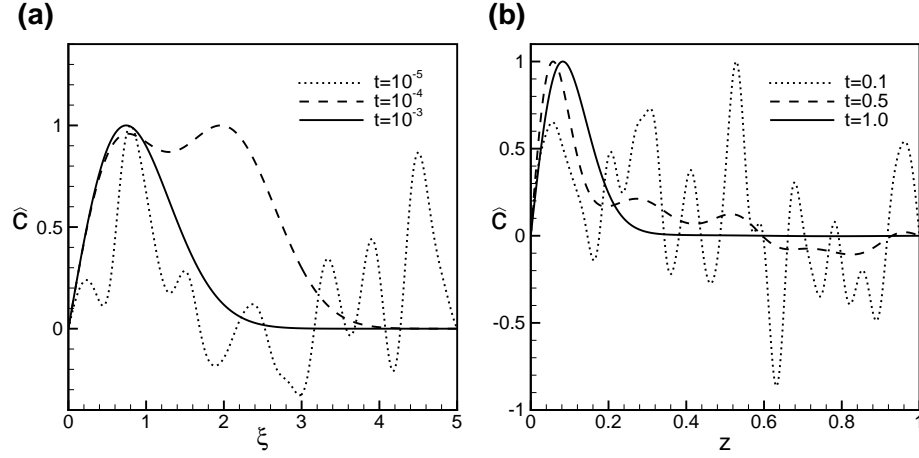


Figure 2.2: Disturbance concentration profile for  $Ra = 500$  and  $k = 0$  at different times, obtained from, (a) the IVP in the  $\xi$ - $t$  coordinate system with (2.21-2.23) and (b) the IVP in the  $z$ - $t$  coordinate system with (2.14-2.18). Random initial conditions are used for both cases. Plot (a) shows that the concentration profile resolves into the correct solution within a very short time, starting from any given set of white noise initial conditions. For the  $z$ - $t$  coordinate system on the other hand, plot (b), convergence is much slower and is strongly dependent on initial conditions.

with

$$\mathcal{L}\phi_n = \lambda_n\phi_n(\xi) = \lambda_n e^{-\xi^2} \mathcal{H}_n(\xi) \quad ; \quad n = 1, 2, 3, \dots \quad (2.28)$$

The eigenfunctions  $\phi_n$  of  $\mathcal{L}$  are the Hermite polynomials  $\mathcal{H}_n(\xi)$  in a semi-infinite domain with weight function  $e^{-\xi^2}$  (Robinson, 1976). The associated eigenvalues are  $\lambda_n = -n$  for  $n = 1, 2, \dots$ , and the dominant mode of the perturbation concentration is  $\phi_1 = \xi e^{-\xi^2}$ . These eigenfunctions, which are localized around the base-state, provide an optimal basis for streamwise perturbations in the semi-infinite domain (Pego & Weinstein, 1994). We note from (2.22) and (2.23) that for  $k = 0$  and using (2.27) the perturbation amplitude can be expressed as

$$\frac{dA_n}{dt} = \lambda_n A_n \quad . \quad (2.29)$$

All modes decay as  $t^{-n}$  for  $k = 0$ , so that the flow is stable in the longwave limit. The perturbation eigenfunction related to the largest eigenvalue,  $\phi_1 = \xi e^{-\xi^2}$ , decays

as  $1/t$ .

We solve the initial-value problem given by (2.21-2.23) to show that the preferred mode of the streamwise perturbations for  $k = 0$  is  $\phi_1$ . Figure 2.2(a) shows that the concentration eigenfunction resolves into the dominant mode of  $\mathcal{L}$ , given by  $\xi e^{-\xi^2}$ , in a very short time ( $t = \mathcal{O}(1/Ra)$ ) for any given set of white-noise initial conditions. We show in § 2.2.3 that the time required for convergence to the first eigenfunction is several orders of magnitude smaller than the critical time for the onset of instability. Therefore, the IVP in  $\xi$ - $t$  coordinates can yield accurate results for short times.

In order to highlight this phenomenon, figure 2.2(b) plots the perturbation eigenfunction in the  $z$ - $t$  coordinates, obtained by solving the IVP, given by (2.14-2.18). Although the white noise initial conditions converge to  $\hat{c} \sim z e^{-z^2 Ra/4t}$ , the time required for convergence is several orders of magnitude larger than in the self-similar coordinates, as shown in figure 2.2(a). Hence, the small-time dynamics in the  $z$ - $t$  coordinate system are obscured during the period it takes for the random initial perturbations to resolve into the dominant mode. This explains why earlier investigations using the IVP in the  $z$ - $t$  coordinate system did not produce accurate results. For the  $\xi$ - $t$  coordinate system, on the other hand, the localized eigenfunctions of  $\mathcal{L}$  converge rapidly to the exact solution, thereby giving an accurate growth rate of the disturbance at small times.

### Dominant mode solution

Robinson (1976) used a one-term approximation to the solutions in his QSSA analysis in  $z$ - $t$  coordinates, and he found that the error is small when compared to expansions using many terms. In the  $\xi$ - $t$  coordinates such a one-term approximation is expected to be even better, because we use an eigenfunctions expansion. We use the leading order approximation for  $\hat{c}$  from (2.27), substitute it into the IVP, given by (2.23), and integrate across the domain to obtain

$$\frac{dA_1}{dt} = -\frac{A_1}{t} - \frac{A_1 k^2}{Ra} + \sqrt{\frac{Ra}{\pi t}} \langle e^{-\xi^2} \hat{w} \rangle, \quad (2.30)$$

where

$$\langle e^{-\xi^2} \hat{w} \rangle = \frac{\int_0^\infty e^{-\xi^2} \hat{w} \, d\xi}{\int_0^\infty \xi e^{-\xi^2} \, d\xi} . \quad (2.31)$$

Again using only the leading order estimate of  $\hat{c}$  to solve for  $\hat{w}$ , we obtain

$$\left( \frac{\partial^2}{\partial \xi^2} - \frac{4tk^2}{Ra} \right) \hat{w} = -\frac{4tk^2}{Ra} A_1 \xi e^{-\xi^2} . \quad (2.32)$$

This can be solved analytically for  $\hat{w}$  to obtain

$$\begin{aligned} \hat{w} = -A_1 k \sqrt{\frac{t}{Ra}} \left\{ e^{2k\sqrt{t/Ra}} \left( \int_0^\xi \xi e^{-2kx\sqrt{t/Ra}-x^2} dx - B_1 \right) \right. \\ \left. - e^{-2k\sqrt{t/Ra}} \left( \int_0^\xi \xi e^{2kx\sqrt{t/Ra}-x^2} dx - B_2 \right) \right\} , \end{aligned} \quad (2.33)$$

where

$$\int_0^\xi \xi e^{-2kx\sqrt{t/Ra}-x^2} dx = -\frac{1}{2} e^{-2k\xi\sqrt{t/Ra}-\xi^2} - \frac{k}{2} \sqrt{\frac{\pi t}{Ra}} e^{k^2} \operatorname{erf} \left( \xi + k \sqrt{\frac{t}{Ra}} \right) , \quad (2.34)$$

and

$$\int_0^\xi \xi e^{2kx\sqrt{t/Ra}-x^2} dx = -\frac{1}{2} e^{2k\xi\sqrt{t/Ra}-\xi^2} + \frac{k}{2} \sqrt{\frac{\pi t}{Ra}} e^{k^2} \operatorname{erf} \left( \xi - k \sqrt{\frac{t}{Ra}} \right) . \quad (2.35)$$

The constants  $B_1$  and  $B_2$  are obtained by satisfying the boundary conditions  $\hat{w} = 0$  at  $\xi = 0, \infty$ . Using this value of  $\hat{w}(\xi, t)$ , we can then solve the integral in (2.31) numerically to obtain the amplitude equation for the dominant mode

$$\frac{dA_1}{dt} = \sigma(t; k) A_1 , \quad (2.36)$$

with growth rate  $\sigma$ . Equation 2.36 shows that the perturbations grow exponentially.

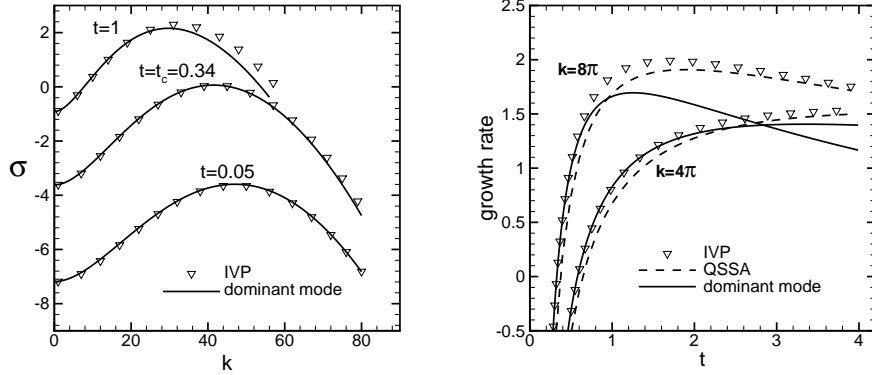


Figure 2.3: (a) Growth rate vs. wavenumber curves for  $Ra = 500$  computed by the dominant mode method and the IVP. The flow is stable for small times. The growth rate increases with time to become positive at the critical time  $t_c$  and the critical wavenumber  $k_c$ . Flow instability increases with time beyond  $t_c$  with both shortwave and longwave cutoffs. Comparison with the IVP shows exact agreement for small times and small wavenumbers. (b) Comparison of the dominant mode method and the QSSA with the initial value problem for two perturbation wavenumbers at  $Ra = 500$ . The dominant mode solution gives exact results for small times but becomes inaccurate for later times particularly for large wavenumbers. The QSSA on the other hand is reasonably accurate for all times.

The growth rate  $\sigma(t; k)$  is obtained without the QSSA and is expected to yield accurate results.

It is interesting to compare the above development for the semi-infinite case with that of the infinite case analyzed by Ben *et al.* (2002). The eigenfunctions of the self-similar operator in the latter case are the full range of Hermite polynomials, The associated eigenvalues are  $\lambda_n = -n/2$ , for  $n = 0, 1, 2, \dots$  resulting in a neutral mode for the zeroth eigenvalue. In a semi-infinite domain, on the other hand, the self-similar operator has eigenfunctions based upon only those Hermite polynomials which satisfy the boundary condition  $\hat{c}(\xi = 0, t) = 0$ . The associated eigenvalues are  $-1, -2, \dots$ ; therefore, a neutral mode is not present.

The presence of a zero eigenvalue in the unbounded case implies a longwave instability ( $\sigma = 0$ ) for  $k = 0$ , such that the flow is always unstable for small wavenumbers. For the semi-infinite domain, on the other hand, the dominant mode decays as  $t^{-1}$ ,

hence  $\sigma = -1/t$  for  $k = 0$ , so that the flow is always stable for small wavenumbers. A longwave cutoff therefore exists along with a critical time at which the flow becomes unstable.

The existence of a critical time as a function of the Rayleigh number has been noted previously (Ennis-King & Paterson, 2003; Ennis-King *et al.*, 2005). However, its exact value as well as the fundamental mechanism have not been given explicitly. Consider the growth rate, given by

$$\sigma(t; k) = -\frac{1}{t} - \frac{k^2}{Ra} + \frac{k}{\sqrt{\pi}} F(t; k) , \quad (2.37)$$

where  $F(t; k)$  is computed numerically from (2.31). Since  $F(t; k) > 0$  the stabilizing effects come from the first two negative terms on the left hand side. The first term,  $-1/t$ , which is due to the nonzero eigenvalue of the dominant mode of  $\mathcal{L}$ , insures that  $\sigma < 0$  for very small times. In physical terms, the flow can become unstable only when the perturbations grow at a rate faster than the decay rate of the first mode of  $\mathcal{L}$ .

It is important to note that selecting only the first mode to capture the perturbation dynamics cannot be accurate for the entire range of length and time scales of interest, in view of the absence of a neutral mode of  $\mathcal{L}$ . We show in § 2.2.3 that the dominant mode solution gives exact results in comparison with the IVP only for small values of  $k\sqrt{t/Ra}$ . Therefore, we use the QSSA for (2.21-2.25), to solve for the growth rates for larger values of  $k\sqrt{t/Ra}$ . We also show that when the QSSA is used with the governing equations in the self-similar coordinates, accurate results are obtained.

## Results

The growth rate vs. wavenumber curves given by both the dominant mode method and the numerical solution of the IVP are shown in figure 2.3(a) for different times. High accuracy numerical simulations of the IVP were carried out for each wavenumber  $k$  on a fine computational grid, by using standard methods for 1-D problems. The

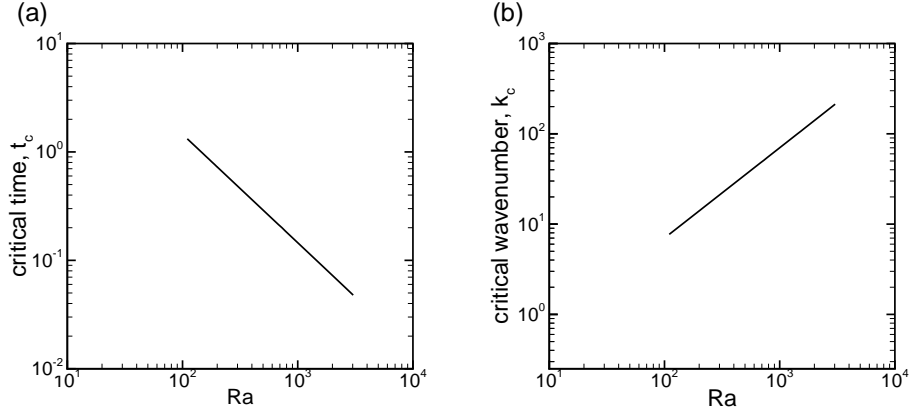


Figure 2.4: (a) Critical time vs.  $Ra$ . (b) Critical wavenumber vs.  $Ra$ , given by the dominant mode solution. The critical time varies as the  $1/Ra$ , while the critical wavenumber scales linearly with  $Ra$ .

evolution of the maximum value of either the concentration or the velocity eigenfunction forms the basis of the growth rate plotted at a particular time for each wavenumber. Completely stable behavior is indicated by  $\sigma < 0$  for all wavenumbers at early time. A critical time,  $t_c$ , is also shown when the growth rate just becomes positive at a critical wavenumber  $k_c$ . At larger times, the stability curve displays a maximum growth rate at a corresponding most dangerous wavenumber, and a longwave and a shortwave cutoff. Comparison of the dominant mode solution with the IVP results shows exact agreement for all wavenumbers at small times when  $k\sqrt{t/Ra}$  is small. For longer times, the growth rate begins to deviate from the IVP result at larger wavenumbers. However, the critical time and the longwave cutoff are computed exactly by the dominant mode solution.

Since the dominant mode solution does not give accurate results for large values of  $k\sqrt{t/Ra}$ , we use the QSSA in self-similar coordinates to compute the growth rates. Figure 2.3(b) compares the growth rate as a function of time obtained from the IVP with the results computed from the dominant mode method and the QSSA, for two wavenumbers. The dominant mode method again gives exact results for small times, but deviates from the IVP solution for large times, particularly for the larger wavenumber. The QSSA, on the other hand, gives reasonably accurate results for

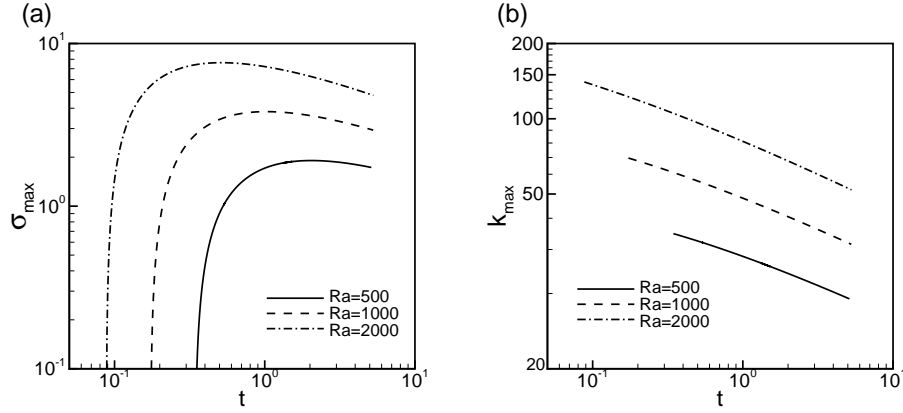


Figure 2.5: (a) Maximum growth rate  $\sigma_{\max}$  as a function of time, and (b) The most dangerous wavenumber  $k_{\max}$  as a function of time, for different Rayleigh numbers. All the results are obtained using the QSSA.

all times. This clearly shows that the QSSA in the self-similar coordinates can be employed to obtain reliable results even for short times.

Figures 2.4(a) and (b) respectively show the critical time and the critical wavenumber as a function of the Rayleigh number computed by the dominant mode method. The critical time varies as  $Ra^{-1}$ , while the critical wavenumber scales linearly with  $Ra$ . Similar scalings have been obtained by Caltagirone (1980), but our analysis eliminates the effect of the initial condition. We obtain  $t_c \approx 146/Ra$  and  $k_c \approx 0.07 Ra$  for the critical time and wavenumber. These relationships apply only when  $\sqrt{4t/Ra} \ll 1$ . The maximum growth rate as a function of time and the corresponding most dangerous mode for various  $Ra$ , computed by the QSSA, are shown in figures 2.5(a) and (b) respectively. The maximum growth rate,  $\sigma_{\max}$ , increases rapidly at early time beyond  $t_c$ , reaches a maximum value and decays approximately as  $t^{1/4}$  at late times. The most dangerous wavenumber  $k_{\max}$  also displays approximately  $t^{1/4}$  scaling.

The evolution of the longwave,  $k_l$ , and the shortwave,  $k_s$ , cutoff is plotted in figure 2.6. The former decays approximately as  $t^{1/5}$ , while the latter decays much faster as approximately  $t^{4/5}$  at long times.



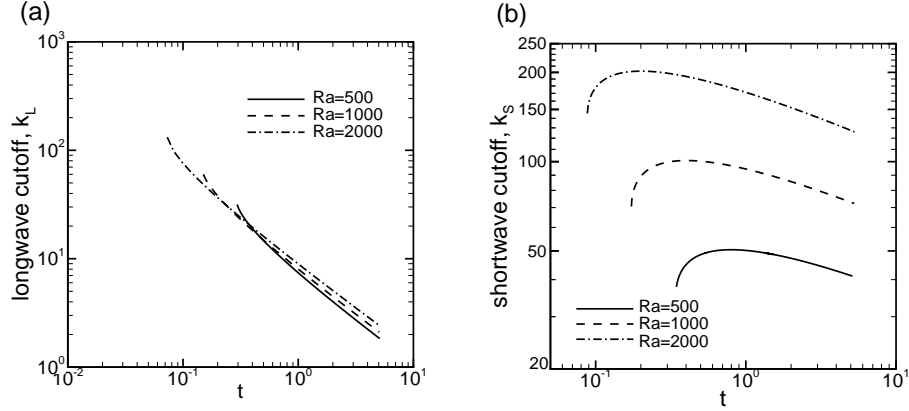


Figure 2.6: (a) The longwave cutoff wavenumber  $k_L$  as a function of time for different Rayleigh numbers, computed by the dominant mode method.  $k_L$  behaves similarly for all  $Ra$  and varies approximately linearly with time. (b) The shortwave cutoff  $k_s$  computed by the QSSA.

## 2.2.4 Direct numerical simulation

### Numerical method and validation of the numerical solution

Nonlinear fingering dynamics govern the long term flow behavior. We solve the nonlinear problem with a high accuracy, vorticity based method proposed by Ruith & Meiburg (2000). This method has been employed successfully to obtain highly accurate results for various miscible flow problems in porous media. (Camhi *et al.*, 2000; Riaz & Meiburg, 2003*b*, 2004*b*). High resolution finite-difference simulations have been reported recently by Otero *et al.* (2004), for high Rayleigh number convection in a porous layer of finite depth. They compare the numerical results with analytical heat flow estimates. We compare our numerical simulations with the results from the linear stability analysis.

The governing equations used for direct numerical simulations are (2.10) and (2.11). We use a vorticity formulation for (2.10) to eliminate pressure. By taking the curl of (2.10) we obtain,

$$\omega = -\frac{\partial C}{\partial x} = -\nabla^2 \psi, \quad (2.38)$$

where  $\omega$  is the vorticity and  $\psi$  is the streamfunction which is related to velocity as

$$w = \frac{\partial \psi}{\partial x} , \quad (2.39)$$

$$u = -\frac{\partial \psi}{\partial z} . \quad (2.40)$$

We assume the vorticity and streamfunction to be periodic in the transverse  $x$ -direction, and for concentration we impose symmetry conditions. The boundary conditions are therefore given by

$$C(z = 0, x, t) = 1 \quad , \quad \frac{\partial C}{\partial z}(z = 1, x, t) = 0 , \quad (2.41)$$

$$\frac{\partial C}{\partial x}(z, x = 0, t) = 0 \quad , \quad \frac{\partial C}{\partial x}(z, x = A, t) = 0 , \quad (2.42)$$

$$w(z = 0, x, t) = 0 \quad , \quad w(z = 1, x, t) = 0 , \quad (2.43)$$

$$u(z, x = 0, t) = 0 \quad , \quad u(z, x = A, t) = 0 . \quad (2.44)$$

The aspect ratio  $A = L/H$ , where  $L$  is the lateral extent of the computational domain and  $H$  is the layer thickness (figure 2.1). The streamfunction  $\psi = 0$  on all boundaries while  $\omega = 0$  at  $x = 0$  and  $x = A$ . Boundary conditions for vorticity at  $z = 0, 1$  are obtained from (2.38).

We solve the Poisson equation (2.38) by expanding  $\omega$  and  $\psi$  in Fourier modes in the  $x$ -direction. We then solve the resulting ODE for the decoupled  $z$ -direction eigenfunctions with 6<sup>th</sup> order compact finite differences (for details see Riaz & Meiburg, 2003b). The velocities are then computed from (2.39) and (2.40), where the derivatives of  $\psi$  are evaluated with 6<sup>th</sup> order compact finite differences. Time integration of (2.11) is carried out using a standard 4<sup>th</sup> order Runge-Kutta method, where all the spatial derivatives are again evaluated with 6<sup>th</sup> order compact finite differences. The resulting numerical scheme resolves all relevant length and time scales accurately. The initial condition for the concentration is given by (2.18) with a starting time of  $t = 0.2$ . The initial condition for velocity is  $w = u = 0$ .

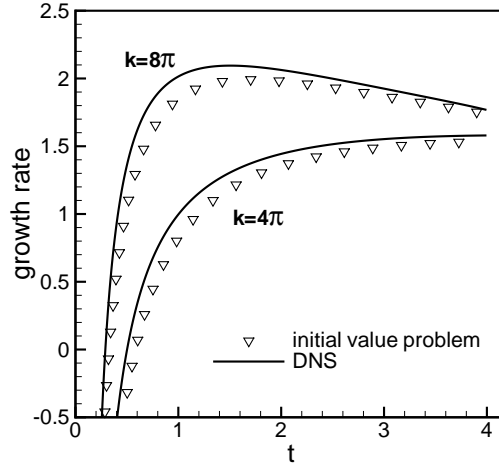


Figure 2.7: Comparison of the growth rates obtained from nonlinear direct numerical simulation and the linear initial value problem, for two different initial perturbations with wavenumber,  $k$ .

The explicit nature of time integration imposes a strict limit on the time steps. Although stable time steps are given by the CFL condition, we use even smaller time steps, on the order of  $10^{-5}$ , to insure accuracy. Spatial resolution of the computational grid ranges from  $512 \times 512$  grid points for small Rayleigh number cases to  $2048 \times 2048$  grid points for larger Rayleigh number cases. These fine spatial and temporal resolutions produce converged results. Appropriate grid spacing for different parameter combinations is obtained by consideration of the cutoff mode provided by the linear stability analysis. The grid spacing is chosen such that it is smaller than the cutoff wavelength. Additionally, the divergence of the velocity field is checked throughout to ensure exact mass conservation for a given grid spacing.

Validation of the numerical simulations was performed by comparing the growth rates with those obtained from the linear stability analysis. The numerical simulations are perturbed with pure sinusoidal modes in the transverse direction, superimposed on the initial concentration profile. The growth rate is measured using the norm of vorticity, defined as

$$\bar{\omega}(t) = \int_0^1 \int_0^A \omega(z, x, t) \, dx \, dz . \quad (2.45)$$

The growth rate for the numerical simulations is then defined as

$$\sigma_{\text{DNS}} = \frac{1}{\Delta t} \ln \left( \frac{\bar{\omega}(t)}{\bar{\omega}(t - \Delta t)} \right) . \quad (2.46)$$

Figure 2.7 shows that the growth rates for the two cases as a function of time for two wavenumbers, although not exactly equal, are in good agreement. The reason for this small discrepancy may be related to the 2-D nature of perturbations in the numerical simulations, which show a slightly higher rate of growth than those in the 1-D initial value problem.

### **The flow structure for $Ra = 4000$**

We begin our discussion of the nonlinear dynamics by analyzing the concentration contours for  $Ra = 4000$ . An aspect ratio,  $A = 1$  will be used throughout unless noted otherwise. In order to observe the nonlinear behavior, we perturb the initial concentration with white noise. The initial disturbances are localized within the diffusive zone to avoid unphysical conditions of  $C > 1$  or  $C < 0$ . The wavelength selection mechanism is largely independent of the amplitude and the particular values of the random initial perturbations.

Figure 2.8 presents the concentration contours at different times. This simulation was carried out with  $1024 \times 1024$  grid points. At an early time of  $t = 1$ , figure 2.8(a) shows a multitude of competing fingers. The number of fingers is about 24, which is close to 22, predicted by the linear stability analysis. In §2.2.4 we will precisely quantify the dominant wavenumber for nonlinear simulations and compare them with the linear stability results.

Figure 2.8(b) shows the concentration contours at a later time of  $t = 1.8$ . The number of fingers is much smaller than that at  $t = 1$ . This increase in the finger wavelength is primarily due to vigorous nonlinear interactions such as merging and shielding. Fingering instability in this case is reminiscent of viscous and gravitational instability of displacement type flows in porous media (Zimmerman & Homsy, 1992;

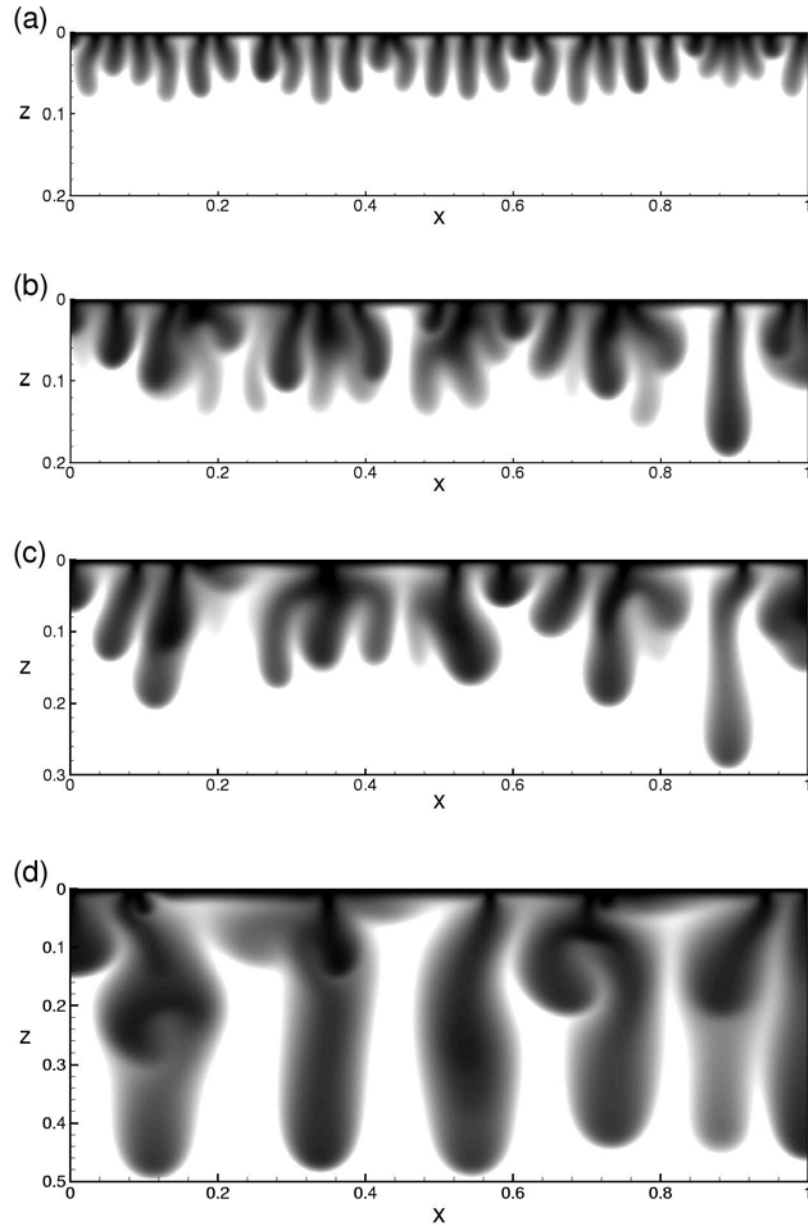


Figure 2.8: Concentration contours at different times for  $Ra = 4000$ . (a)  $t = 1$ , (b)  $t = 1.8$ , (c)  $t = 2.3$  and (d)  $t = 3.8$ . A large number of fingers consistent with the linear stability analysis develop initially. Nonlinear interactions rapidly reduce the number of fingers and give rise to large scale structures at later times. The fingers at later times are connected to the top boundary at discrete locations. These connections act as feeding sites of the high density fluid to the convecting fingers below.

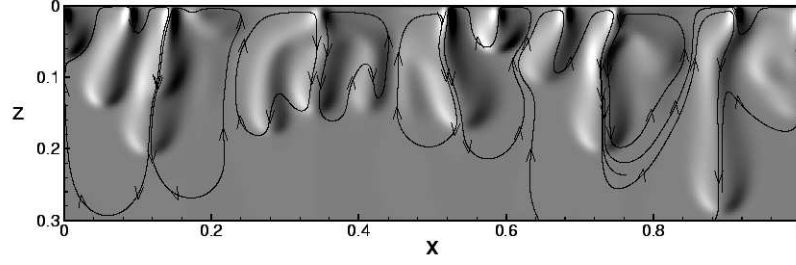


Figure 2.9: Vorticity contours in the background with overlapping streamlines for  $Ra = 4000$ ,  $t = 2.3$ . Corresponding concentration contours are shown in figure 2.8(c). The vorticity field has a dipole structure that drives the high density fluid through the fingers. The stream lines show how the fluid travels laterally and then descends through the isolated feeding sites for the fingers. The direction of fluid circulation is shown by the arrows.

Tchelepi & Orr , 1994; Manickam & Homsy, 1995). The driving force for instability, i.e. the density gradient, is weakened progressively as the fingers move away from the top boundary. In addition to the diffusive spreading, nonlinear finger interactions tend to further smooth out the concentration gradients of a large number of competing fingers. At a later time of  $t = 2.3$  shown in figure 2.8(c), some of the smaller fingers disappear due to diffusive smearing, while others merge to form large-scale structures that develop relatively independently. This trend continues for later times, as shown in figure 2.8(d) for  $t = 3.8$ . It is interesting to note that even at late times, large-scale fingers are connected to the diffusive boundary layer at discrete narrow locations, which serve as feeding sites of high density fluid.

Fingering dynamics are revealed by analysis of the vorticity profile that generates the rotational flow responsible for driving the fingers. Figure 2.9 plots the vorticity field contours for  $Ra = 4000$  at  $t = 2.3$ . The corresponding concentration field is shown in Fig, 2.8(c). Superimposed on the vorticity field in figure 2.9 are the streamlines showing the negative (dashed lines) and positive (solid lines) circulation paths. The vorticity field displays a dipole structure of negative (light) and positive (dark) vorticity pairs. Very high vorticity pairs are concentrated at the root of the fingers, which act as feeding sites for the finger portions away from the top boundary. The corresponding streamlines show how the fluid is drawn from the sides to flow

laterally along the top boundary layer and down through the high-vorticity regions at the finger roots. Although the highest vorticity magnitude occurs at the finger roots, the tips of the fingers also display a moderate accumulation of vorticity.

### Dominant wavenumber of nonlinear flows

As noted above in §2.2.4, the early time wavelength developed by the nonlinear simulations is in close agreement with that predicted by the linear stability analysis. In order to compare the time evolution of the preferred mode of the nonlinear flow, we define a dominant mode as

$$\hat{n} = \frac{\int_0^K k E(k) dk}{\int_0^K E(k) dk} , \quad (2.47)$$

where  $\hat{n}$  is the dominant wavenumber,  $k$  is the Fourier mode and  $E(k)$  is the energy spectrum associated with the Fourier transform of the vorticity field. We compute  $E(k)$  as

$$\sqrt{E(k; t)} = \int_0^x \left( \int_0^1 \omega(z, x, t) dz \right) e^{-ikx} dx . \quad (2.48)$$

The dominant mode  $\hat{n}$  is an integral measure of the transverse perturbation spectrum. We have observed the spectrum to be highly localized around the high energy modes. The magnitude of  $\hat{n}$  is a reasonable approximation of the high energy modes in the spectrum. We have also observed that the energy spectrum is only weakly dependent on the random disturbances introduced as initial conditions. Figure 2.10 shows the evolution of  $\hat{n}$  for various Rayleigh numbers. The most dangerous mode  $k_{\max}$  from the linear stability analysis is also shown for comparison. We observe a good agreement of  $\hat{n}$  with  $k_{\max}$  for short times. The onset of the nonlinear regime leads to the deviation of the dominant mode away from the most dangerous mode. This deviation from  $k_{\max}$  is stronger and occurs earlier for higher values of  $Ra$ , indicating a stronger influence of nonlinearity for larger Rayleigh numbers.

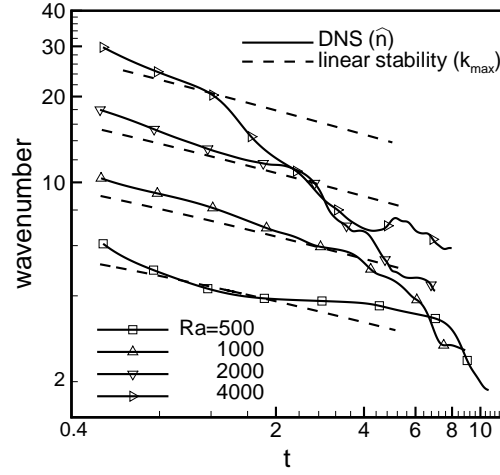


Figure 2.10: The dominant mode of the nonlinear simulations as a function of time for different values of the Rayleigh number. Also shown are the most dangerous modes given by the linear stability analysis. Good agreement is observed between the two for early times. At later times the onset of nonlinear behavior leads to a significant deviation from linear results.

### Influence of the Rayleigh number

Figure 2.10 shows that the nonlinear behavior is strongly dependent on the Rayleigh number. In order to estimate the influence of  $Ra$  on the flow dynamics, we compare the relatively early-time behavior at two Rayleigh numbers. Figure 2.11 plots the concentration contours for  $Ra = 1000$  at  $t = 2.2$  and  $Ra = 8000$  at  $t = 1.6$ . These simulations employ  $512 \times 512$  and  $2048 \times 2048$  grid points, respectively. The concentration front moves much faster for the latter case. The  $Ra = 1000$  case develops a few large fingers and also shows a substantial amount of diffusive smearing in other regions of the concentration front. The large-scale fingers appear to move independently, without interacting with neighboring fingers. The  $Ra = 8000$  case, on the other hand, develops a vigorous instability that results in complex fingering structures. Compared to the  $Ra = 4000$  case shown in figure 2.8(b) at  $t = 0.18$ , the  $Ra = 8000$  case already shows well developed discrete feeding sites. Note that new feeding sites develop as the old ones are abandoned. In other regions, multiple fingers



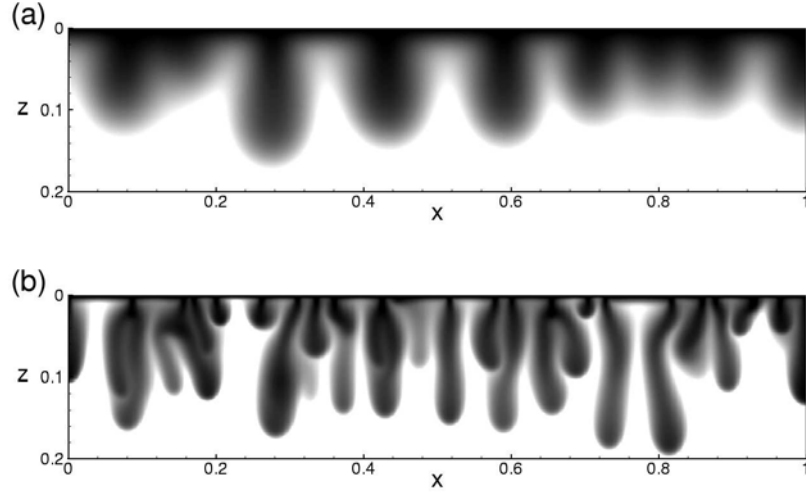


Figure 2.11: Concentration contours for (a)  $Ra = 1000$ ,  $t = 2.2$  and (b)  $Ra = 8000$ ,  $t = 1.6$ . The larger Rayleigh number case is marked by intense nonlinear interaction between competing fingers. The small  $Ra$  case shows larger fingers with a strong diffusive spreading.

can attach to a single feeding site, nonlinear interactions then select finger one over the others as the preferential flow path.

The complexity of the fingering structures suggest that the long term fate of the nonlinear competition cannot be predicted from the concentration profiles at earlier times, especially for large Rayleigh numbers. In order to analyze the fingering dynamics at long times, we plot the concentration profiles in figure 2.12 for various Rayleigh numbers at times when the concentration front reaches the bottom boundary. We designate this time as  $t_b$ . The small Rayleigh case,  $Ra = 1000$  at time  $t_b = 8.9$ , shows that two large fingers survive to reach the bottom boundary. Comparison with figure 2.11(a) shows that the fingering configuration is completely different from that at an earlier time of  $t = 2.2$ . The  $Ra = 2000$  case at  $t_b = 7$  displays slightly narrower fingers, with one isolated finger in the middle making it to the bottom boundary, while two other fingers, attached to a single feeding site, are still in competition. For larger Rayleigh number cases,  $Ra = 4000$ ,  $t_b = 8$  and  $Ra = 8000$ ,  $t_b = 8.5$ , more fingers reach the bottom boundary. Many of these fingers can be observed to undergo strong interactions while others are in the process of fading out. Figures 2.12(c) and

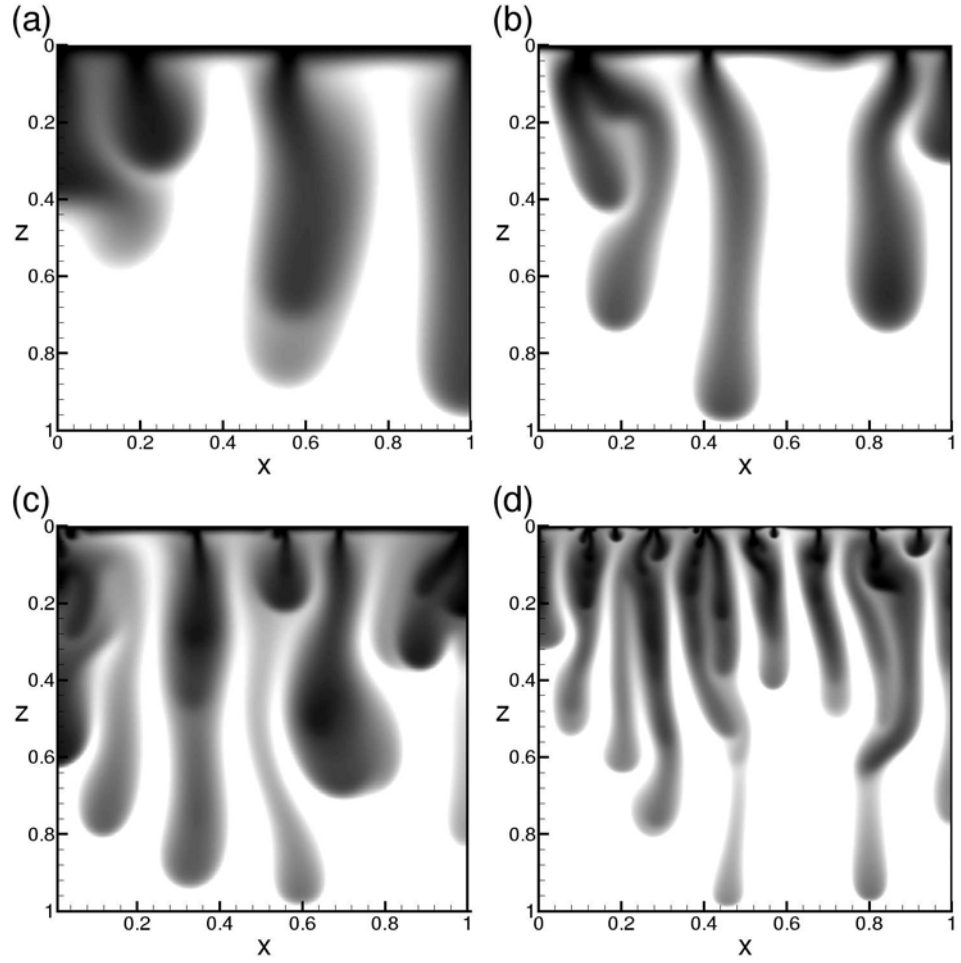


Figure 2.12: Concentration contours at time  $t_b$ , when the concentration front reaches the bottom. (a)  $Ra = 1000$ ,  $t_b = 8.9$ . (b)  $Ra = 2000$ ,  $t_b = 7$ . (c)  $Ra = 4000$ ,  $t_b = 8.0$ . (d)  $Ra = 8000$ ,  $t_b = 8.5$ . The late time dynamics is governed by large scale fingers. Large Rayleigh number cases continue to display vigorous fingering interactions.

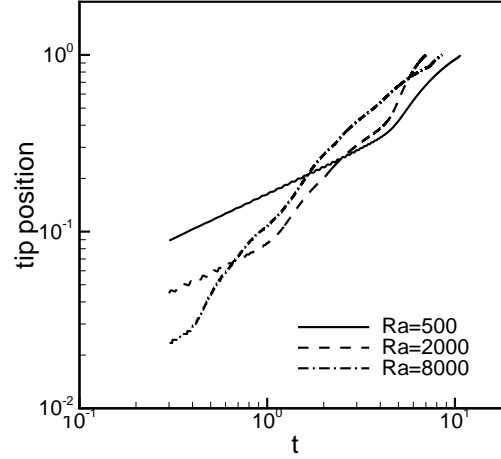


Figure 2.13: The position of the most advanced portion of the front as a function of time for different values of the Rayleigh number. The tip moves faster for larger Rayleigh numbers for early times. Fingering interactions significantly influence the rate of front propagation at later times, particularly for large  $Ra$  cases.

2.12(d) clearly show the fading of the fingers is due to shifts in the feeding sites as well as due to lateral pinch-off, where one diagonally moving finger cuts the fluid supply of a neighboring finger. An interesting consequence of these fingering interactions is an increase in  $t_b$  for larger values of the Rayleigh number, as compared to the small  $Ra$  cases. Note that  $t_b = 8.9$  for  $Ra = 1000$ , it decreases to 7 for  $Ra = 2000$  but then again increases to 8 for  $Ra = 4000$  and then to 8.5 for  $Ra = 8000$ .

The position of the most advanced section of the concentration front, the tip position, as a function of time is shown in figure 2.13 for various Rayleigh numbers. For the small  $Ra = 500$  case, the front initially propagates as  $t^{1/2}$  and then switches to a linear growth for larger times. Higher Rayleigh number cases display the diffusive  $t^{1/2}$  behavior for relatively shorter times. The  $Ra = 2000$  case displays a faster than linear growth of the tip position at later times. The tip travels quickly for the  $Ra = 8000$  case, but for a very small initial time. It is clear that by  $t = 5$  the tip is moving faster for the  $Ra = 2000$  case as compared the  $Ra = 8000$  case. Consequently the time for a finger to reach the bottom boundary is shorter for the  $Ra = 2000$  case.

As shown by the concentration contours in figure 2.12 this behavior is due to more intense finger interaction at higher Rayleigh number cases, such that the interacting fingers do not allow any one finger to clearly breakaway ahead of the front. For the smaller  $Ra$  cases, on the other hand, isolated fingers travel faster due to the absence of interference from neighboring fingers.

### 2.2.5 Discussion

We analyze the stability of a diffusive boundary layer in a semi-infinite domain. This analysis is applicable when the penetration depth of the diffusive boundary layer,  $\delta$ , is small relative to the domain thickness,  $H$ . The penetration depth at the onset of instability is given in dimensional form as  $\delta_c \approx 24\mu D/(K\Delta\rho g)$ . We must have  $\delta_c \ll H$  for the assumption of the semi-infinite domain to be valid. The dimensional critical time, which is then independent of the length scale, is given by

$$t_c = 146 \frac{\phi\mu^2 D}{(K\Delta\rho g)^2} . \quad (2.49)$$

Similarly, we define the dimensional critical wavelength  $\lambda_c$  as

$$\lambda_c = \frac{2\pi\mu D}{0.07K\Delta\rho g} . \quad (2.50)$$

To validate both the linear analysis and the numerical simulations, the predictions of  $t_c$  and  $\lambda_c$  should be compared with experimental observations. Unfortunately Elder (1968) only states the Rayleigh number of his experiments and does not give all the data necessary to calculate  $t_c$  and  $\lambda_c$ . Green & Foster (1975) have reported experiments of a salt solution diffusing into the top of a Hele Shaw cell. The Rayleigh number in their experiment is  $Ra = K\rho g H/(\mu D) = 90500$ . They do not report the onset time, but they give the wavelength of the first observed fingers as  $\lambda = 1.8$  mm and note that this may be an over estimate. For the same parameters, our linear stability analysis predicts a critical time of  $t_c = 4$  s and a critical wavelength of  $\lambda_c = 0.6$  mm. The critical wavelength predicted by linear theory is generally smaller than the wavelength first observed, because the fingers are initially not visible in

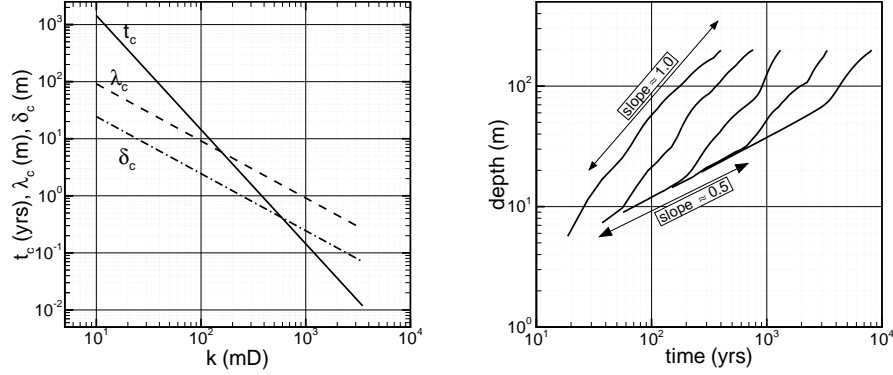


Figure 2.14: (a) Variation with permeability of the critical time,  $t_c$ , the critical wavelength,  $\lambda_c$  and the penetration depth at the critical time,  $\delta_c$ , for  $\Delta\rho = 5 \text{ kg/m}^3$ ,  $\phi = 0.3$ ,  $\mu = 0.5 \text{ cP}$  and  $D = 10^{-9} \text{ m}^2/\text{s}$ . For this range of permeability variation  $t_c$  varies between 2000 yrs and 10 days while  $\lambda_c$  goes from about 100 m to less than a meter. The penetration depth  $\delta_c$  gives information regarding the applicability of our analysis with respect to the layer thickness  $H$ , such that  $\delta_c \ll H$ . (b) The advance of the fastest finger tip is shown until the bottom of the simulation domain is reached. A diffusive,  $t^{0.5}$ , behavior is observed at early times, while the fingers advance proportional to  $t$  at later times.

the experiments. By the time they become observable, they have already coarsened. Given this experimental limitation on the detection of the critical parameters, high resolution numerical studies as reported above are valuable because the growth of perturbations can be detected before they become visible.

The critical time and the critical wavelength can vary by orders of magnitude depending on the properties of the geological formation. While viscosity, diffusion and density difference have more or less similar values for typical aquifers, permeability can vary over a large range of values, and therefore introduces the largest variations in  $t_c$  and  $\lambda_c$ . Figure 2.14(a) shows that  $\delta_c$  decreases from 55 m to about 0.07 m when the permeability increases from 1 mD to 3 D. Hence our results for the semi-infinite domain will apply to high permeability layers with a thickness of few tens of meters, but for low permeability formations the thickness has to be several hundred meters for our results to be applicable. The critical wavelength decreases from  $\lambda_c \approx 200 \text{ m}$  to  $\lambda_c \approx 0.3 \text{ m}$  and the critical time for the onset of the instability decreases from

$t_c \approx 2000$  yrs to  $t_c < 10$  days as the permeability decreases from 3 D to 1 mD.

The critical wavelength,  $\lambda_c$ , is an indication of the length scales that have to be resolved by numerical simulations to capture the convective transport and the resulting solution trapping. In high-permeability aquifers the initial unstable perturbations are much smaller than the size of grid blocks typically used in field-scale reservoir simulations. A numerical study of the high permeability Sleipner injection site by Lindeberg & Bergmo (2003) shows that a grid block size of  $3 \times 4$  cm is necessary to capture the initial fingering with a standard reservoir simulator. For field scale simulation the grid size has to be increased to  $100 \times 100$  m. Lindeberg & Bergmo (2003) show that simulations using such coarse grids delay the time of onset to 100 yrs, so that the onset of convection is delayed by 2 orders of magnitude, compared to the fine grid. Such increases in the onset time may, or may not, be acceptable depending on the time scale of storage. More importantly, the failure to resolve the unstable length scales at small times, may lead to significant errors in the nonlinear regime, even if the dominant length scales at long times are coarse enough to be resolved on the chosen coarse grid. Diersch & Kolditz (2002) have investigated the convergence of the Elder problem. They show that even at late times, when most of the structures are large enough to be resolved on a coarse grid, the solution is sensitive to the grid size.

Following the onset of instability, the strength of convective mixing can be determined qualitatively from the speed of the most advanced finger tip, shown in figure 2.14(b) for several values of the permeability. All other properties are held fixed at the same values as in figure 2.14(a). For all permeability values, the position of the finger tips is initially proportional to  $t^{1/2}$ . Eventually, however, they accelerate and the penetration is approximately proportional to  $t$ . Note that the late time rate of advance is similar for all values of permeability. Larger permeability values simply lead to an earlier switch from  $t^{1/2}$  to the linear regime. In high permeability formations, solution trapping is therefore strongly enhanced by convection, and it may be the dominant mechanism reducing the mass of the CO<sub>2</sub> plume. To assess the safety and effectiveness of CO<sub>2</sub> storage in high-permeability formations, it is therefore necessary to simulate this convective process accurately.

Heterogeneity is important for the miscible, viscous fingering instability (Tchelepi & Orr, 1994; Riaz & Meiburg, 2004b; Prasad & Simmons, 2003). Some attempts have been made to model the effect of heterogeneity on the mechanism of this instability (Gounot & Caltagirone, 1989), but this remains one of the directions of future research. The fine stratigraphic layering of sedimentary rocks causes strong anisotropy of the permeability. In general, the vertical permeability may be several orders of magnitude smaller than that in the horizontal direction. Ennis-King & Paterson (2003) have shown that anisotropy has an equally strong effect on the critical time and wavelength as the magnitude of the permeability. The analysis developed here can easily be extended to include the effects of anisotropy.

Our analysis does not include the full dispersion tensor, which accounts for the influence of velocity induced dispersion (Yortsos & Zeybek, 1988; Tchelepi *et al.*, 1993). Recent work by Riaz & Meiburg (2004a) suggests that for homogeneous porous media, velocity induced dispersion is generally equivalent to a slight increase in the level of molecular diffusion.

### 2.2.6 Conclusions

Accurate numerical simulation of density fingering over long times at the field scale is one of the main challenges in predicting the movement of CO<sub>2</sub> underground. Our theoretical and numerical results are valuable for understanding density driven convection during CO<sub>2</sub> storage in saline aquifers. Our analysis is directly applicable to the thermal instability problem and resolves the issue of the critical time and the critical wavenumber. We also highlight the physical mechanisms of instability that give rise to both the long wavenumber cutoff and the critical time for the onset, in a semi-infinite domain.

The disturbances only become experimentally observable a finite period after the critical time, and it is therefore difficult to measure the critical time with reasonable accuracy. For typical aquifers with moderate permeability, the onset time can be as large as hundreds of years. The prediction of the critical wavelength is crucial in choosing the grid resolution in the numerical simulation. Although the large scale

fingers at later times can be resolved with fewer grid blocks, the errors introduced by ignoring the small-scale dynamics at early times, may have a significant influence on the late time behavior.

The simplifications necessary to treat the problem theoretically may introduce significant errors when such results are applied to real aquifers. The important assumptions are the homogeneity and isotropy of the porous medium, as well as the assumption of single-phase flow and the absence of velocity induced dispersion. The assumption of single-phase flow will break down if capillary forces are significant. Additionally, physical mechanisms related to dissolution, precipitation and geochemical reactions, which are not accounted for in our analysis, can be expected to play a role. Some of these processes may be incorporated in the linear stability analysis, while others can only be investigated with high-resolution nonlinear simulation. The results for the basic gravitational fingering instability presented here, form the basis to investigate the effect and importance of these additional processes.

## 2.3 Convective dissolution rates

Once the onset time for convection in an aquifer has been determined, the evolution of the convective dissolution rate determines the time scale necessary to dissolve the injected  $\text{CO}_2$ . To obtain estimates of the convective dissolution rate, we use direct numerical simulations to study the long-term behavior of the convective mass transport in open and closed systems. In a closed system, the background concentration of dissolved  $\text{CO}_2$  in the domain increases and convection decays as the domain is saturated. In an open system, the domain is infinite so that the background concentration of dissolved  $\text{CO}_2$  remains effectively zero, and convection continues as long as  $\text{CO}_2$  is supplied. Regional saline aquifers are often very large and are likely to behave as open systems, so that dissolution may be a very effective trapping process.

All simulations reported below are solutions to the two-dimensional model problem introduced in § 2.2.1. All results are non-dimensionalized using the characteristic



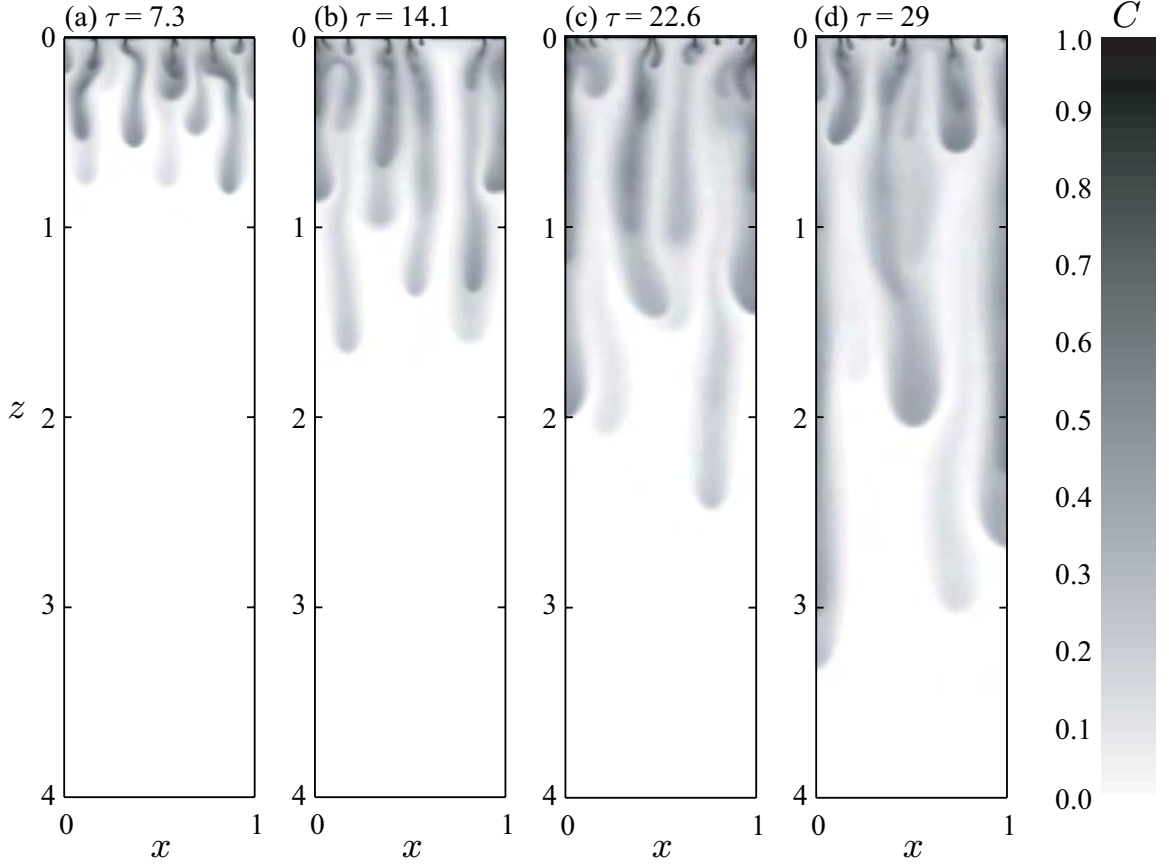


Figure 2.15: Evolution of the concentration in an open aquifer for  $Ra = 4000$ .

scales (2.5) to (2.8), and the concentration of  $\text{CO}_2$  in the brine,  $C = c/c_{eq}$ , is normalized by the equilibrium concentration at the  $\text{CO}_2$ -brine interface,  $c_{eq}$ . The concentration is given by  $c = x_c \rho_c$ , where  $x_c$  is the mass-fraction of  $\text{CO}_2$  in the brine and  $\rho_c$  is the density of the dissolved  $\text{CO}_2$ . As before, the governing parameter is the Rayleigh number,  $Ra = k\Delta\rho gl/\phi\mu D$ , where  $l$  is a suitable length scale specified below.

### 2.3.1 Convection in open systems

We consider an open aquifer of width,  $L$ , and infinite depth. In this case the appropriate length scale,  $l$ , is the width of the domain,  $L$ . For the numerical simulations we choose  $H \gg L$ , and we report results only for the time during which the plumes

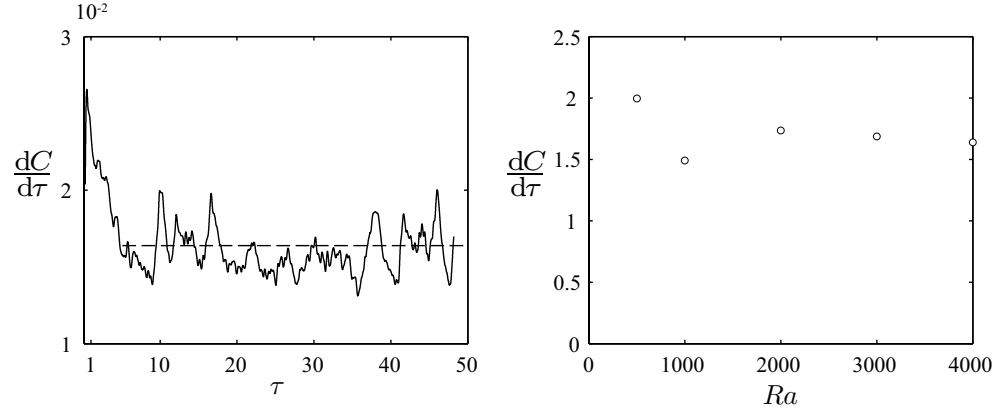


Figure 2.16: (a) Evolution of the dissolution rate at  $Ra = 4000$ . Average dissolution rate over time is shown as dashed line. (b) Time averaged of the dissolution rate for different  $Ra$ .

of dissolved  $\text{CO}_2$  have not reached the bottom of the domain. Figure 2.15 shows the evolution of gravity driven fingers, or plumes, of dense  $\text{CO}_2$ -rich brine in a typical simulation. The nonlinear interactions of the fingers have already been described in § 2.2.4-2.2.4, and here we focus on the evolution of the dissolution rate,  $dC/d\tau$ . We define the dissolution rate as the rate of change of the total dissolved  $\text{CO}_2$  in the domain, given by

$$\frac{dC}{d\tau} \equiv \frac{d}{d\tau} \int_0^L \int_0^H C dx dz. \quad (2.51)$$

Figure 2.16(a) shows the evolution of  $dC/d\tau$ , for a typical simulation at  $Ra = 4000$ . This evolution can be divided into three stages. For  $\tau < 1$  the diffusive boundary layer is stable and the dissolution rate decays as,  $dC/d\tau \propto \tau^{-1/2}$ . After the onset of convection the dissolution rate fluctuates, and the peaks correspond to the growth of large fingers. After an initial transient,  $1 < \tau < 10$ , the dissolution rate fluctuates around a constant value of  $dC/d\tau \approx 0.017$ . We refer to this average value as the open-system dissolution rate,  $\langle dC/d\tau \rangle$ . Figure 2.16(b) shows that  $\langle dC/d\tau \rangle$  is nearly independent of  $Ra$ , because  $Ra$  can be scaled out of the problem in a domain of infinite depth, see also the discussion in § 2.2.3.

This open-system dissolution rate allows simple estimates of the time necessary

to dissolve a given mass of CO<sub>2</sub> injected into a saline aquifer based on its average petrophysical properties. The mass dissolution rate of CO<sub>2</sub> per unit width in the open convection regime is given by

$$\frac{dm_c}{dt} \approx \left\langle \frac{dC}{d\tau} \right\rangle \frac{k\Delta\rho g c_{eq}}{\phi\mu}, \quad (2.52)$$

where  $m_c$  is the total mass of dissolved CO<sub>2</sub>. The onset time,  $\tau_o$ , of the convective mass transport is given by the first minimum in the evolution of the dissolution rate (figure 2.16a, see also figure 2.18a). For the range of  $Ra$  investigated (see figure 2.18b), it is given by

$$t_o = 6215 \frac{\phi\mu^{11/5} D^{6/5}}{(k\Delta\rho g)^{11/5} H^{1/5}}, \quad (2.53)$$

as computed from DNS. This onset time,  $t_o$ , decreases with  $Ra$  and it is larger than the theoretically predicted critical time, given by (2.49), obtained from linear theory in § 2.2.3.

### 2.3.2 Convection in closed systems

If the aquifer is of finite thickness, the suitable length scale,  $l$ , is the aquifer thickness,  $H$ . Figure 2.17 shows how the nature of the concentration field changes after the fingers have started to interact with the bottom boundary. After the fingers reach the bottom the convection cells coarsen rapidly until the size of a convective cell is approximately  $H$ . Figure 2.18(a) shows the evolution of the CO<sub>2</sub> dissolution rate for various values of  $Ra$ . The early phase of the evolution is similar to the semi-infinite aquifer. An initial phase of diffusive mass transport is followed by open-system convective mass transport after the onset time. However, after the fingers have reached the bottom of the aquifer, the dissolution rate decays very rapidly. We refer to this late stage as closed-system convective mass transfer, to distinguish it from the earlier vigorous regime. The time when the plumes start to interact with the bottom boundary,  $\tau_i$ , is independent of  $Ra$  (figure 2.18a). The dimensional form is given by

$$t_i \approx 15 \frac{\phi\mu H}{k\Delta\rho g}. \quad (2.54)$$

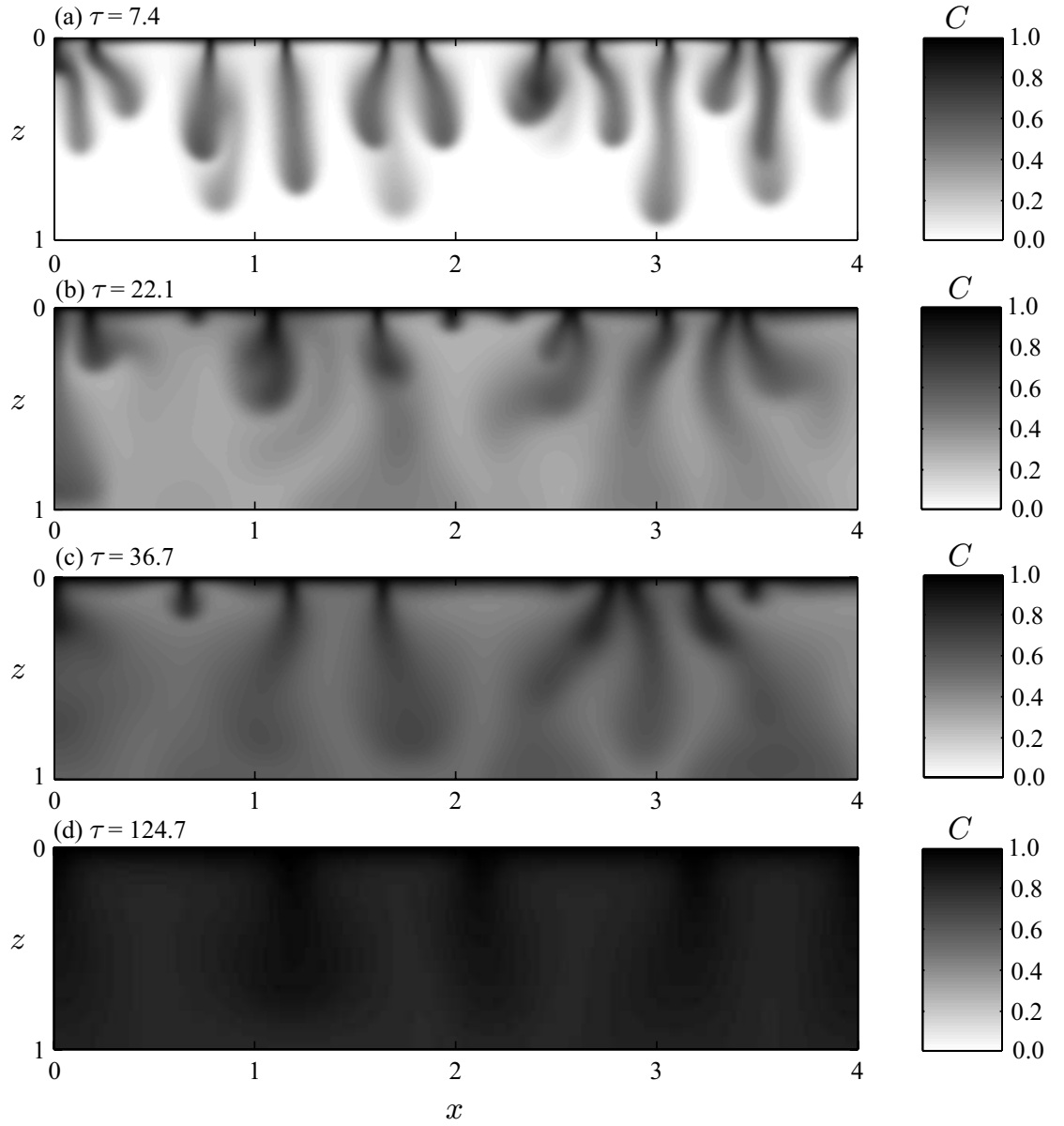


Figure 2.17: Evolution of the concentration in a closed aquifer, for  $Ra = 1000$ . (a) Plumes of dissolved have not reached the base of the aquifer. Convection similar to an open aquifer. (b-d) Convection in a closed aquifer.

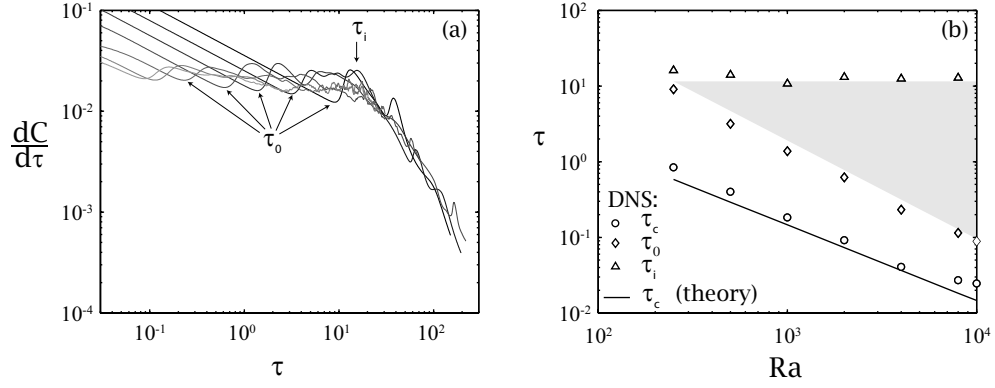


Figure 2.18: (a) Evolution of the dissolution rate,  $dC/d\tau$ , for various  $Ra$  in a closed aquifer. (b) Variation of the time scales discussed in the text as a function of  $Ra$ .

At  $t \approx 15t_i$  the aquifer is saturated to 95%, and convective motion is negligible. If this stage is reached in a  $\text{CO}_2$  storage project, the size of the chosen aquifer is too small to dissolve all the injected  $\text{CO}_2$  into the formation brine. In general, we expect the storage aquifer to be large enough to dissolve several times the volume of the injected  $\text{CO}_2$ .

### 2.3.3 Convective time scales

Using linear theory and high accuracy numerical simulation, we identify three convective time scales:

1. The critical time,  $t_c \propto k^{-2}$ , is the time after which small perturbations grow, it gives an analytic lower bound for the onset of convection.
2. The onset time  $t_o \propto k^{-2.2}$ , marks the transition from diffusive to convective mass transfer, and corresponds to the appearance of the first fingers in the concentration profile. For large  $Ra$ , we expect  $t_o$  to approach  $t_c$  from above.
3. The interaction time,  $t_i \propto H/k$ , marks the transition to a regime of decaying convection, and corresponds to the first fingers interacting with the bottom of the domain.

The first two time scales are independent of the thickness of the aquifer, because they are determined by the growth of the boundary layer, which we assume to be much smaller than  $H$ . The interaction time,  $t_i$ , is of course directly proportional to  $H$ . These time scales identify three dynamic regimes of mass transport in the brine, shown in figure 2.18(b). These three regimes may be characterized as:

1. In the diffusive regime ( $t < t_o$ ) the concentration of dissolved  $\text{CO}_2$  in the aquifer increases proportional to  $t^{1/2}$ , and the dissolution rate of  $\text{CO}_2$  decreases rapidly as  $t^{1/2}$ . In the absence of the gravitational instability this would be the only regime.
2. In the open-system regime ( $t_o < t < t_i$ ) the dynamics are independent of the domain size. In this regime the total concentration increases linearly with  $t$ , and the open-system dissolution rate is given by  $\langle dC/d\tau \rangle \approx 0.017$ . This is the most effective regime of mass transfer (gray triangle in figure 2.18b), and is characterized by rapidly growing fingers with strong nonlinear interactions.
3. The closed-system regime ( $t > t_i$ ), where the finite size of the aquifer influences the dynamics of convection. This regime is characterized by large, slow convective cells. The dissolution rate decays rapidly and dissolved  $\text{CO}_2$  approaches its equilibrium concentration throughout the aquifer.

Consider an aquifer with the following properties:  $H = 200$  m,  $\mu = 5 \cdot 10^{-4}$  Pa s,  $\Delta\rho = 5$  kg/m<sup>3</sup>, and  $D = 10^{-9}$  m<sup>2</sup>s<sup>-1</sup>. We illustrate the effect of permeability variation by considering a high-permeability aquifer with, porosity  $\phi = 0.3$  and permeability  $k = 3400$  mD, and a low-permeability aquifer, with  $\phi = 0.1$  and  $k = 10$  mD. In the high-permeability aquifer, the critical time is 4 days, the onset of convection enhanced dissolution is after 20 days, the plumes reach the base of the aquifer after approximately 80 yrs, and the aquifer would be saturated after approximately 1200 yrs. In the low-permeability aquifer, the critical time is 450 yrs, the onset of convective dissolution is not until 680 yrs, the plumes reach the base of the aquifer after 9510 yrs, and the aquifer would be saturated after 150000 yrs. This simple example illustrates that the time scales of dissolution trapping are strongly dependent on the permeability

of the aquifer. In general, the dissolution of  $\text{CO}_2$  into the brine will be greatly enhanced by density driven convection in large high-permeability aquifers, because the onset time is short, the dissolution rate in the open-system regime is high, and the transition to finite-acting convection is late.

#### **2.3.4 Further work**

The results on the dissolution rate presented above are preliminary; in the future we plan to extend this work to three-dimensions and to heterogeneous domains. These results would allow simple order-of-magnitude estimates of the time necessary to dissolve a given mass of  $\text{CO}_2$  injected, through a given interfacial area. Unless the supercritical  $\text{CO}_2$  has ponded in a structural trap, the area of the interface changes as the supercritical  $\text{CO}_2$  migrates due to buoyancy. In this case, it would be instructive to combine the dissolution rates obtained from high accuracy simulations with the simple models of gravity currents discussed in § 3.

# Chapter 3

## Residual Trapping & CO<sub>2</sub> Gravity Currents

### 3.1 Introduction

The formation of residual saturations is the second primary trapping process that reduces the volume of mobile CO<sub>2</sub>, and therefore determines the duration of the active storage period (figure 1.3). When the saturation of the non-wetting CO<sub>2</sub> decreases, a process referred to as imbibition, an interplay of viscous and capillary forces at the pore-scale leads to the formation of disconnected essentially-immobile bubbles of residual CO<sub>2</sub> (3.1*a*). Imbibition takes place in the wake of the migrating CO<sub>2</sub> plume, and residual trapping continues as long as the CO<sub>2</sub> migrates. To understand residual trapping it is therefore essential to understand the buoyancy driven migration of the CO<sub>2</sub> plume. In the two aquifers shown in figure 1.4(*b*) and (*c*) the CO<sub>2</sub> plume migrates as a gravity current and residual trapping is likely to be an important trapping process. In § 3.1.1 we give a brief introduction to the pore-scale phenomenon, and we introduce a nomenclature suitable for the simple model we adopt. A discussion of the current research on the formation of residual saturations is beyond the scope of this thesis. Instead we adopt the simplest trapping model, and we focus on the interplay between sweep and residual trapping, which has so far not received much attention in CO<sub>2</sub> storage.



After the end of injection the advective forces are small compared to gravitational and capillary forces, and we study the migration of the CO<sub>2</sub> using a simplified model assuming gravity-capillary equilibrium in the vertical direction and a sharp interface between the CO<sub>2</sub> plume and the ambient brine. Vertical-equilibrium sharp-interface models are commonly used in hydrology, petroleum engineering, and applied mathematics, because they allow analytic and semi-analytic solutions that give insight into the underlying dynamics. CO<sub>2</sub> storage in saline aquifers raises new questions that have not been addressed by the literature on vertical-equilibrium sharp-interface models, reviewed in §3.1.2. We focus on the effects of confinement, residual trapping and slope on the migration of CO<sub>2</sub> plumes in saline aquifers. In §3.2 we derive the vertical-equilibrium sharp-interface equations for a confined sloping aquifer with constant residual saturations.

In §3.3 we study the effect of confinement on the spreading of the CO<sub>2</sub> plume, in absence of residual trapping. We use the scaling laws, associated with similarity solutions for confined and unconfined aquifers, to detect the influence of confinement in more general numerical solutions. Using this novel approach, we are able to show that confinement has a strong effect on the migration of the CO<sub>2</sub> plume, due to the less mobile ambient brine. In other words the mobility ratio between the CO<sub>2</sub> and the brine is an important parameter governing the migration of the CO<sub>2</sub>.

In §3.4 we turn our attention to the relation between the sweep of the gravity current and residual trapping. We extend the work on horizontal confined aquifers, presented in §3.3, to include residual trapping, and show that the solutions remain self-similar. This implies that the volume of the current decreases as a power-law in horizontal aquifers. Using the horizontal aquifer as a base case we show that residual trapping is much more effective in sloping aquifers. The hyperbolic limit of the equations allows us to study analytically how far the CO<sub>2</sub> migrates up-dip and how long it remains mobile.

### 3.1.1 Immiscible displacements and residual saturations

In many sedimentary rocks supercritical CO<sub>2</sub> is typically the non-wetting phase relative to the ambient brine. At the front of the CO<sub>2</sub> plume the CO<sub>2</sub> saturation increases, and the brine is drained from the pore space. The capillary entry pressure prevents the drainage of the brine from the smallest pores, resulting in an incomplete displacement (Lenormand *et al.*, 1983). We refer to the brine left behind the advancing CO<sub>2</sub> front as the residual brine,  $S_{br}$ . Bachu & Bennion (2007) showed that  $S_{br}$  can range from 0.2 to 0.68 at storage conditions in saline aquifers. The high end of these values is surprising and may in part be due to heterogeneity and gravity segregation in the experiments. They also show that the presence of residual water reduces the apparent permeability of the CO<sub>2</sub> to approximately 1/5 of the single phase permeability. We refer to this value as the relative permeability of CO<sub>2</sub>, denoted  $k_{rc}$ .

If the CO<sub>2</sub> plume is migrating laterally as a gravity current the CO<sub>2</sub> saturation decreases at the trailing edge of the plume (figure 3.10), and the ambient brine imbibes into the pore space previously occupied by CO<sub>2</sub>. Preferential imbibition of the brine into the smaller pores and interfacial instabilities leave CO<sub>2</sub> behind as disconnected bubbles and ganglia of CO<sub>2</sub> (figure 3.1a), which are effectively immobile (Lenormand *et al.*, 1983). We refer to this immobile CO<sub>2</sub> saturation as the residual CO<sub>2</sub> saturation,  $S_{cr}$ , and to the process as residual trapping. Bachu & Bennion (2007) report values of  $S_{cr}$  from 0.1 to 0.35 for saline aquifers in the Alberta basin, indicating that they will trap CO<sub>2</sub> efficiently.

### 3.1.2 Gravity currents in porous media

While the residual saturation is an upscaled parameter that is determined by viscous and capillary forces on the pore scale, the vertical sweep is a macroscopic quantity that can be studied using fluid mechanical models of gravity currents in porous media. Simple models to describe the fundamental behavior of such flows have been developed independently in several disciplines, including petroleum engineering (Lake, 1989) and hydrology (Bear, 1972). They are based on two common assumptions: hydrostatic distribution of the pressure and complete segregation of the fluids. In this case the

dimensionality of the problem is reduced, and an equation governing the evolution of the interface is obtained. We will refer to such models as vertical-equilibrium sharp-interface models.

Sedimentary rocks are layered, and therefore aquifers may have very large aspect ratios (length:height  $\gg 1$ ). In this case the pressure distribution is close to hydrostatic throughout the aquifer. A hydrostatic pressure distribution indicates that the saturation be given by gravity-capillary equilibrium in the vertical direction. In hydrology this is also called Dupuit's approximation, and in petroleum engineering it is referred to as vertical equilibrium and was first introduced by Dietz (1953). Yortsos (1995) presented a rigorous derivation of the vertical-equilibrium sharp interface model from the full governing equations of incompressible two-phase flow in porous media.

If the thickness of the released fluid is large compared to the capillary transition zone, the saturation in each fluid is approximately constant (figure 3.1*b*). As a first approximation we replace the transition zone by a sharp interface and assume that the saturations above and below the interface are constant.

An additional assumption that is commonly made is that the flow is unconfined. In this case the ambient fluid is assumed to be inviscid, so that the pressure on the interface is constant. This approximation results in the so-called porous medium equation, which has received a lot of attention in the applied mathematics community (Aronson, 1985). Woods (2002) reviewed the large variety of similarity solutions for gravity currents obtained from porous medium type equations. We show in 3.3.2 that this approximation is also valid if the gravity current is much thinner than the aquifer.

The groundwater table is often well described by an unconfined vertical-equilibrium sharp-interface model. This set of approximations gives rise to the Boussinesq's equation (Bear, 1972). Henry (1959) used a confined vertical-equilibrium sharp-interface model to describe a salt-water intrusion into fresh-water aquifers. In petroleum engineering confined vertical-equilibrium sharp-interface models have been used for water or gas injection (Dietz, 1953; Fayers & Muggeridge, 1990). Both disciplines have used unconfined models to describe the upconing of gas-liquid interfaces near wells

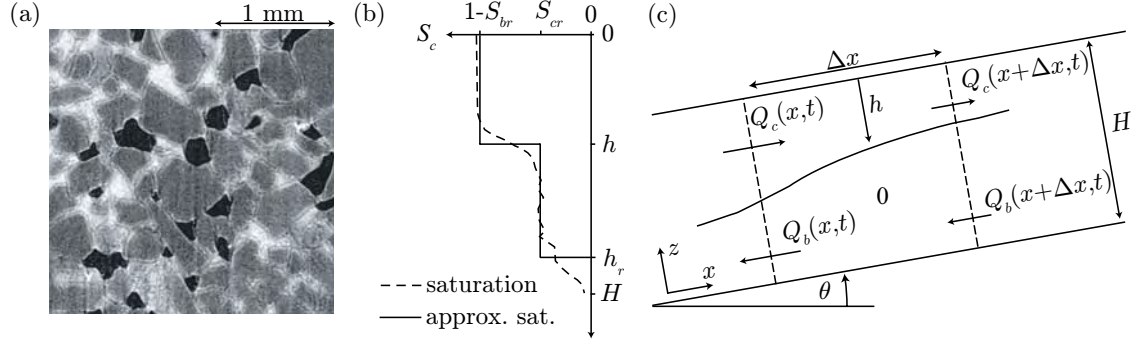


Figure 3.1: (a) Microtomogram of non-wetting CO<sub>2</sub> bubbles (black) and water (white) in the pore space between grains (grey), from Benson *et al.* (2006). (b) Comparison between non-wetting phase saturation profile after imbibition, inferred from a wire-line log (Koperna & Kuuskraa, 2006), and the simplified step function saturation profile corresponding to the sharp-interface approximation. (c) The geometry of the porous layer and the variables used in the derivation are shown.

(Bear, 1972; Lake, 1989). Coats *et al.* (1971) used a vertical-equilibrium model, which accounts for presence of a capillary transition zone, to formulate efficient quasi-three-dimensional reservoir simulators. Parker & Lenhard (1989) introduced a similar model for the migration of non-aqueous phases along the groundwater table.

Nordbotten *et al.* (2005), Lyle *et al.* (2005), Vella & Huppert (2006), and Bickle *et al.* (2007) used sharp-interface models to study the development of CO<sub>2</sub> plumes during the injection period in confined and unconfined aquifers. During injection the CO<sub>2</sub> saturations increase, and no residual CO<sub>2</sub> forms. After several decades the injection of CO<sub>2</sub> ends, and the CO<sub>2</sub> plume migrates as a gravity current for several hundreds or thousands of years, so that the long term evolution of the CO<sub>2</sub> plume may be modeled as an instantaneous release of finite volume. In the post-injection period the CO<sub>2</sub> saturation decreases in the wake of the gravity current, and residual trapping reduces the current volume (figure 3.10). Kochina *et al.* (1983) extended the sharp-interface model to allow for a constant residual saturation, and studied the decay of the plume volume after a finite release. We extend their work to confined sloping aquifers and consider the limiting cases.

## 3.2 Governing equations

### 3.2.1 Derivation

We consider the flow of supercritical CO<sub>2</sub> with density,  $\rho_c = \rho$ , and viscosity,  $\mu_c$ , and of brine with density,  $\rho_b = \rho + \Delta\rho$ , and viscosity,  $\mu_b$ , in a sloping porous layer of constant thickness,  $H$ , with dip angle,  $\theta \geq 0$ , and infinite lateral extent (figure 3.1c). Both fluids are considered incompressible, and we assume that the porous medium is homogeneous and isotropic with permeability,  $k$ , and porosity,  $\phi$ , and that the top and bottom boundaries are impermeable. We also assume that gravity–capillary equilibrium is maintained in any vertical cross section of the current (figure 3.1b), and we replace the transition zone by sharp-interface and assume that the saturations above and below the interface are constant. We denote the thickness of the CO<sub>2</sub> plume by  $h_c = h$  so that the depth of the brine is given by  $h_b = H - h$ . In this case the pressure in the aquifer is given by

$$p = \begin{cases} p_I - g\rho(z - h_b) + P_c, & \text{for } z > h_b, \\ p_I - g(\rho + \Delta\rho)(z - h_b), & \text{for } z \leq h_b, \end{cases} \quad (3.1)$$

where  $p_I$  is the unknown pressure at the interface,  $P_c$  is the constant capillary pressure, and  $g$  is the gravitational acceleration. The volume flux per unit width,  $q_p$ , of phase  $p \in \{c, b\}$  is given by the multiphase extension of Darcy's law  $q_p = -k\lambda_p \partial\phi_p/\partial x$ , where  $\phi_p = p - g\rho_p(x \sin\theta + z \cos\theta)$  is the potential of phase  $p$ , and  $\lambda_p = k_{rp}/\mu_p$  is the mobility of phase  $p$ . The flow rate per unit width of phase  $p$  is given by  $Q_p = h_p q_p$ . In the absence of a source term, and with the assumption of incompressibility the global conservation of volume is given by  $Q_c + Q_b = 0$ . Using this constraint we can eliminate  $\partial p_I/\partial x$  from the expressions for the flow rates, and we obtain

$$Q_c = -Q_b = kg\Delta\rho \frac{h\lambda_c(H-h)\lambda_b}{h\lambda_c + (H-h)\lambda_b} \left( \sin\theta - \cos\theta \frac{\partial h}{\partial x} \right).$$

To obtain an equation for the evolution of the interface, we consider the conservation of the CO<sub>2</sub> volume  $V_c$  over region  $\Delta x$  and time  $\Delta t$  as shown in figure 3.1(c).

$$\Delta V_c = \phi(1 - S_{br}) \Delta h \Delta x = (Q_c|_x - Q_c|_{x+\Delta x}) \Delta t + R_c.$$

The source term,  $R_c$ , accounts for the volume of CO<sub>2</sub> that is lost as residual saturation  $S_{cr}$  in the wake of the plume. Following Kochina *et al.* (1983) we assume a constant residual saturation,  $S_{cr}$ , so that

$$R_c = \begin{cases} -\Delta h \Delta x S_{cr}, & \text{for } \partial h / \partial t < 0, \\ 0, & \text{for } \partial h / \partial t \geq 0. \end{cases}$$

Taking limits for small  $\Delta x$  and  $\Delta t$  the equation for the evolution of the interface is given by

$$\frac{\partial h}{\partial t} = \kappa \frac{\partial}{\partial x} \left[ \frac{h(H-h)}{h(M-1)+H} \left( -\sin \theta + \frac{\partial h}{\partial x} \cos \theta \right) \right], \quad (3.2)$$

where we have introduced two parameters. The conductivity,  $\kappa$ , of the CO<sub>2</sub> is given by

$$\kappa = \begin{cases} \kappa_1 = \frac{k\lambda_c \Delta \rho g}{\phi(1-S_{br}-S_{cr})}, & \text{for } \partial h / \partial t < 0, \\ \kappa_0 = \frac{k\lambda_c \Delta \rho g}{\phi(1-S_{br})}, & \text{for } \partial h / \partial t > 0, \end{cases} \quad (3.3)$$

where  $\kappa_1 \geq \kappa_0$ , and the mobility ratio that is given by  $M = \lambda_c / \lambda_b$ . The mobility ratio  $M$  measures the change in the mobilities across the advancing part of the interface, because we neglect the effect of the residual CO<sub>2</sub> on the mobility of the brine. For geological CO<sub>2</sub> storage the ambient brine is less mobile,  $M > 1$  (Adams & Bachu, 2002), and we restrict the discussion to this range. For  $S_{cr} = 0$  the coefficient 3.3 becomes continuous and equation 3.2 reduces to the form given by Bear (1972).

Note that the parameters are not independent;  $\lambda_c$  occurs in both. This choice of parameters allows a simple reduction of (3.2) in the limits  $\max(h) \ll H$  or  $M \ll 1$ , as discussed in § 3.3.2. In these limits the equation loses its dependence on  $M$ , but retains the parameter  $\kappa$ . To allow this reduction  $\kappa$  must be defined in terms of the mobility of the CO<sub>2</sub>, and must be independent of the mobility of the ambient brine.

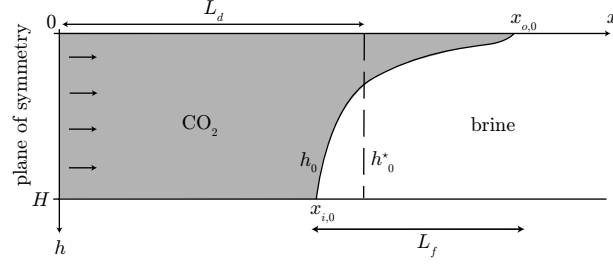


Figure 3.2: The geometry of the initial condition and the three associated length scales  $H$ ,  $L_d$ , and  $L_f$ . A particular initial condition  $h_0[x]$  and the corresponding idealized step function initial condition  $h_0^*[x]$  are shown. The arrows indicate that the fluid has been injected over the entire thickness of the reservoir.

Equation (3.2) is invariant under the substitution

$$h_b = H - h_c, \quad M = \lambda_b/\lambda_c, \quad \kappa = \kappa M = \kappa \lambda_b/\lambda_c, \quad \theta = -\theta. \quad (3.4)$$

This transformation can be used to obtain a similar expression for the evolution of the thickness of the ambient brine  $h_b$  from (3.2).

The thickness of the zone saturated with residual saturation is given by  $h_r[x, t_1] = h_{\max}[x, t_1] - h[x, t_1]$ , where  $h_{\max}$  is the largest thickness the CO<sub>2</sub> plume has achieved at a particular location up to the time of consideration

$$h_{\max}[x, t_1] = \max_{t \leq t_1}(h[x, t]), \quad \forall x.$$

We also refer to  $h_r$  as the residual surface that identifies the fraction of the aquifer swept by the CO<sub>2</sub> plume. In the absence of residual trapping this surface has no significance.

### Initial and boundary conditions

We consider the evolution of the CO<sub>2</sub> plume after injection has stopped ( $t \geq t_0$ ). Figure 3.2 illustrates the plume shape at the end of the CO<sub>2</sub> injection, which serves as the initial condition for the post-injection period under consideration here. We assume that CO<sub>2</sub> has been injected along the whole depth of the aquifer, and that

it has formed a gravity tongue along the upper boundary of the porous layer (Riaz & Tchelepi, 2006). Near the injection site the CO<sub>2</sub> has displaced the water over an average distance of  $L_d$ . The initial saturations in the CO<sub>2</sub> plume and in the brine are  $S_c = 1 - S_{br}$  and  $S_c = 0$ , respectively. This corresponds to a porous medium that is invaded by the released fluid for the first time, which is appropriate for CO<sub>2</sub> storage in saline aquifers. The lateral extent of the fluid invasion is determined by the viscous to gravity ratio  $R_{vg} = (u/L_d)/(u_g/H) = (u\mu_g H)/(k\Delta\rho g L_d)$ , where  $u$  is the average horizontal flow velocity, and  $u_g = k\Delta\rho g/\mu$  is a gravitational velocity (for detailed discussion see Tchelepi, 1994). When  $R_{vg}$  is small, gravitational forces dominate the flow, and a thin gravity tongue forms at the top of the aquifer. When  $R_{vg}$  is large the interface advances over the entire thickness of the aquifer.  $L_d$  increases with time during the injection period, and  $R_{vg}$  generally decreases over time. During CO<sub>2</sub> storage large quantities of fluid are injected, and the horizontal velocity,  $u$ , is high. As a result  $R_{vg}$  is initially large, and the interface advances over across the full thickness of the aquifer. Over time  $R_{vg}$  decreases, and a gravity tongue will form, leading to the initial condition shown in figure 3.2.

The CO<sub>2</sub>-brine interface transitions from  $h_0[x_{i,0}] = H$  to  $h_0[x_{o,0}] = 0$  over a frontal region of width  $L_f = x_{o,0} - x_{i,0}$ . The volume of CO<sub>2</sub> is given by the integral over the initial distribution

$$V = 2\phi(1 - S_{br}) \int_0^{x_{o,0}} H - h_0 \, dx. \quad (3.5)$$

The length scale  $L_d$  is chosen so that an idealized step function initial profile located at  $x = L_d$  has the same CO<sub>2</sub> volume as the particular initial condition ( $V = 2\phi L_d H$ ). The idealized initial condition is

$$h_0^* = \begin{cases} H, & \text{for } |x| \leq L_d, \\ 0, & \text{for } |x| > L_d. \end{cases}$$

This initial configuration imposes three length scales: the layer height  $H$ , the average displacement distance  $L_d$ , and the width of the front at the end of injection  $L_f$  (figure 3.2). The two boundary conditions for (3.2) require that  $h[x, t] \rightarrow 0$  for



$|x| \rightarrow \infty$ .

### 3.2.2 Dimensionless form

We chose the following dimensionless variables

$$\eta = h/H, \quad \xi = x/L, \quad \sigma = \kappa/\kappa_1 \leq 1, \quad t/t^*,$$

In §3.3 the natural length scale is given by  $L = L_d$  because the evolution in a horizontal aquifer is symmetric. In §3.4 we consider sloping aquifers and the natural length scale is  $L = 2L_d$ , so that the initial aspect ratio of the current is therefore given by  $A_0 = L/H$ . We may choose either diffusive or an advective characteristic time scale,  $t^*$ , given by

$$t^a = L(\kappa_1 \sin \theta)^{-1}, \quad \text{or} \quad t^d = L^2(\kappa_1 H \cos \theta)^{-1}, \quad (3.6)$$

so that  $\vartheta = t/t^d$  and  $\tau = t/t^a$ . Substituting these definitions into equation 3.2 we obtain two dimensionless equations

$$\sigma^{-1}\eta_\tau + f_\xi = \text{Pe}^{-1}(f\eta_\xi)_\xi, \quad \text{or} \quad \sigma^{-1}\eta_\vartheta + \text{Pe}f_\xi = (f\eta_\xi)_\xi, \quad (3.7)$$

depending on the choice of the characteristic time scale. The flux function is defined as

$$f = \frac{\eta(1-\eta)}{\eta(M-1)+1}, \quad (3.8)$$

and the dimensionless discontinuous coefficient is given by

$$\sigma = \begin{cases} 1, & \eta_\tau < 0, \text{ or } \eta_\vartheta < 0, \\ 1 - \epsilon, & \eta_\tau > 0, \text{ or } \eta_\vartheta > 0, \end{cases} \quad (3.9)$$

depending on the choice of the characteristic time. Equations 3.7a and b have the same dimensionless governing parameters

$$M = \frac{k_{rc}\mu_b}{\mu_c k_{rb}}, \quad \text{Pe} = A_0 \tan \theta, \quad \epsilon = \frac{S_{cr}}{1 - S_{br}}.$$

The mobility ratio,  $M \geq 0$ , the Peclet-number,  $Pe \geq 0$ , and the residual,  $0 \leq \epsilon < 1$ . The advective and diffusive time scales are related by  $\tau = Pe \vartheta$ . Next, we study the evolution of CO<sub>2</sub> plumes with respect to these three parameters.

### 3.2.3 Discretisation

High accuracy numerical solutions of equation 3.7 were obtained as follows. The spatial domain was divided into  $N$  grid cells of width  $\Delta\xi$  centered at  $\xi_i = (i - \frac{1}{2}) \Delta\xi$ , where  $i \in [1, N]$ . The temporal domain has been divided into  $T$  constant time steps of size,  $\Delta\tau$ , so that the solution is obtained at times  $\tau_n = n\Delta\tau$ , for  $n \in [1, T]$ . The numerical approximation of the cell average in the  $i$ -th cell is given by  $\int_{\xi_{i-1/2}}^{\xi_{i+1/2}} \eta(\xi, \tau_n) dx = \eta_i^n + \mathcal{O}(\Delta\xi^2)$ . The right hand side of (3.7) was discretised in divergence form to ensure discrete conservation (Leveque, 2002), and central differences were used for all spatial derivatives. The time derivative was discretised using the explicit forward Euler method with a constant time step  $\Delta\tau$ . The update formula is given by

$$\eta_i^{n+1} = \eta_i^n - \frac{\Delta\tau}{\Delta\xi} (F_{i+1/2}^n - F_{i-1/2}^n). \quad (3.10)$$

The numerical flux function  $F_{i+1/2}^n = \mathcal{F}[\eta_i^n, \eta_{i+1}^n]$  is given by

$$\mathcal{F}[\eta_i^n, \eta_{i+1}^n] = -\frac{\eta_{i+1/2}^n (1 - \eta_{i+1/2}^n)}{\eta_{i+1/2}^n (M - 1) + 1} \frac{\eta_{i+1}^n - \eta_i^n}{\Delta\xi}, \quad (3.11)$$

where  $\eta_{i+1/2}^n = (\eta_{i+1}^n + \eta_i^n) / 2$ . The numerical results were validated against the early similarity solution derived in §3.3.1 (see figure 3.6a).

## 3.3 Regime transition: confined to unconfined

First we study the effect of the mobility ratio,  $M$ , on a finite release in a two-dimensional horizontal and confined aquifer without residual trapping ( $Pe = \epsilon = 0$  or  $S_{cr} = S_{br} = \theta = 0$ ). We choose this simple model problem, illustrated in figure 3.3, to study how the transition from confined to unconfined flow depends on the mobility

ratio. The current is initially given by two tilting interfaces and later by a spreading mound. The tilting interfaces correspond to self-similar solutions of (3.2) for a confined aquifer that predict that the tips of the interface propagate as  $x \propto t^{1/2}$ . At late time the governing equation simplifies to the porous medium equation for an unconfined aquifer. The spreading mound is a similarity solution to the porous-medium equation and predicts tip propagation as  $x \propto t^{1/3}$ . We use these scaling laws, which are predicted by the similarity solutions, to study when this transition occurs and how the transition from confined to unconfined flow depends on the mobility ratio.

### 3.3.1 Self-similar solution at early times

For  $L_f < L_d$  the fronts are initially separated, and the finite propagation speeds of the tips of the two interfaces ensure that the fronts will evolve independently until their inward propagating tips collide (figure 3.3b). As a result, during the early period each front can be analysed in isolation, and it is convenient to shift it to the origin ( $\hat{x} = x - L_d$ ), so that the initial condition becomes

$$\hat{h}_0 = \begin{cases} H, & \text{for } \hat{x} \leq \hat{x}_{i,0}, \\ h_0 [\hat{x} + L_d], & \text{for } \hat{x}_{i,0} < \hat{x} < \hat{x}_{o,0}, \\ 0, & \text{for } \hat{x} \geq \hat{x}_{o,0}. \end{cases}$$

The new boundary conditions are

$$\hat{h}[\hat{x} \rightarrow -\infty] = H, \quad \hat{h}[\hat{x} \rightarrow \infty] = 0. \quad (3.12)$$

The early evolution of the interface is independent of the front separation  $2L_d$ , but the duration of this early period depends on  $L_d$ .

### Dimensional analysis

We follow the general procedure for dimensional analysis given by Barenblatt (1996). The problem defined above has three dimensions: length  $L$ , height  $H^*$ , and time  $T$ . The dimensions of the variables and parameters appearing in (3.2) and the initial

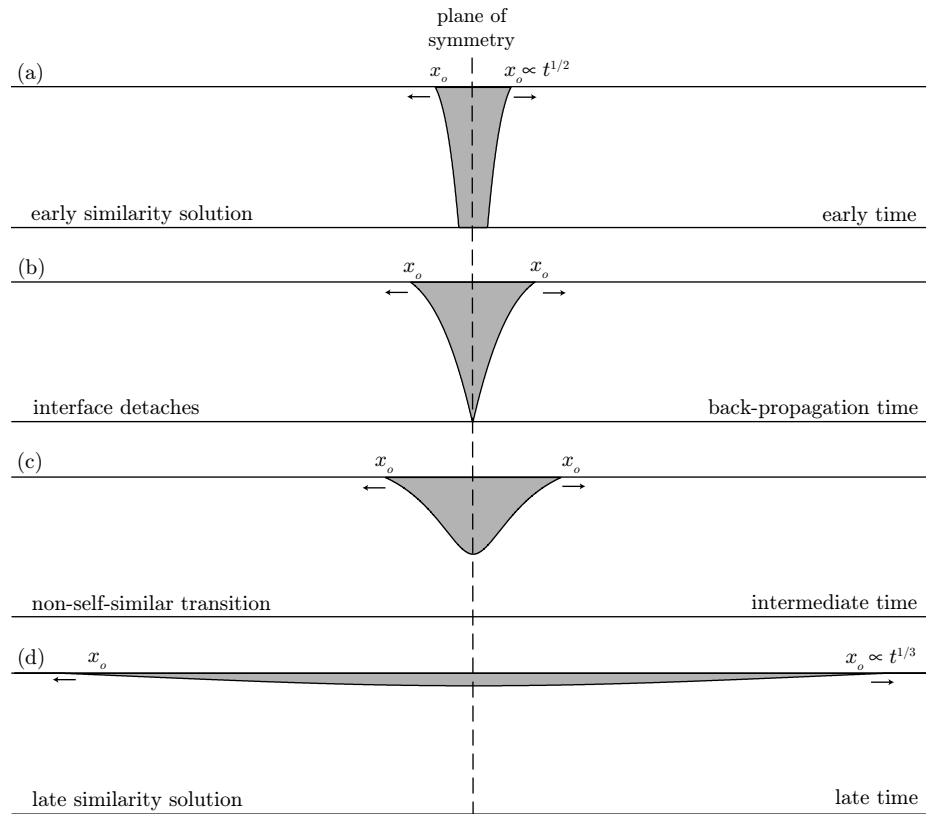


Figure 3.3: The evolution of buoyant CO<sub>2</sub>-vapor (gray) released into a horizontal porous layer saturated by brine (white). The outward propagating tip of the interface is marked by  $x_o$ . All figures are exaggerated in the vertical direction, to make the late solution (d) visible. In many situations of interest the width of the invaded region in figure (a) is several times larger than the aquifer thickness.

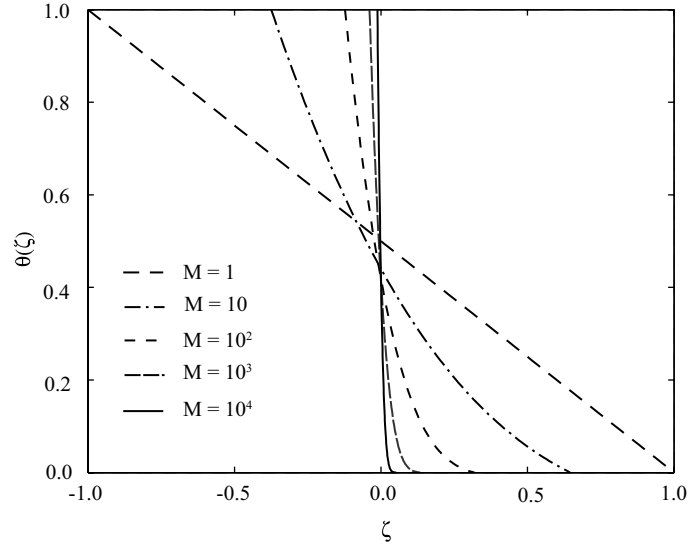


Figure 3.4: Similarity solution is shown for different values of  $M$ . The variable  $\theta$  is the non-dimensional thickness of the CO<sub>2</sub>, it is measured from the top of the aquifer.

condition are

$$[\hat{h}] = [H] = H^*, \quad [\hat{x}] = [L_f] = L, \quad [t] = T, \quad [\kappa] = L^2 H^{*-1} T^{-1}, \quad [M] = 1.$$

The dimensions of the parameters  $\kappa$ ,  $H$ , and  $t$  are independent, and the parameters give the length scale  $l = (\kappa H t)^{\frac{1}{2}}$ . We obtain the dimensionless parameters

$$\Pi = \frac{\hat{h}}{H}, \quad \Pi_1 = \zeta = \frac{\hat{x}}{(\kappa H t)^{\frac{1}{2}}}, \quad \Pi_2 = \zeta_f = \frac{L_f}{(\kappa H t)^{\frac{1}{2}}}, \quad \Pi_3 = M. \quad (3.13)$$

The non-dimensional interface height  $\Pi$  can be written as a dimensionless function,  $\psi$ , of the dimensionless variables  $\Pi = \psi[\Pi_1, \Pi_2, \Pi_3]$ . We seek a similarity solution for times after the details of the particular initial condition have disappeared. As time increases  $\Pi_2 \rightarrow 0$ , while  $\Pi_3$  remains finite, and  $\hat{x}$  can always be chosen so that  $\Pi_1$  is finite. Following the procedure given by Barenblatt (1996) we assume complete similarity in the parameter  $\Pi_2$ , and we seek a solution of the form  $\Pi = \psi[\Pi_1, 0, \Pi_3] =$

$\theta [\Pi_1, \Pi_3]$ . The expressions for  $\hat{h}$  and  $\hat{x}$  in these variables are

$$\hat{h} = H\theta [\zeta, M], \quad \hat{x} = \zeta [M] (\kappa Ht)^{\frac{1}{2}}. \quad (3.14)$$

Dimensional analysis shows that the tip propagation is proportional to  $t^{1/2}$  when this scaling analysis is valid. The inner tip position is given by  $\hat{x}_i = \zeta_i [M] (\kappa Ht)^{1/2}$ , and the outer tip position by  $\hat{x}_o = \zeta_o [M] (\kappa Ht)^{1/2}$ , where  $\zeta_i$  and  $\zeta_o$  are dimensionless quantities that depend only on the mobility ratio  $M$ . Substituting relationships (3.14) into (3.2), we obtain a nonlinear ordinary differential equation for  $\theta$ :

$$-\frac{\zeta}{2} \frac{d\theta}{d\zeta} = \frac{d}{d\zeta} \left( \frac{\theta(1-\theta)}{\theta(M-1)+1} \frac{d\theta}{d\zeta} \right). \quad (3.15)$$

The mobility ratio  $M$  is the only parameter determining the shape of the similarity solution at early times. The inner and outer boundaries of integration  $\zeta_i$  and  $\zeta_o$  are unknown, and must be determined as part of the solution. The boundary conditions are:

$$\theta(\zeta_i) = 1, \quad \left. \frac{d\theta}{d\zeta} \right|_{\zeta_i} = \frac{\zeta_i M}{2}, \quad \theta(\zeta_o) = 0, \quad \left. \frac{d\theta}{d\zeta} \right|_{\zeta_o} = -\frac{\zeta_o}{2}.$$

The boundary conditions on  $\theta$  are the non-dimensional form of (3.12), and the conditions on  $d\theta/d\zeta$  come from inserting the conditions on  $\theta$  into (3.15). Equation (3.15) and the boundary conditions are invariant under reflection in  $\zeta$ , so that if  $\theta_1(\zeta)$  is a particular solution  $\theta_1(-\zeta)$  is also a solution. The physical interpretation of this reflection is exchanging the position of the fluids on either side of the initially vertical interface. The evolution of the interface at early times has been reduced to a nonlinear eigenvalue problem for a second order ordinary differential equation, with two unknown eigenvalues and four boundary conditions. The two additional boundary conditions allow the unique determination of the eigenvalues as a function of the mobility ratio  $M$ . For unit mobility ratio (3.15) reduces to a simpler equation

$$-\frac{\zeta}{2} \frac{d\theta}{d\zeta} = \frac{d}{d\zeta} \left( \theta(1-\theta) \frac{d\theta}{d\zeta} \right) \quad (3.16)$$

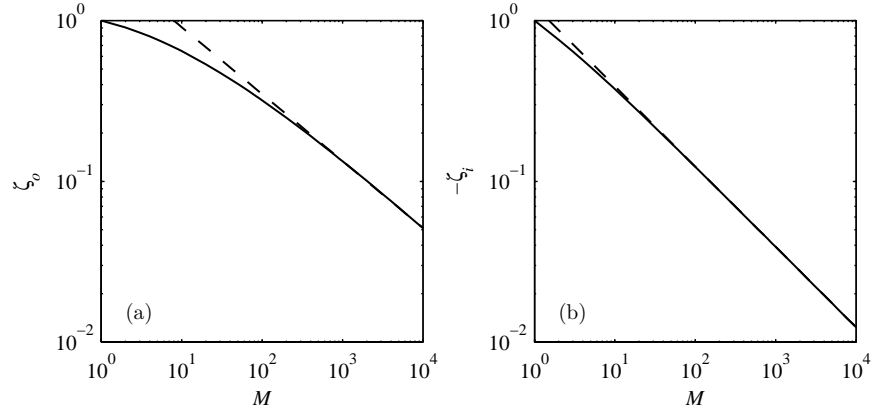


Figure 3.5: The numerical values for the outer (a) and inner (b) tip positions are shown as a function of  $M$  (solid lines). The scaling laws (3.17) and (3.18) are shown as dashed lines.

that has been obtained by Huppert & Woods (1995). The solution is symmetric with respect to the origin, and the eigenvalues become  $\zeta_i = -\zeta_o = 1$ . Huppert & Woods (1995) have obtained the solution  $\theta = \frac{1}{2}(1 + \zeta)$ . We note that  $\zeta_i = -\zeta_o = -1$  and  $\theta = \frac{1}{2}(1 - \zeta)$  is also a solution. In the numerical solutions for the case  $M \neq 1$  we have chosen  $\zeta_i < 0$  and  $\zeta_o > 0$  (see figure 3.4). This choice places the CO<sub>2</sub> on the left side and the brine on the right side of the tilting interface and is consistent with geometry shown in figure 3.2.

### Numerical solution of eigenvalue problem

The nonlinear eigenvalue problem is solved numerically for the shape of the interface and the tip positions as a function of  $M$ . We only need to obtain numerical solutions for  $M > 1$ , the corresponding solutions for  $M < 1$  can be obtained from the transformation (3.4). A shooting method is used to integrate inward from both boundaries of the domain. The mismatch of  $\theta$  and  $d\theta/d\zeta$  at the origin was minimized to determine the eigenvalues for a given value of  $M$ . The analytical solution for  $M = 1$  was used as an initial guess for  $\zeta_i$  and  $\zeta_o$ , and  $M$  was increased incrementally to obtain solutions

for  $M > 1$ . The resulting interface shapes are shown in figure 3.4.

As the mobility ratio increases a gravity tongue develops along one of the horizontal boundaries. In the limit of  $M \rightarrow \infty$  the interface appears to approach a vertical line. The CO<sub>2</sub> viscosity,  $\mu_c$ , is kept constant, because the similarity variable  $\zeta$  depends on  $\mu_c$  through  $\kappa$ . Assuming  $k_{rc}$  and  $k_{rb}$  are constant, increasing the mobility,  $M = \mu_b/\mu_c \cdot k_{rc}/k_{rb}$ , we increase  $\mu_b$ , and in the limit  $\mu_b \rightarrow \infty$  the brine becomes immobile and the interface remains vertical.

Figure 3.5(a, b) shows the position of the inner and outer tips as a function of increasing mobility ratio. For large values of  $M$  the positions of the tips follow scaling laws given by

$$\zeta_i = -e^{0.2210} M^{-0.4997} \approx -\frac{1.24}{\sqrt{M}}, \quad \text{for } M > 10, \quad (3.17)$$

$$\zeta_o = e^{0.8645} M^{-0.4163} \approx \frac{2.37}{M^{0.42}}, \quad \text{for } M > 200, \quad (3.18)$$

which are shown as dashed lines in figure 3.5. The outward propagating non-dimensional tip position for  $M < 1$  is obtained from the following argument

$$\hat{x}_o[M_p < 1] = -\hat{x}_i[M_q > 1] = -\zeta_i[M_q] (\kappa_q H t)^{\frac{1}{2}} = -\zeta_i[M_p^{-1}] \left( \frac{\kappa_p H t}{M_p} \right)^{\frac{1}{2}}.$$

The inward propagating tip  $x_i[M_p < 1]$  can be obtained by an analogous argument. The self-similar tip positions for  $M < 1$  are given by  $\zeta_o[M < 1] = -\zeta_i[M^{-1}]/\sqrt{M}$  and  $\zeta_i[M < 1] = -\zeta_o[M^{-1}]/\sqrt{M}$ . The position of the outward propagating tip of the interface at early times is given by

$$x_o^e = \begin{cases} L_d + \zeta_o[M] (\kappa H t)^{\frac{1}{2}}, & M \geq 1, \\ L_d - \zeta_i[M^{-1}] \left( \frac{\kappa H t}{M} \right)^{\frac{1}{2}}, & M < 1, \end{cases} \quad (3.19)$$

where the superscript  $e$  is used to indicate the scaling for the early similarity solution.



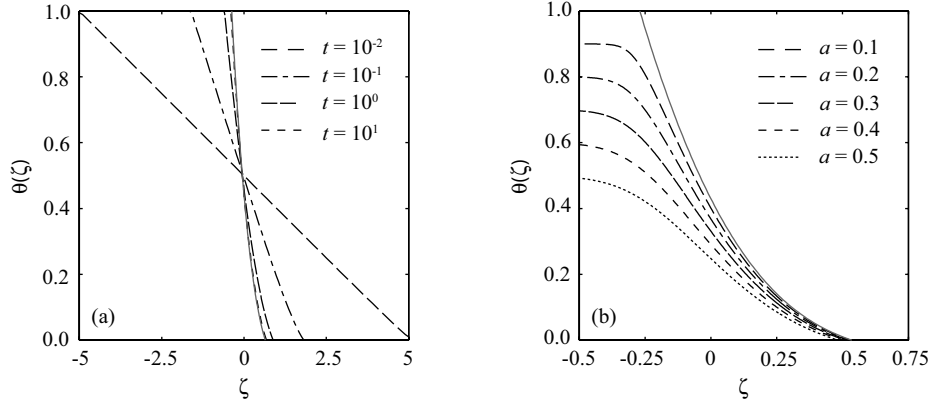


Figure 3.6: (a) The numerical solution to (3.2) with initial condition (3.22) and  $M = 10$  is plotted at various times,  $t$ , and compared to the self-similar solution obtained from (3.15) (solid grey line). (b) Numerical solutions to (3.2) with  $M = 20$  and initial condition (3.25) is shown for several values of the parameter  $a$  in the initial condition and compared to the solution of (3.15) with  $a = 0$  (solid grey line).

The position of the inward propagation tip is given by

$$x_i = \begin{cases} L_d + \zeta_i [M] (\kappa H t)^{\frac{1}{2}}, & M \geq 1, \\ L_d - \zeta_o [M^{-1}] \left(\frac{\kappa H t}{M}\right)^{\frac{1}{2}}, & M < 1. \end{cases} \quad (3.20)$$

The numerical values of  $\zeta_o$  and  $\zeta_i$  can be obtained from figure 3.5 or from (3.17) and (3.18) in the appropriate limits.

### Range of validity of the early similarity solution

The similarity solutions described above were obtained under the assumption of complete similarity in  $\Pi_2$ , which corresponds to a step function initial profile ( $L_f = 0$ ). Barenblatt & Zeldovich (1972) have shown that similarity solutions are intermediate asymptotic solutions for a much larger class of initial conditions. Therefore, the analysis presented above also applies to initial profiles with a finite front width ( $L_f \neq 0$ ), for which  $\Pi_2 \neq 0$ . For this larger class of initial conditions the similarity solution will be valid after the details of the initial conditions have dissipated, because  $\Pi_2 = L_f / (\kappa H t)^{1/2}$  approaches zero for  $L_f \ll (\kappa H t)^{1/2}$ . Hence every particular initial

condition will be asymptotic to the similarity solution for

$$t \gg t_e = \frac{L_f^2}{\kappa H}. \quad (3.21)$$

This is illustrated for a particular initial condition in figure 3.6(a). The initial condition is a ramp defined by

$$\hat{h}_0 = \begin{cases} 0, & \hat{x} < -0.5, \\ \hat{x} + 0.5, & -0.5 \leq \hat{x} \leq 0.5, \\ 1, & \hat{x} > 0.5. \end{cases} \quad (3.22)$$

In this case  $L_f = \kappa = H = 1$ , and we have chosen a mobility ratio of  $M = 10$ . The partial differential equation (3.2) was solved numerically (see §3.2.3), and the solutions at various times are plotted as dashed lines. The similarity solution obtained from the eigenvalue problem is shown for comparison. The particular solution is essentially identical to the similarity solution at  $t = 10$ , which is only an order of magnitude larger than the lower bound  $t_e = 1$ .

For  $t \gg t_e$  the similarity solution is valid until the inward propagating tip reaches the origin  $x_i(t_b) = 0$ , where  $t_b$  is the back-propagation time (figure 3.3b). Solving (3.20) for  $t_b$  we obtain

$$t_b = \begin{cases} \frac{L_d^2}{\kappa H \zeta_i[M]^2}, & M \geq 1, \\ \frac{L_d^2 M}{\kappa H \zeta_o[M^{-1}]^2}, & M < 1. \end{cases} \quad (3.23)$$

Hence the early self-similar solution is valid for  $t_e \ll t \ll t_b$ . We can also define a new length scale  $L_b = 2x_o(t_b)$ , the width of the current at the back-propagation time. For small  $M$ ,  $L_b$  provides a suitable initial length scale for the late similarity solution in §3.3.2.  $L_b$  is given by

$$L_b = \begin{cases} 2L_d \left( 1 + \frac{\zeta_i[M^{-1}]}{\zeta_o[M^{-1}]} \sqrt{M} \right), & M < 1, \\ 2L_d \left( 1 + \frac{\zeta_o[M]}{\zeta_i[M]} \right), & M \geq 1. \end{cases} \quad (3.24)$$

In some situations the CO<sub>2</sub> may not fill the entire depth of the domain, so that the

idealized initial condition is given by

$$h_0^* = \begin{cases} H - a, & \text{for } |x| \leq L_d, \\ 0, & \text{for } |x| > L_d, \end{cases} \quad (3.25)$$

where  $a < H$  is the thickness of the brine in the injection zone. Figure 3.6(b) compares numerical solutions to (3.2) with  $M = 20$  for various values of  $a$ , with the solution to (3.15), which corresponds to  $a = 0$ . Solutions for  $a \neq 0$  are also self-similar in the early similarity variable, so that the outward propagating tip propagates as  $t^{1/2}$  for  $a \neq 0$ . The position of the tip  $\zeta_o$  in self-similar coordinates decreases with increasing  $a$ , but for  $a/H < 0.2$  the difference is less than 10% compared to the values of  $\zeta_o$  given in figure 3.5(a). The evolution of currents that do not occupy the full thickness of the layer is similar to those investigated here and follows the same early scaling law. These results indicate clearly that the viscosity of the brine cannot be neglected, even if the CO<sub>2</sub> plume does not occupy the full thickness of the aquifer. A full investigation of this larger family of similarity solutions for  $a \neq 0$  is beyond the scope of this investigation.

### 3.3.2 Self-similar solution at late times

#### Reduction to the porous medium equation

At the back-propagation time  $t_b$  the interface detaches from one of the horizontal boundaries, and the thickness,  $h$ , of the CO<sub>2</sub> decreases monotonically as a function of time (figure 3.3c, d). At late times  $h \ll H$ , and we expect the solution for a finite layer to be similar to the solution in a half-space. The equation for the half-space can be obtained from (3.2) by taking the limit for  $H \rightarrow \infty$ , for finite  $h$  and  $M$ , or equivalently taking the limit  $h \rightarrow 0$  for finite  $H$  and  $M$ . Consider the limit of the nonlinear diffusion coefficient in (3.2) for small  $h$ , keeping  $M$  and  $H$  constant,

$$\lim_{h \rightarrow 0} \frac{h(H - h)}{h(M - 1) + H} = h. \quad (3.26)$$

In this limit (3.2) reduces to the porous medium equation

$$\frac{\partial h}{\partial x} = \kappa \frac{\partial}{\partial x} \left( h \frac{\partial h}{\partial x} \right), \quad (3.27)$$

which has been studied intensively, and the similarity solution for a finite release of fluid into a two-dimensional porous half-space was found by Barenblatt (1952).

We expect that the limit (3.26) becomes a good approximation even if  $h \ll H$  is finite, and (3.27) becomes a good approximation for (3.2) after some time. The parameter  $M$  can vary over several orders of magnitude, and we need to consider its effect on the validity of approximation (3.26). Consider the approximation in the denominator of (3.26) for finite but small values of  $h$

$$h(M - 1) + H \approx H.$$

Large values of  $M$  require even smaller values of  $h$  to allow this approximation. Since  $h$  is a monotonically decreasing function of time, the half-space approximation will become valid for all  $M$  eventually. In § 3.3.3 we develop an expression for the onset of half-space behaviour as a function of  $M$ . For small  $M$  the half-space approximation becomes valid very quickly. In the limit of small mobility ratios we obtain

$$\lim_{M \rightarrow 0} \frac{h(H - h)}{h(M - 1) + H} = h, \quad (3.28)$$

and (3.2) reduces to (3.27) at all times and for all values of  $h$  and  $H$ . As mentioned in § 3.1.2, the simplification in this limit is responsible for the success of (3.27) in problems of unconfined flow, where the ambient fluid is a gas ( $M \ll 1$ ).

Equation (3.27) depends only on the CO<sub>2</sub> mobility,  $\lambda_c$ , not on the mobility ratio  $M$ . From the global conservation of mass  $Q_c + Q_b = 0$ , we can obtain an expression for the Darcy velocity  $q_b$  in the ambient fluid

$$q_b = -\frac{h_c q_c}{(H - h_c)}. \quad (3.29)$$

For finite  $h$  and  $q_c$  the flux in the brine  $q_b$  becomes negligible as  $H \rightarrow \infty$ . In contrast

to the early evolution, where  $M$  is the governing parameter, the problem becomes independent of the mobility ratio at late times, because the brine is stationary.

### Barenblatt's solution

In either limit the initial condition for the porous medium equation is a particular gas distribution  $\tilde{h}[x]$ , with finite width  $L_b$ , in a half-space otherwise saturated by water. The volume of current is given by

$$V = \int \tilde{h}[x] dx = 2L_d H. \quad (3.30)$$

A similarity solution in the parameters

$$h = \left( \frac{V^2}{\kappa t} \right)^{\frac{1}{3}} \varphi[\varsigma] \quad \text{and} \quad x = \varsigma(\kappa V t)^{\frac{1}{3}} \quad (3.31)$$

has been found by Barenblatt (1952) and is given by

$$h[x, t] = \begin{cases} \frac{1}{6} \left( \frac{V^2}{\kappa t} \right)^{\frac{1}{3}} \left( \varsigma_o^2 - \frac{x^2}{(\kappa V t)^{\frac{2}{3}}} \right), & \text{for } |x| \leq x_o^l, \\ 0, & \text{for } |x| > x_o^l. \end{cases} \quad (3.32)$$

From the definition of the self-similar coordinate,  $\varsigma$ , the tip propagation at late times is proportional to  $t^{1/3}$ , and the front position at late time is given by

$$x_o^l = (9\kappa L_d H t)^{\frac{1}{3}}. \quad (3.33)$$

The superscript  $l$  identifies the tip scaling for the late similarity solution. The late similarity solution depends on the CO<sub>2</sub> volume  $V = 2\phi L_d H$ , but it is independent of the local length scale  $L_f$  of the initial front, and the mobility ratio  $M$ . In contrast the early tip scaling (3.19) is independent of the global length scale  $L_d$ , but depends on  $L_f$  and  $M$ .

The similarity solution obtained for the idealized initial condition is an intermediate asymptotic solution for a larger range of initial conditions with  $L_b \neq 0$ , for times

larger than

$$t \gg t_l = \tilde{t} + \frac{L_b^3}{2\kappa_g L_d H}, \quad (3.34)$$

where  $\tilde{t}$  is the time at which (3.26) becomes valid. This lower bound becomes important when  $M \ll 1$ , and the porous medium equation becomes valid very quickly. In this case  $\tilde{t} = t_b$  and (3.24) is a suitable initial length scale  $L_b$ , so that  $t_l$  becomes

$$t_l = \frac{L_d^2}{\kappa H} \left( 8 \left( \frac{1 + \sqrt{M} \zeta_i [M^{-1}]}{\zeta_o [M^{-1}]} \right)^3 - \frac{M}{\zeta_o [M^{-1}]^2} \right). \quad (3.35)$$

### 3.3.3 Non-self-similar transition

We obtain a description of the front propagation speed at early times from the similarity solution describing a tilting interface (§ 3.3.1). At late times the governing equations simplify to (3.27), and the similarity solution of Barenblatt (1952) gives the propagation speed at late times. The transition from the early to the late similarity solution will not be self-similar, and must be investigated numerically.

We study this transition as a function of the dimensionless mobility ratio,  $M$ . We consider initial distributions that are symmetric with respect to the origin, so that we only need to consider the spatial domain  $[0, a]$ , where  $a > 0$  is chosen larger than the maximum propagation distance estimated from (3.33). The initial condition in all simulations is the following step function

$$\eta[\xi, \vartheta = 0] = \begin{cases} 1, & \xi \leq 1, \\ 0, & \xi > 1. \end{cases} \quad (3.36)$$

The problem is symmetric with respect to the origin, so that the boundary condition at the origin is  $\partial\eta(0, \vartheta)/\partial\xi = 0$ , and the outer boundary condition is  $\eta(a, \vartheta) = 0$ .

#### Transition time

The two examples in figures 3.7(a) and 3.7(b) show the numerical transition from the early to the late similarity solution. The initial condition is the early similarity

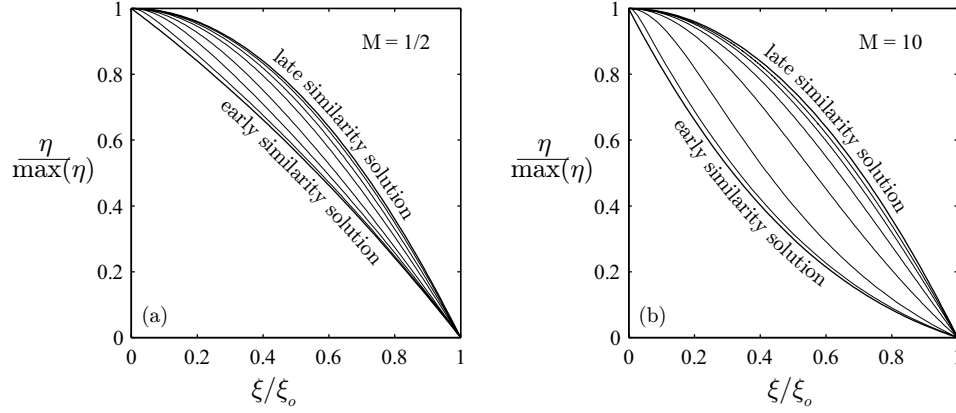


Figure 3.7: The transition of the numerical solution (light lines) from the early to the late similarity solution (both heavy lines) is shown in scaled coordinates. (a) The numerical solution is shown at  $\vartheta = \vartheta_b + \{1, 4, 10, 30, 100\}$ , where  $\vartheta_b = 0.61$ ; (b) The numerical solution is shown at  $\vartheta = \vartheta_b + \{10^1, 10^2, 10^3, 10^4, 10^5\}$ , where  $\vartheta_b = 7.1$ .

solution at the non-dimensional back-propagation time  $\vartheta_b$  given by

$$\vartheta_b = \begin{cases} \frac{1}{\zeta_i[M]^2}, & M \geq 1, \\ \frac{M}{\zeta_o[M^{-1}]^2}, & M < 1. \end{cases} \quad (3.37)$$

In figure 3.7(a) the evolution is shown for  $M = 1/2$ . In this case the curvature of the early and the late similarity solution is of the same sign. The main difference between them is the slope at the origin, where the early similarity solution has a finite slope, but the late similarity solution has zero slope. In this case the transition period is relatively short, and the late similarity solution is a good approximation to the solution for  $\vartheta > 100$ . Figure 3.7(b) shows the transition for the case  $M = 10$ . In this case the curvature of the early and the late similarity solution is of opposite sign. The numerical solution adjusts very slowly and the transition period is very long.

### Transition of the scaling for the tip position

Figure 3.8(a-d) shows the numerical results for the non-dimensional position of the outward propagating tip  $\xi_o$  of the CO<sub>2</sub> as a function of non-dimensional time  $\vartheta$ . The figure shows the effect of increasing the mobility ratio  $M$  on the tip propagation and the timing of the transition. The scaling laws for the tip position obtained from the early and late similarity solutions are also shown. In non-dimensional coordinates these scaling laws (3.19, 3.33) simplify to

$$\xi_o^e = \begin{cases} 1 + \zeta_o [M] \vartheta^{\frac{1}{2}}, & M \geq 1, \\ 1 - \zeta_i [M^{-1}] \vartheta^{\frac{1}{2}} M^{-\frac{1}{2}}, & M < 1, \end{cases} \quad (3.38)$$

$$\xi_o^l = (9\vartheta)^{\frac{1}{3}}, \quad (3.39)$$

respectively. The shifted tip position  $\xi_o - 1$  is plotted as a function of time in logarithmic axes, so that the early scaling law (3.38) plots as a straight line with slope  $1/2$ . In these variables the late scaling law (3.39) does not plot as a straight line, but it approaches a straight line with slope  $1/3$  for large times, where it becomes valid. The late scaling law is independent of  $M$ , and therefore represented by the same curve in all four figures, while the straight line corresponding to the early similarity solution is shifted downward as  $M$  increases.

Comparison of the numerical results with the scaling laws from the early and late similarity solutions leads to the following four observations:

1. The numerical tip position initially follows the early scaling law  $\xi_o \propto \vartheta^{1/2}$ , and then the scaling law for late times  $\xi_o \propto \vartheta^{1/3}$ .
2. The transition time  $\vartheta_t$  increases monotonically with increasing  $M$ . Comparison of figures 3.8(a) and 3.8(b) shows that this increase is very small for  $M < 10^{-1}$ . Figures 3.8(c) and 3.8(d) show a rapid increase of the transition time for  $M > 10^{-1}$ .
3. The transition from early to late scaling is short for  $M \approx 10^{-1}$  (figure 3.8b), and increases rapidly for  $M > 10^{-1}$  (figure 3.8d).



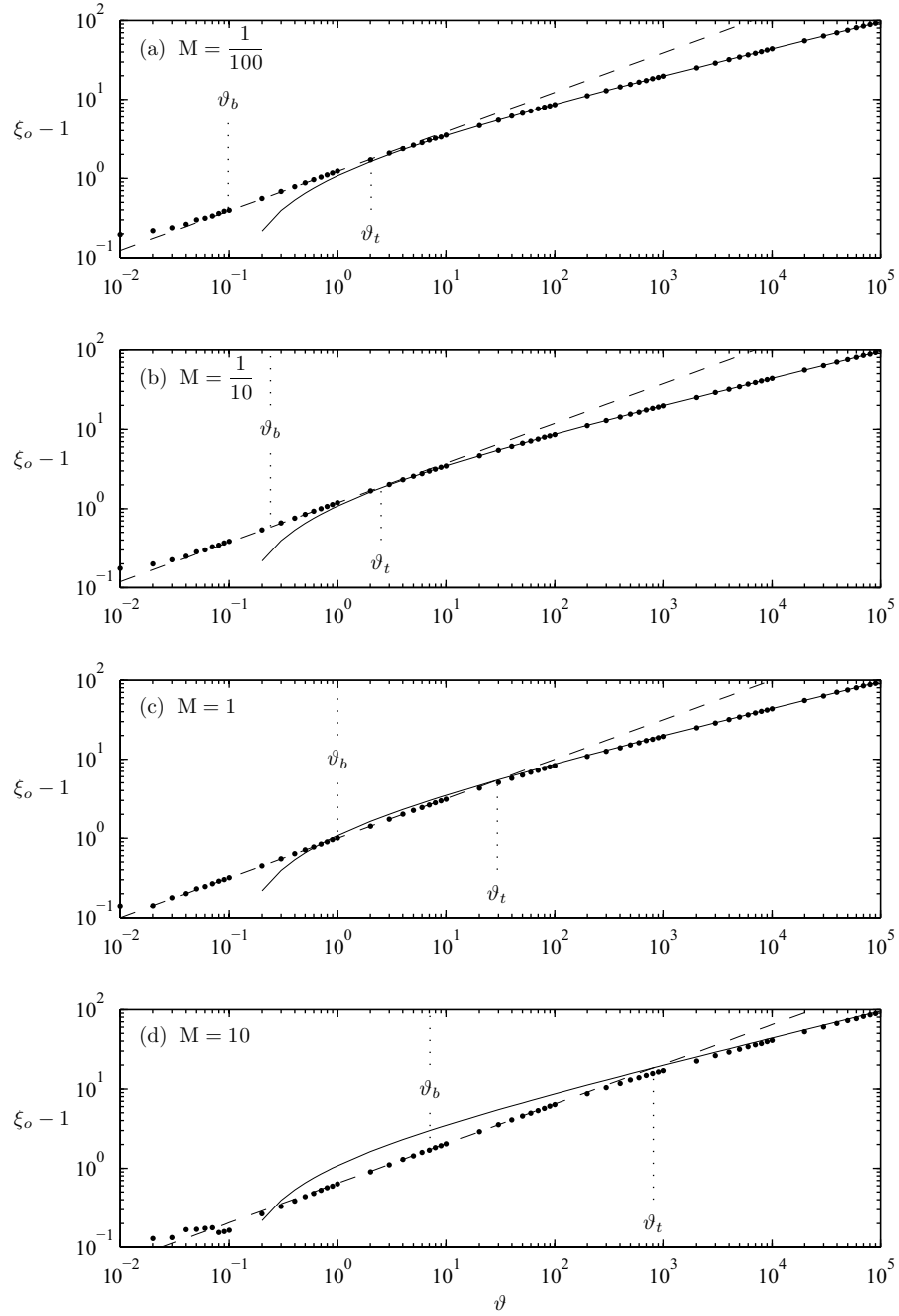


Figure 3.8: The numerical results for the non-dimensional tip position  $\xi_o$  are shown as a function of non-dimensional time  $\vartheta$ , for different mobility ratios  $M$ . In all figures the numerical solution is given by dots ( $\cdots$ ), the tip scaling from the early similarity solution by a dashed line ( $- -$ ), and the tip scaling from the late similarity solution as a full line ( $—$ ). (a)  $\vartheta_t = 2.0$ ,  $\vartheta_b = 0.1$ ; (b)  $\vartheta_t = 2.5$ ,  $\vartheta_b = 0.24$ ; (c)  $\vartheta_t = 29.3$ ,  $\vartheta_b = 1$ ; (d)  $\vartheta_t = 811.3$ ,  $\vartheta_b = 1$ ; (d)  $\vartheta_t = 811.3$ ,  $\vartheta_b = 7.1$ .

4. The tip position follows the early scaling law  $\xi_o \propto \vartheta^{1/2}$  even after the early similarity solution has become invalid at  $\vartheta_b$  (3.37). In figure 3.8(a-c) the early scaling law continues to be valid almost up to  $\vartheta_t$ . This shows that the finite depth of the layer continues to have a strong effect on the solution, even after the interface has detached from one of the boundaries.

Although the early and late scaling behaviours are separated by a transition period, it is useful to define a dimensionless transition time  $\vartheta_t$  that falls within this transition period. This transition time defines a lower bound for the validity of the late similarity solution. The difference between the early and the late scaling laws is given by

$$f[\vartheta; M] = (\xi_o^l - 1) - \xi_o^e, \quad (3.40)$$

where  $\xi_o^l$  is given by (3.39), and  $\xi_o^e$  by (3.38). We use the substitution  $\vartheta = y^6$  to eliminate  $\vartheta^{1/2}$  and  $\vartheta^{1/3}$  and obtain a cubic in  $y$ . Let  $M_t$  denote the value of  $M$ , where the early scaling law is tangent to the late scaling law such that  $f(\vartheta; M_t) = 0$ . For  $M \geq M_t$  the non-dimensional transition time  $\vartheta_t$  can be defined as the intersection of the early and late time scaling laws (figure 3.8c, d), and is therefore given by the largest real root of  $f(\vartheta; M \geq 1) = 0$ . For  $M < M_t$  the two scaling laws do not intersect, but the transition time can be defined as the point of minimal vertical distance between the two scaling laws (figures 3.8c and 3.8d) given by the local minimum of (3.40). Solving for the appropriate root and the minimum we obtain the following expression for the non-dimensional transition time

$$\vartheta_t = \begin{cases} \frac{1}{9\zeta_o[M]^6} \left(1 + 2 \cos \left[\frac{\pi}{3} - \frac{\theta}{3}\right]\right)^6, & M \geq 1, \\ \frac{M^3}{9\zeta_i[M^{-1}]^6} \left(1 + 2 \cos \left[\frac{\pi}{3} - \frac{\theta}{3}\right]\right)^6, & M_t \leq M \leq 1, \\ \frac{64M^3}{9\zeta_i[M^{-1}]^6}, & M \leq M_t, \end{cases} \quad (3.41)$$

where  $\theta$  is the principle argument of the following complex numbers

$$\theta = \begin{cases} \text{Arg} \left[ -2 + 3\zeta_o[M]^2 + i\zeta_o[M] \sqrt{12 - 9\zeta_o[M]} \right], & M \geq 1, \\ \text{Arg} \left[ -2M^{\frac{3}{2}} + 3\sqrt{M}\zeta_i \left[\frac{1}{M}\right]^2 - i\zeta_i \left[\frac{1}{M}\right] \sqrt{3M \left(4M - 3\zeta_i \left[\frac{1}{M}\right]^2\right)} \right], & M_t \leq M \leq 1. \end{cases}$$

Due to the change in the definition of the transition time at  $M_t$  the graph is not smooth at this point (figure 3.9). For  $M < M_t$  the transition time increases very slowly with  $M$ , while it increases strongly for  $M \geq M_t$  (figure 3.9).  $M_t$  can be obtained by finding the value of  $M$  for which the local minimum of (3.40) is zero.

$$M_t - \frac{3}{4}\zeta_i [M_t^{-1}]^2 = 0. \quad (3.42)$$

This equation must be solved numerically, because  $\zeta_i [M_t^{-1}]$  is not known analytically, and we obtain  $M_t = 0.1839$ . For large values of  $M$ ,  $\xi_o(\vartheta_t) \gg 1$ , and (3.40) simplifies to  $f \approx \hat{f} = \xi_o^l - \xi_o^e$  and gives a scaling law for the transition time  $\vartheta_t = 0.45M^{5/2}$ . For small values of  $M$ , (3.20) can be used to simplify (3.41) to obtain a constant  $\vartheta_t = 1.96$ . Equation 3.41 is complicated to evaluate, and we therefore introduce a simple expression based on the two limits discussed above and a simple fit for intermediate values.

$$\vartheta_t \approx \begin{cases} 0.45M^{5/2}, & 10^2 < M, \\ 36.6M^{3/2}, & M_t \geq M \leq 10^2, \\ 2, & M < M_t. \end{cases} \quad (3.43)$$

### 3.3.4 Regime diagram

We summarize our results on the evolution of a finite release of CO<sub>2</sub> into a horizontal aquifer saturated with brine, where the density difference between the immiscible fluids is the only driving force. Figure 3.9 combines all time scales into a  $M$ - $\vartheta$  regime diagram that describes the evolution of a finite CO<sub>2</sub> plume. The only parameter in this problem is the mobility ratio,  $M = \lambda_c/\lambda_b$ , between the CO<sub>2</sub> and the brine. The magnitude of a particular dimensional time scale is given by the characteristic time  $t^d = L_d^2 \kappa^{-1} H^{-1}$  formed using the displacement distance  $L_d$ , the conductivity of the CO<sub>2</sub> given by  $\kappa$ , and the height of the layer  $H$ . The CO<sub>2</sub> mobility,  $\lambda_c$ , appears in  $\kappa$ , and  $\kappa$  enters the characteristic time  $t^d$  used for the non-dimensionalisation, hence  $\lambda_c$  is constant and changes in  $M$  are due to changes in  $\lambda_b$ . For all finite values of  $M$  the evolution can be divided into three dynamic stages: an early self-similar regime, a transition period, and a late self-similar regime.

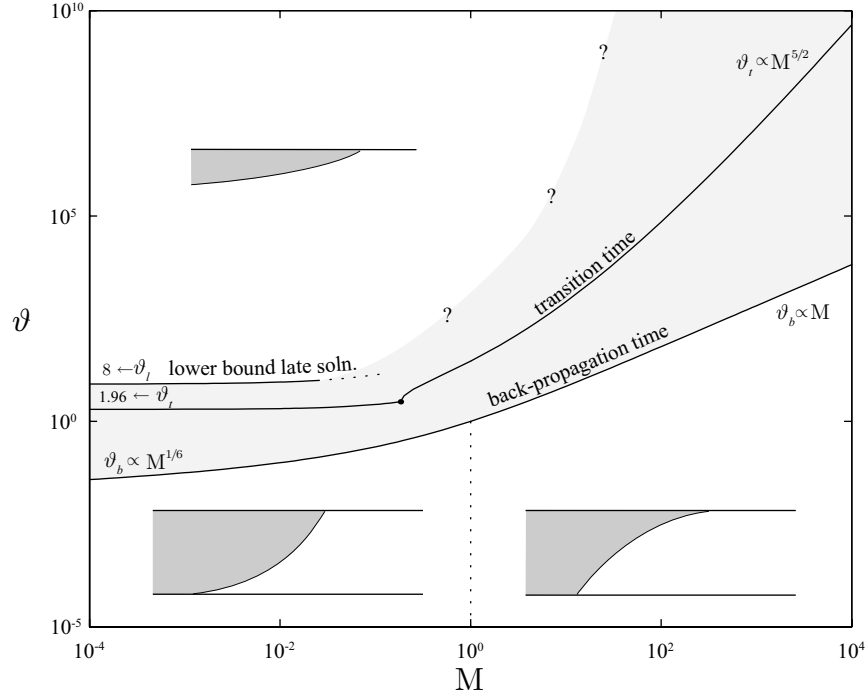


Figure 3.9: Regime diagram for a finite release of fluid into a horizontal porous slab, showing the non-dimensional time scales obtained in this study, and the shapes of the gravity current as a function of the mobility ratio  $M$ . The shaded region indicates the transition period between the similarity solutions. The characteristic time to dimensionalize all results is  $t^d = L_d^2 \kappa^{-1} H^{-1}$

After the details of the initial condition are lost, the interface shape and dynamics are asymptotic to an early similarity solution that corresponds to a tilting interface. The early similarity variable is  $\zeta = x(\kappa H t)^{-1/2}$ , so that the non-dimensional tip position is given by  $\xi_o \propto \vartheta^{1/2}$ . During this period the left and the right interfaces evolve independently, and the length scale of their separation,  $2L_d$ , does not appear in the similarity variable. In this phase, both fluids move with non-zero velocities, and therefore the mobility ratio  $M$  determines the shape of the interface. We have not plotted the lower bound for the onset of the early similarity solution (3.21), because this time scale depends on the initial width of the front  $L_f$ , which is given by  $\vartheta_e = (L_f/L_d)^2$ . The validity of the early similarity solution ends at the back-propagation time,  $\vartheta_b$ ,

because the inward propagating tips of the two initially separated fronts begin to interact at the origin (figure 3.3*b*). Figure 3.9 shows that  $\vartheta_b$  increases monotonically with time, and follows simple scaling laws for small and large  $M$ . Physically we can explain the increase of  $\vartheta_b$  with increasing  $M$  by the increasing viscosity of the brine, which slows down the inward propagating tip of the tilting interface. The period during which the early similarity solution is valid increases with increasing  $M$ , because the  $\vartheta_e \neq \vartheta_e[M]$ . As long as  $L_f \neq 0$  there are always values  $M \leq M_c$  such that  $\vartheta_e \geq \vartheta_b$ , and hence the early similarity solution is not realized.  $M_c$  is determined by the equation  $L_f/L_d = \sqrt{M_c}/\zeta_o[M_c^{-1}]$  for  $M_c < 1$ , a similar equation can be found for  $M_c > 1$ . Even in the case  $L_f = 0$  the early similarity solution will not be realized in the limit  $M \rightarrow 0$ , because  $\vartheta_b \rightarrow 0$ . Figure 3.8 shows that the scaling law for the non-dimensional tip position  $\xi_o \propto \vartheta^{1/2}$  is valid for a significant time even after the early similarity solution itself has become invalid at  $\vartheta_b$ .

The initial similarity solution is followed by a period where the solution is not self-similar and must be obtained numerically (figure 3.7). For  $M \ll 1$  we can define the transition period as  $\vartheta_b < \vartheta < \vartheta_t$ , where  $\vartheta_t$  is given by (3.35). The duration of the transition period increases as  $M \rightarrow 0$ , because the upper boundary is constant  $\vartheta_t = 8$ , while the lower boundary is proportional to  $\vartheta_b \propto M^{1/6}$ . For  $M > 1$  we have no estimate of the upper boundary of the transition period. The numerical results in figure 3.8(*b-d*) show that the transition period increases with increasing  $M$ . From the transition of the scaling laws for the tip position we have defined a transition time  $\vartheta_t$ , that provides a lower bound on the onset of the late similarity solution. Equation 3.41 or (3.43) shows a rapid increase of  $\vartheta_t$  with increasing  $M$  for  $M > M_t$ .

After the transition period the late similarity solution becomes valid, because the CO<sub>2</sub> occupies only a small fraction of the thickness of the aquifer, and (3.2) reduces to (3.27). Equation 3.27 admits a similarity transformation in the variable  $\varsigma = x/(\kappa V t)^{-1/3}$ , and the analytical solution was obtained by Barenblatt (1952). In contrast to the early similarity solution, this late similarity solution is independent of  $M$  and depends on the volume of the gravity current, given by  $V = 2L_d H$ . In this limit the velocity of the brine is negligible, which explains why the problem is now independent of the mobility of the brine, and hence the mobility ratio  $M$ .

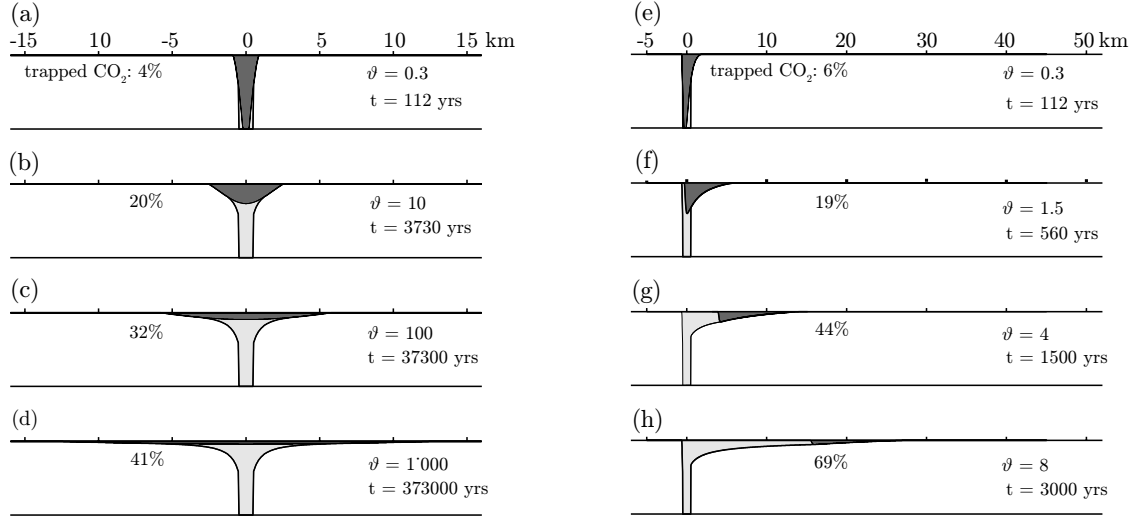


Figure 3.10: Current evolution in an aquifer with 30 mD permeability, for details of the physical properties see § 3.5.2. CO<sub>2</sub> currents (dark grey) and the zone containing residual saturation in their wake. Figures *a* to *d* show the evolution in a horizontal aquifer. These figures are equivalent to figure 3.3, but they include the effect of residual trapping. Figures *e* to *h* show the evolution in an equivalent aquifer sloping with 5°.

When the late similarity solution is valid, the non-dimensional tip position is given by  $\xi_o \propto \vartheta^{1/3}$ . Again the scaling for the tip position becomes valid before the solution is fully self-similar.

### 3.4 Gravity currents with residual trapping

The regime diagram of gravity currents in horizontal aquifers (figure 3.9) shows clearly that the confined nature of the aquifer has to be taken into account if gravity currents with  $M > 1$  are considered. The mobility ratio for the migration of the CO<sub>2</sub> plume is  $M \approx 5$ , so that we have to study the effect of residual trapping on a CO<sub>2</sub> plume migrating in a confined aquifer. In particular the early similarity solution (figure 3.4) shows that a gravity tongue forms for  $M > 1$ , which reduces the vertical sweep of the CO<sub>2</sub> plume. Most research on residual trapping during CO<sub>2</sub> storage has focused on the effect of hysteresis on the magnitude of  $S_{cr}$ , and the design of injection strategies

that maximize residual trapping during or shortly after the injection period (Mo *et al.*, 2005; Juanes *et al.*, 2006; Ide *et al.*, 2007). We focus on the effect of the vertical sweep efficiency,  $\mathcal{S}$ , which is defined as the fraction of the aquifer contacted by the CO<sub>2</sub> plume during its buoyancy-driven migration in the post-injection period. A volume balance argument shows that the up-dip migration distance,  $x_{\uparrow}$ , is approximately given by

$$x_{\uparrow} \approx V_c / (\phi H \mathcal{S} S_{cr}), \quad (3.44)$$

where  $V_c$  is the volume of CO<sub>2</sub>,  $H$  the thickness of the aquifer, and  $\phi$  the porosity. Ennis-King & Paterson (2002) used this relationship to highlight the sensitivity of the migration distance to the magnitude of  $S_{cr}$ . Equation (3.44) shows that the effect of  $\mathcal{S}$  on the migration distance of the CO<sub>2</sub> plume is comparable to that of  $S_{cr}$ . The sweep is expected to be less than unity, because gravity segregation and viscous instabilities lead to the formation of a gravity tongue along the top of the aquifer.

### 3.4.1 Parabolic limit: horizontal aquifers

Here we extend the analysis presented in § 3.4 to include the effect of residual trapping. In the presence of residual trapping an analogous transition from an early to a late scaling law is observed. However, we show below that the exponents of the early scaling laws are independent of the residual, while Bear & Ryzhik (1998) showed that the exponents of the late scaling laws are a function of the residual. In the terminology of Barenblatt (1996), the evolution of the current transitions from a similarity solution first kind to a similarity solution of the second kind.

#### Early similarity solutions with loss

Initially the two interfaces of the current evolve independently and symmetrically (figure 3.10a). Until they interact they evolve as tilting interfaces described by a self similar solution given by a step function initial condition

$$\eta = \begin{cases} a, & \xi < \tilde{\xi}, \\ b, & \xi \geq \tilde{\xi}, \end{cases} \quad (3.45)$$

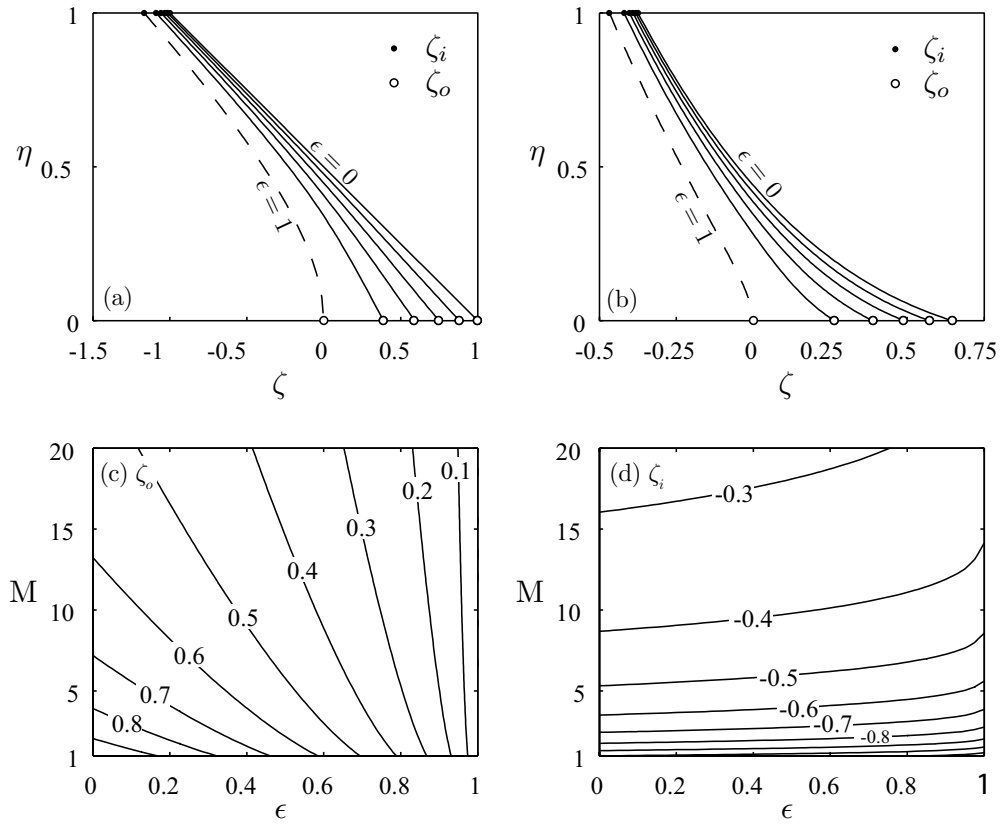


Figure 3.11: (a) Interface shapes for  $M = 1$  and  $\epsilon$  increasing from 0 to 1 in 0.2 increments. (b) Interface shapes for  $M = 10$  and  $\epsilon$  increasing from 0 to 1 in 0.2 increments. (c) Contours of the outward propagating tip position,  $\zeta_o$ . (d) Contours of the inward propagating tip position,  $-\zeta_i$ .



where  $\tilde{\xi}$  is the initial position of the interface. Here we consider only the cases  $a = 1$  and  $b = 0$ , but self-similar solutions are not limited to this choice. The outward and inward propagating tips of the interface are denoted by  $\xi_o$  and  $\xi_i$  respectively. For  $\tilde{\xi} < \xi \leq \xi_o$  the interface is advancing, and the thickness of the current is increasing,  $\eta_\vartheta > 0$ , so that  $\sigma = 1 - \epsilon$ . For  $\xi_i \leq \xi < \tilde{\xi}$  the interface is receding, and the thickness of the current is decreasing,  $\eta_\vartheta < 0$ , so that  $\sigma = 1$ . The location  $\tilde{\xi}$  of the discontinuity in the coefficient is constant at early times.

Equation 3.7b and the initial condition (3.45) are self-similar in the variable  $\zeta = \xi/\vartheta^{1/2}$ . Therefore, the propagation of the plume tip at early time is given by the scaling law  $\xi_o = a[\epsilon, M]\vartheta^{1/2}$ , where  $a$  is a constant that decreases with increasing  $\epsilon$ . Inserting  $\text{Pe} = 0$  and the similarity variable into (3.2b), we obtain the ordinary differential equation

$$-\frac{\zeta}{2} \frac{d\eta}{d\zeta} = \tilde{\sigma} \frac{d}{d\zeta} \left( \frac{\eta(1-\eta)}{\eta(M-1)+1} \frac{d\eta}{d\zeta} \right), \quad (3.46)$$

where  $\sigma[\eta_\zeta \zeta_\vartheta] = \tilde{\sigma}[\eta_\zeta]$ . The mobility ratio,  $M$ , and the residual,  $\epsilon$ , determine the shape of the similarity solution at early times. The inner and outer boundaries of integration  $\zeta_i$  and  $\zeta_o$  are unknown, and they are generally functions of both  $M$  and  $\epsilon$ . These eigenvalues must be determined as part of the solution, requiring two additional constraints. The boundary conditions on the inward and outward propagating tips are given by

$$\eta[\zeta_i] = 1, \quad \left. \frac{d\eta}{d\zeta} \right|_{\zeta_i} = \frac{\zeta_i M}{2}, \quad (3.47)$$

$$\eta[\zeta_o] = 0, \quad \left. \frac{d\eta}{d\zeta} \right|_{\zeta_o} = \frac{-\zeta_o}{2(1-\epsilon)}. \quad (3.48)$$

respectively. The conditions on  $\eta$  specify the vertical extent of the interface. The conditions on  $\eta_\zeta$  have no direct physical interpretation, but they are required to satisfy (3.15) at the boundaries  $\zeta_i$  and  $\zeta_o$ , and they provide the two additional constraints necessary to determine the eigenvalues. Together (3.46) and (3.47) form a nonlinear eigenvalue problem for the shape of the interface and the two unknown tip positions,

$\zeta_i$  and  $\zeta_o$ . This eigenvalue problem is solved numerically as a function of  $M$  and  $\epsilon$  using a shooting method.

Figures 3.11(*a-b*) show that increasing  $M$  leads to the formation of a gravity tongue, while increasing  $\epsilon$  tends to shorten the gravity tongue and may lead to an inflection in the interface. For  $M \geq 1$  the outward propagating tip position,  $\zeta_o$ , is mostly a function of  $\epsilon$ , while the inward propagating tip position,  $\zeta_i$ , is more strongly affected by  $M$  (figure 3.11*c-d*). In the limit where all fluid is trapped,  $\epsilon = 1$ , the interface does not propagate,  $\xi_o = \tilde{\xi}$ , but the interface does recede,  $\xi_i \neq \tilde{\xi}$ . However, the distinction between the fluids across the receding interface is lost, and the interface loses its physical significance. The evolution of this imaginary interface is still given by (3.46), but it does not correspond to any fluid movement.

The early similarity solution shows that residual trapping has only a weak influence on the evolution of the receding part of the interface. Instead residual trapping slows down the advancing interface, because less fluid is supplied from the receding part. A similar behavior is observed in the hyperbolic model discussed in § 3.4.2.

### Regime transition and late solution

In § 3.3.2 we show that  $f \rightarrow \eta$  at late times when the current is much thinner than the thickness of the aquifer, so that (3.7*b*) reduces to

$$\eta_\theta = \sigma (\eta \eta_\xi)_\xi, \quad (3.49)$$

for all  $M$ . The only parameter in this equation is the residual,  $\epsilon$ , in the discontinuous coefficient,  $\sigma$ . Semi-analytical solutions for the interface shape are available for the radial (Kochina *et al.*, 1983; Barenblatt, 1996), and linear cases (Bear & Ryzhik, 1998).

For a compact initial condition, the solution of a parabolic equation with a moving discontinuous coefficient is a similarity solution of the second kind (Barenblatt, 1996). These solutions are characterized by an anomalous exponent in the scaling laws that

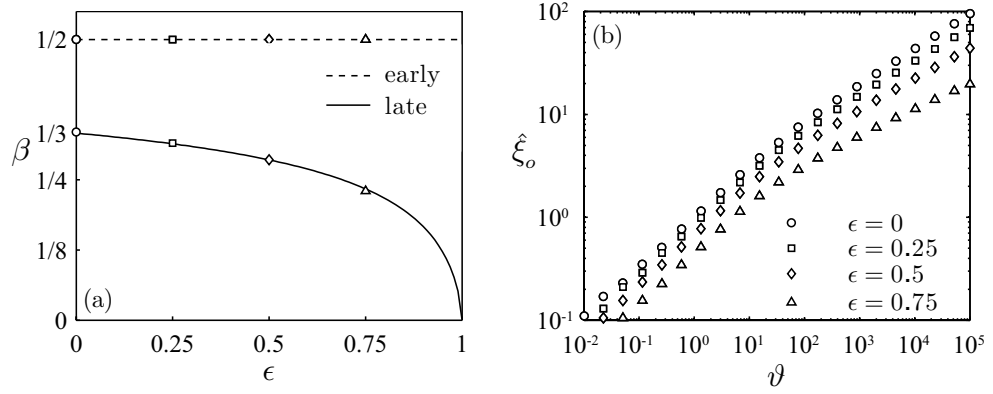


Figure 3.12: Change of the solution from the early to the late scaling law ( $M = 1$ ). (a) The scaling laws for  $\xi_o \propto v^\beta$  at early and late times as a function of the residual,  $\epsilon$ . The symbols at  $\epsilon$  of 0, 1/4, 1/2, and 3/4 show the exponents obtained by fitting the numerical data shown in figure b. For the early scaling law the data was fit for  $v$  between 0.1 and 10 and for the late scaling law the data was fit for  $v > 1000$ . (b) The shifted tip position,  $\hat{\xi} = \xi_o - \tilde{\xi}$ , is shown as function of  $v$ , for increasing residuals, where  $\tilde{\xi} = 1$ .

govern the solution. In this case we obtain

$$\xi_o = c_1 [\epsilon, M, \eta_0] v^{\beta(\epsilon)}, \quad (3.50)$$

$$\eta_{\max} = c_2 [\epsilon, M, \eta_0] v^{2\beta(\epsilon)-1}, \quad (3.51)$$

$$\mathcal{V} = c_3 [\epsilon, M, \eta_0] v^{3\beta(\epsilon)-1}, \quad (3.52)$$

for the tip of the plume, the height of the plume, and the volume of the plume. Figure 3.12(a) shows the decrease of the anomalous exponent  $\beta$  with increasing  $\epsilon$ . For (3.49) the exponent must be determined numerically from a nonlinear eigenvalue problem (see Bear & Ryzhik, 1998). As expected the increasing residual trapping leads to a faster decrease of the plume volume and slower tip propagation. Another characteristic of this type of solution is that the constants of proportionality ( $c_1$ - $c_3$ ) in these scaling laws depend on the initial condition.

Figure 3.12(b) shows transition in the scaling law for the tip position from the early scaling law, with the exponent 1/2, to the late scaling law with the anomalous

exponent  $\beta \leq 1/3$ . Initially only the constant in the scaling law is affected by  $\epsilon$ , but at late times both the coefficient and the exponent depend on  $\epsilon$ . The sharp-interface model presented here predicts that the volume of the current always decays as a power-law in horizontal aquifers. In this case the current is never exhausted and continues to spread. Capillary forces, which have been neglected in our model, will arrest the movement of the current once it becomes too thin.

### 3.4.2 Hyperbolic limit: sloping aquifers

For confined sloping aquifers the current evolution is not self-similar, and no general solutions to (3.2) are known. For large  $Pe$ , equation 3.7a reduces to a simpler equation that allows an analysis of the current evolution. For  $Pe \rightarrow \infty$  we obtain the following quasi-linear hyperbolic equation

$$\eta_\tau + \sigma \lambda \eta_\xi = 0, \quad (3.53)$$

where the derivative of the flux function is denoted  $\lambda \equiv f_\eta$ .

#### Riemann problems

First we consider the two Riemann problems to understand the effect of trapping, i.e. the discontinuous coefficient  $\sigma$ , on rarefactions and shocks. Then we consider a hat function initial condition, representing a finite release of fluid, and the resulting wave interaction. For non-zero values of loss, the wave interaction will lead to an extinction of the current in finite time.

**Rarefaction** Consider the piecewise constant initial data

$$\eta[\xi, \tau = 0] = \begin{cases} 1, & \xi \leq \tilde{\xi}, \\ 0, & \xi > \tilde{\xi}. \end{cases} \quad (3.54)$$

The weak solution, a spreading wave or rarefaction, is obtained by the method of characteristics. This rarefaction is a tilting interface analogous to the self-similar

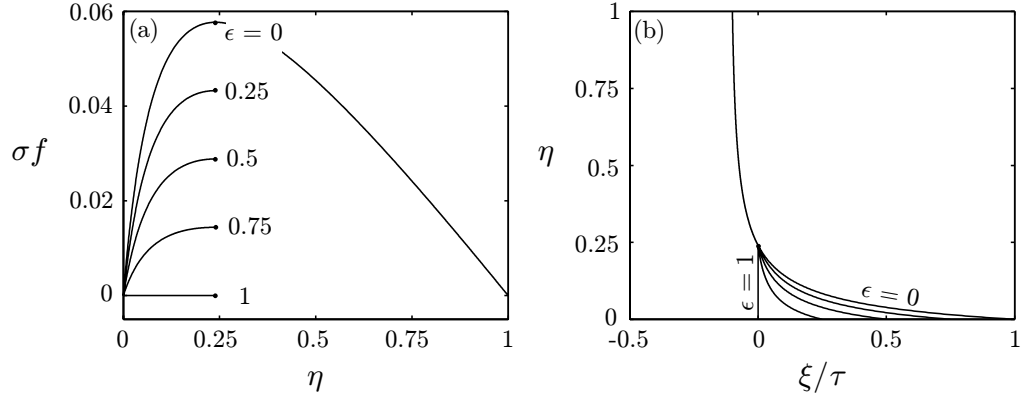


Figure 3.13: (a) The flux function  $f$  is shown for  $M = 10$  and increasing trapping  $\epsilon$ . (b) The corresponding solution profiles given by (3.56) in self-similar coordinates.

solutions presented in §3.4.1. Following the notation introduced there, we refer to the tip propagating to the left as  $\xi_i$  and to the tip propagating to the right as  $\xi_o$ . The characteristics of the solution originating at the discontinuity are given by

$$\xi = \sigma[\eta_\tau] \lambda[\eta] \tau + \tilde{\xi}, \quad (3.55)$$

therefore all solutions are self-similar in the coordinate  $\xi/\tau$ . The discontinuity in  $\sigma$  leads to a discontinuity of the slope of the interface at  $\tilde{\xi}$ , but the interface itself remains continuous, because  $\lambda = 0$  at  $\tilde{\xi}$ . The equation for the evolution of  $\eta[\xi, \tau]$ , given by inverting (3.55) is

$$\eta[\xi, \tau; \epsilon < 1, M \neq 1] = \begin{cases} 1, & \xi \leq \xi_i, \\ \frac{-\tau + \hat{M}(\xi_0 - \xi) + \sqrt{M\tau(\tau + \hat{M}(\xi - \xi_0))}}{\hat{M}(\tau + \hat{M}(\xi - \xi_0))}, & \xi_i < \xi < \tilde{\xi}, \\ \frac{1}{(1 + \sqrt{M})}, & \xi = \tilde{\xi}, \\ \frac{-\tau\hat{\epsilon} + \hat{M}(\xi_0 - \xi) + \sqrt{M\tau\hat{\epsilon}(\tau\hat{\epsilon} + \hat{M}(\xi - \xi_0))}}{\hat{M}(\tau\hat{\epsilon} + \hat{M}(\xi - \xi_0))}, & \tilde{\xi} < \xi \leq \xi_o, \\ 0, & \xi_o < \xi, \end{cases} \quad (3.56a)$$

where  $\hat{M} = M - 1$ ,  $\hat{\epsilon} = 1 - \epsilon$ . For  $M = 1$  the solution becomes piecewise linear and is given by

$$\eta[\xi, \tau; \epsilon < 1, M = 1] = \begin{cases} 1, & \xi \leq \xi_i, \\ \frac{1}{2} \left( \frac{\xi_0 - \xi}{2\tau} + 1 \right), & \xi_i < \xi < \tilde{\xi}, \\ \frac{1}{2}, & \xi = \tilde{\xi}, \\ \frac{1}{2} \left( \frac{\xi_0 - \xi}{2\tau(1-\epsilon)} + 1 \right), & \tilde{\xi} < \xi \leq \xi_o, \\ 0, & \xi_o < \xi, \end{cases} \quad (3.56b)$$

where the positions of the outward and inward propagating tips of the rarefaction are given by

$$\xi_o = (1 - \epsilon)\tau + \tilde{\xi}, \quad \text{and} \quad \xi_i = -\frac{\tau}{M} + \tilde{\xi}. \quad (3.57)$$

For tilting interfaces in the parabolic limit we have shown that  $\xi_i$  is a stronger function of  $M$  than  $\epsilon$ . In the hyperbolic limit the entire receding interface has lost its dependence on  $\epsilon$ . Where the interface is advancing,  $f$  is scaled by  $\sigma = 1 - \epsilon$  (figure 3.13a), and the residual reduces the propagation speed of the advancing interface (figure 3.13b). This behaviour is analogous to the self-similar solutions in the parabolic limit. The solution for  $\epsilon = 1$  is still given by (3.56), but the advancing interface is replaced by a discontinuity at  $\tilde{\xi}$  with a jump from 0 to  $\eta_{\max}$ . A comparison of figures 3.11b and figure 3.13b shows that  $M$  and  $\epsilon$  have a similar effect on the shape of the interface in both the parabolic and hyperbolic limits.

For  $M = 0$ , equation 3.53 reduces to the linear advection equation

$$\eta_\tau + \sigma\eta_\xi = 0, \quad (3.58)$$

with a moving discontinuity in the velocity,  $\sigma$ . In this limit an ambiguity arises in  $\sigma(\eta_\tau)$ , because  $\eta_\tau$  is singular at the discontinuity. The solution to (3.58) can be obtained taking the limit of (3.56) as  $M \rightarrow 0$  and requiring that the solution changes continuously with changes in the parameter  $M$ . In this limit the rarefaction

degenerates to a contact discontinuity

$$\eta[\xi, \tau; M = 0] = \begin{cases} 1, & \xi \leq \Lambda_c \tau + \tilde{\xi}, \\ 0, & \Lambda_c \tau + \tilde{\xi} < \xi, \end{cases} \quad (3.59)$$

where  $\Lambda_c = 1 - \epsilon$  is the speed of the discontinuity.

**Shock** Consider the piecewise constant initial data

$$\eta[\xi, \tau = 0] = \begin{cases} \eta_L, & \xi \leq \tilde{\xi}, \\ \eta_R, & \xi > \tilde{\xi}, \end{cases} \quad (3.60)$$

where  $\eta_L < \eta_R$ . The weak solution of (3.53) with (3.60) is a shock of strength,  $\eta_s = \eta_R - \eta_L$ , given by

$$\eta[\xi, \tau; M] = \begin{cases} \eta_R, & \xi \leq \Lambda \tau + \tilde{\xi}, \\ \eta_L, & \Lambda \tau + \tilde{\xi} < \xi, \end{cases} \quad (3.61)$$

where  $\Lambda$  is the shock speed. Similar to (3.58) an ambiguity arises, because  $\eta_\tau$  is singular at the shock. Therefore we define the shock speed considering (3.53) regularized by a diffusion term

$$\eta_\tau + \sigma[\eta_\tau] f_\eta \eta_\xi = \nu \eta_{\xi\xi}, \quad (3.62)$$

where  $\nu > 0$ . For initial data (3.60) the entropy-satisfying solution to (3.53) is defined by the solution of (3.62) in the limit of small  $\nu$ , the so-called vanishing viscosity solution. We assume the solution of (3.62) with (3.60) takes the form of a traveling wave with constant speed  $\Lambda_\nu$ , so that  $\eta[\xi, \tau] = \hat{\eta}[\zeta]$ , where the traveling wave coordinate is,  $\zeta = \xi - \Lambda_\nu \tau$ . For a steady traveling wave the time derivative that determines the value of  $\sigma$  is given by

$$\eta_\tau = \zeta_\tau \hat{\eta}_\zeta = -\Lambda_\nu \hat{\eta}_\zeta. \quad (3.63)$$

For initial data (3.60) we expect the solution to be monotonically increasing,  $\hat{\eta}_\zeta > 0$ , so that the sign of  $\eta_\tau$  is determined by the direction of wave propagation, given by the sign of  $\Lambda_\nu$ . The constant wave speed implies that  $\eta_\tau$  does not change sign, and hence

$\sigma$  is continuous, but its magnitude depends on the sign of the wave speed,  $\sigma = \hat{\sigma} [\Lambda_\nu]$ .

In the moving coordinate system (3.62) reduces to the ordinary differential equation with the boundary conditions  $\hat{\eta} \rightarrow \eta_R$  for  $\zeta \rightarrow +\infty$ , and  $\hat{\eta} \rightarrow \eta_L$  for  $\zeta \rightarrow -\infty$ . After integrating once and eliminating the constant of integration with either boundary condition, the following expression is obtained

$$\hat{\eta}_\zeta = \frac{\sigma M (\hat{\eta} - \eta_L) (\eta_R - \hat{\eta})}{\nu (\hat{M}\hat{\eta} + 1) (\hat{M}\eta_L + 1) (\hat{M}\eta_R + 1)}. \quad (3.64)$$

This confirms our assumption that  $\hat{\eta}_\zeta > 0$  for  $\eta_L < \hat{\eta} < \eta_R$ . Equation (3.64) does not depend on the wave speed, because consistency with both boundary conditions requires that the wave speed be given by

$$\Lambda_\nu = \sigma \frac{1 - \hat{M}\eta_R\eta_L - \eta_L - \eta_R}{(\hat{M}\eta_L + 1) (\hat{M}\eta_R + 1)}, \quad (3.65)$$

which has already been substituted into (3.64). For  $M = 1$  the solution to (3.64) is

$$\hat{\eta} = \frac{1}{2} \left( \eta_L + \eta_R + (\eta_R - \eta_L) \tanh \left( \frac{(\zeta - C\nu)\sigma(\eta_R - \eta_L)}{2\nu} \right) \right), \quad (3.66)$$

where  $C$  is a constant of integration that can be determined by the initial position of the discontinuity,  $\tilde{\xi}$ , and  $\sigma$  is given by (3.9). Equations (3.63) and (3.64) allow us to write an equivalent definition of  $\sigma$  in terms of the sign of the wave speed

$$\sigma [\eta_\tau] = \hat{\sigma} [\Lambda_\nu] = \begin{cases} 1, & \Lambda_\nu > 0, \\ 1 - \epsilon, & \Lambda_\nu < 0. \end{cases} \quad (3.67)$$

This definition is not ambiguous at discontinuities in the limit  $\nu \rightarrow 0$ . With this definition of  $\sigma$  the Rankine-Hugoniot jump condition for the shock is

$$\Lambda = \hat{\sigma} \frac{f[\eta_L] - f[\eta_R]}{\eta_L - \eta_R} = \Lambda_\nu, \quad (3.68)$$

so that the shock speed of the limiting solution is identical to the wave speed of the



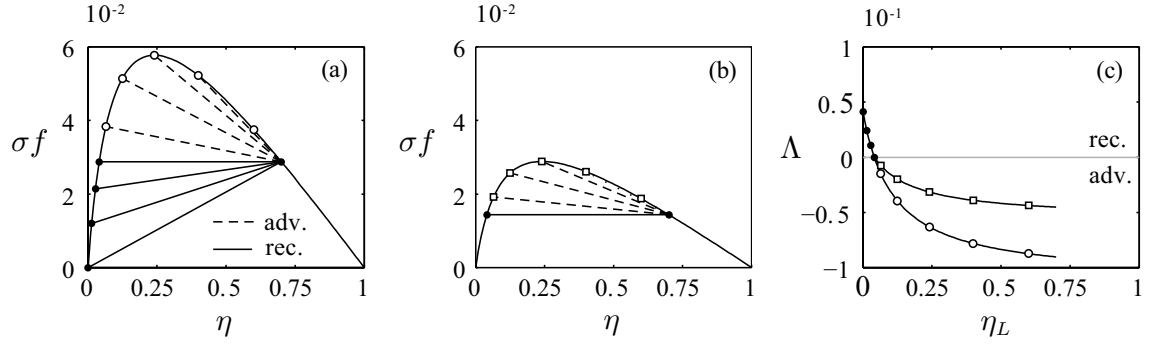


Figure 3.14: Shock construction for  $M = 10$ . (a) In the absence of trapping,  $\epsilon = 0$ , the construction for advancing and receding shocks is the same. (b) In the presence of trapping,  $\epsilon = 1/2$ , the shock construction for advancing shocks is modified. (c) Shock speed as function of  $\eta_L$ , for  $\eta_L > \eta_c$  the shock speed depends on the amount of trapping.

viscous solution.

The geometric interpretation of the jump condition (3.68), is a cord joining  $f[\eta_L]$  and  $f[\eta_R]$ , as shown in figure 3.14a and b. For a given  $\eta_R$  and  $M$  the direction of wave propagation as function of  $\eta_L$  is given by

$$\Lambda_\nu \begin{cases} < 0, & \eta_c < \eta_L < \eta_R, \\ = 0, & \eta_L = \eta_c, \\ > 0, & 0 < \eta_L < \eta_c, \end{cases} \quad (3.69)$$

where

$$\eta_c = \frac{1 - \eta_R}{(M - 1)\eta_R + 1}, \quad (3.70)$$

which corresponds to a horizontal tangent and a stationary shock.

The speed of shocks moving to the right is not affected by trapping, while the speed of waves traveling to the left is reduced due to trapping (figure 3.14c). This behavior of the shock is analogous to the behavior of the rarefaction. In both cases the speed of the interface is reduced, by a factor  $1 - \epsilon$  due to trapping, when it is advancing, but it is not affected if the interface is receding. However, the parameter that identifies whether the interface recedes or not is different for the rarefaction and

the shock. For an interface with a finite slope, i.e. a rarefaction, the change of the height of the interface with time,  $\eta_\tau$ , determines which parts of the interface recede. For a vertical interface, i.e. a shock, the sign of shock speed,  $\Lambda$ , determines whether the interface recedes across the shock or not.

### Wave interaction

The evolution of a finite release of fluid is governed by the interaction of the shock at the back of the current with the rarefaction at the front of the current. In the presence of trapping this interaction leads to a rapid reduction of current volume, and give rise to a finite migration distance and time. Consider the piecewise constant initial data

$$\eta_H = \begin{cases} 1, & |\xi| \leq 1/2, \\ 0, & |\xi| > 1/2. \end{cases} \quad (3.71)$$

Initially the solution of the front is a rarefaction given by 3.56 with  $\tilde{\xi} = \frac{1}{2}$ , for all  $M > 0$ , and the evolution of the back is a stationary shock ( $A$  to  $B$  in figure 3.15) with constant shock strength (figure 3.16*b*), because  $\Lambda = 0$  for  $\eta_L = 0$  and  $\eta_R = 1$  for all  $M > 0$ . When the back end of the rarefaction reaches the shock, the shock strength decreases, and it begins to move. The solution,  $\eta$ , will then be given by (3.56), but  $\eta[\xi < \xi_s] = 0$ , where the  $\xi_s$  is the shock position.

**Shock evolution** The waves begin to interact at the transition time,  $\tau_t = M$  ( $B$  in figure 3.15), and the shock speed begins to increase as the shock strength decreases. Considering the shock strength,  $\eta_s$ , as a parameter along the shock path ( $B$  to  $D$ ), so that  $\tau = \tau[\eta_s]$ , and  $\xi = \xi[\eta_s]$ , we differentiate (3.55) and (3.68) to obtain two differential equations

$$\xi_{\eta_s} = \lambda_{\eta_s}[\eta_s] \tau + \lambda[\eta_s] \tau_{\eta_s} \quad \text{and} \quad \eta_s \xi_{\eta_s} = f[\eta_s] \tau_{\eta_s}. \quad (3.72)$$

Eliminating  $\xi_{\eta_s}$  we obtain the differential equation

$$\frac{d\eta_s}{d\tau} = \frac{f[\eta_s] - \eta_s \lambda[\eta_s]}{\eta_s \lambda_{\eta_s}[\eta_s] \tau}, \quad (3.73)$$

for the evolution of the shock strength. Together with the initial condition  $\eta_s[\tau_t] = 1$ , it determines the evolution of the shock strength (figure 3.16b). Once  $\eta_s$  is known, the shock position is given by  $\xi_s = \lambda[\eta_s]\tau + \frac{1}{2}$ . We solve for  $\eta_s$  instead of  $\xi_s$ , because (3.73) is always separable.

If trapping occurs,  $\epsilon \neq 0$ , then the evolution of  $\eta_s$  is divided into an early period,  $\tau_t \leq \tau \leq \tau_p$ , during which the shock interacts with the receding portion of the rarefaction ( $B$  to  $C$  in figure 3.15), and a later period  $\tau_p < \tau \leq \tau_f$ , where the shock interacts with the advancing portion of the rarefaction ( $C$  to  $D$ ). Hence, the problem has three time scales: the transition time,  $\tau_t$ , when interaction between waves begins ( $B$ ), the passing time,  $\tau_p$ , when the shock passes the stationary point of the rarefaction and starts to interact with the advancing section of the rarefaction ( $C$ ), and the final migration time,  $\tau_f$ , when the volume of the current goes to zero ( $D$ ).

In the early period the shock strength and position are independent of  $\epsilon$  and are given by

$$\eta_s = \frac{1}{1 - M + \sqrt{M}\tau} \quad \text{and} \quad \xi_s = -\frac{1}{2} + \left(\sqrt{M} - \sqrt{\tau}\right)^2. \quad (3.74)$$

We have shown in (§3.4.2) that the receding section of the interface is not affected by trapping. Therefore, the shock strength and position are independent of the amount of trapping. The early period extends until the shock migrates past the initial extent of the current,  $\xi_s < \frac{1}{2}$ . The passing time and the shock strength at the passing time are given by

$$\tau_p = \left(1 + \sqrt{M}\right)^2 \quad \text{and} \quad \eta_s[\tau_p] = \frac{1}{1 + \sqrt{M}}. \quad (3.75)$$

In the absence of trapping (3.74) remain valid for all  $\tau > \tau_t$  (dashed line in figure 3.16). After  $\tau_p$  an explicit expression for  $\eta_s$  and  $\xi_s$  is only obtained for  $M = 1$ . We give the full details for the case  $M = 1$  to illustrate the structure of the solution, and for  $M > 1$  we integrate (3.73) numerically, using (3.75) as an initial condition. For  $\tau_p \leq \tau \leq \tau_f$

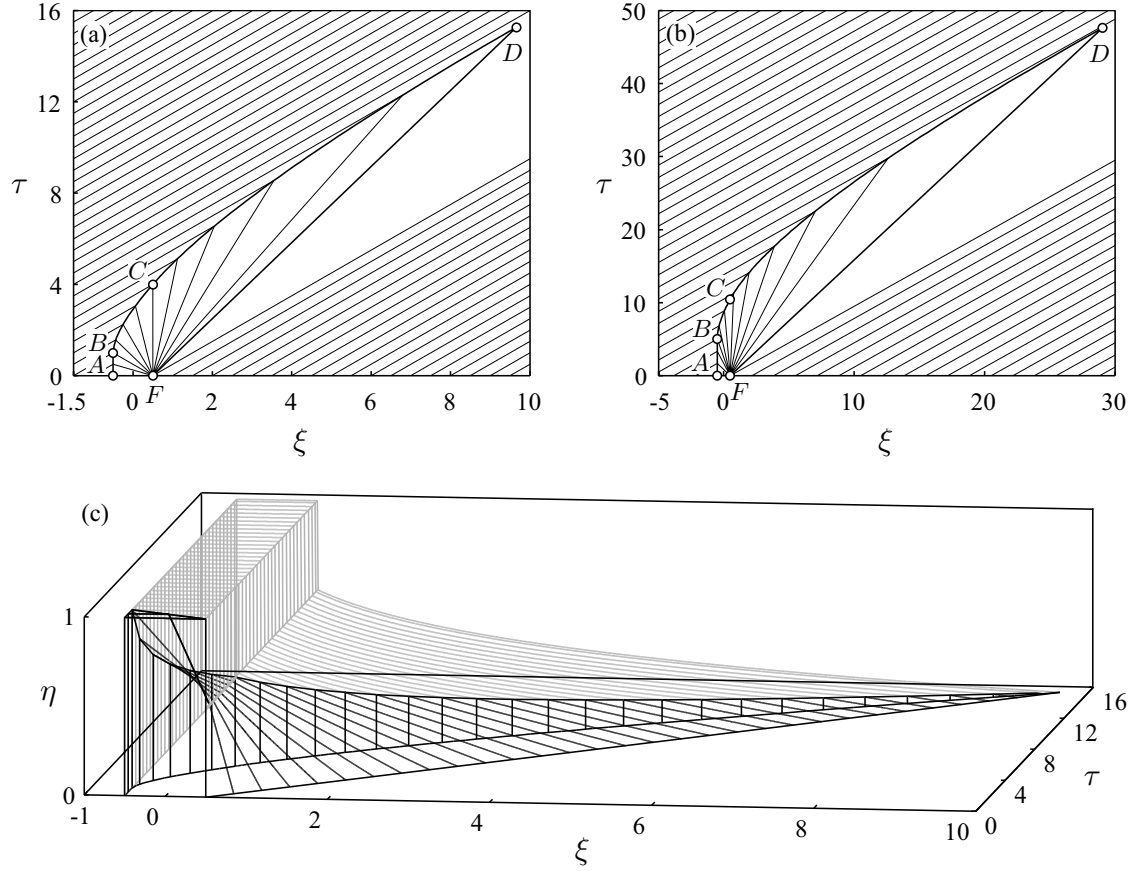


Figure 3.15: Characteristic portraits of the evolution of initial data (3.71), in the  $\xi\tau$ -plane. The current is bounded by the shock,  $A$  to  $D$ , in the back and the leading characteristic of the rarefaction,  $F$  to  $D$ , in the front. (a) Analytic solution for  $M = 1$  and  $\epsilon = 0.4$ . (b) Semi-analytic solution for  $M = 5$  and  $\epsilon = 0.4$ . (c) Evolution of the current interface (black) and the residual surface (grey).

the shock strength for  $M = 1$  is given by

$$\eta_s = \begin{cases} \frac{\epsilon - 2^{1+\frac{1}{\epsilon-1}} t^{-1-\frac{1}{2(\epsilon-1)}}}{2^{\epsilon-1}}, & \epsilon \neq \frac{1}{2}, \\ \log\left(\frac{2}{\sqrt{t}}\right) + \frac{1}{2}, & \epsilon = \frac{1}{2}. \end{cases} \quad (3.76)$$

For  $\epsilon = \frac{1}{2}$  the right hand side of (3.73) loses the explicit dependence on  $\eta_s$ , leading to a simplified expression. The expression for the shock path is given by

$$\xi_s = \begin{cases} \frac{(\epsilon-1)}{2^{\epsilon-1}} \left( t - 2^{2+\frac{1}{\epsilon-1}} t^{\frac{1}{2-2\epsilon}} \right) + \frac{1}{2}, & \epsilon \neq \frac{1}{2}, \\ \frac{1}{2} (\log(\frac{t}{4})t + 1), & \epsilon = \frac{1}{2}. \end{cases} \quad (3.77)$$

In the second phase the shock speed and position depend strongly on the amount of trapping. Figure 3.16a illustrates the effect of increasing trapping on the current evolution in the  $\xi\tau$ -plane for  $M = 1$ , and similar behavior is observed numerically for other  $M$  (figure 3.15b). From (3.77), (3.76), and (3.56) the aspect ratio of the current is given by

$$\mathcal{A} = \frac{\xi_o - \xi_s}{\eta_s} = \begin{cases} 1 + (1 - \epsilon)\tau, & \tau < 1, \\ 2\tau - \epsilon\tau^{3/2}, & 1 < \tau \leq 4, \\ 2(1 - \epsilon)\tau, & 4 < \tau < \tau_f, \end{cases} \quad (3.78)$$

for  $M = 1$ . Even in the presence of trapping  $\mathcal{A}$  is always increasing for  $M \geq 1$ . The final residual surface,  $\eta_r$ , is the interface that divides the part of the aquifer that has been invaded by the current, and now contains trapped fluid, from the region of the aquifer that has not been invaded. The final residual surface for  $\xi < \frac{1}{2}$  is the initial condition. For  $\xi > \frac{1}{2}$  the final residual surface is defined as  $\eta_r = \eta_s[\xi_s]$  and can be calculated by eliminating  $\tau$  between (3.76) and (3.77) to obtain  $\xi = \xi[\eta_r]$ . However, it is not possible to invert this relationship to obtain an explicit expression for  $\eta_r$

$$\xi = \begin{cases} \frac{1}{2} + \frac{(\epsilon-1)}{2^{\epsilon-1}} \left( \varphi(\eta_r) - 2^{2+\frac{1}{\epsilon-1}} \varphi(\eta_r)^{\frac{1}{2-2\epsilon}} \right), & \epsilon \neq \frac{1}{2}, \\ e^{1-2\eta_r} (2 - 4\eta_r) + \frac{1}{2}, & \epsilon = \frac{1}{2}. \end{cases} \quad (3.79)$$

were  $\varphi[\eta_r] = \left( 2^{-\frac{\epsilon}{\epsilon-1}} (-2\epsilon\eta_r + \eta_r + \epsilon) \right)^{\frac{1}{2\epsilon-1}-1}$ . The shape of the final residual surface

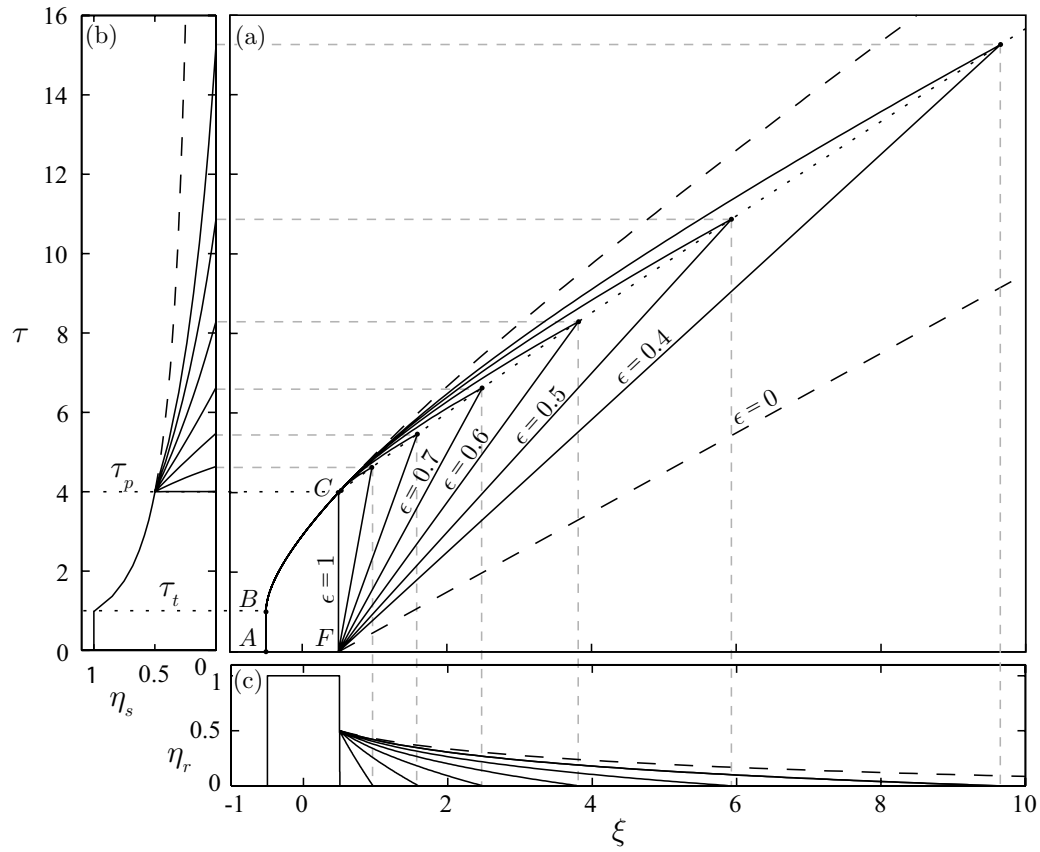


Figure 3.16: (a) Portrait of the shock path and the leading characteristic of the rarefaction, for increasing residual. The locus of the termination points,  $\tau_f = \tau_f[\xi_\uparrow]$ , is shown as a dotted line. (b) The corresponding temporal evolution of the shock strength,  $\eta_s$ . (c) The corresponding final residual surfaces,  $\eta_r = \eta_r[\tau_f]$ .

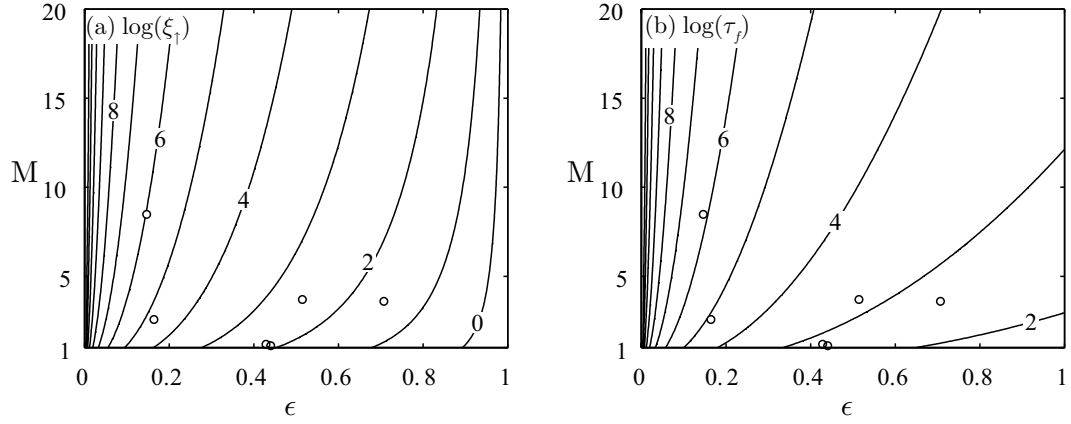


Figure 3.17: Contour plots of the up-dip migration distance,  $\log(\xi_{\uparrow})$ , on the left and of the total migration time,  $\log(\tau_f)$ , on the right. The data for several potential storage aquifers in Alberta, Canada, is shown as circles to indicate typical parameter values (Bachu & Bennion, 2007).

is shown in figure 3.16c for increasing residual saturations.

**Final migration time and distance** The finite migration distance is an important characteristic of the hyperbolic limit, in contrast to the self-similar solutions for the horizontal case. The maximum migration distance and the corresponding total migration time are amongst the most important time and length scales for CO<sub>2</sub> storage, and the analytic and semi-analytic results (figure 3.17) presented here show how these scales depend on the governing parameters.

The total migration distance,  $\xi_{\uparrow}$ , is given by

$$\xi_{\uparrow} = \begin{cases} \frac{1}{2} - 2^{1+\frac{1}{2\epsilon-1}}(\epsilon-1)\epsilon^{\frac{1}{2\epsilon-1}-1}, & \epsilon \neq \frac{1}{2}, \\ \frac{1}{2} + 2e, & \epsilon = \frac{1}{2}. \end{cases} \quad (3.80)$$

Increasing mobility increases  $\xi_{\uparrow}$ , because a gravity tongue forms at the top of the aquifer and only a small fraction of the aquifer is swept and contributes to residual trapping.

The final migration time for  $M = 1$  is given by

$$\tau_f = \begin{cases} \left(2^{-1-\frac{1}{\epsilon-1}}\epsilon\right)^{-\frac{2(\epsilon-1)}{2(\epsilon-1)+1}}, & \epsilon \neq \frac{1}{2}, \\ 4e, & \epsilon = \frac{1}{2}. \end{cases} \quad (3.81)$$

The dimensionless final migration time increases strongly with increasing  $M$ . The dimensionless time is only based on the properties of the released fluid. As  $M$  increases the released fluid becomes increasingly less mobile, which retards the movement of the released fluid.

**Volume evolution** The final migration time,  $\tau_f$ , bounds the time available for leakage from the storage reservoir. For smaller times the volume of mobile CO<sub>2</sub> is a basic quantity necessary to estimate maximum potential leakage over time. Analytic expressions for the evolution of the current volume are given by integrating (3.56) over the extent of the plume. The normalized current volume  $\mathcal{V} = V(\tau)/V(\tau_0)$  is given by

$$\mathcal{V} = \int_{\xi_s}^{\xi_o} \eta \, d\xi = 1 - \tau\epsilon \left(1 + \sqrt{M}\right)^{-2} \quad (3.82a)$$

for  $\tau < \tau_p$ . In this early period both the shock and the receding part of the rarefaction are independent of  $\epsilon$ , and therefore the area containing residual saturation is also independent of  $\epsilon$ . Hence, the current volume decreases proportional to  $\epsilon$ . The decay of the current volume slows down with increasing  $M$ , because the receding interface slows down. This behavior that is also observed in semi-analytic solutions for  $\tau > \tau_p$ . At later times the lower limit of the integral is only known for  $M = 1$ , and in this case the current volume is given by

$$\mathcal{V} = \begin{cases} \frac{1-\epsilon}{t(1-2\epsilon)^2} \left(2^{-\frac{\epsilon}{1-\epsilon}} t^{\frac{1}{2(1-\epsilon)}} - \epsilon t\right)^2, & \epsilon \neq \frac{1}{2}, \\ \frac{t}{8} \left(\log\left(\frac{t}{4}\right) - 1\right)^2, & \epsilon = \frac{1}{2}, \end{cases} \quad (3.82b)$$

for  $\tau < \tau_f = 4e$ . Figure 3.18(a) shows how strongly the current volume is affected by the magnitude of  $\epsilon$ . This evolution is distinctly different from the power-law decay obtained from the self-similar solutions for horizontal aquifers. It suggests that sloping



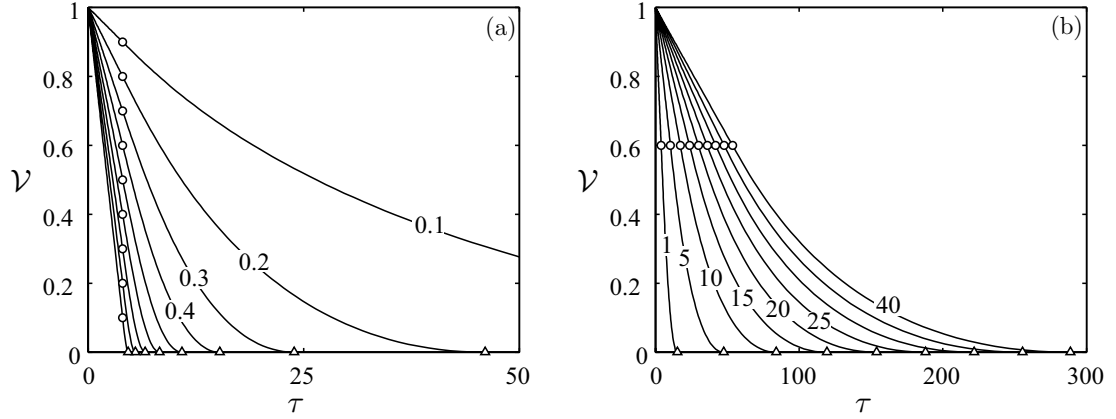


Figure 3.18: The effect of the governing parameters on the evolution of the current volume. The passing and final migration times, are shown as circles and triangles. (a) Increasing the residual,  $\epsilon$ , from 0.1 to 0.9 at constant  $M = 1$ . (b) Increasing the mobility ratio,  $M$ , from 1 to 40 at constant  $\epsilon = 0.4$ . Circles denote

aquifers reduce the current volume particularly effectively. An evolution similar to (3.82) is observed for a wide range of  $M$  (figure 3.18b).

The residual volume is given by  $\mathcal{V}_r = 1 - \mathcal{V}$ , and from (3.82) we see that volume of trapped CO<sub>2</sub> initially increases linearly as  $\mathcal{V}_r \propto \tau$ , and it increases more slowly for  $\tau > \tau_p$ . The efficiency of residual trapping decreases with time, because the size of the receding interface,  $\eta_s$ , decreases rapidly, once the shock is interacting with the advancing section of the rarefaction.

### 3.4.3 Numerical results

In this section we present numerical solutions to (3.7) and show that the current evolution for intermediate values of  $Pe$  can be understood in terms of an early essentially parabolic period followed by a late near hyperbolic regime. We also discuss important length and time scales of the solution as a function of increasing  $Pe$ . The numerical solutions were computed using standard finite volume techniques and explicit time integration (Leveque, 2002).

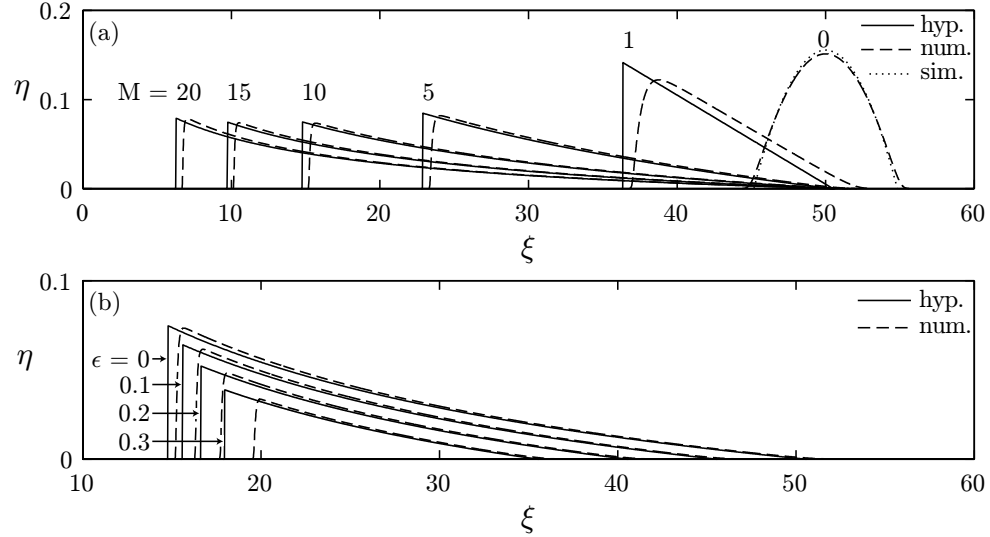


Figure 3.19: This figure shows several comparisons between the numerical solution ( $\Delta\xi = 0.01$ ) to (3.7a) and the hyperbolic solution for  $Pe = 2$  at  $\tau = 50$ . (a) Increasing  $M$  at constant  $\epsilon = 0$ . (b) Increasing  $\epsilon$  at constant  $M = 10$ .

### Near hyperbolic behavior for large $M$

In CO<sub>2</sub> storage  $Pe$  is not necessarily large, but the mobility ratio is generally larger than unity,  $M \approx 5$ . Here we show that the particular shape of  $f$  leads to near hyperbolic behavior of (3.7a) for small  $Pe$  and large  $M$ . Consider the differentiated form of (3.7a) given by

$$\sigma^{-1}\eta_\tau + \lambda\eta_\xi = Pe^{-1}(\lambda(\eta_\xi)^2 + f\eta_{\xi\xi}). \quad (3.83)$$

In the absence of source terms the thickness  $\eta$  of the current decreases monotonically with time and for  $M \gg 1$  the current takes the shape of a triangle composed of a very elongate, flat, advancing tongue in the front and a short, steep, receding tongue in the back (figure 3.10g-h). This asymmetry increases with  $Pe$ ,  $M$ , and  $\tau$ . The hyperbolic approximation introduced in § 3.4.2 replaces the short, steep, receding interface of the current by a shock.

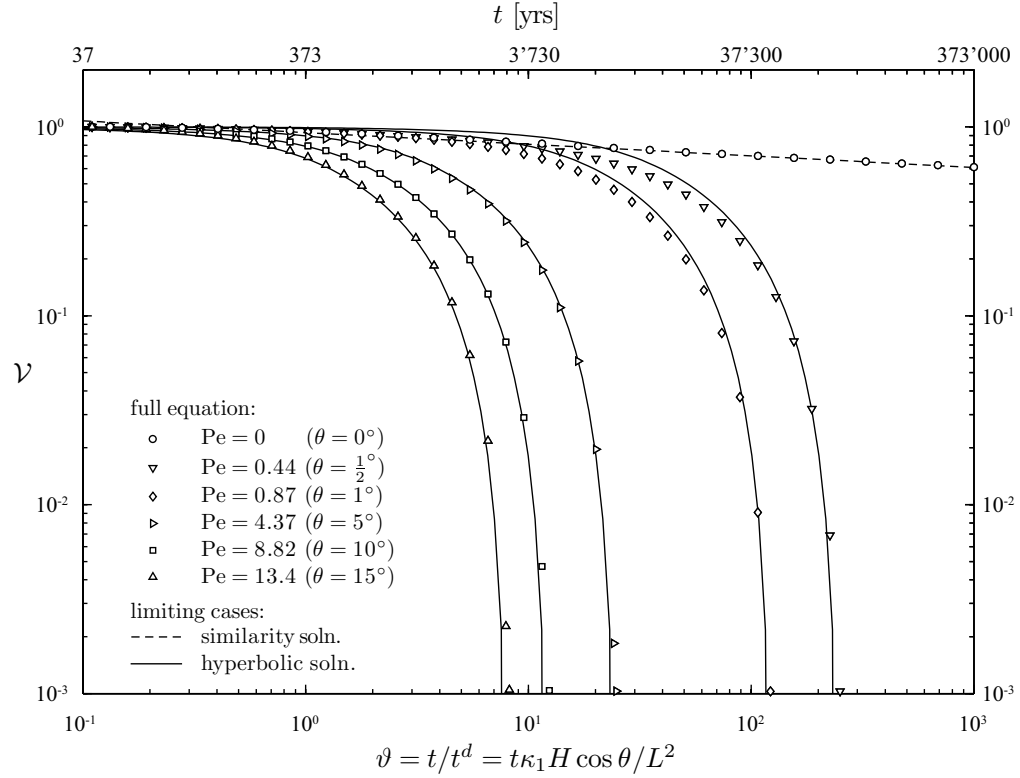


Figure 3.20: Evolution of the current volume,  $\mathcal{V}$ , as a function of diffusive dimensionless time,  $\vartheta$ , for  $M = 5$  and increasing  $Pe$ . The time axis at the top gives dimensional values corresponding to the parameter choice discussed in § 3.5.2, assuming  $\cos \theta \approx 1$ .

In the advancing tongue  $\eta_{\xi\xi} \ll \eta_\xi \ll 1$ , and hence both the diffusive,  $f\eta_{\xi\xi}$ , and the second order term,  $\lambda\eta_\xi^2$  are small. The diffusive term is reduced further over the entire current, because  $\max(f) = 1/(1 + \sqrt{M})^2$  decreases with increasing  $M$ . The second order term  $\eta_\xi^2$  is not small in the steep receding back of the current, and figure 3.19 shows that the error in the hyperbolic approximation is localized there.

Figure 3.19(a) illustrates how the error introduced by the hyperbolic approximation decreases with increasing  $M$ . For  $M > 5$  and  $\tau > 2\tau_p$  the only significant error in the hyperbolic approximation is due to small off-set in the shock position. In the limit  $M = 0$  a similarity solution to the full equation is available (Huppert & Woods, 1995), and it is shown to provide an indication of the accuracy of the numerical method used.

Once loss is introduced,  $\epsilon > 0$ , the small differences in the sweep of the full solution and the hyperbolic solution lead to differences in plume volume at any given time. This volume error accumulates over time and leads to differences between the shock location in the hyperbolic model and the back of the plume in the numerical solution (figure 3.19b).

### Transition from parabolic to hyperbolic behavior

In gently sloping media the current transitions from initial parabolic behavior to hyperbolic behavior at late times (figure 3.20). Due to the distinctly different behavior of these limiting cases for  $\epsilon > 0$  the transition is apparent in the evolution of the current volume. An initial power-law decay of the current volume is followed by a much more rapid decay characteristic of the hyperbolic limit.

For very large  $Pe$  the plume volume is given 3.82 and its semi-analytic extension to  $M \neq 1$ . This limiting solution is plotted in figure 3.20 as a function of the diffusive dimensionless time,  $\vartheta = \tau/Pe$ , so that changes in  $Pe$  correspond to a stretching of the time axis. We observe that the limiting solution describes the rapid decay of the current volume at late times, even for  $Pe < 1$ .

### Length & time scales for gravity currents with residual

The length and time scales that are important for gravity currents in sloping layers are the propagation distance against gravity,  $\xi_{\downarrow}$ , and the time of the associated reversal in the direction of the interface movement,  $\tau_t$ . For a buoyant current the down-dip propagation of the interface is due to the parabolic part of the equation. The reversal of the interface movement indicates the transition from early near-parabolic to late near-hyperbolic behavior. The continued volume loss and the resulting extinction of the current give rise to additional length and time scales, the up-dip migration distance,  $\xi_{\uparrow}$ , and the final migration time,  $\tau_f$ . Numerical results for all four scales as a function of increasing  $Pe$  are shown in figure 3.21. To determine the scales associated with the end of the current the numerical simulation was terminated at  $\mathcal{V} = 10^{-3}$ . This value was chosen to allow a reasonable detection of the gravity current tips,

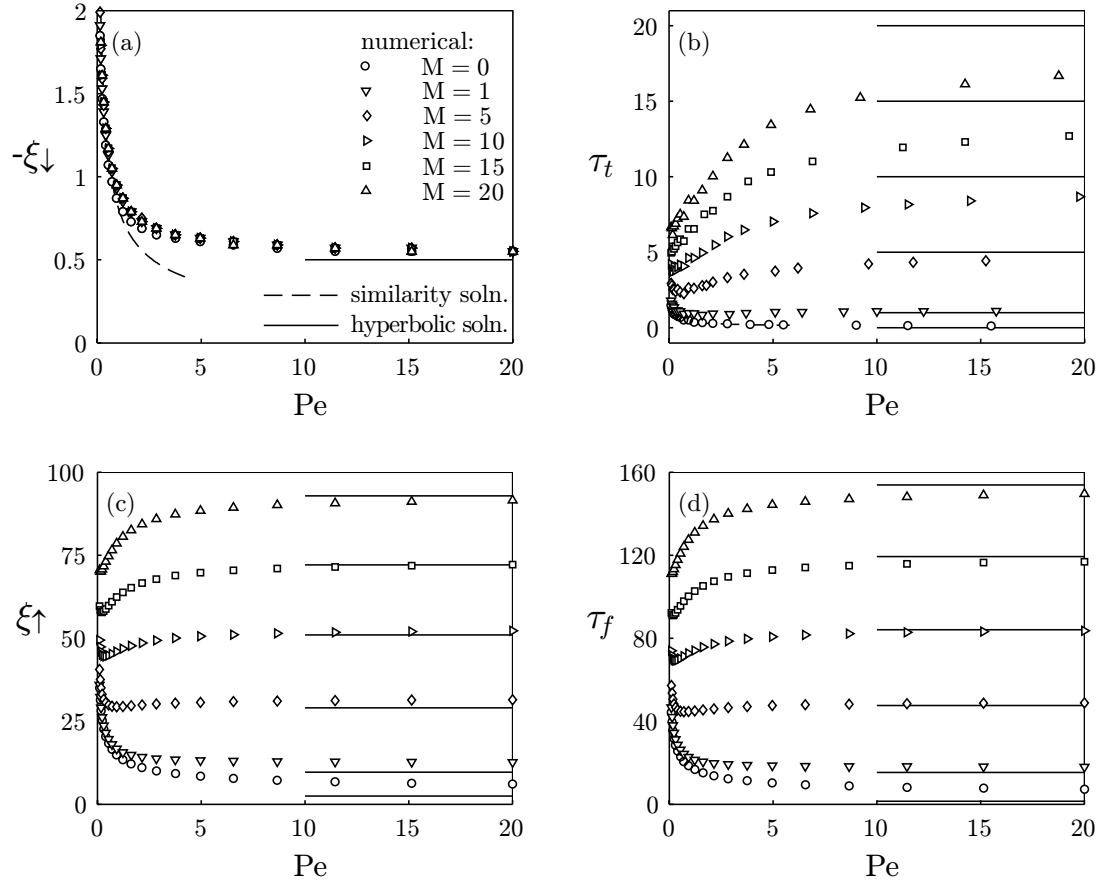


Figure 3.21: Time and length scales obtained from the numerical solution of (3.7) are shown as symbols ( $\Delta\xi = 0.01$ ). All results are for a residual of  $\epsilon = 0.4$ . The limiting hyperbolic and self-similar solutions are indicated by full and dashed lines. (a) Down-dip migration distance,  $\xi_{\downarrow}$ . (b) Transition time,  $\tau_t$ . (c) Up-dip migration time,  $\xi_{\uparrow}$ . (d) Final migration time,  $\tau_f$ .

which become strongly affected by numerical diffusion for smaller cut-off volumes. The rapid decay of the plume volume at late times (figure 3.20) suggests that the results are not very sensitive to the cut-off, and the reasonable agreement between numerical and limiting analytic results in figure 3.17 confirms this.

The down-dip migration distance,  $\xi_{\downarrow}$ , is not very sensitive to  $M$  or  $\epsilon$ . For small  $Pe$  it follows the relation  $\tau_t = 1/\sqrt{6Pe}$  obtained for the similarity solution for  $M = \epsilon = 0$ . As the  $\tau_t$  increases with decreasing  $Pe$  the current thickness decreases as well, and the similarity solution for the unconfined aquifer becomes a better approximation. As  $Pe$  increases  $\xi_{\downarrow}$  approaches the position of the initial condition, which is also the down-dip migration distance in the hyperbolic limit. The transition time,  $\tau_t$ , appears to approach the limiting hyperbolic solution much slower than the other parameters.

The up-dip migration distance,  $\xi_{\uparrow}$ , and the final migration time,  $\tau_f$ , show a more complicated behavior as  $Pe$  increases. As  $Pe$  goes to zero both become very large, and this is consistent with the late similarity solution for the limiting case  $Pe = 0$ , introduced in section §3.4.2. As  $Pe$  increases the hyperbolic limit is approached quickly, except for  $M = 0$ . However, for  $Pe \approx 0.2 - 0.5$  a minimum in both quantities is observed for  $M > 1$ . Hesse *et al.* (2006) showed that both  $\xi_{\uparrow}$  and  $\tau_f$  decrease with increasing  $Pe$  for  $M = 0$ . Figures 3.17(c-d) show a similar behavior of  $\xi_{\uparrow}$  and  $\tau_f$  for  $M < 1$ , but we observe an increase of  $\xi_{\uparrow}$  and  $\tau_f$  for  $M > 1$  for  $Pe > 1$ .

## 3.5 Discussion

### 3.5.1 Assumptions

The most limiting assumptions in the derivation of the governing equations are the homogeneity of the porous medium, the uniform saturation in the CO<sub>2</sub> plume, and the incompressibility of the CO<sub>2</sub>. While simple forms of heterogeneity in the across slope direction can be included (Huppert & Woods, 1995) general forms of heterogeneity require a full numerical solution. Ide *et al.* (2007) investigated gravitational spreading of a CO<sub>2</sub> plume in a horizontal, two-dimensional, heterogeneous aquifers with a reservoir simulator. They showed that the effect of capillary forces on residual trapping

is larger than the effect of moderate permeability heterogeneity. In the absence of capillary forces, their numerical simulations resemble figure 3.10(*a-d*). Simulations including capillary forces lead to a thicker gravity current with a non-uniform vertical saturation profile and an increase in capillary trapping (Mo & Akervoll, 2005).

It may therefore be interesting, to extend the model presented here to non-uniform saturation distributions. The infinitely spreading solution obtained for horizontal aquifers is a direct result of neglecting capillary forces. The current will stop propagating once the hydrostatic potential at the tip of the plume decreases below the entry pressure necessary for the CO<sub>2</sub> to invade the largest pores. Even in very gently dipping aquifers, the CO<sub>2</sub> may rise vertically by several hundred meters, if the up-dip migration distance is large. In these cases, the expansion of the CO<sub>2</sub> will lead to an increase in plume volume that may be significant, in particular if the CO<sub>2</sub> becomes gaseous.

In the hyperbolic model for sloping aquifers we neglect the second order term,  $\lambda(\eta_\xi)^2$ . This simplification leads to an unphysical vertical interface at the trailing end of the current. Despite this simplification, we find that the resulting quasi-linear hyperbolic model describes many characteristics of the current evolution very well. The minimum in the migration distance and time observed in figure 3.21 is not explained by the limiting cases we study. The most likely explanation is the down-dip migration of the current against gravity. This down-dip migration is represented by the second order term,  $\lambda(\eta_\xi)^2$  we have neglected. Inclusion of this term leads to a fully nonlinear hyperbolic model

$$\sigma^{-1}\eta_\tau + \lambda\eta_\xi = \text{Pe}^{-1}\lambda(\eta_\xi)^2, \quad (3.84)$$

which is likely to exhibit this behavior. This model could still be solved by the method of characteristics allowing fast and accurate solutions to be obtained by numerical integration.

In terms of geological CO<sub>2</sub> storage we have neglected the dissolution of CO<sub>2</sub> into the brine. Two types of dissolution must be distinguished, direct dissolution of CO<sub>2</sub> into the residual brine and the enhanced dissolution of CO<sub>2</sub> at the interface between

CO<sub>2</sub> and brine due to convective currents in the underlying brine, see § 2. The direct dissolution into the residual brine can be modeled in this framework, but the effect is likely to be small compared with residual trapping. The enhanced dissolution due to convective transport may become important at later times, because the gravity tongue provides a large interfacial area. This process could be modeled conceptually through an effective loss term. Detailed information regarding the convective dissolution rates, similar to those presented in § 2.3, will allow us to estimate the magnitude of this loss term. An extension of the model presented here would then allow for a comparison of the relative contributions of dissolution and residual trapping.

The leading edge of the CO<sub>2</sub> plume is both by gravitationally and viscously unstable and this leads to the formation of a gravity tongue in our solutions. Riaz & Tchelepi (2006) have shown that this gravity tongue is also the dominant feature in high resolution numerical simulations of two-dimensional vertical displacements. The displacement may also be viscously unstable in the transverse direction, similar to the Saffman-Taylor instability in a Hele-Shaw cell (Saffman & Taylor, 1958), or the instability of viscous currents on inclined planes discussed by Lister (1992). The linear instability of an immiscible displacement in a porous medium has been studied by Yortsos & Hickernell (1989) and Riaz & Meiburg (2004a). However, these studies consider advection dominated one dimensional base flows and not the two-dimensional base flow in gravity-capillary equilibrium that is of interest here. The study of the stability of the two-dimensional flows presented here is an interesting direction for future research, but beyond the scope of this contribution.

### 3.5.2 Implications for CO<sub>2</sub> storage in saline aquifers

We model the migration and the associated residual trapping of CO<sub>2</sub> plumes in saline aquifers using vertical-equilibrium sharp-interface models. The analysis of these simplified models shows us how the most important dynamical parameters affect the evolution of the footprint of the CO<sub>2</sub> plume over time and the efficiency of residual trapping. First, we compare the evolution of CO<sub>2</sub> plumes in horizontal and sloping aquifers. Then we consider a particular field case and show how our results have first



order implications on the selection of storage sites.

### Residual trapping in horizontal and sloping aquifers

Let us consider a deep saline aquifer with the following constant properties:  $H \approx 20$  m,  $k \approx 30$  mD, and  $\phi \approx 0.1$ . In addition, we assume the following constant fluid properties:  $\Delta\rho \approx 300$  kg/m<sup>3</sup>,  $S_{cr} = S_{br} = 0.2$ ,  $\mu_c \approx 0.06 \cdot 10^{-3}$ ,  $\mu_b/\mu_c \approx 10$ ,  $k_{rc} \approx 0.2$ , and at the advancing interface  $k_{rb} = 1$ . In this case, the mobility ratio is  $M \approx 5$ , so that we expect the formation of a gravity tongue of CO<sub>2</sub> along the top of the aquifer. Finally, we assume that the aquifer has been invaded by CO<sub>2</sub> over a distance of  $L_d \approx 500$  m, so that the aspect ratio at the end of injection is given by  $A = 2 \cdot L_d/H \approx 50$ .

**Horizontal aquifers** The evolution of the CO<sub>2</sub> plume in a horizontal aquifer with these properties is shown in figure 3.10(a-d), and the evolution of the volume of the mobile CO<sub>2</sub> plume is given in figure 3.20. For gravity currents with  $M \approx 5$  we expect an extended early period where the tip position is given by  $x \propto t^{1/2}$  (figure 3.9). The regime diagram in figure 3.9 does not account for the effect of residual trapping, but figure 3.12(b) shows that the transition from the early to the late scaling law is similar for  $\epsilon = 0.25$  and  $\epsilon = 0$ . We can therefore use the theory developed in §3.3 to estimate the duration of the early period, given by  $t_b$ , and the time,  $t_t$ , after which we can expect the late scaling law to hold.

For  $M = 5$ , the dimensionless time scales are given by  $\vartheta_b \approx 4$  and  $\vartheta_t \approx 265$ , and the characteristic time is  $t^d = L_d^2(\kappa_1 H)^{-1} \approx 250$  yrs. The interface will detach from the aquifer after approximately  $t_b \approx 1000$  yrs. At this time the footprint of the CO<sub>2</sub> plume is 4.6 km. In the period right after the detachment of the CO<sub>2</sub> plume residual trapping is the most effective, and the fraction of CO<sub>2</sub> trapped as residual saturation increases to 20% (figure 3.10b). The period that corresponds to rapid residual trapping in a horizontal aquifer is approximately given by  $t_b$  to  $3t_b$ .

The tip of the CO<sub>2</sub> plume will continue to propagate proportional to  $t^{1/2}$  until  $t_t \approx 66000$  yrs, when the footprint of the plume is 20 km. Therefore, although the CO<sub>2</sub> plume shown in figure 3.10(c) is already very thin compared to the thickness of

the aquifer, the plume tips are still propagating according to the early scaling law,  $x \propto t^{1/2}$ . This illustrates that the effects of confinement, expressed in the mobility ratio, must be taken into account to understand the evolution of the CO<sub>2</sub> plume. In particular, confinement has an effect on the propagation of the gravity current long after the CO<sub>2</sub> plume has detached from the base of the aquifer at  $t_b$ .

After  $t_t$  the spreading of the CO<sub>2</sub> plume slows down significantly, and in figure 3.10(d) the tips of the plume propagate according to the late scaling law. In this late stage, residual trapping decreases the propagation velocity in a manner similar to figure 3.12. As the plume slows down, residual trapping decreases rapidly. From figure 3.10(a) to (d) we can see that it takes 3,000 yrs to trap the first 20%, about 30,000 yrs to trap the next 10%, and approximately 300,000 yrs to trap an additional 10%. This drastic decay of the rate of residual trapping in horizontal aquifers is a consequence of the self-similar nature of the solution at late times, which requires that the volume of the mobile CO<sub>2</sub> plume decays as a power-law.

**Sloping aquifers** Figure 3.20 shows that the effectiveness of residual trapping increases dramatically even for small dip angles. The evolution of the interface shape for  $\theta = 5^\circ$  is shown in figure 3.10(e-h). We see that the migration time of the current is reduced from approximately 40,000 yrs for a slope of  $1/2^\circ$  to approximately 2,000 yrs for a slope of  $15^\circ$ . The up-dip migration distance decreases from 85.6 km at  $1/2^\circ$  to a minimum of 82.8 km at  $1^\circ$  and slowly increases again to 84.5 km at  $15^\circ$ .

As the slope of the aquifer increases the distance the plume can migrate before it reaches the surface decreases. For an injection depth of 2 km, only angles of  $1/2^\circ$  and  $1^\circ$  prevent the CO<sub>2</sub> from reaching the surface, and even for  $\theta = 1/2^\circ$  the CO<sub>2</sub> rises 750 m vertically. Therefore, the depth of the current at the end of migration is the important criterion for storage security. Given the dimensionless initial depth  $d_0 = D_0/L$  the dimensionless final depth is  $d = -d_0 + \xi_\uparrow \sin \theta$ . We can define the critical angle at which the injected CO<sub>2</sub> reaches the surface as

$$\theta_c = \arcsin \left( \frac{d_0}{\xi_\uparrow} \right) \quad (3.85)$$

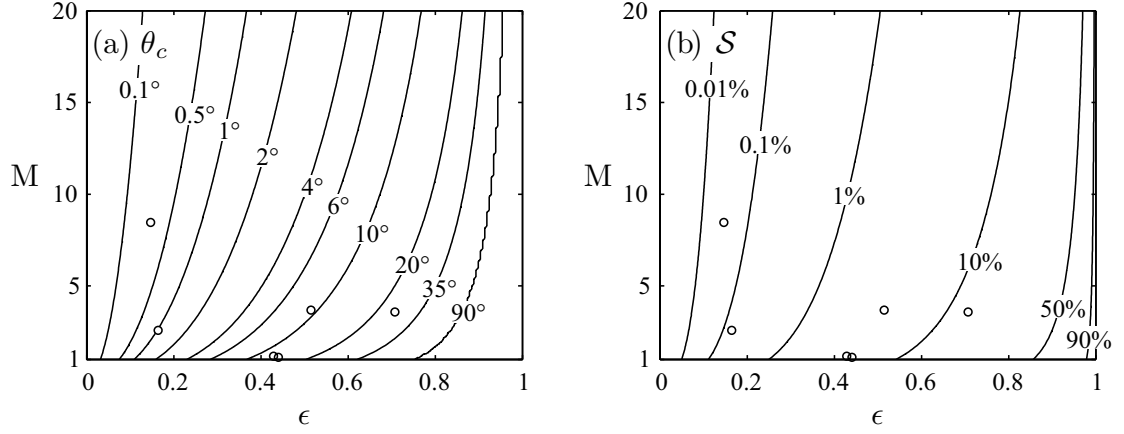


Figure 3.22: Contour plots of the critical angle,  $\theta_c$ , assuming  $d_0 = 2$  and the sweep,  $\mathcal{S}$ , as function of  $M$  and  $\epsilon$ . The data for several potential storage aquifers in Alberta, Canada, is shown as circles to indicate typical parameter values (Bachu & Bennion, 2007).

Figure 3.22(a) shows that the critical angle,  $\theta_c$ , increases with  $\epsilon$  and decreases with  $M$ . For a given  $M$  and  $\epsilon$  the CO<sub>2</sub> will not reach the surface for  $\theta < \theta_c$ . The optimal storage aquifer therefore has a few degrees of slope, just enough to cause lateral up-dip migration and the corresponding efficient residual trapping, but without reducing the distance to the surface too much.

Despite rapid trapping compared to the horizontal case, CO<sub>2</sub> storage in saline aquifers is limited by the poor vertical sweep,  $\mathcal{S}$ , and the resulting long migration distances. The vertical sweep can be defined as  $\mathcal{S} = \langle h_r \rangle / H = \langle \eta_r \rangle$ , where  $\langle h_r \rangle$  is the average residual surface. The initial volume of mobile CO<sub>2</sub> is given by  $\phi(1 - S_{br})HL$ , and the residual volume of CO<sub>2</sub> at the end of the migration is given by  $\phi S_{cr} \langle h_r \rangle (x_{\uparrow} - x_{\downarrow})$ . An expression for the vertical sweep,  $\mathcal{S}$ , can be obtained from the conservation of volume and is given by

$$\mathcal{S} = \frac{\epsilon}{\xi_{\uparrow} - \xi_{\downarrow}}, \quad (3.86)$$

where  $\xi_{\downarrow} \approx 0$  in the hyperbolic limit. Figure 3.22(b) shows that the sweep is a strong function of  $\epsilon$ , increasing monotonically from zero at  $\epsilon = 0$  to unity for  $\epsilon = 1$ . For the data from Bachu & Bennion (2007), the sweep,  $\mathcal{S}$ , can vary from less than  $10^{-3}$  to

more than  $10^{-1}$ , roughly three orders of magnitude, while the residual,  $\epsilon$ , itself only varies between 0.1 and 0.7. Therefore, the residual CO<sub>2</sub> saturation,  $S_{cr}$ , influences the up-dip migration distance given by (3.44) more strongly through its influence on the sweep than through its direct volumetric effect.

### Large scale CO<sub>2</sub> storage: Carrizo-Wilcox aquifer in Texas

Nicot (2008) considered the storage of roughly a fifth of the CO<sub>2</sub> emissions from coal power stations in the state of Texas over the next 50 years. This would require the injection of approximately  $370 \cdot 10^6$  m<sup>3</sup>/yr of supercritical CO<sub>2</sub>, equivalent to 50 MtCO<sub>2</sub>/yr, into the central section of the Carrizo-Wilcox aquifer. They envisioned a line of 50 wells aligned perpendicular to the dip of the aquifer with a 1.6 km spacing. These wells act as a 80 km long line source and our one-dimensional solution is a reasonable approximation of the displacement away from the edges.

To obtain first order estimates of the migration distance of the injected CO<sub>2</sub> we assume the following constant aquifer properties estimated from the data given in Nicot (2008):  $H \approx 200$  m,  $k \approx 500$  mD,  $\phi \approx 0.15$ , the average depth of injection 2.7 km, the average distance to the outcrop 100 km, and therefore an average dip angle,  $\theta \approx 1.5^\circ$ . We assume the following fluid properties:  $\Delta\rho \approx 300$  kg/m<sup>3</sup>,  $S_{cr} = S_{br} = 0.2$ ,  $\mu_c \approx 0.06 \cdot 10^{-3}$ ,  $\mu_b/\mu_c \approx 10$ ,  $k_{rc} \approx 0.2$ ,  $k_{rb} = 1$  (at the advancing interface).

Given this data the appropriate length scale at the end of 50 years of injection is  $L \approx 10$  km, so that the initial aspect ratio is  $A = L/H \approx 50$ . The three governing parameters are therefore  $M \approx 5$ ,  $\epsilon \approx 0.25$ , and  $Pe = A \tan \theta \approx 1.4$ . Figure 3.21 shows that the migration distance and time for  $M = 5$  are already close to the hyperbolic limit for  $Pe = 1.4$ , so that we obtain  $\xi_\uparrow \approx 80$  and  $\tau_f \approx 110$  from figure 3.17.

The along slope migration distance would be approximately  $\xi_\uparrow L = 800$  km, so that the migration distance exceeds the up-dip extent of the aquifer significantly. Under the simplifying assumptions made here, this particular injection scenario does not ensure that all CO<sub>2</sub> would be trapped by residual saturation alone. The initial length scale  $L$  would have to be reduced to  $100 \text{ km}/\xi_\uparrow = 1.25$  km to achieve residual trapping of all injected CO<sub>2</sub>. This could be achieved by increasing the width of the injection zone from 80 to approximately 620 km. Another option would be to reduce

the volume injected into this aquifer from 50 to roughly 6.5 MtCO<sub>2</sub>/yr, assuming the original injection width of 80 km. In this case the CO<sub>2</sub> would remain mobile for 1550 years after the end of injection.

### 3.6 Conclusion

We derive a vertical-equilibrium sharp-interface model governing the migration of an immiscible gravity current in a two-dimensional confined aquifer. A simple model of residual trapping allows the analysis of the relationship between the vertical sweep of CO<sub>2</sub> plume and residual trapping.

In the parabolic limit of the governing equations, corresponding to a horizontal aquifer, the evolution of the CO<sub>2</sub> plume is divided into three regimes. The mobility ratio  $M$  is the parameter that determines the time scales separating these regimes.

We have obtained new similarity solutions in the variable  $\zeta = x(\kappa H t)^{-1/2}$  that are valid at early times when the interface is tilting, due to a horizontal exchange flow. These similarity solutions are a strong function of the mobility ratio  $M$ , and of the residual,  $\epsilon$ . In this regime the position of the tip of the interface is given by  $x \propto t^{1/2}$ , so that the exponent is independent of  $\epsilon$ . The numerical solution continues to follow the early scaling law long after the interface has detached from one boundary. This indicates that the finite thickness of the aquifer is important for gravity currents with  $M > 1$ , and solutions that assume infinite depth are not valid until the current has become very thin.

In the limits  $h \rightarrow 0$  and  $M \rightarrow 0$ , the governing equation simplifies to the porous medium equation. For  $\epsilon = 0$ , this equation admits a similarity solution in the variable  $\varsigma = x/(\kappa V t)^{-1/3}$ , where the position of the tip of the interface is given by  $x \propto t^{1/3}$ . For  $\epsilon \neq 0$ , the exponent in is a function of  $\epsilon$ ,  $x \propto t^{\beta(\epsilon)}$ . This dependence is given by a nonlinear eigenvalue problem. We obtain an expression for the transition time  $t_t$  from the  $t^{1/2}$  to the  $t^{\beta(\epsilon)}$  scaling. The transition time,  $t_t$ , increases monotonically with  $M$ , but it is a weak function of  $M$  for  $M < 0.18$ , and it increases rapidly for  $M > 0.18$ . The two self-similar regimes are separated by a transition period that is roughly centered on  $t_t$ . Numerical solutions of the governing partial differential equation are used to

describe the evolution during the non-self-similar transition period. Numerical results show good agreement with the early and the late similarity solutions.

During CO<sub>2</sub> storage in horizontal saline aquifers  $M \approx 5$ , and we expect a prolonged period where the current spreads according to the early scaling law. Residual trapping will be most effective in the time just after the current detaches from the base of the aquifer. In the long term limit, the the current spreads very slowly and residual trapping becomes less important. Despite continued loss of volume, the current is never reduced to zero and continues to spread. This behavior is an artefact of the model that neglects capillary pressure.

In the hyperbolic limit of the governing equations, appropriate for dipping aquifers, the current is described by a travelling wave with hysteresis. The leading edge of the interface is a rarefaction, and the trailing edge is a shock. The current volume is reduced continuously by the residual, and the volume is reduced to zero in finite time. We have obtained expressions for the up-dip migration distance and the final migration time of the current.

In both the parabolic self-similar solutions and the hyperbolic rarefaction and shock we observe that residual trapping affects the advancing section of the interface more strongly than the receding section of the interface. Although trapping occurs at the receding interface, the advancing interface is affected more strongly because less fluid is supplied to it from the receding section.

In gently sloping aquifers, an initial near-parabolic regime with power-law decay of the volume is followed by a near-hyperbolic regime with very rapid volume decay. Increasing the slope of the aquifer or the initial aspect ratio of the current reduces the duration of initial parabolic period.

Our results suggest that lateral migration of the injected CO<sub>2</sub> along the seal will trap the CO<sub>2</sub> relatively quickly as residual saturation. Residual trapping is optimized in sloping aquifers with small mobility ratios and high residual CO<sub>2</sub> saturations. However, the long migration distances of CO<sub>2</sub>, due to the formation of a gravity tongue, may limit the volume of CO<sub>2</sub> that can be stored in sloping regional aquifers.

## Chapter 4

# Multiscale simulation of CO<sub>2</sub> storage in saline aquifers

### 4.1 Introduction

#### 4.1.1 Challenges in the numerical simulation of CO<sub>2</sub> storage in saline aquifers

The simulation of CO<sub>2</sub> storage in saline aquifers is challenging because: the dominant physical processes change as the plume evolves, the domain may be very large, several key physical processes as well as geological heterogeneity require high spatial resolution, and the uncertainty in the geological parameters is large.

During the relatively short injection phase, advection and gravitational forces are expected to be important, while gravitational and capillary forces dominate the long post-injection period. Finally, geochemical reactions that bind the CO<sub>2</sub> in minerals will become important. This change in the dominant processes over time limits the use of highly specialized and efficient numerical methods, such as streamline simulations (Jessen *et al.*, 2005; Kovscek & Wang, 2005), or vertical equilibrium models discussed in § 3, which exploit the dominance of particular terms in the governing equations.

The size of the simulation domain is another main challenge in the numerical simulation of geological CO<sub>2</sub> storage. In comparison to reservoir simulation for oil

recovery, much larger domains have to be simulated and over much longer time periods. The CO<sub>2</sub> plume may migrate laterally over 10's to 100's of kilometers in regional aquifers, and toward the surface along wells and fractures. Nordbotten *et al.* (2004) and Silin *et al.* (2006) showed that the interaction of the CO<sub>2</sub> with shallower aquifers and aquitards along the leakage pathway can reduce the leakage rate to the atmosphere significantly. It may therefore be necessary to simulate fluid movement in the overburden of the storage site, leading to even larger simulation domains. In addition, large quantities of CO<sub>2</sub> have to be injected to lead to a meaningful reduction of CO<sub>2</sub> emissions, and this may lead to displacements of the interface between brine and potable groundwater on a basin scale (Nicot, 2008).

On the other hand, geological porous media, including saline aquifers, are heterogeneous on all length scales (Journel, 1986), and numerical simulation with very high spatial resolution is necessary to capture the complex flow patterns that develop in unstable displacements (Tchelepi & Orr, 1994). The simulation of CO<sub>2</sub> storage also requires high numerical resolution to capture the small length-scales associated with important physical processes, such as diffusion and dispersion. In §2 we show that buoyancy driven fingers in the brine determine the dissolution rate of CO<sub>2</sub>, and may require even higher decimeter-scale resolution. In §3 we show that the adverse mobility ratio leads to dynamical instabilities such as long thin gravity tongues and viscous fingers that require sub-meter-scale resolution in numerical simulation. The length and time scales associated with the physical mechanisms during CO<sub>2</sub> storage may span six orders of magnitude in a sloping high-permeability aquifer, and this range of scales considers only the continuum description where Darcy's law is thought to apply.

Finally, the uncertainty in the description of the geological storage site requires many simulations to assess the uncertainty in model predictions (Kovscek & Wang, 2005). Similarly, the updating of the geological model through monitoring data requires a large number of simulations (Doughty *et al.*, 2007). Current reservoir simulation technology may not be able to provide adequate numerical resolution to capture physical processes and at the same time allow for the reasonable exploration of the



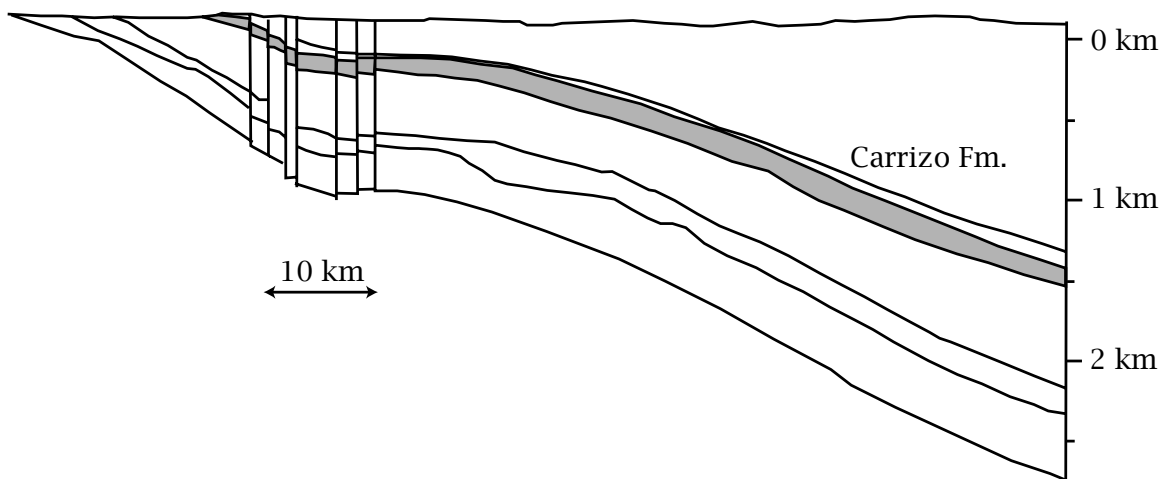


Figure 4.1: An example of a typical regional aquifer under consideration for CO<sub>2</sub> storage, the Carrizo Formation in east Texas is shown in grey. The figure is vertically exaggerated 16:1, so that the true aspect ratio is much larger than it appears in the figure. The sketch is simplified from Nicot (2008).

uncertainty through the investigation of many equally probable geostatistical realizations of the storage site. We therefore aim to develop computationally efficient solution algorithms that can provide high resolution locally to capture the fine-scale details of the flow field in very large simulation domains.

The fraction of the simulation domain that requires these high resolutions is generally small and may be associated with several features, such as multiple CO<sub>2</sub> plumes and interfaces between brine and potable groundwater. Recently multiscale methods have been developed that can resolve the large-scale flow on a coarse grid, using numerical basis functions and have the ability to reconstruct fine-scale flow features locally. Multiscale methods offer the desired adaptivity in highly heterogeneous domains through the selective reconstruction and updating of basis functions (Jenny *et al.*, 2005). We focus on the multiscale finite volume (MSFV) method introduced by Jenny *et al.* (2003). The MSFV method is currently the only multiscale method for modeling flow in porous media that has been extended to most of the physical processes necessary for CO<sub>2</sub> storage in saline aquifers: compressibility (Lunati & Jenny, 2006; Zhou & Tchelepi, 2008), gravity (Lunati & Jenny, 2008), and wells (Lee

*et al.*, 2008).

Grids with high aspect ratios are common in reservoir simulation, because oil reservoirs are kilometers in areal extent and tens of meters thick, leading to simulation domains with high aspect ratios (100:1 in 2D). In addition, geological layering and fractures can introduce severe anisotropy, which is often miss-aligned with the computational grid. Grid aspect ratios and permeability anisotropy have similar effects on the numerical discretization (see § 4.3.1) and can lead to significant challenges in numerical modeling.

Large regional aquifers extend for several tens or even a few hundred kilometers, but they are at most a few hundred meters thick (figure 4.1), leading to even larger aspect ratios than in reservoir simulation of oil and gas fields (1000:1 in 2D). Therefore, the problems with accurate and robust numerical discretization of anisotropic domains with high aspect ratios are even more relevant in CO<sub>2</sub> storage than in conventional reservoir simulation. The original MSFV method, however, is only robust for uniform grids and isotropic fine-scale permeability (Kippe *et al.*, 2007; Lunati & Jenny, 2007). The development of a multiscale finite volume discretization that is robust for large aspect ratios is therefore an important step towards the simulation of CO<sub>2</sub> storage at the field scale.

### 4.1.2 Incompressible two-phase flow in porous media

Using a simple model problem, we illustrate the structure of the governing equations that have to be solved for field-scale simulation of CO<sub>2</sub> storage. We show how an elliptic equation for the pressure arises. The repeated solution of this equation is numerically expensive and multiscale solution algorithms are necessary to solve the very large problems arising in CO<sub>2</sub> storage in regional aquifers.

We consider the case of immiscible two-phase (supercritical CO<sub>2</sub> and brine) flow in a heterogeneous porous medium. For incompressible fluids and rock, the conservation

equation for each phase can be written as

$$\phi \frac{\partial S_c}{\partial t} + \nabla \cdot \mathbf{u}_c = -f_p, \quad (4.1)$$

$$\phi \frac{\partial S_b}{\partial t} + \nabla \cdot \mathbf{u}_b = -f_p, \quad (4.2)$$

where  $S_i$ ,  $\mathbf{u}_i$ , and  $f_i$  denote the saturation, Darcy velocity and source term (well) of fluid phase  $i$ , and  $\phi$  is the porosity. The subscripts  $c$  and  $b$  for the phase denote  $CO_2$  and brine. The saturation,  $S_i$ , is the volume fraction of phase  $i$  in the pore space, so that  $S_c + S_b = 1$ . For our problem, the viscosities of the  $CO_2$  and brine phases can be different, but the viscosity of each phase is assumed to be constant. We also assume that capillarity and gravity effects are negligible, so that Darcy's law in terms of the phase mobility,  $\lambda_i$ , is given by

$$\mathbf{u}_i = -\lambda_i \nabla p = -\mathbf{K}(\mathbf{x}) \frac{k_{ri}(S_i)}{\mu_i} \nabla p, \quad (4.3)$$

where  $\mathbf{K}(\mathbf{x})$  is the absolute permeability tensor field,  $p$  is the pressure, and  $k_{ri}$  and  $\mu_i$  are the relative permeability and viscosity of phase  $i$ . Summing the conservation equations of both phases we obtain

$$\nabla \cdot \mathbf{u} = f, \quad (4.4)$$

where  $f = -f_c - f_b$ ,  $\mathbf{u} = \mathbf{u}_c + \mathbf{u}_b = -\lambda \nabla p$  is the total velocity, and the total mobility,  $\lambda$ , is defined as

$$\lambda(\mathbf{x}, S_i) = \mathbf{K}(\mathbf{x}) \left( \frac{k_{rc}(S_c)}{\mu_c} + \frac{k_{rb}(S_b)}{\mu_b} \right). \quad (4.5)$$

This system of equations is supplemented with appropriate initial and boundary conditions. In reservoir simulation, the system is often assumed to be closed, so that no-flow boundary conditions are imposed at the periphery.

The total velocity,  $\mathbf{u}$ , defined above allows us to rewrite (4.1) in terms of the fractional flow,  $f_i = \mathbf{u}_i / \mathbf{u}$ , of phase  $i$ . Incompressible two-phase flow in porous media

is therefore governed by the following coupled elliptic-hyperbolic system of equations

$$-\nabla \cdot [\lambda(\mathbf{x}, S_i) \nabla p] = f, \quad (4.6)$$

$$\phi \frac{\partial S_i}{\partial t} - \nabla \cdot [f_i(S_i) \lambda(\mathbf{x}, S_i) \nabla p] = -f_i. \quad (4.7)$$

Equations (4.6) and (4.7) are usually referred to as the flow and transport problems, respectively. The flow problem is an elliptic equation for  $p$ , and the transport problem is a hyperbolic conservation law for  $S_i$ . They are coupled through the dependence of  $\lambda$  on the saturations  $S_i$ , which are a function of space and time. These equations are representative of the type of system that must be solved accurately and efficiently by a simulator for CO<sub>2</sub> storage.

At every time step,  $t^n$ , in the solution process (4.6) has to be solved for the pressure field, and in this context the total mobility is only a function of space. Therefore, we drop the dependence of  $\lambda$  on  $\mu_p$  and  $k_{rp}$  in (4.5) and set  $\lambda(\mathbf{x}, t^n) = \mathbf{K}(\mathbf{x})$  to emphasize its tensorial nature.

### 4.1.3 Multiscale methods for porous media

Natural porous media are heterogeneous at all length scales, and current advances in data integration and subsurface description provide increasingly detailed descriptions of the subsurface. Numerical methods for incompressible flow in porous media therefore lead to discrete elliptic problems with highly oscillatory coefficients. Full resolution of the fine-scale features of the coefficient in realistic problems is often too expensive. In the last few years, several multiscale methods have been developed to reduce the computational complexity by incorporating fine-scale features into a set of coarse grid equations. A characteristic of multiscale methods for flow in porous media is that they allow a reconstruction of an approximate fine-scale solution from the coarse solution. The fine-scale reconstruction of the flow field ( $p$  and  $\mathbf{u}$ ) is necessary for the subsequent transport calculations, which are very difficult to upscale. Methods designed for flow in porous media include the multiscale finite element method (Hou & Wu, 1997), the mixed multiscale finite element method (Chen & Hou, 2002;

Aarnes, 2004), the two-scale conservative subgrid approach (Arbogast, 2002), the finite difference heterogeneous multiscale method (Abdulle & E, 2003), the variational multiscale method (Juanes & Dub, 2008), and many others.

We discuss the *multiscale finite volume* (MSFV) method for elliptic problems, which was introduced by Jenny *et al.* (2003, 2005, 2006). The method described in §4.2 is identical to the original MSFV method, but we describe it from a different perspective that motivated the new results and developments presented in §4.4 & §4.6. For simplicity, we restrict the discussion to a two-dimensional (2D) orthogonal grid. In §4.1.2 we show that the pressure field in incompressible porous media flows is given by the scalar elliptic boundary value problem (4.6). Introducing operator notation the complete definition of the flow problem is

$$\begin{aligned} Lp(\mathbf{x}) &= f(\mathbf{x}) & (\mathbf{x} \in \Omega), \\ L^\Gamma p(\mathbf{x}) &= g(\mathbf{x}) & (\mathbf{x} \in \Gamma := \partial\Omega). \end{aligned} \quad (4.8)$$

Here  $\mathbf{x} = (x, y)$ , and  $\Omega \subset \mathbb{R}^2$  is a rectangular open domain with boundary  $\partial\Omega$ .  $L$  is the linear elliptic operator on  $\Omega$  and  $L^\Gamma$  represents the linear boundary operators. The elliptic operator  $L$  is defined by

$$L[\bullet] = -\nabla \cdot (\mathbf{K}(\mathbf{x})\nabla\bullet), \quad (4.9)$$

where the tensor  $\mathbf{K}$  is symmetric positive definite. In problems of flow and transport in porous media the pressure equation, (4.8), is coupled to one or more transport equations, given by (4.7).

#### 4.1.4 Fine-scale problem

The hyperbolic nature of the transport equations requires that any numerical approximation of  $L$  be conservative, so that the corresponding flux field matches source terms exactly. The finite volume approximation of (4.8) is given by

$$\begin{aligned} L_h p_h(x_i, y_j) &= f_h(x_i, y_j) & ((x_i, y_j) \in \Omega_h), \\ L_h^\Gamma p_h(x_i, y_j) &= g_h(x_i, y_j) & ((x_i, y_j) \in \partial\Omega_h). \end{aligned} \quad (4.10)$$

Here  $h$  is a discretization parameter defining the centers of the finite control volumes or cells  $\mathbf{G}_h := \{(x, y) : x_i = (i + \frac{1}{2})h, y_j = (j + \frac{1}{2})h; i \in (0, \dots, n-1), j \in (0, \dots, m-1)\}$ , where  $m$  and  $n$  are the number of cells in the  $x$ - and  $y$ -directions. We only consider square grids, because simple forms of grid stretching and skewness can be absorbed into an effective permeability tensor, see §4.3.1. The control volume centered on  $(x_i, y_j)$  is denoted  $\bar{\Omega}_{h_{ij}}$ , and the four interaction regions that connect it to the surrounding eight neighbors are labeled  $\tilde{\Omega}_{h_{ij}}^{(d)}$ , where  $d \in (1, 2, 3, 4)$ . When we discuss a control volume and its associated interaction regions, we drop the  $i, j$  subscript (figure 4.2). The discrete operator for the  $ij$ -th cell is given by

$$L_h p_h(x_i, y_j) = \sum_{a,b=-1}^1 m_{a,b} p_h(x_i + ah, y_j + bh) = [m_{a,b}]_h p_h, \quad (4.11)$$

where we have dropped the  $i, j$  subscript on the discrete operator,  $L_h$ , and the coefficients,  $m_{a,b}$ , for clarity. For homogeneous problems it is convenient to express the discrete operator using the stencil notation (Trottenberg *et al.*, 2001)

$$L_h p_h = [m_{a,b}]_h p_h = \begin{bmatrix} m_{-1,1} & m_{0,1} & m_{1,1} \\ m_{-1,0} & m_{0,0} & m_{1,0} \\ m_{-1,-1} & m_{0,-1} & m_{1,-1} \end{bmatrix}_h p_h. \quad (4.12)$$

To represent a constant solution exactly the coefficients  $m_{a,b}$  must satisfy

$$\sum_{a,b=-1}^1 m_{a,b} = 0. \quad (4.13)$$

A stencil with  $n$  non-zero coefficients will be referred to as a  $n$ -point stencil. The discrete problem 4.10 gives rise to the linear system,  $\mathbf{L}_h \mathbf{p}_h = \mathbf{f}_h$ , and the stencil,  $[m_{a,b}]_h$ , corresponds to the non-zero entries in a row of  $\mathbf{L}_h$  for a cell in the interior of  $\Omega_h$ .

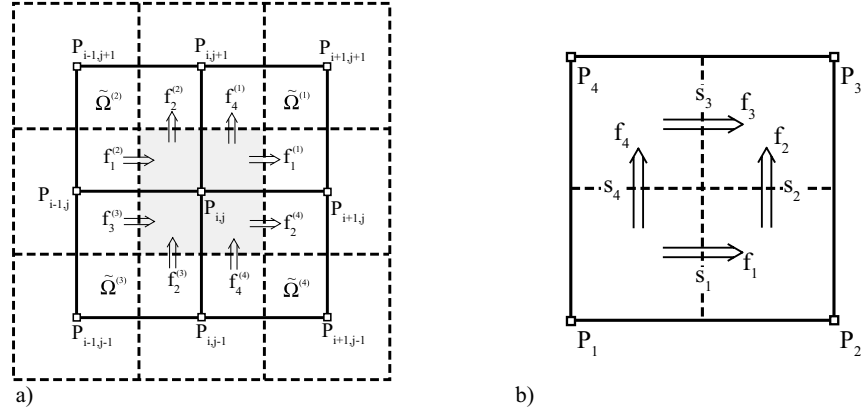


Figure 4.2: (a) Nine cells of the finite volume grid are shown by dashed lines. The four dual interaction regions,  $\tilde{\Omega}^{(1)}$  to  $\tilde{\Omega}^{(4)}$ , which connect the shaded finite volume cell in the center to its eight nearest neighbors are shown by solid lines. (b) A dual interaction region is shown with the four coarse cell boundary segments labeled  $s_1$  to  $s_4$  and the corresponding fluxes  $f_1$  to  $f_4$ .

#### 4.1.5 Multipoint flux approximations

On rectangular grids with aligned anisotropy finite volume methods use central differences to approximate the fluxes across cell boundaries. Such two-point approximations for the fluxes give rise to a 5-point stencil that gives a second-order approximation to  $L$ . On general non-orthogonal grids, as well as for non-diagonal tensors, two-point flux approximations are not a consistent approximation of (4.8), and lead to errors that do not diminish with grid refinement. *Multipoint flux approximations* (MPFA) have been introduced to give a more accurate approximation of the fluxes in these cases (for an introduction, see Aavatsmark, 2002). The properties of porous media can exhibit very strong anisotropies and robust discretizations,  $L_h$ , for these cases have been discussed by several authors (Aavatsmark *et al.*, 1996; Lee *et al.*, 1998; Edwards & Rogers, 1998; Aavatsmark, 2002; Lee *et al.*, 2002; Nordbotten & Aavatsmark, 2005; Nordbotten *et al.*, 2007). Although other MPFA methods are possible, we use the term for methods that approximate the fluxes using a subset of the six nodes surrounding the face through which the flux is computed (figure 4.2). This gives rise to a 9-point stencil that approximates the integral form of (4.10) in

each cell  $\bar{\Omega}_{h_{ij}}$  in the interior of  $\Omega_h$

$$L_h p_h = [m_{a,b}]_h p_h \approx \int_{\bar{\Omega}_h} L p \, d\Omega. \quad (4.14)$$

With (4.13) the stencil  $[m_{a,b}]_h$  has eight degrees of freedom. These eight coefficients are determined by considering the fluxes induced across the cell boundaries by unit sources in the eight neighboring cells (figure 4.2a). Every cell is linked to its eight neighbors by four interaction regions,  $\tilde{\Omega}^{(1)}$  to  $\tilde{\Omega}^{(4)}$ . Each interaction region contains four cell boundary segments  $s_1$  to  $s_4$  (figure 4.2b). When considering a single interaction region the pressures in the corners are labeled  $p_1$  to  $p_4$  as shown in figure 4.2b.

In this contribution we only consider MPFA schemes based on the interaction regions shown in figure 4.2a. Other choices of the interaction regions are possible and have been discussed by Lambers *et al.* (2008). The MPFA schemes considered here assume that the fluxes  $f_1$  to  $f_4$  across cell boundaries in each interaction region can be expressed as a linear combination of the four coarse pressures  $p_1$  to  $p_4$  in the corners of the dual

$$\begin{pmatrix} f_1 \\ f_2 \\ f_3 \\ f_4 \end{pmatrix} = \begin{pmatrix} t_{1,1} & t_{1,2} & t_{1,3} & t_{1,4} \\ t_{2,1} & t_{2,2} & t_{2,3} & t_{2,4} \\ t_{3,1} & t_{3,2} & t_{3,3} & t_{3,4} \\ t_{4,1} & t_{4,2} & t_{4,3} & t_{4,4} \end{pmatrix} \begin{pmatrix} p_1 \\ p_2 \\ p_3 \\ p_4 \end{pmatrix}. \quad (4.15)$$

Therefore, we need to determine the sixteen coefficients of the transmissibility matrix  $\mathbf{T} = \{t_{m,k}\}$  that represent fluxes induced across the four boundary segments  $s_m$  by the four pressures  $p_k$ . Once the four matrices  $\mathbf{T}^{(1)}$  to  $\mathbf{T}^{(4)}$  are known the discrete



operator  $L_h$  is given by Lee *et al.* (1998) as

$$m_{1,0} = t_{1,2}^{(1)} + t_{4,2}^{(1)} - t_{4,3}^{(4)} + t_{3,3}^{(4)} \quad (4.16)$$

$$m_{-1,0} = t_{2,1}^{(2)} - t_{1,1}^{(2)} - t_{3,4}^{(3)} - t_{2,4}^{(3)} \quad (4.17)$$

$$m_{0,1} = t_{1,4}^{(1)} + t_{4,4}^{(1)} - t_{1,3}^{(2)} + t_{2,3}^{(2)} \quad (4.18)$$

$$m_{0,-1} = -t_{2,2}^{(3)} - t_{3,2}^{(3)} - t_{4,1}^{(4)} + t_{3,1}^{(4)} \quad (4.19)$$

$$m_{1,1} = t_{1,3}^{(1)} + t_{4,3}^{(1)} \quad (4.20)$$

$$m_{-1,1} = -t_{1,4}^{(2)} + t_{2,4}^{(2)} \quad (4.21)$$

$$m_{-1,-1} = -t_{2,1}^{(3)} - t_{3,1}^{(3)} \quad (4.22)$$

$$m_{1,-1} = t_{3,2}^{(4)} - t_{4,2}^{(4)}, \quad (4.23)$$

where  $[m_{a,b}]_h$  differs from Lee *et al.* (1998) by a minus sign due to the definition of  $L_h$ . The form of these equations can be understood from figure 4.2a.

In this framework, any method that determines  $\mathbf{T}$  will lead to a conservative discretization,  $L_h$ . Originally MPFA methods were developed for a full tensor permeability field that is constant in every control volume,  $\bar{\Omega}_h$ , and analytical considerations have been used to obtain the entries in  $\mathbf{T}$  (Aavatsmark, 2002). In reservoir engineering the tensor permeability field is usually computed using upscaling techniques (Darlowski, 1991).

## 4.2 Multiscale finite volume method

The spatial structure of  $\mathbf{K}$  is often very complex, and it may contain discontinuities of several orders of magnitude as well as patterns on many different length scales. The grid size,  $h$ , for (4.10) must be chosen to resolve all features of the tensor  $\mathbf{K}$  that are considered important for the subsequent solution of the transport equations. In the case of flow and transport in porous media this is often the geostatistical grid (Journel, 1986) and in the context of the multiscale method it is referred to as the fine grid. In applications of petroleum engineering and groundwater hydrology the fine grid is generally too large to allow direct numerical simulation at reasonable cost.

The MSFV method addresses this problem by a three step procedure (Jenny *et al.*, 2003): 1) Local numerical fine-scale solutions in each interaction region, are used to construct a coarse operator that accounts for fine-scale information on a coarser grid. 2) Problem 4.8 is solved on the coarse grid with the coarse operator. 3) A locally conservative fine-scale flux field is reconstructed solving local fine-scale problems in each coarse cell. The MSFV flux reconstruction on the fine-scale is consistent with the fluxes of the coarse pressure field. The MSFV method is distinguished from other upscaling methods by the construction of the coarse operator and the locally conservative flux reconstruction that is consistent with the coarse operator.

The geostatistical or fine-scale permeability field is commonly isotropic Journal (1986), although skewed and stretched grids can introduce an effective fine-scale permeability anisotropy (see § 4.3.1). All multiscale methods introduced in § 4.1.3 consider isotropic fine-scale permeability fields on rectangular grids, corresponding to a diagonal effective fine-scale permeability tensor field. The multiscale method discussed here also assumes a diagonal fine-scale permeability tensor, except in § 4.4 where fine-scale anisotropy is introduced to allow an analysis of the MSFV method for the homogeneous case.

### 4.2.1 The coarse operator

The coarse elliptic problem is defined by

$$\begin{aligned} L_H p_H(x_i, y_j) &= f_H(x_i, y_j) \quad ((x_i, y_j) \in \Omega_H), \\ L_H^\Gamma p_H(x_i, y_j) &= g_H(x_i, y_j) \quad ((x_i, y_j) \in \partial\Omega_H). \end{aligned} \tag{4.24}$$

The coarse grid has a grid size  $H = n_c h$ , where the integer  $n_c$  is the coarsening ratio, assumed to be the same in both directions. In porous media applications values of  $n_c$  between 3 and 15 are a common choice, so that the coarse linear system can be up two orders of magnitude smaller than the fine system in two dimensional problems (Jenny *et al.*, 2003). The centers of the coarse finite control volumes are defined by  $\mathbf{G}_H := \{(x, y) : x_i = (i + \frac{1}{2})H, y_j = (j + \frac{1}{2})H; i \in (0, \dots, N - 1), j \in (0, \dots, M - 1)\}$ . The coarse control volume centered on node  $(x_i, y_j)$  is denoted by  $\bar{\Omega}_{H_{ij}}$ . The coarse

grid operator of the MSFV method in stencil notation is given by

$$L_H p_H = [m_{a,b}]_H p_H, \quad (4.25)$$

and the corresponding coarse linear system is denoted by  $\mathbf{L}_H \mathbf{p}_H = \mathbf{f}_H$ , so that  $[m_{a,b}]_H$  contains the non-zero entries in a row of  $\mathbf{L}_H$  in the interior of  $\Omega_H$ . The coarse operator  $L_H$  of the MSFV method incorporates the fine-scale information of  $\mathbf{K}$  through a series of local elliptic solutions on portions of the fine grid that allow the determination of the coefficients in the coarse stencil  $[m_{a,b}]_H$ . Even if  $\mathbf{K}$  is diagonal on the fine-scale, the heterogeneity may give rise to an effective anisotropy on the coarse scale (Durlofsky, 1991; Wu *et al.*, 2002; Jenny *et al.*, 2003; Chen *et al.*, 2007). The coarse operator  $L_H$  of the MSFV method is designed to capture this effective anisotropy on the coarse scale. This contribution focuses on the construction of  $L_H$  from the local elliptic problems and the resulting properties of the coarse operator  $L_H$ .

The control volumes shown in figure 4.2a correspond to the coarse cells  $\bar{\Omega}_{H_{ij}}$  in the MSFV method and the interaction regions form the dual cells  $\tilde{\Omega}_{H_{ij}}^{(i)}$ . These coarse grids are underlain by a fine grid containing the detailed structure of  $\mathbf{K}$ . Numerical solutions of local elliptic problems in the dual interaction regions are used in the MSFV method to obtain the entries of  $\mathbf{T}^{(i)}$ . In the MSFV method the entire set of fine fluxes along each boundary segment,  $s_m$ , is necessary for the reconstruction (§4.2.3), therefore the vectors of fine transmissibilities are stored instead of the total transmissibilities (figure 4.3). In analogy to (4.15) the matrix of fine transmissibilities  $\mathbf{T}^* = \{\mathbf{t}_{m,k}^*\}$  is defined as

$$\mathbf{T}^* = \begin{pmatrix} \mathbf{t}_{1,1}^* & \mathbf{t}_{1,2}^* & \mathbf{t}_{1,3}^* & \mathbf{t}_{1,4}^* \\ \mathbf{t}_{2,1}^* & \mathbf{t}_{2,2}^* & \mathbf{t}_{2,3}^* & \mathbf{t}_{2,4}^* \\ \mathbf{t}_{3,1}^* & \mathbf{t}_{3,2}^* & \mathbf{t}_{3,3}^* & \mathbf{t}_{3,4}^* \\ \mathbf{t}_{4,1}^* & \mathbf{t}_{4,2}^* & \mathbf{t}_{4,3}^* & \mathbf{t}_{4,4}^* \end{pmatrix}. \quad (4.26)$$

The  $\mathbf{t}_{m,k}^*$  are column vectors and the matrix is of size  $(4 \cdot n_s) \times 4$ , where  $n_s$  is the number of fine cells on the coarse boundary segment. The transmissibilities on the coarse-scale,  $\mathbf{T}$ , can be obtained by summing the column vectors in  $\mathbf{T}^*$ . Therefore, the

coarse operator of the MSFV method,  $L_H$ , is defined analogous to MPFA methods, and the coefficients of the coarse stencil  $[m_{a,b}]_H$  are given by (4.16) to (4.23). The  $L_H$  is therefore similar to discretizations  $L_h$  for non-diagonal tensors on the fine grid. There is a large body of work in this field, and we use these results to understand the properties of  $L_H$  in the MSFV method.

### 4.2.2 Local elliptic problems — basis functions

In the general heterogeneous case  $\mathbf{T}^{(i)}$  will be different in every dual interaction region, but the determination of  $t_{m,k}$  in the MSFV method is identical in all four dual interaction regions. Therefore, we restrict the discussion to a single dual, and we drop the superscript indicating the dual. The sixteen degrees of freedom  $t_{m,k}$  in each dual are determined by any four linearly independent elliptic solutions,  $\phi_{h_l}$ , in  $\tilde{\Omega}_H$ . The  $l$ -th local solution in the dual interaction region is given by

$$\begin{aligned} \tilde{L}_h \phi_{h_l} &= 0 & ((x_i, y_j) \in \tilde{\Omega}_H), \\ \tilde{L}_{h_l}^\Gamma \phi_{h_l} &= \tilde{g}_{h_l}(\mathbf{p}_k) & ((x_i, y_j) \in \tilde{\Gamma} := \partial\tilde{\Omega}_H). \end{aligned} \quad (4.27)$$

Here the linear operator  $\tilde{L}_h$  is the restriction of  $L_h$  to the open domain  $\tilde{\Omega}_H \subset \Omega_h$ , and  $\tilde{L}_h^\Gamma$  is the linear boundary operator. The local support of the  $\tilde{L}_h$  requires that artificial boundary conditions are imposed on  $\tilde{\Gamma}$ . The choice of  $\tilde{L}_{h_l}^\Gamma$  is an important design choice in the MSFV method. The two most common choices for  $\tilde{L}_{h_l}^\Gamma$ , are the linear boundary condition and the oscillatory boundary condition, both were introduced by Hou & Wu (1997) in the context of the multiscale finite element method.

For any vector  $\mathbf{p}_k$  that contains the solution in the corners of  $\tilde{\Omega}_H$ , the boundary condition  $\tilde{g}_{h_l}(\mathbf{p}_k)$  interpolates the solution values onto the sides of  $\tilde{\Omega}_H$ . The simplest choice is linear interpolation, in this case  $\tilde{L}_{h_l}^\Gamma := I$ , where  $I$  is the identity and the boundary condition is given by

$$\phi_{h_l} = \tilde{g}_{h_l}(\mathbf{p}_k) = (1 - x_b/H) p_n + x_b/H p_{n+1} \quad (4.28)$$

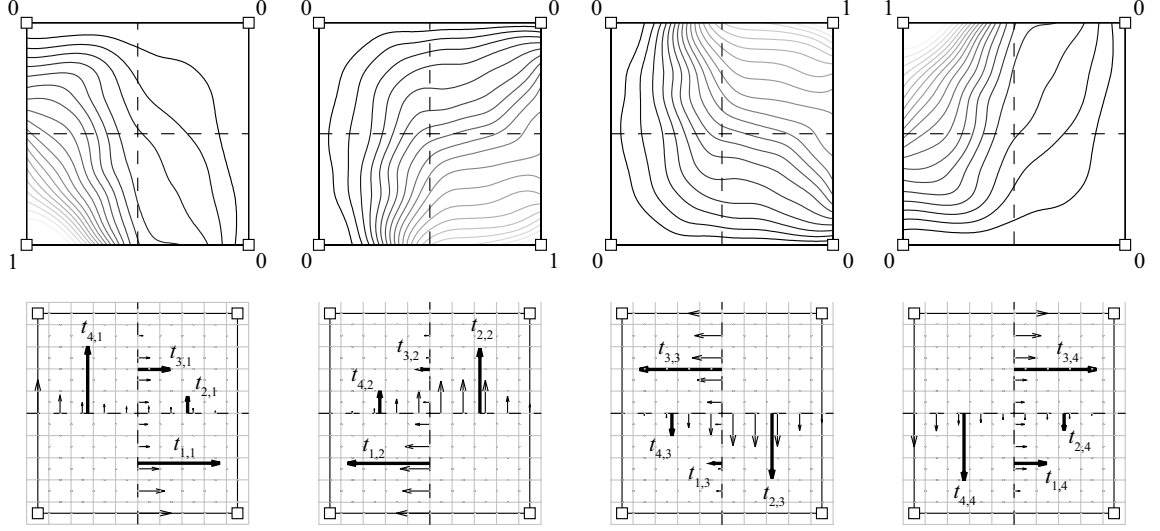


Figure 4.3: The top row shows contour plots of the four standard basis functions of the MSFV method, calculated numerically for a heterogeneous, isotropic fine permeability distribution. The second row shows the underlying dual interaction region with the fine grid and the fine fluxes  $\mathbf{t}_{m,k}^*$  along the coarse boundaries (small arrows) and the total coarse fluxes  $t_{m,k}$  integrated over each face (big arrows).

where  $n \in (1, 2, 3, 4)$  is circular, and  $x_b$  is the appropriate coordinate along the boundary. The oscillatory boundary condition is obtained by solving a reduced elliptic problem along the boundary of  $\tilde{\Omega}_H$ . The reduced boundary operator is defined by

$$\begin{aligned} \tilde{L}_{h_l}^\Gamma \phi_{h_l} &= -\frac{\partial}{\partial x_b} k_b \frac{\partial \phi_j}{\partial x_b} = 0, & (x_b \in \tilde{\Gamma}_n) \\ \phi_{h_l}(x_b = 0) &= p_n, \quad \phi_{h_l}(x_b = H) = p_{n+1} \end{aligned} \quad (4.29)$$

where  $n \in (1, 2, 3, 4)$  is circular,  $k_b$  is the component of the permeability tensor along the boundary, and  $\tilde{\Gamma}_n$  is the boundary segment between  $p_n$  and  $p_{n+1}$ . In the context of the MSFV method oscillatory boundary conditions are referred to as reduced boundary conditions, and they are used to improve the accuracy of the MSFV solution in problems with strong heterogeneity (Jenny *et al.*, 2003).

While the reduced boundary condition is optimal for space-separable problems, either choice introduces an error localized in a boundary layer,  $\delta$ , near  $\tilde{\Gamma}$ . It has been

shown that local oversampling can reduce this error at higher computational cost (Hou & Wu, 1997; Hou *et al.*, 1999). In all results presented in this paper the domain has not been oversampled, but all developments presented below can be used with oversampling.

In the MSFV method these four local solutions are interpreted as basis functions, and the vectors of corner pressures are chosen as  $\mathbf{p}_k = [\delta_{1k}, \delta_{2k}, \delta_{3k}, \delta_{4k}]^T$ , where  $\delta_{ik}$  is the Kronecker delta. In the homogeneous case the solution to (4.27) reduces to the bilinear basis functions known from finite element methods. We also use the term bilinear local problem or basis function for heterogeneous problems with the same  $\mathbf{p}_k$ . Similarly we use the term linear basis function or local problem for cases where the homogeneous limit admits a linear solution. Figure 4.3 shows these solutions for a heterogeneous, isotropic permeability field. From each of the four local solutions we obtain a vector of fine transmissibilities,  $\mathbf{t}_{m,k}^*$ , across each of the coarse cell boundary segments. These vectors contain the fine transmissibilities ordered by increasing  $x$  or  $y$ -coordinate. At the boundaries the dual interaction regions overlap by a fine cell so that the corresponding entries in  $\mathbf{t}_{m,k}^*$  are half of the associated fine-scale flux. The coarse transmissibilities are given by  $t_{m,k} = \sum_{i=1}^{n_s} (\mathbf{t}_{m,k}^*)_i$ , where  $n_s$  is the number of fine cells along the coarse boundary segment. The four local problems give a total of sixteen constraints that determine  $\mathbf{T}$  uniquely in a given dual interaction region  $\tilde{\Omega}_H$ . The MSFV basis functions are a particularly convenient way of determining the entries of  $\mathbf{T}$ , because the entries can be obtained directly by integrating the fluxes in the local problems along the coarse cell boundaries (figure 4.3). In general any set of four linearly independent local pressure solutions can be used to determine  $\mathbf{T}$ .

Once the transmissibility matrices are known for all dual interaction regions  $\tilde{\Omega}_{H_{ij}}^{(d)}$ , the coarse operator can be assembled. The coarse solution  $p_H$  is obtained from the coarse linear system,  $\mathbf{L}_H \mathbf{p}_H = \mathbf{f}_H$ .

### 4.2.3 Reconstruction of the fine-scale flux field

A conservative fine-scale flux field can be reconstructed from  $p_H$ , solving Neumann problems in each coarse cell (Gautier *et al.*, 1999; Jenny *et al.*, 2005). The Neumann

problem for a particular coarse cell  $\bar{\Omega}_H$  is defined as

$$\begin{aligned}\bar{L}_h \bar{p}_h &= 0 & ((x_i, y_j) \in \bar{\Omega}_H), \\ \bar{L}_h^\Gamma \bar{p}_h &= \bar{g}(p_H) & ((x_i, y_j) \in \bar{\Gamma} := \partial \bar{\Omega}_H).\end{aligned}\tag{4.30}$$

Here the linear elliptic operator  $\bar{L}_h$  is the restriction of  $L_h$  onto the open domain  $\bar{\Omega}_H \subset \Omega_h$ , and  $\bar{L}_h^\Gamma$  is the linear boundary operator. To obtain a fine reconstruction that is locally conservative on  $\Omega_h$  the linear boundary operator  $\bar{L}_h^\Gamma$  must impose the fluxes on  $\bar{\Gamma}$ , and is hence defined by

$$\bar{L}_h^\Gamma \bar{p}_h := -k_n \frac{\partial \bar{p}_h}{\partial x_n} = \bar{g}(p_H),\tag{4.31}$$

where  $x_n$  is the direction normal to the boundary, and  $k_n$  is the permeability in direction  $x_n$ . The fluxes  $\bar{g}(p_H)$  are informed by the coarse solution  $p_H$ . Jenny *et al.* (2003) use the superposition of a second set of basis functions to obtain  $\bar{g}(p_H)$ . This method becomes inefficient, if the basis functions have to be updated frequently. Lunati & Jenny (2006) avoid the second set of basis functions and extract  $\bar{g}(p_H)$  from the interpolation of the coarse solution onto the fine grid, using the MSFV basis functions.

If the MSFV method is formulated in terms of  $\mathbf{T}^*$  as above, the fluxes on the boundary  $\bar{g}(p_H)$  can be obtained directly without explicitly interpolating the coarse solution. In each of the four dual interaction regions,  $\tilde{\Omega}$ , surrounding the coarse cell,  $\bar{\Omega}$ , the fine fluxes on the coarse boundary segments  $s_1$  to  $s_4$  can be evaluated from

$$\underbrace{\begin{pmatrix} \mathbf{f}_1^* \\ \mathbf{f}_2^* \\ \mathbf{f}_3^* \\ \mathbf{f}_4^* \end{pmatrix}}_{(4 \cdot n_s) \times 1} = \underbrace{\begin{pmatrix} \mathbf{t}_{1,1}^* & \mathbf{t}_{1,2}^* & \mathbf{t}_{1,3}^* & \mathbf{t}_{1,4}^* \\ \mathbf{t}_{2,1}^* & \mathbf{t}_{2,2}^* & \mathbf{t}_{2,3}^* & \mathbf{t}_{2,4}^* \\ \mathbf{t}_{3,1}^* & \mathbf{t}_{3,2}^* & \mathbf{t}_{3,3}^* & \mathbf{t}_{3,4}^* \\ \mathbf{t}_{4,1}^* & \mathbf{t}_{4,2}^* & \mathbf{t}_{4,3}^* & \mathbf{t}_{4,4}^* \end{pmatrix}}_{(4 \cdot n_s) \times 4} \underbrace{\begin{pmatrix} p_1 \\ p_2 \\ p_3 \\ p_4 \end{pmatrix}}_{4 \times 1},\tag{4.32}$$

where  $n_s$  is the length of the boundary segments and  $(p_1, p_2, p_3, p_4)^T$  are the values of the coarse solution  $p_H$  in the corners of the dual interaction region. Once the fine

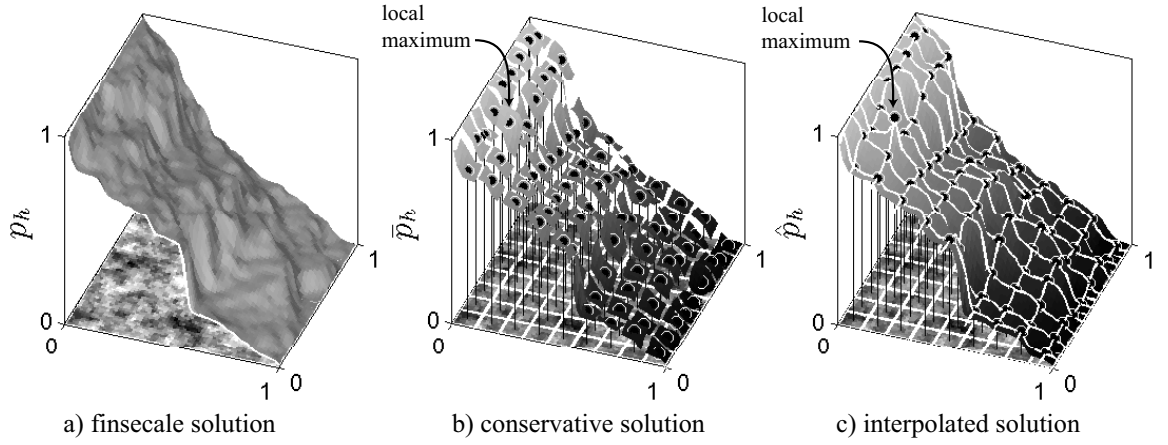


Figure 4.4: The fine-scale solution as well as the reconstructed conservative and the interpolated multiscale solutions are shown for the same problem. The log of the permeability is shown at the base of each figure. A unit pressure gradient is applied in the  $x$ -direction, and homogeneous Neumann boundary conditions are applied in the  $y$ -directions. (a) The fine-scale solution,  $p_h$ . (b) The conservative solution from the flux reconstruction on the fine grid,  $\bar{p}_h$ . (c) The coarse solution,  $p_H$ , interpolated onto the fine grid using the MSFV basis functions,  $\hat{p}_h$ . In (b) and (c) the coarse solution,  $p_H$ , is shown as large black dots.

fluxes in all dual interaction regions are known, the fluxes on the entire boundary of the coarse cell  $\bar{g}(p_H)$  can be assembled. Again, care should be taken to properly treat the fine-scale fluxes at the boundaries of dual interaction regions; these fluxes receive contributions from two interaction regions. To specify the unknown constant in (4.30) the fine solution is set to the coarse solution at the center of the coarse cell. The reconstructed solution is conservative on the fine grid, and the corresponding fine flux field can be used in transport calculations.

In §4.4.2 the coarse operator,  $L_H$ , is modified by changing the entries of  $\mathbf{T}^*$ , and it is important to maintain consistency between the coarse operator and the reconstruction. The reconstruction of the flux boundary condition given in (4.32) is always consistent with  $L_H$ .



#### 4.2.4 Properties of the MSFV solution

Figure 4.4a shows the reference fine-scale solution for a heterogeneous permeability field. Figure 4.4b shows that the solution obtained from the reconstruction of fine fluxes,  $\bar{p}_h$ , is discontinuous at the coarse cell boundaries. These discontinuities are not merely a function of the arbitrary constants in problem (4.30). There is no set of pressure constants that eliminates the discontinuities in the reconstructed solutions. The presence of strong heterogeneity leads to peaks at  $\partial\bar{\Omega}_H$ , if the boundary condition forces a high flux into a fine cell with low permeability. The magnitude of these peaks in the fine solution is not bounded by the surrounding coarse solution. This leads to the loss of monotonicity in the reconstructed fine-scale solution even if the coarse solution is monotone. The variational multiscale method exhibits a similar loss of monotonicity in the fine-scale pressure reconstruction Juanes & Dub (2008). Despite these undesirable features of the reconstructed fine solution, the associated flux field is generally a good approximation, and it has been used successfully in transport calculations (Jenny *et al.*, 2003; Juanes & Dub, 2008).

Figure 4.4c shows the interpolation of the coarse solution onto the fine grid using the bilinear basis functions. This solution is denoted  $\hat{p}_h$  and defined in each dual interaction region,  $\tilde{\Omega}_H$ , by

$$\hat{p}_h = \sum_{l=1}^4 \phi_{h_l} p_{H_l}, \quad (4.33)$$

where  $p_{H_l}$  are the coarse pressures in the corners of  $\tilde{\Omega}_H$ .

This interpolated solution is not necessary for the MSFV method described above, but has some attractive properties. Given a monotone coarse solution,  $p_H$ , the interpolation,  $\hat{p}_h$ , is monotone, because each of the numerical basis functions used for interpolation is monotone. The interpolation  $\hat{p}_h$  is not conservative along the boundaries of the dual interaction regions on the fine grid. The fine fluxes derived from the interpolation  $\hat{p}_h$  are therefore not locally conservative and cannot be used for transport calculations. The interpolation  $\hat{p}_h$  is only continuous for pure Dirichlet local boundary conditions in (4.27) without oversampling.

### 4.3 Anisotropy and monotonicity

Kippe *et al.* (2007) and Lunati & Jenny (2007) have shown that the MSFV method leads to unphysical oscillations in the coarse solution and unphysical recirculation in the reconstructed fine-scale velocity field, if the aspect ratio of the grid is not close to unity. Figure 4.4*b* & *c* show a local maximum in the coarse solution of the MSFV method inside the domain even for an isotropic, heterogeneous problem.

#### 4.3.1 Effective permeability tensor

In § 4.1.4 we introduced the discrete fine-scale operator,  $L_h$  for a uniform square grid. A uniform rectangular grid with permeability tensor  $\mathbf{K}_r$  is equivalent to a uniform square grid with an effective permeability tensor,  $\mathbf{K}$ , given by

$$\mathbf{K} = \begin{pmatrix} a & c \\ c & b \end{pmatrix} = \frac{1}{\Delta x \Delta y} \begin{pmatrix} \Delta y & 0 \\ 0 & \Delta x \end{pmatrix} \mathbf{K}_r \begin{pmatrix} \Delta y & 0 \\ 0 & \Delta x \end{pmatrix}, \quad (4.34)$$

where  $\Delta x$  and  $\Delta y$  are the length of the finite control volumes on the rectangular grid. The relation between the aspect ratio,  $A = \Delta x / \Delta y$ , used by Kippe *et al.* (2007) and Lunati & Jenny (2007), and the effective permeability tensor used here is therefore  $a/b \propto A^{-2}$ . In all heterogeneous numerical examples  $\mathbf{K}_r$  is isotropic and  $\mathbf{K}$  is diagonal, in this case  $a/b = A^{-2}$ .

To understand the loss of monotonicity of the MSFV method we need to understand the effect of coarse-scale anisotropy introduced by heterogeneity on the fine scale. However, it is difficult to analyze the properties of multiscale methods for heterogeneous cases with long correlation length. Durlofsky (1991) shows that the effect of the fine-scale heterogeneity on the coarse scale is equivalent to a homogeneous anisotropic fine-scale permeability. This equivalent fine-scale permeability is generally not aligned with the grid,  $c \neq 0$ . In § 4.4 we use this analogy to study the properties of the coarse operator of the MSFV method on a homogeneous anisotropic fine-scale permeability field. Numerical examples in § 4.7 show that the behavior of MSFV for these problems gives a good indication of its accuracy and robustness for

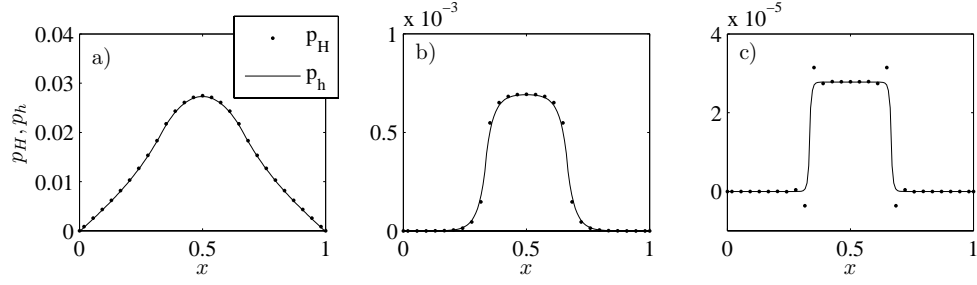


Figure 4.5: Three solution profiles in the  $x$ -direction located at  $y = 1/2$  are shown for increasing values of the ratio  $a/b$  with  $c = 0$ . (a) anisotropy ratio,  $a/b = 1 > 1/3$ , corresponding to  $A = \Delta x/\Delta y = 1$ . (b) anisotropy ratio,  $a/b = 1/100 < 1/3$ , corresponding to  $A = 10$ . (c) anisotropy ratio,  $a/b = 1/2500 < 1/3$ , corresponding to  $A = 50$ .

problems with anisotropy resulting from fine-scale heterogeneity.

Therefore, we introduce a rotated fine-scale permeability tensor only for the analysis of homogeneous problem in § 4.4, while we assume  $\mathbf{K}$  to be diagonal otherwise. Since  $\mathbf{K}$  is symmetric positive definite, the components of the effective tensor are required to satisfy  $a > 0$ ,  $b > 0$ , and  $c^2 < ab$ . So that  $a$ ,  $b$ , and  $c$  can also be expressed as a rotation of a diagonal tensor

$$\begin{pmatrix} a & c \\ c & b \end{pmatrix} = \begin{pmatrix} \cos \theta & \sin \theta \\ -\sin \theta & \cos \theta \end{pmatrix} \begin{pmatrix} \lambda_1 & 0 \\ 0 & \lambda_2 \end{pmatrix} \begin{pmatrix} \cos \theta & -\sin \theta \\ \sin \theta & \cos \theta \end{pmatrix}, \quad (4.35)$$

where  $\lambda_1$  and  $\lambda_2$  are the principle components of the effective tensor ( $\lambda_1 \geq \lambda_2$ ) and  $\theta$  is the angle between the  $x$ -axis and the eigenvector associated with  $\lambda_1$ .

### Loss of monotonicity

Incompressible flow in porous media leads to elliptic problems with strongly heterogeneous anisotropic coefficients. Many numerical discretizations of the elliptic operators lead to unphysical oscillatory solutions, and the design of robust schemes has received a lot of attention. Generally it is not possible to construct a 9-point discretization that is locally conservative, exact for linear pressure fields, and monotonic for all

admissible  $a$ ,  $b$  and  $c$  (Nordbotten *et al.*, 2007). Diagonal dominance and the M-matrix property together ensure the monotonicity of the discrete scheme, where an M-matrix is defined as a nonsingular matrix  $\mathbf{A} = \{a_{ij}\}$  whose off-diagonal elements are non-positive ( $a_{ij} \leq 0$  for  $i \neq j$ ) and whose inverse is monotone,  $\mathbf{A}^{-1} > 0$  (Bunse & Bunse-Gerstner, 1985). Nordbotten *et al.* (2007) have obtained less restrictive conditions sufficient for monotonicity. For homogenous uniform grids considered in this section their results reduce to

$$m_{0,0} > 0, \quad (4.36)$$

$$\max(m_{1,0}, m_{0,1}) < 0, \quad (4.37)$$

$$m_{0,0} + 2 \max(m_{1,0}, m_{0,1}) > 0, \quad (4.38)$$

$$m_{1,0}m_{0,1} - \max(m_{1,1}, m_{-1,1})m_{0,0} > 0. \quad (4.39)$$

Kippe *et al.* (2007) and Lunati & Jenny (2007) have reported unphysical oscillatory solutions that occur when the MSFV method is applied to heterogeneous anisotropic problems. In heterogeneous domains it is not clear whether the loss of monotonicity is caused by the assumptions on the boundary condition of the local problems 4.27, or by the properties of  $L_H$  itself. The following example will show that  $p_H$  has oscillations even in homogeneous domains, indicating loss of monotonicity of the coarse operator  $L_H$ .

Consider (4.10), with  $\Omega_h = (0, 1) \times (0, 1)$ , a square grid of  $135 \times 135$  fine cells, homogeneous Dirichlet boundary conditions, so that  $L_h^\Gamma = I$  and  $g_h = 0$ , the source term

$$f_h = \begin{cases} 1 & 1/3 < x, y < 2/3, \\ 0 & \text{otherwise,} \end{cases} \quad (4.40)$$

and aligned anisotropy ( $c = 0$ ). The source term is non-negative,  $f_h \geq 0$ , in  $\Omega_h$  and therefore  $p_h$  should be non-negative and have no local minimum in  $\Omega_h$  by Hopf's maximum principle (Strauss, 1992). For grid aligned anisotropy the discrete operator on the fine grid  $L_h$  is the standard 5-point stencil. Figures 4.5a-c show that  $p_h$  obeys Hopf's maximum principle, because the 5-point stencil satisfies conditions 4.36 to 4.39 for all ratios  $a/b$ .

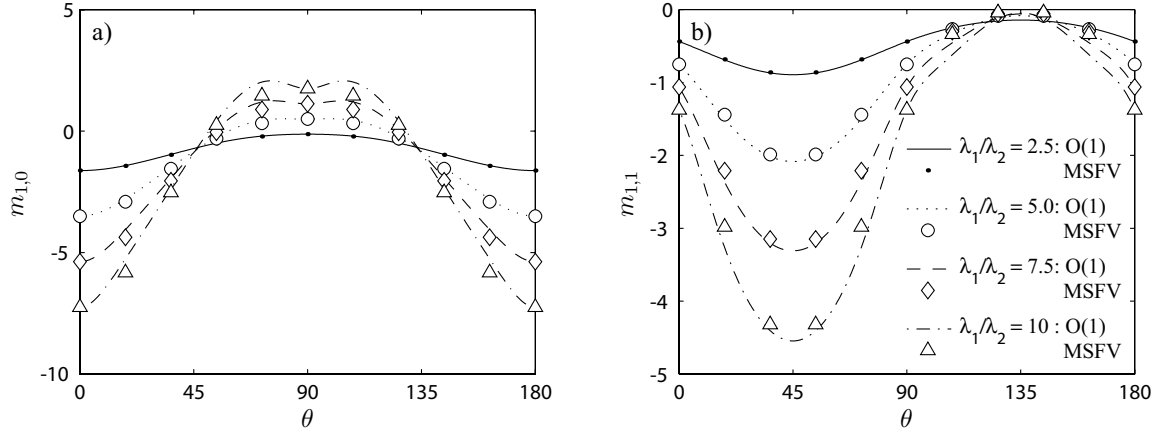


Figure 4.6: Numerical results for the stencil components  $m_{1,0}$  and  $m_{1,1}$  of the MSFV method are compared to the analytic expressions of the MPFA O(1) method. The components are shown as a function of the orientation of the tensor,  $\theta$ , for several ratios of the principal components,  $\lambda_1/\lambda_2$ .

Consider the same problem solved with the MSFV method with a coarsening ratio  $n_c = 5$ , giving  $27 \times 27$  coarse cells. Figures 4.5a & b show that the coarse solution  $p_H$  is monotonic for  $a/b$  close to unity, but figure 4.5c shows that oscillations and local minima occur as  $a/b$  decreases further.

## 4.4 Coarse operator for homogeneous problems

The properties of the MSFV coarse operator are analyzed with respect to anisotropy and monotonicity. This section focusses on homogenous anisotropic permeability fields. In this case the oscillatory local boundary conditions (4.29) reduce to linear interpolations (4.28).

### 4.4.1 Original coarse operator

In §4.1.5 we show that the MSFV coarse operator is completely determined by  $\mathbf{T}$  and (4.16) to (4.23). In the homogenous case the transmissibilities  $t_{m,k}$  of the MSFV method are determined by the four bilinear basis functions in the dual interaction

region. For grid aligned anisotropy,  $c = 0$ , the basis functions are given by

$$\phi_1 = (1-x)(1-y), \quad \phi_2 = x(1-y), \quad \phi_3 = xy, \quad \text{and} \quad \phi_4 = (1-x)y.$$

The analytical solutions for the bases functions are not known for anisotropy not aligned with the grid ( $c \neq 0$ ), but these basis functions can be calculated numerically. The discussion is therefore, initially restricted to problems with aligned anisotropy, and in this case the matrix  $\mathbf{T}$  is given by

$$\mathbf{T} = \frac{1}{8} \begin{pmatrix} 3a & -3a & -a & a \\ b & 3b & -3b & -b \\ a & -a & -3a & 3a \\ 3b & b & -b & -3b \end{pmatrix}. \quad (4.41)$$

From (4.16) to (4.23) we obtain the coarse operator of the MSFV method as

$$L_H = [m_{a,b}]_H = \frac{1}{8} \begin{bmatrix} -(a+b), & 2(a-3b), & -(a+b) \\ 2(b-3a), & 12(a+b), & 2(b-3a) \\ -(a+b), & 2(a-3b), & -(a+b) \end{bmatrix}_H, \quad (4.42)$$

for homogeneous problems with aligned anisotropy,  $c = 0$ . The coefficients  $m_{\pm 1,0}$  and  $m_{0,\pm 1}$  in the stencil are only non-positive for an anisotropy ratio,  $a/b$ , between  $1/3$  and  $3$ , outside this narrow interval  $L_H$  violates (4.37). This is the cause of the oscillations in homogeneous problems with aligned anisotropy observed in §4.3.1. The violation of (4.36) to (4.39) does not immediately lead to a coarse solution  $p_H$  that violates Hopf's maximum principle. In figure 4.5b the coarse solution  $p_H$  is still oscillation free although  $L_H$  violates (4.37), but oscillations occur eventually if the anisotropy increases further.

The coarse operator of the MSFV method is similar to the MPFA  $O(\eta)$  method, for  $\eta = 1$ . This family of schemes was first introduced by Edwards & Rogers (1998), however we follow the parametrization of Nordbotten *et al.* (2007) in terms of the parameter  $\eta \in [0, 1)$ . Although the general construction of the  $O(\eta)$  method requires

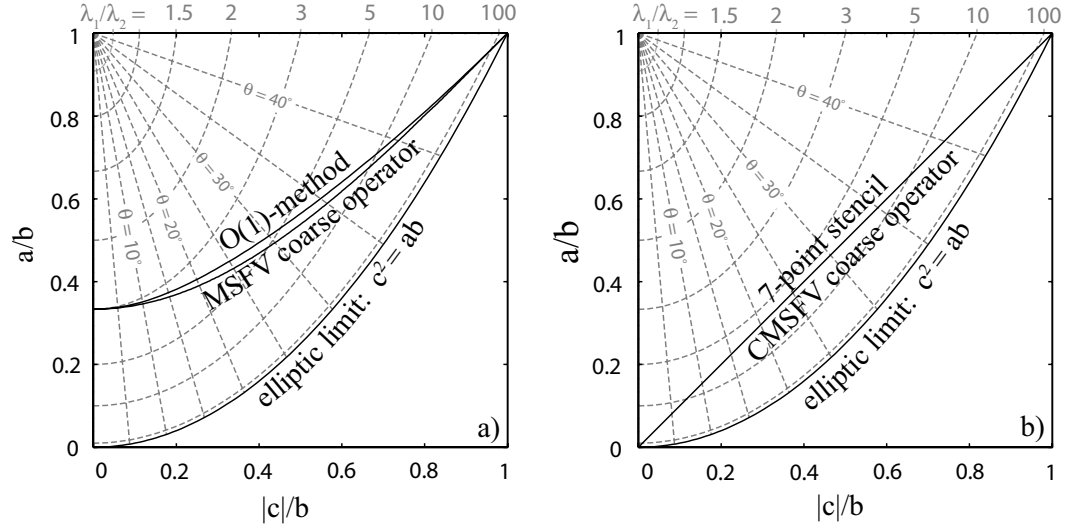


Figure 4.7: The monotonicity regions of the original and compact coarse operator are shown in the parameter space  $a/b$  vs.  $|c|/b$ . A gray grid shows the corresponding angle,  $\theta$ , and the ratio of principal components,  $\lambda_1/\lambda_2$  in the effective permeability tensor given by (4.35). All methods are monotone above the labeled line. (a) The monotonicity regions of both the MPFA O(1) method and the coarse operator of the MSFV method are compared. (b) The monotonicity region of the CMSFV method equals that of the 7-point stencil.

$\eta \in [0, 1)$ , for the homogeneous case the O(1) method is well defined Nordbotten *et al.* (2007). Previously the O(0) method has been emphasized by Aavatsmark (2002), the O(1/2) method by Edwards & Rogers (1998), and the O(0.9) method by Pal *et al.* (2007).

For homogeneous problems with aligned anisotropy ( $c = 0$ ) the MSFV coarse operator is identical to the MPFA O(1) method. For  $c \neq 0$  we have used numerical solutions on the fine grid to compute the MSFV coarse operator. The MPFA O(0) method was used to compute the basis functions on the fine grid. Figure 4.6 compares the numerical results for the MSFV method to the analytic expression for the O(1) method. Both methods have a similar behavior as the tensor is rotated. The difference between the methods increases as the ratio of the principal components of  $\mathbf{K}$  increases.

The region where a stencil satisfies (4.36) to (4.39) will be referred to as the monotonicity region of the stencil. The monotonicity region of the MSFV method is shown in figure 4.7a and has the same characteristics as that of the O(1) method. The monotonicity of both methods is very limited when anisotropy is aligned with the grid and largest, if the tensor is rotated by  $45^\circ$ . This unusual property of the original MSFV method is an unanticipated consequence of using bilinear dual basis functions within the finite volume framework of § 4.1.5.

#### 4.4.2 Compact coarse operator

The limited monotonicity region of the MSFV coarse operator, when the anisotropy is aligned with the grid, prevents the application of the MSFV method to many realistic problems in subsurface flow, where grids with high aspect ratios are commonly used. In §4.2 the MSFV method was formulated in terms of a MPFA method. It has been shown that it is possible to construct MPFA methods with different monotonicity properties while maintaining accuracy and convergence (Edwards & Rogers, 1998; Nordbotten *et al.*, 2007). For homogeneous anisotropic problems the following 7-point stencil

$$[m_{a,b}]_h = \begin{bmatrix} (c - |c|)/2 & -b + |c| & -(c + |c|)/2 \\ -a + |c| & 2(a + b - |c|) & -a + |c| \\ -(c + |c|)/2 & -b + |c| & (c - |c|)/2 \end{bmatrix}_h, \quad (4.43)$$

is second order accurate. Two of the diagonal neighbors are always zero depending on the sign of  $c$ , and therefore the stencil has 7 non-zero entries for  $c \neq 0$ . All four diagonal neighbors are zero for  $c = 0$ , and the method reduces to the standard 5-point stencil. Nordbotten *et al.* (2007) have shown that the 7-point stencil has an optimal monotonicity region, in the sense that no other 9-point stencil satisfies conditions 4.37 to 4.39 over a larger range of parameters (figure 4.7b). For homogeneous problems and inside its monotonicity region this 7-point stencil also leads to a linear system, where  $\mathbf{L}_h$  is a M-matrix. The 7-point stencil can be characterized using a 3-point flux approximation (figure 4.8), leading to one zero entry in every row of the



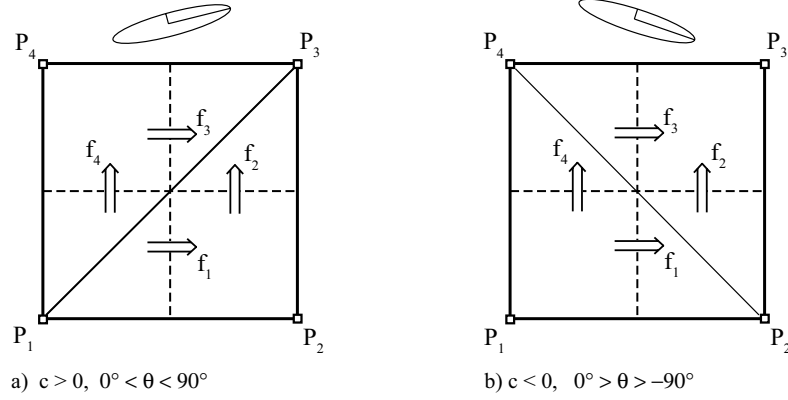


Figure 4.8: The triangular domains of dependence of the fluxes in a dual interaction region are shown for both signs of  $c$ . The corresponding orientation of the permeability tensor is indicated by the ellipses.

transmissibility matrix

$$\mathbf{T} = \begin{cases} \frac{1}{2} \begin{pmatrix} a, & c - a, & -c, & 0 \\ c, & b - c, & -b, & 0 \\ c, & 0, & -a, & a - c \\ b, & 0, & -c, & c - b \end{pmatrix} & c \geq 0, \\ \frac{1}{2} \begin{pmatrix} a - c, & -a, & 0, & c \\ 0, & b, & c - b, & -c \\ 0, & -c, & c - a, & a \\ b - c, & c, & 0, & -b \end{pmatrix} & c < 0, \end{cases} \quad (4.44)$$

whose position depends on the sign of the off-diagonal component,  $c$ . Figure 4.8 shows that the domain of dependence of each flux is aligned with the direction of maximum connectivity. We refer to a stencil with three non-zero entries in each row of  $\mathbf{T}$  as a compact operator. The definition is based on  $\mathbf{T}$  rather than the resulting stencil, because the latter may lose its zero entries in the heterogeneous case, while the zero entries in  $\mathbf{T}$  always remain.

## 4.5 Compact coarse operator for heterogeneous problems

To obtain a multiscale finite volume method with better monotonicity properties, a compact coarse operator is introduced that reduces to the 7-point stencil in the homogeneous limit. The resulting *compact multiscale finite volume* (CMSFV) method is otherwise identical to the original MSFV method proposed by Jenny *et al.* (2003). The framework presented in §4.2 allows the necessary modification of  $\mathbf{T}$  without introducing inconsistencies in the reconstruction.

Four degrees of freedom are necessary to modify  $\mathbf{T}$  to obtain a compact operator, the corresponding compact transmissibility matrix is denoted  $\bar{\mathbf{T}}$ . These degrees of freedom are obtained by reducing the number of local solutions from four to three, providing twelve constraints on the sixteen unknown transmissibilities  $t_{m,k}$ . Instead of the four basis functions of the original MSFV method, defined in §4.2.2 the basis

$$\Phi_1 = \sum_{i=1}^4 \phi_i, \quad \Phi_2 = \phi_1 + \phi_4, \quad \Phi_3 = \phi_1 + \phi_2, \quad \text{and} \quad \Phi_4 = \phi_4,$$

can be used to determine the transmissibilities  $t_{m,k}$ . This change in the basis does not affect the coarse operator, but it separates the linear and the bilinear parts of the solution. Linear solutions can be represented exactly by the first three bases, and we eliminate  $\Phi_4$  to obtain the four degrees of freedom necessary to modify  $\mathbf{T}$ . The first three basis functions  $\Phi_1$  to  $\Phi_3$  provide the following twelve constraints

$$\mathbf{0} = \bar{\mathbf{T}} \begin{pmatrix} 1 & 1 & 1 & 1 \end{pmatrix}^T, \quad (4.45)$$

$$\mathbf{f}^x = \bar{\mathbf{T}} \begin{pmatrix} 1 & 0 & 0 & 1 \end{pmatrix}^T, \quad (4.46)$$

$$\mathbf{f}^y = \bar{\mathbf{T}} \begin{pmatrix} 1 & 1 & 0 & 0 \end{pmatrix}^T, \quad (4.47)$$

on  $\bar{\mathbf{T}}$ . The definition of  $\bar{\mathbf{T}}$  is completed by placing a zero entry in each row. As in the homogeneous case the zeros are placed to align the stencil with the principle direction of anisotropy, which can be determined from the local flow information in (4.46) and

(4.47). The compact transmissibility matrix,  $\bar{\mathbf{T}}$ , has the following rows,

$$\begin{pmatrix} \bar{t}_{1,1} & \bar{t}_{1,2} & \bar{t}_{1,3} & \bar{t}_{1,4} \end{pmatrix} = \begin{cases} \begin{pmatrix} f_1^x & f_1^y - f_1^x & -f_1^y & 0 \end{pmatrix}, & f_1^y \geq 0, \\ \begin{pmatrix} f_1^x - f_1^y & -f_1^x & 0 & f_1^y \end{pmatrix}, & f_1^y < 0, \end{cases} \quad (4.48)$$

$$\begin{pmatrix} \bar{t}_{2,1} & \bar{t}_{2,2} & \bar{t}_{2,3} & \bar{t}_{2,4} \end{pmatrix} = \begin{cases} \begin{pmatrix} f_2^x & f_2^y - f_2^x & -f_2^y & 0 \end{pmatrix}, & f_2^x \geq 0, \\ \begin{pmatrix} 0 & f_2^y & f_2^x - f_2^y & -f_2^x \end{pmatrix}, & f_2^x < 0, \end{cases} \quad (4.49)$$

$$\begin{pmatrix} \bar{t}_{3,1} & \bar{t}_{3,2} & \bar{t}_{3,3} & \bar{t}_{3,4} \end{pmatrix} = \begin{cases} \begin{pmatrix} f_3^y & 0 & -f_3^x & f_3^x - f_3^y \end{pmatrix}, & f_3^y \geq 0, \\ \begin{pmatrix} 0 & -f_3^y & f_3^y - f_3^x & f_3^x \end{pmatrix}, & f_3^y < 0, \end{cases} \quad (4.50)$$

$$\begin{pmatrix} \bar{t}_{4,1} & \bar{t}_{4,2} & \bar{t}_{4,3} & \bar{t}_{4,4} \end{pmatrix} = \begin{cases} \begin{pmatrix} f_4^y & 0 & -f_4^x & f_4^x - f_4^y \end{pmatrix}, & f_4^x \geq 0, \\ \begin{pmatrix} f_4^y - f_4^x & f_4^x & 0 & -f_4^y \end{pmatrix}, & f_4^x < 0, \end{cases} \quad (4.51)$$

expressed in terms of the transmissibilities  $\mathbf{f}^x$  and  $\mathbf{f}^y$  of the new bases functions  $\Phi_2$  and  $\Phi_3$ . This definition of the compact transmissibility matrix reduces to (4.44) in the homogeneous, anisotropic case. Since the MSFV method does not compute an explicit upscaled effective permeability tensor, the orientation of the domain of dependence is based on the numerically computed fluxes rather than the off-diagonal component of the effective tensor.

The corresponding compact coarse operator is given by (4.16) to (4.23), where  $t_{m,k}$  has been replaced by  $\bar{t}_{m,k}$  in all equations. For the homogeneous case the compact coarse operator is identical to the 7-point stencil, and hence the monotonicity of the CMSFV method in the homogeneous parameter space is identical to that of the 7-point stencil (figure 4.7b). In the general heterogeneous case the entries of  $\bar{\mathbf{T}}$  are calculated numerically from the basis functions  $\Phi_2$  and  $\Phi_3$ . The choice of boundary conditions for these local problems is discussed in §4.6.3.

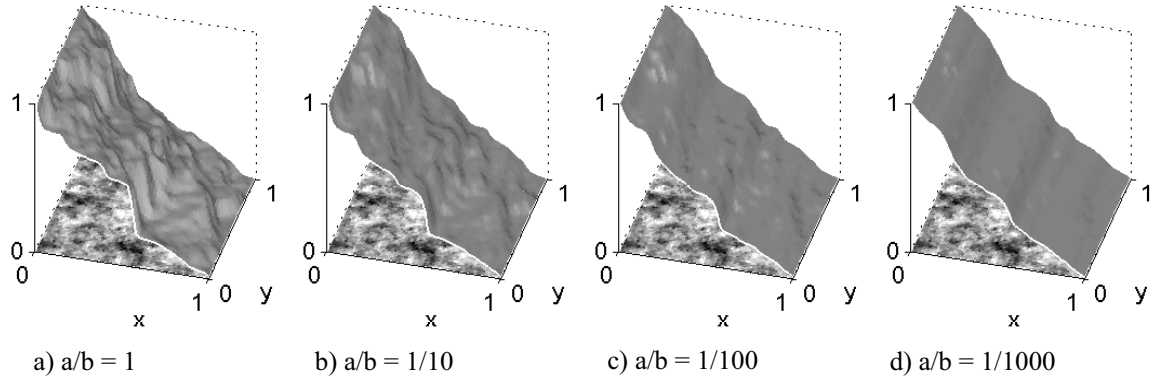


Figure 4.9: The approach of the global fine-scale solution to transverse equilibrium, as the effective anisotropy  $a/b$  increases. The boundary conditions for this problem are  $p(x = 0, y) = 1$ ,  $p(x = 1, y) = 0$ , and  $p_y(x, y = 0, 1) = 0$  and the effective permeability on the fine-scale is diagonal,  $c = 0$ . The log of the permeability field is shown at the base.

## 4.6 Localization of fine-scale problems

The boundary conditions that are used to localize the elliptic problems in the dual interaction regions,  $\tilde{L}_h^\Gamma$ , have a strong influence on the properties of the coarse operator for heterogeneous problems. Two common choices, linear and reduced boundary conditions have been introduced in §4.2.2. Either choice introduces an error into the basis functions that is localized in a boundary layer. In many anisotropic porous media problems the boundary layer quickly grows to the size of the local domain, and local oversampling cannot eliminate the error introduced by the local boundary conditions. However, in these cases the solution has a simple form, and this is exploited here to construct local solutions that lead to a robust and accurate coarse operator. A different approach to this problem is to introduce global information into the basis functions (Chen & Durlofsky, 2006; Efendiev *et al.*, 2006; Durlofsky *et al.*, 2007), which leads to improved accuracy but at increased computational cost.

### 4.6.1 Transverse equilibrium

Problems of flow in porous media are often characterized by domains with high effective anisotropy and homogeneous Neumann boundary conditions. This allows the solution of the elliptic problem to reach *transverse equilibrium* (TVE). Transverse equilibrium is characterized by negligible gradients in the direction of high effective permeability. This property has been exploited in the derivation of simplified analytical models (Yortsos, 1995), and efficient pseudo three-dimensional numerical methods (Coats *et al.*, 1971).

Consider the elliptic problem given by (4.8) with a diagonal permeability tensor, where the components of the tensor  $a(\mathbf{x})$  and  $b(\mathbf{x})$  are related by a constant  $a(\mathbf{x}) = A^{-2}b(\mathbf{x})$ . This is the typical effective permeability tensor arising from isotropic problems in stretched domains, where  $A = \Delta x / \Delta y$ . The pressure equation is then given by

$$\frac{1}{A^2} \frac{\partial}{\partial x} \left( b(\mathbf{x}) \frac{\partial p(\mathbf{x})}{\partial x} \right) + \frac{\partial}{\partial y} \left( b(\mathbf{x}) \frac{\partial p(\mathbf{x})}{\partial y} \right) = 0. \quad (4.52)$$

Consider the case where homogenous Neumann boundary conditions are applied in the  $y$ -direction, and constant Dirichlet conditions on the remaining boundaries, so that an overall pressure gradient in the positive  $x$ -direction is imposed. The numerical solutions in figure 4.9 show that the solution becomes one-dimensional in the  $x$ -direction in the limit of large  $A$ . We integrate (4.52) in the  $y$ -direction to obtain an expression for the effective one-dimensional pressure equation

$$\frac{1}{A^2} \frac{\partial}{\partial x} \int_0^1 b(\mathbf{x}) \frac{\partial p(\mathbf{x})}{\partial x} dy + \left( b(\mathbf{x}) \frac{\partial p(\mathbf{x})}{\partial y} \right) \Big|_0^1 = 0. \quad (4.53)$$

The second term is zero due to the homogeneous Neumann boundary conditions. In a boundary layer,  $\delta_y \propto A$ , near the Neumann boundaries the transverse gradients in the solution vanish,  $\partial p / \partial y \approx 0$ . In the limit of large  $A$  the boundary layers from the opposite sides of the domain merge so that  $p$  is in TVE and no longer a function of  $y$ , and (4.53) is approximately equal to

$$\frac{1}{A^2} \frac{\partial}{\partial x} \left( \int_0^1 b(\mathbf{x}) dy \frac{\partial p(x)}{\partial x} \right) = \frac{\partial}{\partial x} \left( \langle a \rangle_y(x) \frac{\partial p(x)}{\partial y} \right) \approx 0, \quad (4.54)$$

where  $\langle a \rangle_y(x)$  is the average of  $a(\mathbf{x})$  in the  $y$ -direction.

### 4.6.2 Bilinear local problems with Dirichlet boundary conditions

The local elliptic problems, introduced in §4.2.2, are constructed with Dirichlet boundary conditions, and their behavior for large effective anisotropy is different from the limit of the global solution with homogeneous Neumann boundary conditions. In particular the second term of (4.53) is not zero and the limit of (4.52) for large  $A$  is

$$\frac{\partial}{\partial y} \left( b(y; x) \frac{\partial p(y; x)}{\partial x} \right) \approx 0. \quad (4.55)$$

The solution consists of a family of decoupled one dimensional problems in the  $y$ -direction, which are parameterized by  $x$ . Unless the pressures specified at the  $y$ -boundaries are equal there will be significant fluxes in the  $y$ -direction.

When basis functions are constructed for problems with high effective anisotropy, the boundary layer containing the error introduced by the localization spreads through the entire dual interaction region and dominates the solution. Since it is not possible to eliminate the localization error by oversampling, it appears that the MSFV method cannot be accurate for high aspect ratios. However, it has been shown above that the solution has a simple form as it approaches transverse equilibrium with increasing anisotropy. If the local boundary conditions are chosen to allow transverse equilibrium in the local solution, then the MSFV method can produce good results at high aspect ratios.

We have shown in §4.4.1 that very large transverse fluxes occur in homogeneous problems at high effective anisotropy and lead to the loss of monotonicity of the coarse operator. The compact coarse operator is designed to minimize these fluxes and give the largest possible monotone domain. To retain a monotone coarse operator for heterogeneous problems, it is therefore important that the local elliptic problems do not introduce artificial gradients in the transverse direction. Given a coarse pressure field in transverse equilibrium,  $\partial p_H / \partial y = 0$ , the local solutions must be able to interpolate the coarse pressure onto the fine grid without introducing artificial gradients in the

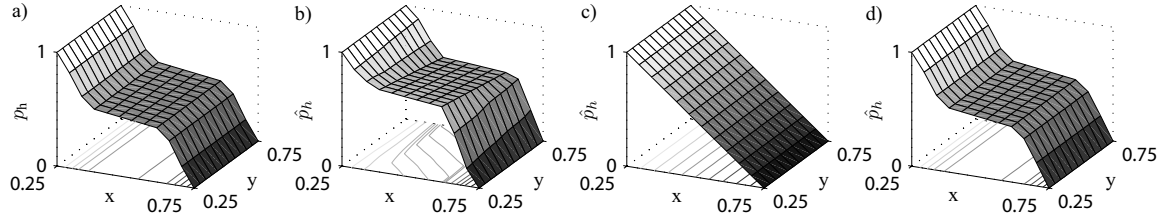


Figure 4.10: Comparison between the fine-scale solution  $p_h$  and the interpolated pressure field  $\hat{p}_h = \phi_{h_1} + \phi_{h_4}$  in a dual crossing the high permeability channel at  $a/b = 1/1000$ . (a) Fine-scale solution,  $p_h$ , in the dual, rescaled to a unit pressure gradient, is in transverse equilibrium. (b) Interpolated fine pressure  $\hat{p}_h$  with reduced boundary conditions. (c) Interpolated fine pressure  $\hat{p}_h$  with linear boundary conditions. (d) Interpolated fine pressure  $\hat{p}_h$  with hybrid boundary conditions.

$y$ -direction.

Consider a domain with a high permeability channel in the  $y$ -direction, small amplitude random noise, an effective anisotropy  $a/b = 1/1000$ , and the boundary conditions  $p(x = 0, y) = 1$ ,  $p(x = 1, y) = 0$ , and  $p_y(x, y = 0, 1) = 0$ . Figure 4.10a shows that the fine-scale solution is in transverse equilibrium, and the reduced one dimensional problem in the  $x$ -direction reflects the high permeability channel.

The advantage of the reduced boundary conditions is that they are also solutions to one dimensional problems, and therefore recognize the high permeability channel. Figure 4.10b shows that the channel is reflected in the superposition of the local solutions. The reduced boundary conditions sample different realizations of the permeability and are therefore not identical. This introduces finite transverse gradients,  $\partial \hat{p}_h / \partial y \neq 0$ , even if the coarse pressure is in transverse equilibrium. Even small transverse pressure gradients lead to very large fluxes as the effective anisotropy increases, and this leads to the loss of monotonicity of the coarse operator even for the compact stencil. Eliminating these gradients is therefore the key to a monotone coarse operator and a robust MSFV method for heterogeneous anisotropic problems.

Linear boundary conditions are identical by construction and do not introduce artificial transverse gradients. Therefore, linear boundary conditions give rise to a

more robust coarse scale operator, but figure 4.10c shows that they give poor accuracy. In this case the linear boundary conditions have a large error. For isotropic problems this error would be localized in a narrow boundary layer, but for high effective anisotropy the error spreads through the entire dual interaction region. Linear boundary conditions therefore give a robust operator, but they may lead to poor accuracy.

### 4.6.3 Linear local problems with hybrid boundary conditions

For highly anisotropic problems with homogeneous Neumann boundaries on the global domain, the boundary conditions for the local elliptic problems must have the following properties: To ensure robustness it is essential that the local elliptic problems can reach transverse equilibrium. To ensure accuracy in the isotropic case the boundary condition should be close to the reduced boundary condition. In the limit of high effective anisotropy the local elliptic problem should reduce to a close approximation of the one dimensional problem (4.54). To allow a simple implementation the boundary condition should adjust automatically to the magnitude of the effective anisotropy.

We propose hybrid boundary conditions for the local elliptic problems that ensure transverse equilibrium, give good accuracy for all aspect ratios, and are parameter free. To allow the local problems to reach transverse equilibrium homogeneous Neumann boundary conditions need to be imposed in the direction of TVE instead of Dirichlet boundary conditions. For the linear basis functions already introduced in §4.4.2, homogeneous Neumann boundary conditions can be imposed naturally on the faces perpendicular to the imposed gradient. The linear local problems are defined by 4.27, with the boundary operator given as

$$\tilde{L}_{h_2}^\Gamma = I, \quad \tilde{g}_{h_2} = 1, \quad (x_i = 0, y_i), \quad (4.56)$$

$$\tilde{L}_{h_2}^\Gamma = I, \quad \tilde{g}_{h_2} = 0, \quad (x_i = 1, y_i), \quad (4.57)$$

$$\tilde{L}_{h_2}^\Gamma = \frac{\partial}{\partial y}, \quad \tilde{g}_{h_2} = 0, \quad (x_i, y_i = 0) \text{ and } (x_i, y_i = 1) \quad (4.58)$$



for linear gradient,  $\Phi_{h_2}$ , in the  $x$ -direction, and

$$\tilde{L}_{h_3}^\Gamma = I, \quad \tilde{g}_{h_3} = 1, \quad (x_i, y_i = 0), \quad (4.59)$$

$$\tilde{L}_{h_3}^\Gamma = I, \quad \tilde{g}_{h_3} = 0, \quad (x_i, y_i = 1), \quad (4.60)$$

$$\tilde{L}_{h_3}^\Gamma = \frac{\partial}{\partial x}, \quad \tilde{g}_{h_3} = 0, \quad (x_i = 0, y_i) \text{ and } (x_i = 1, y_i), \quad (4.61)$$

for linear gradient,  $\Phi_{h_3}$ , in the  $y$ -direction. We can use these two solutions to define the boundary conditions for a bilinear local problem  $\Phi_{h_4}$

$$\tilde{L}_{h_4}^\Gamma = I, \quad \tilde{g}_{h_4} = \Phi_{h_2}, \quad (x_i, y_i = 1), \quad (4.62)$$

$$\tilde{L}_{h_4}^\Gamma = I, \quad \tilde{g}_{h_4} = 1 - \Phi_{h_3}, \quad (x_i = 0, y_i), \quad (4.63)$$

$$\tilde{L}_{h_4}^\Gamma = I, \quad \tilde{g}_{h_4} = 0, \quad (x_i = 1, y_i) \text{ and } (x_i, y_i = 0). \quad (4.64)$$

Together with the constraint,  $\vec{0} = \mathbf{T}\vec{1}$ , these three problems determine the coarse operator uniquely. The standard set of bilinear basis functions can be obtained from  $\Phi_{h_2}$  to  $\Phi_{h_4}$  through linear superposition. These bilinear basis functions have hybrid boundary conditions and hence the transmissibility matrix  $\mathbf{T}$  and the coarse operator  $L_H$  are modified. This modification is independent from the implementation of the compact coarse operator.

The local problems defined above attain transverse equilibrium at high anisotropy by construction (figure 4.10d). Transverse gradients in the local problems are reduced faster than in the global fine-scale solution, because the domain is smaller and therefore boundary layers merge earlier. Therefore, hybrid boundary conditions have robustness similar to linear boundary conditions. Section 4.11 shows that the accuracy of the hybrid boundary conditions is similar to that of the reduced boundary conditions at low anisotropy. At high anisotropy the accuracy of the hybrid boundary conditions is good if  $\langle a \rangle_y$  in the dual interaction region is a good representation of  $\langle a \rangle_y$  in the global domain.

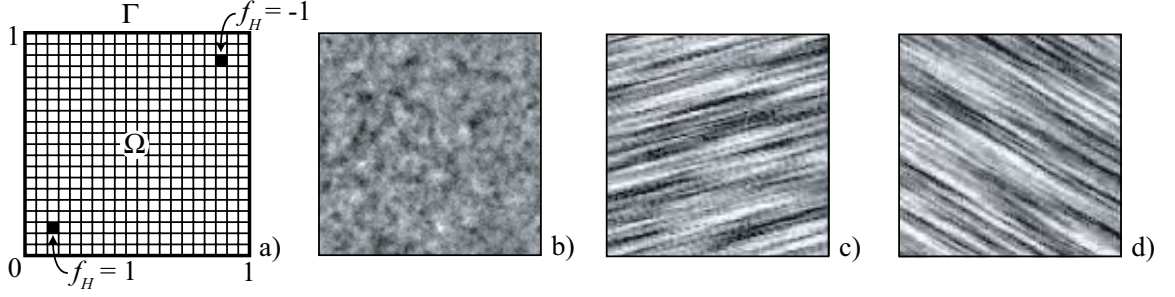


Figure 4.11: (a) The unit square domain  $\Omega$ , with a  $20 \times 20$  coarse grid. The back squares indicate coarse blocks with sources  $f_H = \pm 1$ . In these blocks the fine-scale permeability is constant at the mean to give a uniform distribution of the fine-scale flux. (b) A realization of the permeability field with small correlation length. Figures c and d show realizations of the layered permeability fields at angles of  $15^\circ$  and  $-30^\circ$  respectively. The logarithm of the permeability is shown in all cases.

## 4.7 Numerical results for heterogeneous problems

Two coarse scale operators and three local boundary conditions have been introduced above, allowing six different combinations in addition to the fine-scale solution. To distinguish the resulting combinations we denote the original operator by, MSFV, the compact operator by, CMSFV, and the reduced, linear and hybrid local boundary conditions by the post fix *-red*, *-lin*, and *-hyb*, respectively. This section focuses mostly on the comparison between MSFV-*red* that is most commonly used and CMSFV-*hyb* presented above.

In all tests a unit square domain has been used, and a diagonal pressure gradient has been imposed by introducing coarse source terms  $f_H$  in opposing corners. This is similar to the quarter five spot configuration commonly used in reservoir simulation (figure 4.11a). The fine grid has a dimension of  $100 \times 100$ , and it has been coarsened uniformly by a factor of five to produce a  $20 \times 20$  coarse grid. Two types of permeability fields were used; fields with short correlation length resulting in a patchy pattern, and fields with a short and a long correlation length resulting in a layered pattern. Twenty realizations of the patchy permeability field with a log-normal distribution, a variance of  $\log k$  of 2.0, a mean of 3.0, a dimensionless correlation length

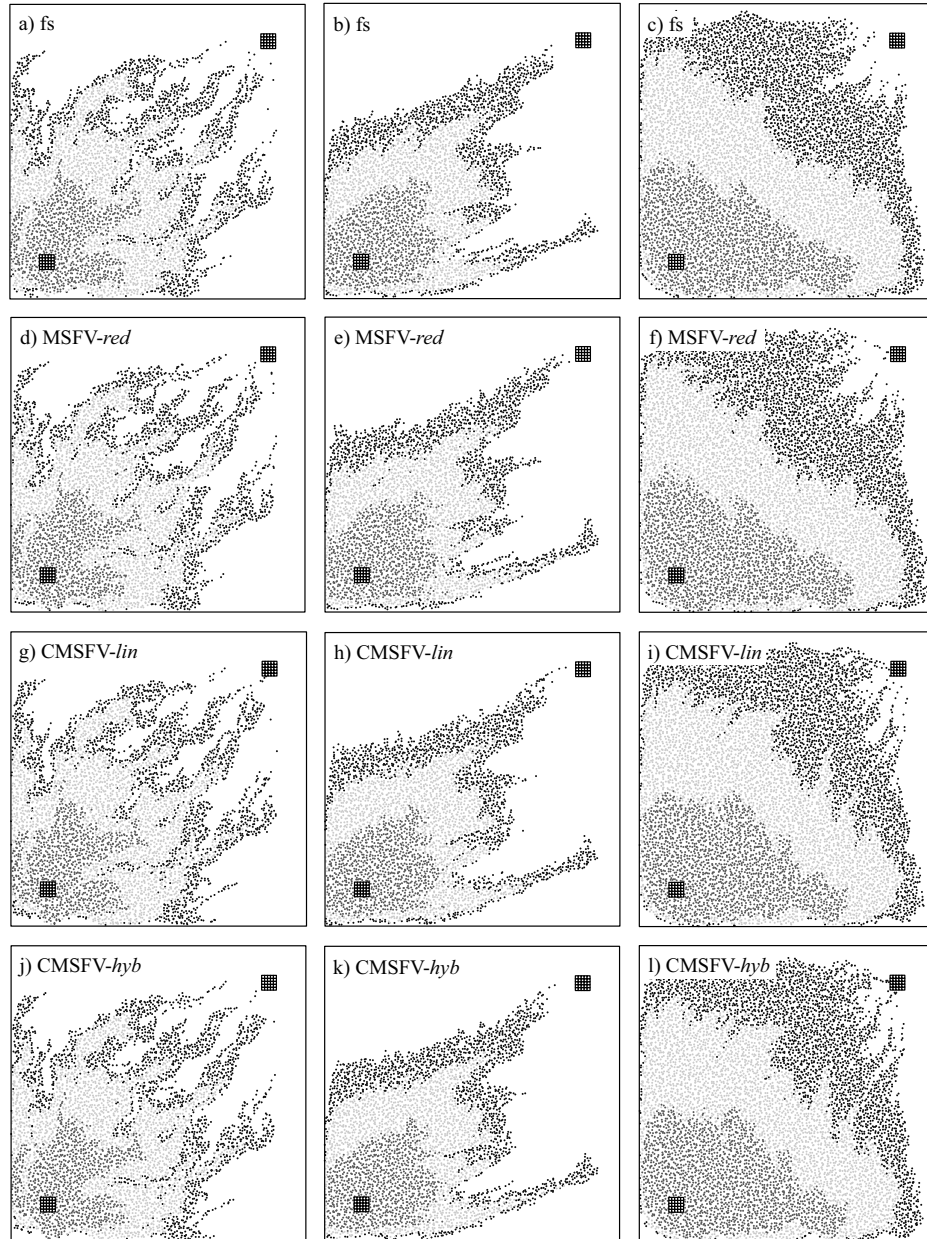


Figure 4.12: Comparison of time of flight maps between multiscale methods and the fine-scale solution for three isotropic but heterogeneous fine-scale permeability fields. All solutions are shown at the same injected volume, corresponding to the breakthrough of the fine-scale solution. The fine-scale solution,  $fs$ , is shown in the first row,  $a$  to  $c$ , the original  $MSFV-red$  method in the second row,  $d$  to  $f$ , the  $CMSFV-lin$  method in the third row,  $g$  to  $i$ , and the  $CMSFV-hyb$  method in the fourth row,  $j$  to  $l$ . The first column shows solutions for a realization of the permeability field shown in figure 4.11b, columns 2 to 3 show solutions for realizations of layered permeability fields at  $15^\circ$  and  $-30^\circ$  (figure 4.11c and d).

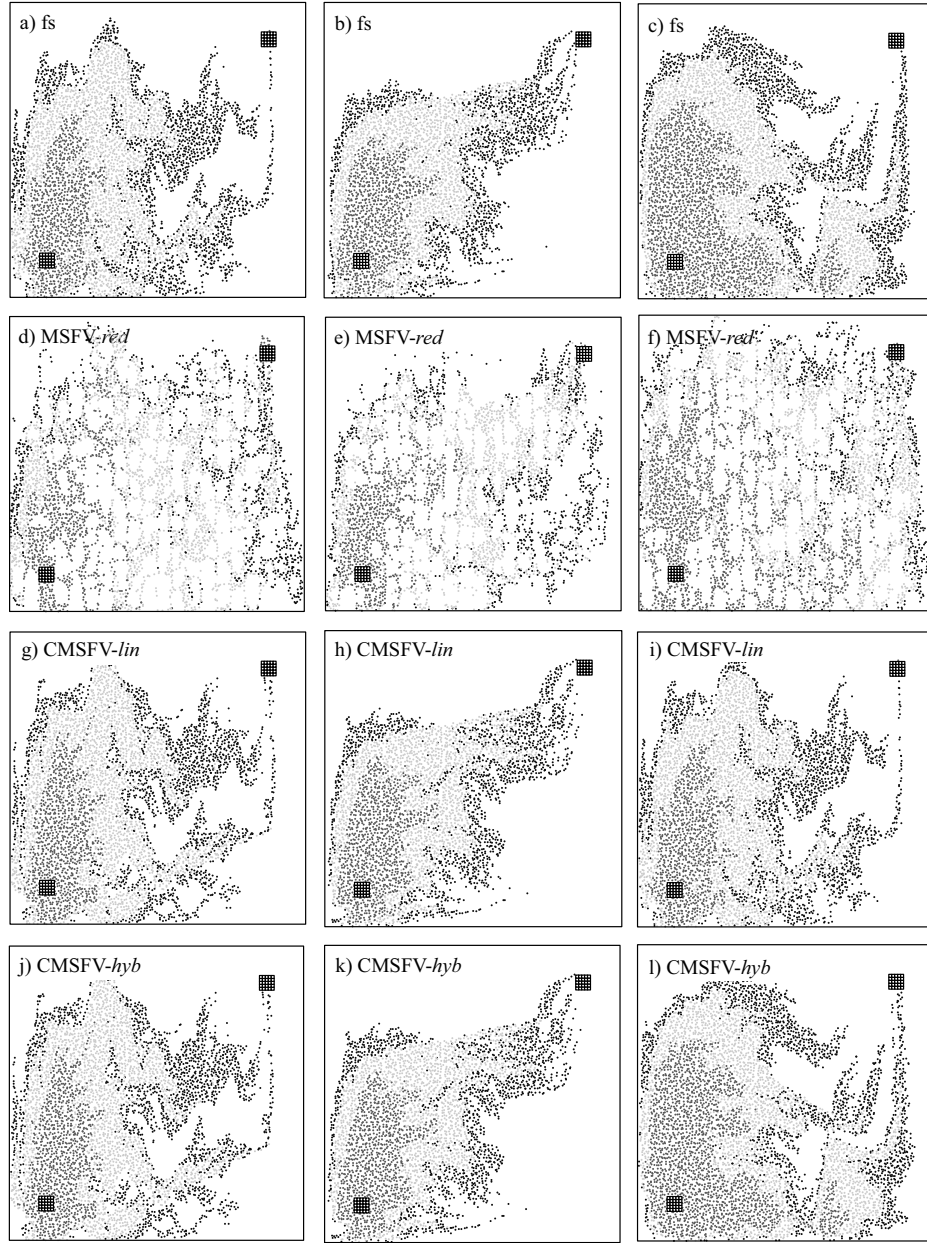


Figure 4.13: Comparison of time of flight maps between multiscale methods and the fine-scale solution for three heterogeneous fine-scale permeability fields with grid aligned fine-scale anisotropy,  $a/b = 0.01$ . All solutions are shown at the same injected volume, corresponding to the breakthrough of the fine-scale solution. The figure layout is the same as in figure 4.12.

$\lambda_1 = \lambda_2 = 0.05$ , and a spherical variogram have been generated with sequential gaussian simulation (figure 4.11*b*). Layered permeability fields with a log-normal distribution, a variance of  $\log k$  of 2.0, a mean of 3.0, a dimensionless correlation length  $\lambda_1 = 0.5$ , and  $\lambda_2 = 0.02$ , and a spherical variogram have been generated with sequential gaussian simulation (Chen *et al.*, 2007). The angle  $\theta$  between the direction of long correlation and the horizontal has been varied between  $\theta = -45^\circ$  and  $45^\circ$  in  $15^\circ$  intervals (figure 4.11*c&d*). For each angle, 20 realizations have been created and all values reported are averages and standard deviations over all realizations.

For transport in porous media a major objective of multiscale methods is to obtain accurate transport on the fine-scale. Comparing error norms of the reconstructed fine-scale pressure does not give a good indication of the quality of the fine-scale transport. Therefore, it is common to assess the quality of multiscale methods designed for transport in porous media by comparing the concentration fields of a passive tracer advected on the fine scale (Jenny *et al.*, 2003; Aarnes, 2004). To eliminate numerical diffusion introduced by advection schemes, the tracer distribution is calculated using particles.

First we consider the domain shown in figure 4.11*a* with homogeneous Neumann boundary conditions, so that the solution approaches transverse equilibrium at high anisotropy. Figure 4.12 shows the tracer particles introduced at the source in the bottom left corner. The particles are colored according to the time since they have been introduced into the domain, their *time of flight* (TOF). For isotropic fine-scale permeability fields both the MSFV-*red* method and the CMSFV-*hyb* method are able to reproduce the fine-scale structure in the tracer field. In these cases where the MSFV-*red* method performs well the quality of the CMSFV-*hyb* solution is comparable to the MSFV-*red* solution.

Figure 4.13 shows the tracer maps for the same permeability fields that are shown in figure 4.12, but with uniform, grid aligned, fine-scale anisotropy of  $a/b = 0.01$ , corresponding to an orthogonal grid with aspect ratio 1 : 10. The MSFV-*red* solution shows unphysical recirculation cells. The CMSFV-*hyb* solution shows no such recirculation cells, has a monotonic coarse scale solution, and recovers the fine-scale

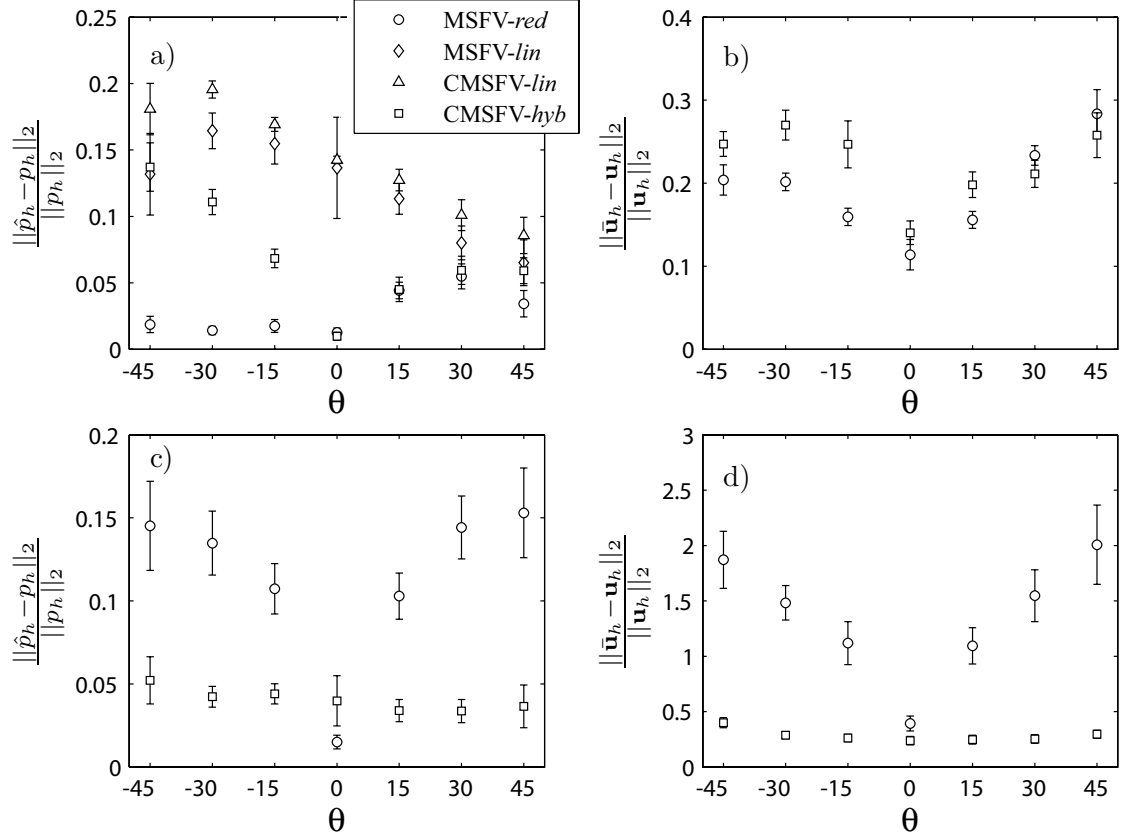


Figure 4.14: Figures *a* and *b* show the mean  $L_2$ -errors of the interpolated solution  $\hat{p}_h$  and the reconstructed flux field  $\bar{\mathbf{u}}_h = -k\nabla\bar{p}_h$  as function of the orientation,  $\theta$ , of the fine-scale layering for isotropic fine-scale permeability,  $a/b = 1$ . Figures *c* and *d* show the same for grid aligned fine-scale anisotropy  $a/b = 0.04$  ( $\Delta x/\Delta y = 5$ ). All values shown are means over 20 realizations and the standard deviations are shown as vertical bars, if they are larger than the symbols.

detail of the tracer distribution. In the presence of fine-scale anisotropy the CMSFV-*hyb* solution is a good approximation to the fine-scale solution, while the MSFV-*red* solution has large errors and unphysical behavior.

The linear boundary conditions give comparable results for isotropic problems, but lose accuracy as the aspect ratio increases. For flow across layers the errors are largest (figure 4.13*i*), as expected from the discussion in §4.6.2.

Error norms for the pressure and the reconstructed flux obtained by both methods are shown in figure 4.14. The interpolated pressure  $\hat{p}_h$  is proportional to the error in the coarse solution, while the reconstructed, fine-scale flux  $\bar{\mathbf{u}}_h$  is proportional to the error in the reconstructed pressure  $\bar{p}_h$ . Figure 4.14*a* shows that linear boundary conditions lead to larger errors than reduced or hybrid boundary conditions for both coarse operators. For clarity, the results for linear boundary conditions are omitted from the other graphs. Figures 4.14*a* and *b* show that for isotropic fine-scale permeability fields the errors in the MSFV-*red* and the CMSFV-*hyb* solutions are of the same order of magnitude for flow along layers ( $0^\circ < \theta < 45^\circ$ ). For flow across layers ( $-45^\circ < \theta < 0^\circ$ ) the error in the MSFV-*red* solution is significantly smaller, because the reduced boundary condition is optimal for this special case. However, for any significant anisotropy on the fine-scale the CMSFV-*hyb* solution becomes more accurate than the MSFV-*red* for all angles (figure 4.14*c* and *d*).

Figures 4.15*a* and *b* show that for both the MSFV-*red* and the CMSFV-*red* solutions the errors in the flux,  $\bar{\mathbf{u}}_h$ , grow exponentially with increasing fine-scale anisotropy, while the errors for both the MSFV-*hyb* and the CMSFV-*hyb* remain bounded. Therefore, in problems where the fine solution approaches transverse equilibrium, the hybrid local boundary condition rather than the compact operator lead to a monotone multiscale solution.

Consider the domain shown in figure 4.11*a* with homogeneous Dirichlet boundary conditions, so that the solution cannot approach transverse equilibrium with increasing anisotropy. Figure 4.16 shows that both the MSFV-*lin* and the MSFV-*hyb* solution have lost monotonicity and the streamlines show unphysical recirculation cells. The CMSFV-*hyb* solution has remained monotone and captures the fine-scale transport. Similar behavior has been observed in §4.3.1 for homogeneous problems,

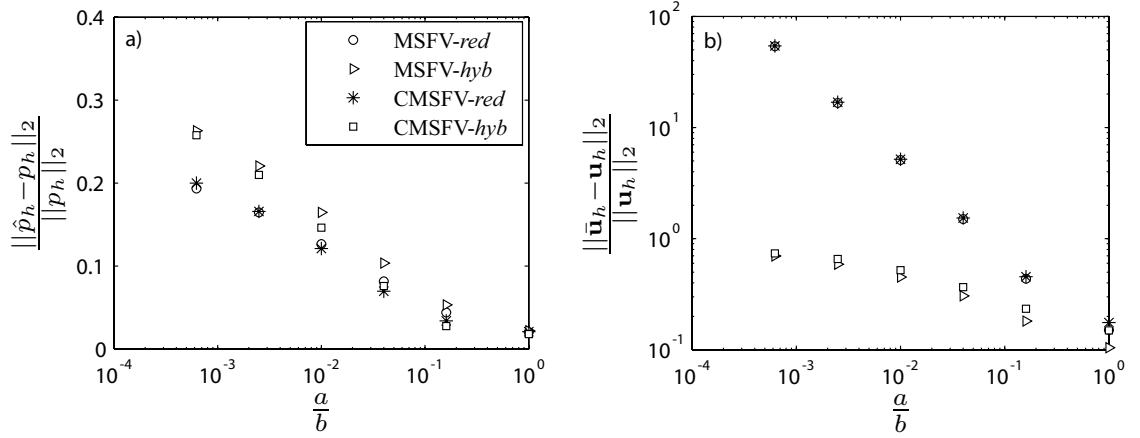


Figure 4.15: Figures *a* and *b* show the mean  $L_2$ -errors of the interpolated solution  $\hat{p}_h$  and the reconstructed flux field as function of increasing fine-scale anisotropy  $a/b$ . All values shown are means over 20 realizations of the permeability field shown in figure 4.11a.

where all local boundary conditions become linear. Therefore, the compact operator is necessary to obtain a monotone solution for strongly constrained pressure fields. A similar situation is shown in figure 4.4c where a local maximum occurs in the coarse solution computed by the MSFV-*red* method even for an isotropic problem with Dirichlet constraints on only two boundaries. The compact operator gives a monotone coarse solution in this case, demonstrating that it improves the monotonicity even for isotropic problems with few constraints. Such situations arise commonly in reservoir engineering in areas with horizontal wells that constrain the pressure over many gridblocks.

In cases with or without transverse equilibrium the compact operator leads to a linear system,  $\mathbf{L}_H$ , much closer to an  $M$ -matrix. A simple measure  $M(\mathbf{L}_H)_i$  given by the ratio of the largest and smallest off-diagonal entries,

$$M(L_{H_{i,j}})_i = -\frac{\max((L_{H_{i,j \neq i}}))}{\min((L_{H_{i,j \neq i}}))}, \quad (4.65)$$

is introduced to quantify the magnitude of the violation of the  $M$ -matrix condition



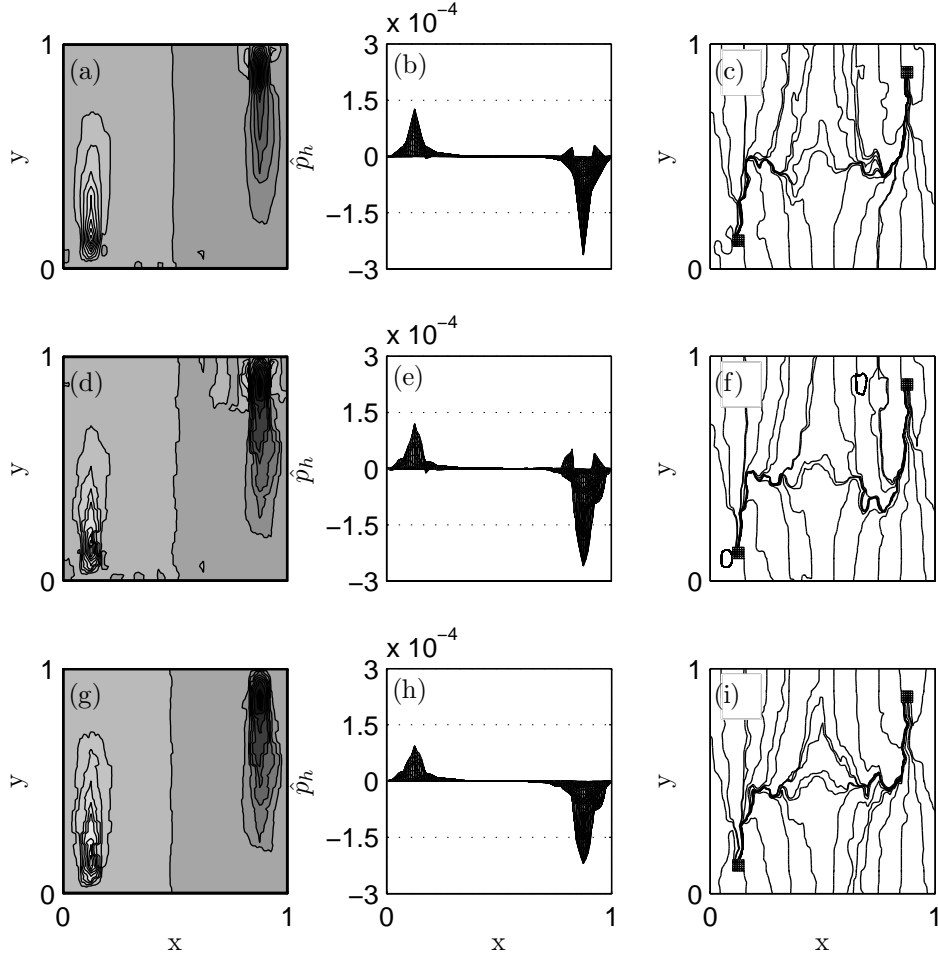


Figure 4.16: Results for the quarter 5-spot shown in figure 4.11a with homogeneous Dirichlet boundary conditions. The first column shows contour maps of  $\hat{p}_h$ , the second column shows a horizontal view of  $\hat{p}_h$  along the  $y$ -axis, and the third column shows streamlines obtained from the conservative reconstruction  $\bar{p}_h$ . Figures *a* to *c* show the results for MSFV-*lin*, figures *d* to *f* show results for MSFV-*hyb*, and figures *g* to *i* show results for CMSFV-*hyb*.

in the  $i$ -th row of the system matrix  $\mathbf{L}_H$ . If  $M(\mathbf{L}_H)_i$  is non-positive, then the  $i$ -th row of  $\mathbf{L}_H$  satisfies the  $M$ -matrix condition. As the magnitude of  $M(\mathbf{L}_H)_i$  increases the violation of the  $M$ -matrix condition becomes stronger. The norm  $\|M(\mathbf{L}_H)\|$  allows us to quantify the quality of the coarse linear system resulting from a multiscale discretization.

For heterogeneous problems  $\mathbf{L}_H$  does generally not satisfy the  $M$ -matrix property, for any choice of operator and local boundary conditions, but the compact operator always gives a system much closer to an  $M$ -matrix. The violations of the  $M$ -matrix property are larger in magnitude (figure 4.17a and c) and much more common (figure 4.17b and d) in the coarse linear system arising from the original coarse operator. For isotropic fine-scale permeability fields the dependence of  $\|M(\mathbf{L}_H)\|$  on the orientation of the layering, shown in figures 4.14a&b, is analogous to the homogeneous analysis in §4.4. For the original operator the violation of the  $M$ -matrix property is largest for grid aligned layering and smallest for layering oriented at  $45^\circ$ , corresponding to the region of monotonicity shown in figure 4.7a, which is most limited for anisotropy at  $0^\circ$  and unlimited for anisotropy at  $45^\circ$  to the grid. The compact operator on the other hand produces linear systems with a maximum in  $\|M(\mathbf{L}_H)\|$  for layering oriented between  $15^\circ$  and  $30^\circ$ , corresponding to the region of monotonicity shown in figure 4.7b, which is unlimited for anisotropy at  $0^\circ$  and  $45^\circ$ . The improvement in the quality of  $\mathbf{L}_H$  relative to the original operator is largest for layering that is aligned, or close to aligned, with the grid. Comparing the first and second row of figure 4.17, we see that the violations of the  $M$ -matrix criterion produced by the MSFV operator increase rapidly with increasing fine-scale anisotropy,  $a/b \rightarrow 0$ , while the CMSFV-*hyb* remains close to a  $M$ -matrix.

## 4.8 Discussion

In the formulation presented in §4.2 the MSFV method is defined by the properties of the transmissibility matrix,  $\mathbf{T}^*$ . The integrated form of  $\mathbf{T}^*$  directly defines the coarse operator through (4.16) to (4.23) and the reconstruction of the conservative fine-scale velocity is defined by  $\mathbf{T}^*$  through (4.32). The properties of  $\mathbf{T}^*$  are therefore

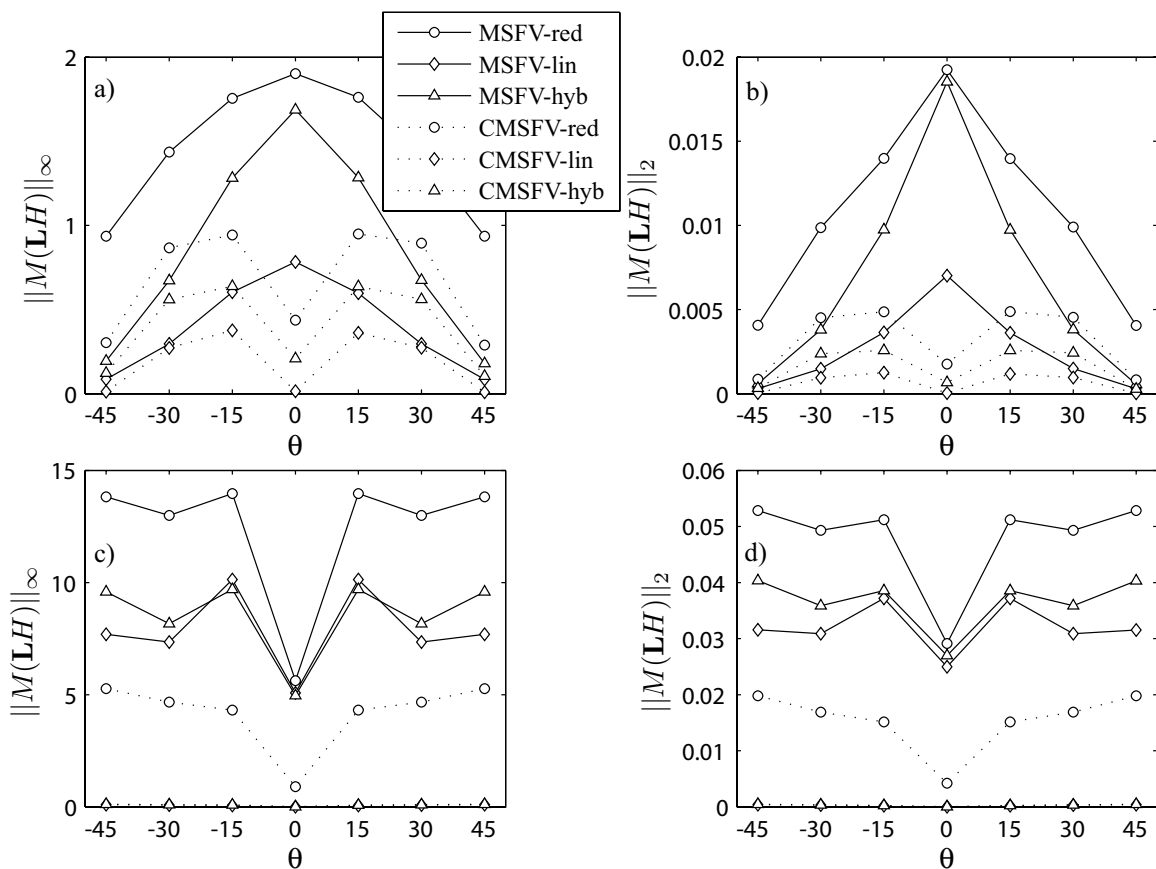


Figure 4.17: The  $L_\infty$  and  $L_2$ -norms of  $M(\mathbf{L}_H)$  are shown as a function of the angle of the layering. Figures *a* and *b* show results for a isotropic fine-scale permeability field ( $a/b = 1$ ), while figures *c* and *d* are for a fine-scale anisotropy  $a/b = 1/100$ .

the starting point for the analysis of MSFV formulations and  $\mathbf{T}^*$  provides a direct link to MPFA methods. This link has made it possible to take advantage of the existing analysis of MPFA methods and to formulate the compact coarse operator for the MSFV method. The construction of many other coarse operators is possible in this framework, and as long as the modification is done at the level of  $\mathbf{T}^*$ , the resulting MSFV method will be: 1) conservative on the coarse level; 2) the fine scale reconstruction of the fluxes will be locally conservative; 3) the fine-scale fluxes will be consistent with the coarse fluxes.

The CMSFV method described here has been designed to give a coarse operator with optimal monotonicity, but other design criteria, e.g. rotational invariance of the discretization, may lead to other preferred coarse operators. The formulation given here provides a consistent framework for the design of coarse operators by modifying  $\mathbf{T}^*$ . In a parallel Aavatsmark *et al.* (2008) have developed a compact MPFA method with improved monotonicity for non-orthogonal quadrilateral grids with piecewise constant, full-tensor permeability fields.

Our framework emphasizes that local elliptic solutions determine the numerical entries of  $\mathbf{T}^*$ , rather than their role as basis functions used for the interpolation of the coarse solution. The concept of the basis function has been important in the development of the MSFV method, but the formation of the coarse operator and the fine-scale reconstruction of the conservative velocity field do not require explicit basis functions. In the framework presented here coarse operators, which are not naturally associated with a set of basis functions, can be considered, e.g. the compact operator. In these cases the interpolation of the coarse solution with the standard basis functions still gives a good approximation of the fine-scale solution, but the corresponding fine fluxes are not consistent with the coarse fluxes. This is generally not a problem since the fluxes derived from the interpolated solution are not used for transport.

The original bilinear basis functions require Dirichlet boundary conditions, which are too restrictive for many anisotropic problems. Once the local elliptic problems are not interpreted as basis functions, a larger range of local problems and local boundary conditions can be considered. This allows the design of local problems that take advantage of simplifications in the fine-scale solution, such as the linear

flow problems with hybrid boundary conditions that are designed to capture TVE. Lunati & Jenny (2007) modify the boundary condition for the flux reconstruction,  $\tilde{L}_h^\Gamma$ , to eliminate recirculation cells in the velocity field. Here we modify the boundary condition of the local elliptic problems,  $\bar{L}_h^\Gamma$ , and hence the coarse operator to achieve a monotone coarse pressure, which eliminates the unphysical recirculation cells.

The CMSFV-*hyb* method introduced here is only based on local information, because local methods are computationally efficient. It has been shown that the accuracy of purely local methods may be low if the permeability field has structures with very long correlation lengths. Several authors have suggested the incorporation of global data to increase accuracy at increased cost (Chen & Durlofsky, 2006; Efendiev *et al.*, 2006; Durlofsky *et al.*, 2007). The coarse operator introduced here may also increase the robustness of these applications.

Most recent studies of multiscale methods for flow in porous media have been restricted either to tracer flow or to immiscible two phase flow (Chen & Hou, 2002; Jenny *et al.*, 2003, 2005; Aarnes, 2004; Juanes & Dub, 2008). In these problems only the flux field is necessary for the solution of the transport problem, while the quality of the solution itself - the pressure field - is not important. In many applications, such as the three-phase black-oil formulation recently presented by Lee *et al.* (2008), mass transfer between phases is an important physical mechanism. In particular strongly non-linear phenomena such as phase appearance and disappearance are a strong function of the pressure. For these applications the increased robustness of the CMSFV-*hyb* method for the pressure equation will increase the stability of the coupled problem. In these cases the pressure interpolation,  $\hat{p}_h$ , may be more appropriate for the evaluation of the phase properties.

In the general heterogeneous anisotropic case neither coarse operator leads to a linear system where  $\mathbf{L}_H$  is an M-matrix. However, compared to the original coarse operator the compact operator leads to a  $\mathbf{L}_H$  with fewer positive off-diagonal entries and these entries have a smaller magnitude. The performance of algebraic multigrid solvers will not deteriorate seriously, unless the off-diagonal entries are substantial (Ruge & Stüben, 1987). Therefore, we expect that the CMSFV method will avoid problems with the performance of the linear solver.

## 4.9 Conclusion

The construction of the MSFV coarse operator is identical to the construction of a certain type of MPFA methods. The MSFV method is a natural extension of these MPFA methods to numerical evaluation of the transmissibility matrix. Therefore, the rich literature on the analysis of MPFA methods is directly relevant to the design and analysis of MSFV methods.

The original MSFV coarse operator has a limited region of monotonicity for aligned anisotropy. This leads to loss of monotonicity of the coarse pressure in problems with Dirichlet boundary conditions with increasing anisotropy.

A compact coarse operator for the MSFV method that reduces to a 7-point stencil in the homogeneous case has been introduced. This compact operator has the largest possible monotonicity region. In particular it is always monotone for grid aligned anisotropy in homogeneous problems. In heterogeneous problems the compact operator leads to coarse linear systems that are close to a  $M$ -matrix. The compact operator eliminates oscillations in anisotropic problems with Dirichlet boundary conditions.

For anisotropic problems with homogeneous Neumann boundary conditions the fine-scale solution approaches transverse equilibrium as the anisotropy increases. To obtain a monotone, accurate, multiscale solution the local boundary conditions must be able to reach transverse equilibrium as well. A hybrid boundary condition has been introduced that naturally allows transverse equilibrium and gives accurate solutions for anisotropic problems.

The compact coarse operator in combination with the hybrid boundary condition is the most robust multiscale finite volume formulation for large anisotropy and similar in accuracy to the original MSFV method for isotropic problems.

# Chapter 5

## Conclusions

Saline aquifer storage of  $\text{CO}_2$  has the potential to reduce the emissions from fossil energy significantly. The leakage of  $\text{CO}_2$  from the storage aquifer back into the atmosphere is a main concern in developing this technology. Carbon dioxide can leak from the geological storage formation back into the atmosphere, because it is mobile and buoyant relative to the resident brine. Therefore, any process that immobilizes the injected  $\text{CO}_2$ , makes it negatively buoyant, or both, is considered a trapping mechanism. The competition between leakage and trapping processes will determine what fraction of the injected  $\text{CO}_2$  will remain in the subsurface permanently. While mineral trapping offers permanent storage, leakage is unlikely after the  $\text{CO}_2$  has dissolved into the brine or has become disconnected at the pore-scale, as a residual saturation. Consequently dissolution and residual trapping determine the length of the active storage period, during which leakage is possible.

### 5.1 Results

We studied dissolution and residual trapping using two different approaches. In order to resolve the small length and time scales associated with buoyancy driven miscible convection, we employed an innovative linear stability analysis in self-similar coordinates, and we performed high accuracy nonlinear simulations to study the nonlinear evolution of the instability.

To study the migration and residual trapping of immiscible CO<sub>2</sub> plumes in the post-injection period, we employed vertical-equilibrium sharp-interface models, in which the dimensionality of the problem is reduced in favor of the ability to focus on the first-order behavior of the gravity current.

The dominant physical and chemical processes during CO<sub>2</sub> storage in saline aquifers change with time, and natural geologic formations are strongly heterogeneous. Predictions of the flow and transport behaviors for a particular storage site must account for the presence of heterogeneity and be able to model the wide range of length and time scales associated with the physical and chemical processes. To make numerical modeling of such systems possible, we extend the multiscale finite volume (MSFV) method to highly anisotropic problems. This will allow the robust numerical modeling of CO<sub>2</sub> storage in saline aquifers that commonly have large aspect ratios.

### 5.1.1 Dissolution trapping & convection

Dissolution is the dominant trapping process, if the CO<sub>2</sub> has ponded in a structural trap. Dissolution trapping will be effective, if the increased density of the saturated brine induces convective currents. The permeability,  $k$ , of a formation is the most important physical parameter controlling convective dissolution. Linear stability theory has shown that the critical time for the onset of the convective motion is proportional to  $1/k^2$  and the associated critical wavelength is proportional to  $1/k$ . Direct numerical simulations confirm the predictions of the linear theory at early times, and we use them to study the nonlinear evolution of the dissolution rate of CO<sub>2</sub> after the onset of convection. In very large aquifers, the long-term dissolution rate is essentially constant over time, independent of the  $Ra$  number, and proportional to the permeability. In closed aquifers, the dissolution rate evolves in a manner similar to open aquifers until the plumes of dissolved CO<sub>2</sub> reach the base of the aquifer. Once these plumes interact with the base of the aquifer the dissolution rate decays very rapidly.

We conclude that dissolution trapping is favored in large high-permeability aquifers, because the onset of convection is early, the dissolution rate is high, and it remains



nearly constant for long times.

### 5.1.2 Residual trapping & gravity currents

In situations where the buoyant supercritical  $\text{CO}_2$  migrates as a gravity current along the top of the aquifer, residual saturation forms continuously in its wake. In this case, residual trapping is likely to be the dominant trapping process. The effectiveness of residual trapping is determined by the magnitude of the residual saturation and the sweep efficiency of the  $\text{CO}_2$  plume. We have studied the interplay between the vertical sweep of the  $\text{CO}_2$  plume and residual trapping analytically, using models of gravity currents that assume vertical equilibrium and a sharp interface. We have identified the mobility ratio between the  $\text{CO}_2$  and the brine as a key physical parameter governing the spreading of the current and the sweep during the migration. In sloping aquifers, the volume of the mobile  $\text{CO}_2$  plume is reduced to zero in finite time, while it decays as a power-law in horizontal aquifers. Residual trapping is more efficient in sloping aquifers, because the  $\text{CO}_2$  plume migrates along-slope at constant speed, while the speed of migration decays in horizontal aquifers. For sloping aquifers, we obtain semi-analytic estimates of the migration distance of the  $\text{CO}_2$  plume and the duration of the active storage period.

Our results show that the poor vertical sweep of the  $\text{CO}_2$  plume gives rise to long migration distances that may limit the storage capacity of saline aquifers. Increasing the slope of the aquifer leads to faster residual trapping, without increasing the maximum migration distance of the  $\text{CO}_2$  plume significantly. However, for any given injection depth, the along-slope distance to the surface decreases rapidly with increasing dip of the aquifer. Leakage of  $\text{CO}_2$  at an outcrop of the aquifer will occur, if the maximum migration distance of the  $\text{CO}_2$  plume exceeds the available along-slope distance between the injection site and the outcrop. To reduce the duration of the active storage period, potential storage aquifers should have enough dip to induce lateral migration of the  $\text{CO}_2$  plume. However, the reduced along-slope distance to the outcrop for large dip angles limits the volume of  $\text{CO}_2$  that can be stored. Therefore, high-permeability, gently-dipping, and deep saline aquifers are optimal targets

for CO<sub>2</sub> storage, because they have relatively short active storage periods and large storage capacities.

### 5.1.3 Multiscale methods for porous media

We developed a robust compact multiscale finite volume (CMSFV) method for heterogeneous anisotropic elliptic equations, which describe the flow (pressure) field in porous media. The original multiscale finite volume (MSFV) method loses monotonicity in the presence of moderate grid aligned anisotropy or equivalently for stretched grids. By comparison with multipoint flux approximations, we show that the coarse operator of the original MSFV method has a limited region of monotonicity, and we introduce a new compact coarse operator with an optimal stability region. We also show that the construction of the boundary conditions of the local elliptic problems must allow for transverse equilibrium to increase the monotonicity of the coarse operator in heterogeneous problems.

We introduced new local elliptic problems with hybrid boundary conditions that allow for transverse equilibrium and lead to a robust multiscale discretization in the presence of strong heterogeneity. This compact discretization will allow the application of the (C)MSFV method to CO<sub>2</sub> storage in strongly heterogeneous and anisotropic saline aquifers with large aspect ratios.

## 5.2 Future work

Here we briefly outline some of the research directions that follow directly from the work presented in this thesis.

**Convective dissolution** The direct numerical simulations should be extended to three-dimensions and the inclusion of permeability heterogeneity in order to obtain, more realistic estimates of the long-term dissolution rate. These results will allow simple estimates of the time necessary to dissolve a volume of CO<sub>2</sub> through a given interfacial area, an important quantity currently not available.

**Gravity currents** The most interesting continuation of the work presented in § 3 is the extension of the model to include the effects of  $\text{CO}_2$  dissolution into the brine. The resulting relatively simple model would capture some of the main aspects of residual and dissolution trapping and allow a comparison between trapping mechanisms. If a simple model of leakage is included, the competition between leakage and trapping processes can be investigated. Such a model may allow the computation of semi-analytic versions of figure 1.3, which show the contribution of each trapping process. The three scenarios shown in figure 1.4 are likely to produce qualitatively different features in figure 1.3, which may form the basis of a classification of storage sites.

**Multiscale simulation of  $\text{CO}_2$  storage** The MSFV method has been extended to include all the necessary physics: gravity and capillary forces, compressibility, wells, and three-phase problems. We have extended it to problems with severe anisotropy, expected in regional aquifers. Adaptivity criteria have been developed for the pressure solver as well as for the solution of the transport equation promising large speed-up compared to conventional simulations. We therefore plan to demonstrate the application of the MSFV method to saline aquifer storage in the near future.

## Bibliography

- AARNES, J. E. 2004 On the use of a mixed multiscale finite element method for greater flexibility and increased speed or improved accuracy in reservoir simulation. *Multiscale Model. Simul.* **2** (3), 421–439.
- AAVATSMARK, I. 2002 An introduction to multipoint flux approximations for quadrilateral grids. *Comput. Geosci.* **6**, 405–432.
- AAVATSMARK, I., BARKVE, T., BØE, Ø. & MANNSETH, T. 1996 Discretization on non-orthogonal, quadrilateral grids for inhomogeneous, anisotropic media. *J. Comput. Phys.* **127**, 2–14.
- AAVATSMARK, I., EIGESTAD, G. T., MALLISON, B. T. & NORDBOTEN, J. M. 2008 A compact multipoint flux approximation method with improved robustness. *Numer. Meth. for Part. Diff. Eqns.*, DOI 10.1002/num.20320 (In Press) .
- ABDULLE, A. & E, W. 2003 Finite difference heterogeneous multi-scale method for homogenization problems. *J. Comput. Phys.* **191** (1), 18–39.
- ADAMS, J. J. & BACHU, S. 2002 Equations of state for basin geofluids: algorithm review and intercomparison for brines. *Geofluids* **2**, 257271.
- ARBOGAST, T. 2002 Implementation of a locally conservative numerical subgrid upscaling scheme for two-phase darcy flow. *Comput. Geosci.* **6** (3-4), 453481.
- ARONSON, D. G. 1985 *The Porous Medium Equation, Lecture Notes in Mathematics*, vol. 1224. Springer-Verlag.
- BACHU, S. 2003 Screening and ranking of sedimentary basins for sequestration of CO<sub>2</sub> in geological media in response to climate change. *Environmental Geology* **44**, 277–289.
- BACHU, S. & ADAMS, J. J. 2003 Sequestration of CO<sub>2</sub> in geological media in response to climate change: capacity of deep saline aquifers to sequester CO<sub>2</sub> in solution. *Energy Convers. Manage.* **44**, 31513175.

- BACHU, S. & BENNION, B. 2007 Effects of in-situ conditions on relative permeability characteristics of CO<sub>2</sub>-brine systems. *Environ. Geol.* (doi 10.1007/s00254-007-0946-9).
- BACHU, S. & STEWART, S. 2002 Geological sequestration of anthropogenic carbon dioxide in the western canada sedimentary basin: Suitability analysis. *Can. J. Petrol. Tech.* **41** (2), 32–40.
- BARENBLATT, G. I. 1952 On some unsteady motions of fluids and gases in a porous medium. *Appl. Math. Mech.-Engl. (PMM)* **16**, 67–78.
- BARENBLATT, G. I. 1996 *Scaling, self-similarity, and intermediate asymptotics*. Cambridge University Press.
- BARENBLATT, G. I. & ZELDOVICH, YA. B. 1972 Self-similar solutions as intermediate asymptotics. *Annual Reviews in Fluid Mechanics* **4**, 285–312.
- BEAR, J. 1972 *Dynamics of Fluids in Porous Media*. American Elsevier Pub. Co.
- BEAR, J. & RYZHIK, V. 1998 On displacement of NAPL lenses and plumes in a phreatic aquifer. *Transport Porous Med.* **33**, 227–255.
- BEN, Y., DEMEKHIN, E. A. & CHANG, H.-C. 2002 A spectral theory for small-amplitude miscible fingering. *Phys. Fluids* **14** (3), 999.
- BENSON, S. M., TOMUTSA, L., SILIN, D. & KNEAFSEY, T. 2006 Core scale and pore scale studies of carbon dioxide migration in saline formations. In *Proceedings GHGT-8*. Trondheim, Norway.
- BICKLE, M., CHADWICK, A., HUPPERT, H. E., HALLWORTH, M. & LYLE, S. 2007 Modelling carbon dioxide accumulation at Sleipner: Implications for underground carbon storage. *Earth Planet. Sc. Lett.* **255**, 164–176.
- BONDOR, P. L. 1992 Applications of carbon dioxide in enhanced oil recovery. *Energy Convers. Manage.* **33** (5-8), 579–586.

- BUNSE, W. & BUNSE-GERSTNER, A. 1985 *Numerische lineare algebra*. Stuttgart: Teubner.
- VAN DER BURGT, M. J., CANTLE, J. & BOUTKAN, V. K. 1992 Carbon dioxide disposal from coal-based IGCC's in depleted gas fields. *Energy Convers. Manage.* **33** (5-8), 603–610.
- CALTAGIRONE, JEAN-PAUL 1980 Stability of a saturated porous layer subject to a sudden rise in surface temperature: comparison between linear and energy methods. *Q. J. Mech. Appl. Math.* **33**, 47–58.
- CAMHI, E., RUITH, M. & MEIBURG, E. 2000 Miscible rectilinear displacements with gravity override. Part 2. Heterogeneous porous media. *J. Fluid Mech.* **420**, 259.
- CHANG, H.-C., DEMEKHIN, E. A. & KAL Aidin, E. 1998 Generation and suppression of radiation by solitary pulses. *SIAM J. App. Math.* **58**, 1246.
- CHEN, Y. & DURLOFSKY, L. J. 2006 Efficient incorporation of global effects in up-scaled models of two-phase flow and transport in heterogeneous formations. *SIAM Multiscale Model. Simul.* **5**, 445–475.
- CHEN, Y., MALLISON, B. T. & DURLOFSKY, L. J. 2007 Nonlinear two-point flux approximations for modelling full-tensor effects in subsurface flow simulations. *Comput. Geosci., Special Issue on Multiscale Methods for Flow and Transport in Heterogeneous Porous Media*, DOI 10.1007/s10596-007-9067-5 (In Press) .
- CHEN, Z. & HOU, T. Y. 2002 A mixed multiscale finite element method for elliptic problems with oscillating coefficients. *Math. Comp.* **72** (242), 541–576.
- COATS, K. H., DEMPSEY, J. R. & HENDERSON, J. H. 1971 The use of vertical equilibrium in two-dimensional simulation of three-dimensional reservoir performance. *Soc. Petrol. Eng. J.* **251** (March), 63–71.

- DIERSCH, H. J. G. & KOLDITZ, O. 2002 Variable-density flow and transport in porous media: approaches and challenges. *Advances in Water Resources* **25**, 899–944.
- DIETZ, D. N. 1953 A theoretical approach to the problem of encroaching and by-passing edge water. *Akad. van Wetenschappen, Proc.* **V.56 B**, 83–92.
- DOUGHTY, C., FREIFELD, B. M. & TRAUTZ, R. C. 2007 Site characterization for CO<sub>2</sub> geologic storage and vice versa: the Frio brine pilot, Texas, USA as a case study. *Environ. Geol.* (doi 10.1007/s00254-007-0946-9).
- DRAZIN, P. G. & REID, W. H. 1981 *Hydrodynamic Stability*. Cambridge University Press.
- DURLOFSKY, L. J. 1991 Numerical calculation of equivalent grid block permeability tensors for heterogeneous media. *Water Resour. Res.* **27**, 699–708.
- DURLOFSKY, L. J., EFENDIEV, Y. & GINTING, V. 2007 An adaptive local-global multiscale finite volume element method for two-phase flow. *Adv. Water Resour.* **30**, 576–588.
- EBIGBO, A., CLASS, H. & HELMIG, R. 2006 CO<sub>2</sub> leakage through an abandoned well: problem-oriented benchmarks. *Computat. Geosci.* **11** (2), 103–115.
- EDWARDS, M. G. & ROGERS, C. F. 1998 Finite volume discretization with imposed flux continuity for the general tensor pressure equation. *Comput. Geosci.* **2**, 259–290.
- EFENDIEV, Y., GINTING, V., HOU, T. & EWING, R. 2006 Accurate multiscale finite element methods for two-phase flow simulations. *J. Comput. Phys.* **220**, 155174.
- ELDER, J. W. 1967 Transient convection in a porous medium. *J. Fluid Mech.* **27**, 609–623.
- ELDER, J. W. 1968 The unstable thermal interface. *J. Fluid Mech.* **32**, 69–96.

- ENNIS-KING, J. & PATERSON, L. 2002 Engineering aspects of geological sequestration of carbon dioxide. In *Asia Pacific Oil and Gas Conference and Exhibition*. Melbourne, Australia.
- ENNIS-KING, J. & PATERSON, L. 2003 Role of convective mixing in the long-term storage of carbon dioxide in deep saline formations. *SPE 84344* pp. 1–12.
- ENNIS-KING, J., PRESTON, I. & PATERSON, L. 2005 Onset of convection in anisotropic porous media subject to a rapid change in boundary conditions. *Phys. Fluids* **17** (8).
- FAYERS, F. J. & MUGGERIDGE, A. H. 1990 Extensions to Dietz theory and behavior of gravity tongues in slightly tilted reservoirs. *Soc. Petrol. Eng. Res. Eng.* **5**, 487–494.
- FOSTER, T. 1965 Stability of a homogeneous fluid cooled uniformly from above. *Phys. Fluids* **8**, 1249–1257.
- FOSTER, T. 1968 Effect of boundary conditions on the onset of convection. *Phys. Fluids* **11**, 1257–1262.
- GASDA, S. E., BACHU, S. & CELIA, M. A. 2004 Spatial characterization of the location of potentially leaky wells penetrating a deep saline aquifer in a mature sedimentary basin. *Environ. Geol.* **46** (6-7), 707–720.
- GAUTIER, Y., BLUNT, M. J. & CHRISTIE, M. A. 1999 Nested gridding and streamline-based simulation for fast reservoir performance prediction. *Comput. Geosci.* **3** (3-4), 295–320.
- GOUNOT, J. & CALTAGIRONE, JEAN-PAUL 1989 Stabilité et convection naturelle au sein d'une couche poreuse non homogène. *International Journal of Heat and Mass Transfer* **32**, 1131–1140.
- GREEN, L. L. & FOSTER, T. 1975 Secondary convection in a Hele Shaw cell. *J. Fluid Mech.* **71**, 675–687.



- GRESHO, P. M. & SANI, R. L. 1971 The stability of a fluid layer subjected to a step change in temperature: Transient vs. frozen time analysis. *Int. J. Heat Mass Transfer* **14**, 207.
- GUNTER, W. D., WIWCHAR, B. & PERKINS, E. H. 1997 Aquifer disposal of CO<sub>2</sub>-rich greenhouse gases: extension of the time scale of experiment for CO<sub>2</sub>-sequestering reactions by geochemical modelling. *Miner Petrol* **59**, 121–140.
- HENRY, H. R. 1959 Salt intrusion into fresh-water aquifers. *J. Geophys. Res.* **64**, 1911–1919.
- HESSE, M. A., TCHELEPI, H. A. & F. M. ORR JR. 2006 Scaling analysis of the migration of CO<sub>2</sub> in saline aquifers. In *SPE Annual Technical Conference and Exhibition*. San Antonio, TX.
- HOLLOWAY, S & SAVAGE, D. 1993 The potential for aquifer disposal of carbon-dioxide in the UK. *Energy Convers. Manage.* **34** (9-11), 925–932.
- HOLTZ, M. H. 2002 Residual gas saturation to aquifer influx: A calculation method for 3-D computer reservoir model construction. In *SPE Gas Technologies Symposium*. Calgary, Alberta, Canada.
- HOMSY, G. M. 1973 Global stability of time-dependent flows: impulsively heated or cooled fluid layers. *J. Fluid Mech.* **60**, 129–139.
- HOU, T. Y. & WU, X.-H. 1997 A multiscale finite element method for elliptic problems in composite materials and porous media. *J. Comput. Phys.* **134**, 169–189.
- HOU, T. Y., WU, X.-H. & CAI, Z. 1999 Convergence of a multiscale finite element method for elliptic problems with rapidly oscillating coefficients. *Math. Comp.* **68** (227), 913–93.
- HOUSE, K. Z., D. P. SCHRAG, C. F. HARVEY & LACKNER, K. S. 2006 Permanent carbon dioxide storage in deep-sea sediments. *P. Natl. Acad. Sci. USA* **103**, 12291–12295.

- HUPPERT, H. E. & WOODS, A. W. 1995 Gravity-driven flows in porous media. *J. Fluid Mech.* **292**, 55–69.
- IDE, S. T., JESSEN, K. & F. M. ORR JR. 2007 Storage of CO<sub>2</sub> in saline aquifers: effects of gravity, viscous, and capillary forces on amount and timing of trapping. *Int. J. Greenh. Gas Control* **1** (4), 481–491.
- JENNY, P., LEE, S. H. & TCHELEPI, H. A. 2003 Multi-scale finite-volume method for elliptic problems in subsurface flow simulation. *J. Comput. Phys.* **187**, 47–67.
- JENNY, P., LEE, S. H. & TCHELEPI, H. A. 2005 Adaptive multiscale finite volume method for multi-phase flow and transport. *SIAM Multiscale Model. Simul.* **3** (1), 50–64.
- JENNY, P., LEE, S. H. & TCHELEPI, H. A. 2006 Adaptive fully implicit multi-scale finite-volume method for multi-phase flow and transport in heterogeneous porous media. *J. Comput. Phys.* **217**, 627–641.
- JESSEN, K., KOVSCEK, A. R. & F. M. ORR JR., 2005 Increasing CO<sub>2</sub> storage in oil recovery. *Energy Conv. Manag.* **46** (2), 293–311.
- JHAVERY, B. S. & HOMSY, G. M. 1982 The onset of convection in fluid layer heated rapidly in a time-dependent manner. *J. Fluid Mech.* **114**, 251.
- JOHNSON, J. W. & NITAO, J. J. 2003 Reactive transport modeling of geologic CO<sub>2</sub> sequestration at Sleipner. In *Proceedings of the 6th International Conference on Greenhouse Gas Technologies* (ed. J. Gale & Y. Kaya), , vol. 1, pp. 327–333. Elsevier Science Ltd.
- JOURNEL, A. G. 1986 Geostatistics - models and tools for the Earth-sciences. *Mathematical Geology* **18** (1), 119–140.
- JUANES, R. & DUB, F.-X. 2008 A variational multiscale method with locally conservative treatment of multiscale source terms. *Comput. Geosci., Special Issue on Multiscale Methods for Flow and Transport in Heterogeneous Porous Media*, doi 10.1007/s10596-007-9070-x (In Press) .

- JUANES, R., SPITERI, E. J., F. M. ORR JR. & BLUNT, M. J. 2006 Impact of relative permeability hysteresis on geological CO<sub>2</sub> storage. *Water Resour. Res.* **42** (W12418), 1–13.
- KAARSTAD, O. 1992 Emission-free fossil energy from norway. *Energy Convers. Manage.* **33** (5-8), 781786.
- KATZER, J. 2007 The future of coal, options for a carbon constrained world. *Tech. Rep.*. Massachusetts Institute of Technology.
- KAVIANY, M. 1984 Onset of thermal convection in a saturated porous medium: experiment and analysis. *International Journal of Heat and Mass Transfer* **27**, 2101–2110.
- KIPPE, V., AARNES, J. E. & LIE, K.-A. 2007 A comparison of multiscale methods for elliptic problems in porous media flow. *Comput. Geosci., Special Issue on Multiscale Methods for Flow and Transport in Heterogeneous Porous Media*, DOI 10.1007/s10596-007-9074-6 (In Press) .
- KOCHINA, I. N., MIKHAILOV, N. N. & FILINOV, M. V. 1983 Groundwater mound damping. *Int. J. Eng. Sci.* **21**, 413–421.
- KOIDE, H., SHINDO, Y., TAZAKI, Y., IIJIMA, M., ITO, K., KIMURA, N. & OMATA, K. 1997 Deep sub-seabed disposal of CO<sub>2</sub> - the most protective storage. *Energy Convers. Manage.* **38**, S253–S258.
- KOIDE, H., TAKAHASHI, M., TSUKAMOTO, H. & SHINDO, Y. 1995 Self-trapping mechanisms of carbon-dioxide in the aquifer disposal. *Energy Convers. Manage.* **36** (6-9), 505–508.
- KOIDE, H., TAZAKI, Y., NOGUCHI, Y., NAKAYAMA, S., IIJIMA, M., ITO, K. & SHINDO, Y. 1992 Subterranean containment and long-term storage of carbon dioxide in unused aquifers and in depleted natural gas reservoirs. *Energy Convers. Manage.* **33** (5-8), 619626.

- KOPERNA, G. J. & KUUSKRAA, V. A. 2006 Assessing technical and economic recovery of oil resources in residual oil zones. *Tech. Rep.*. Advanced Resources International, 4501 Fairfax Drive, Suite 910, Arlington, VA 22203 USA.
- KOVSEK, A. R. & CAKICI, C. M. 2005 Geological storage of carbon dioxide and enhanced oil recovery I. Cooptimization of storage and recovery. *Energy Conv. Manag.* **46** (11-12), 1941–1956.
- KOVSEK, A. R. & WANG, Y. 2005 Geological storage of carbon dioxide and enhanced oil recovery I. Uncertainty quantification employing a streamline based proxy for reservoir simulation. *Energy Conv. Manag.* **46** (11-12), 1920–1940.
- KUMAR, A., OZAH, R., NOH, M., POPE, G. A., BRYANT, S., SEPEHRNOORI, K. & LAKE, L. W. 2005 Reservoir simulation of CO<sub>2</sub> storage in deep saline aquifers. *Soc. Petrol. Eng. J.* pp. 336–348.
- LAKE, L. L. 1989 *Enhanced Oil Recovery*. Prentice-Hall, Inc.
- LAMBERS, J. V., GERRITSEN, M. G. & MALLISON, B. T. 2008 Accurate local upscaling with variable compact multi-point transmissibility calculations. *Comput. Geosci., Special Issue on Multiscale Methods for Flow and Transport in Heterogeneous Porous Media*, doi 10.1007/s10596-007-9068-4 (In Press) .
- LEE, S. H., DURLOFSKY, L. J., LOUGH, M. F. & CHEN, W. H. 1998 Finite difference simulation of geologically complex reservoirs with tensor permeabilities. *Soc. Petrol. Eng. Res. Eval. & Eng.* pp. 567–574.
- LEE, S. H., TCHELEPI, H. A., JENNY, J. & DECHANT, L. J. 2002 Implementation of a flux-continuous finite-difference method for stratigraphic hexahedron grids. *Soc. Petrol. Eng. J.* pp. 267–277.
- LEE, S. H., WOLFSTEINER, C. & TCHELEPI, H. A. 2008 Multiscale finite-volume method for multiphase flow in porous media: Black oil formulation of compressible, three phase flow with gravity and capillary force. *Comput. Geosci., Special Issue*

- on Multiscale Methods for Flow and Transport in Heterogeneous Porous Media*, doi 10.1007/s10596-007-9069-3 (In Press) .
- LEGG, J. F. 1992 Overview of carbon dioxide removal and disposal in canada. *Energy Convers. Manage.* **33** (5-8), 787–794.
- LENORMAND, R., ZARCONE, C. & SARR, A. 1983 Mechanisms of the displacement of one fluid by another in a network of capillary ducts. *J. Fluid Mech.* **135**, 123132.
- LEONENKO, Y. & KEITH, D. W. 2008 Reservoir engineering to accelerate the dissolution of CO<sub>2</sub> stored in aquifers. *Environ. Sci. Technol.* **42** (8), 2742–2747.
- LEVEQUE, R. J. 2002 *Finite Volume Methods for Hyperbolic Problems*. Cambridge University Press.
- LEVINE, J. S., MATTER, J. M., GOLDBERG, D., COOK, A. & LACKNER, K. S. 2007 Gravitational trapping of carbon dioxide in deep sea sediments: permeability, buoyancy, and geomechanical analysis. *Geophys Res. Lett.* **34** (L24703).
- LICK, W. 1964 The instability of a fluid layer with time-dependent heating. *J. Fluid Mech.* **21**, 565–576.
- LINDEBERG, E. & BERGMO, P. 2003 The long-term fate of CO<sub>2</sub> injected into an aquifer. In *Proceedings of the 6th International Conference on Greenhouse Gas Technologies* (ed. J. Gale & Y. Kaya), , vol. 1, pp. 489 – 494. Elsevier Science Ltd.
- LINDEBERG, E. & WESSEL-BERG, D. 1997 Vertical convection in an aquifer column under a gas cap of CO<sub>2</sub>. *Energy Conservation and Management* **38**, SS229–SS234.
- LISTER, J. R. 1992 Viscous flows down an inclined plane from point and line sources. *J. Fluid Mech.* **242**, 631–653.
- LUNATI, I. & JENNY, P. 2006 Multiscale finite-volume method for compressible multiphase flow in porous media. *J. Comput. Phys.* **216**, 616–636.
- LUNATI, I. & JENNY, P. 2007 Treating highly anisotropic subsurface flow with the multiscale finite-volume method. *SIAM Multiscale Model. Simul.* **6** (1), 308–318.

- LUNATI, I. & JENNY, P. 2008 Multiscale finite-volume method for density-driven flow in porous media. *Comput. Geosci., Special Issue on Multiscale Methods for Flow and Transport in Heterogeneous Porous Media*, doi 10.1007/s10596-007-9071-9 (In Press) .
- LUND, J. W., FREESTON, D. H. & BOYD, T. L. 2005 Direct application of geothermal energy: 2005 worldwide review. *Geothermics* **34** (6), 691–727.
- LYLE, S., HUPPERT, H. E., HALLWORTH, M., BICKLE, M. & CHADWICK, A. 2005 Axisymmetric gravity currents in a porous medium. *J. Fluid Mech.* **543**, 293–302.
- MANICKAM, O & HOMS, G. M. 1995 Fingering instability in vertical miscible displacement flows in porous media. *J. Fluid Mech.* **288**, 75.
- MARCHETTI, S. 1977 On geoengineering and the CO<sub>2</sub> problem. *Climatic Change* **1**, 59–68.
- MCGRAIL, B. P., SCHAEF, H. T., HO, A. M., CHIEN, Y.-J., DOOLEY, J. J. & DAVIDSON, C. L. 2006 Potential for carbon dioxide sequestration in flood basalts. *J. Geophys. Res.* **111** (B12), B12201.
- VAN DER MEER, L. G. H. 1992 Investigations regarding the storage of carbon dioxide in aquifers in the Netherlands. *Energy Convers. Manage.* **33** (5-8), 611–618.
- METZ, B., DAVIDSON, O., DE CONINCK, H., LOOS, M. & MEYER, L., ed. 2006 *Special Report on Carbon Dioxide Capture and Storage*. Cambridge University Press.
- MO, S. & AKERVOLL, I. 2005 Modeling long-term CO<sub>2</sub> storage in aquifer with a black-oil reservoir simulator. In *SPE/EPA/DOE Exploration and Production Environmental Conference*. Galveston, TX.
- MO, S., ZWEIGEL, P., LINDEBERG, E. & AKERVOLL, I. 2005 Effect of geologic parameters on CO<sub>2</sub> storage in deep saline aquifers. In *SPE Eurospec/EAGE Annual Conference*. Madrid, Spain.

- NICOT, J.-P. 2008 Evaluation of large-scale CO<sub>2</sub> storage on fresh-water sections of aquifers: An example from the Texas Gulf Coast Basin. (*In Press*) *Int. J. Greenh. Gas Control* .
- NIELD, D. A. & BEJAN, A. 1999 *Convection in porous media*, 2nd edn. Springer Verlag.
- NORDBOTTEN, J. M. & AAVATSMARK, I. 2005 Monotonicity conditions for control volume methods on uniform parallelogram grids in homogeneous media. *Comput. Geosci.* **9**, 61–72.
- NORDBOTTEN, J. M., AAVATSMARK, I. & EIGESTAD, G. T. 2007 Monotonicity of control volume methods. *Numer. Math.* **106**, 255–288.
- NORDBOTTEN, J. M., CELIA, M. A. & BACHU, S. 2005 Injection and storage of CO<sub>2</sub> in deep saline aquifers: Analytical solution for the CO<sub>2</sub> plume evolution during plume injection. *Transport Porous Med.* **58**, 339–360.
- NORDBOTTEN, J. N., CELIA, M. A. & BACHU, S. 2004 Analytical solutions for leakage rates through abandoned wells. *Water Resour. Res.* **40** (4), W04204.
- OLDENBURG, C. M. & UNGER, A. J. A. 2005 Coupled vadose zone and atmospheric surface-layer transport of carbon dioxide from geologic carbon sequestration sites. *Vadose Zone J.* **3** (3), 848–857.
- OTERO, J., DONTCHEVA, L. A., JOHNSTON, H., WORTHING, R. A., KURGANOV, A., PETROVA, G. & DOERING, C. R. 2004 High-rayleigh-number convection in a fluid-saturated porous layer. *J. Fluid Mech.* **500**, 263–281.
- PACALA, S. W. & SOCOLOW, R. 2004 Stabilization wedges: solving the climate problem for the next 50 years with current technologies. *Science* **305**, 968–972.
- PAL, M., EDWARDS, M. G. & LAMB, A. R. 2007 Convergence study of a family of flux-continuous finite-volume schemes for the general tensor pressure equation. (*submitted*) *Int. J. Num. Meth. in Fluids* .

- PARKER, J. C. & LENHARD, R. J. 1989 Vertical integration of three-phase flow equations for analysis of light hydrocarbon plume movement. *Transport Porous Med.* **5**, 187–206.
- PEGO, R. L. & WEINSTEIN, M. I. 1994 Asymptotic stability of solitary waves. *Commun. Math. Phys.* **104**, 305.
- PRASSAD, A. & SIMMONS, C. T. 2003 Unstable density driven flow in heterogeneous porous media: A stochastic study of the Elder [1967b] “short heater” problem. *Water Resour. Res.* **39**, 1–21.
- PRITCHARD, D. 2004 The instability of thermal and fluid fronts during radial injection in porous media. *J. Fluid Mech.* **508**, 133.
- PRUESS, K. 2005 Numerical studies of fluid leakage from a geologic disposal reservoir for CO<sub>2</sub> show self-limiting feedback between fluid flow and heat transfer. *Geophysical Research Letters* **32** (L14404), 1–4.
- REED, A. C., MATHEWS, J. L., BRUNO, M. S. & OLMSTEAD, S. E. 2002 Safe disposal of one million barrels of NORM in Louisiana through slurry fracture injection. *SPE Drill. Completion* **17** (2), 72–81.
- RIAZ, A. & MEIBURG, E. 2003a Radial source flows in porous media: Linear stability analysis of axial and helical perturbations in miscible displacements. *Phys. Fluids* **15** (4), 938.
- RIAZ, A. & MEIBURG, E. 2003b Three-dimensional miscible displacement simulations in homogeneous porous media with gravity override. *J. Fluid Mech.* **494**, 95.
- RIAZ, A. & MEIBURG, E. 2004a Linear stability of radial displacements in porous media: influence of velocity-induced dispersion and concentration-dependent diffusion. *Phys. Fluids* **16** (10), 3592.



- RIAZ, A. & MEIBURG, E. 2004*b* Vorticity interaction mechanisms in variable-viscosity heterogeneous miscible displacements with and without density contrast. *J. Fluid Mech.* **517**, 1.
- RIAZ, A. & TCHELEPI, H. A. 2006 Numerical simulation of immiscible two-phase flow in porous media. *Physics of Fluids* **18** (014104).
- ROBINSON, J. L. 1976 Theoretical analysis of convective instability of a growing horizontal thermal boundary layer. *Physics of Fluids* **19**, 778–791.
- RUGE, J. W. & STÜBEN, K. 1987 *Multigrid Methods*, chap. 4, pp. 73–130. SIAM.
- RUITH, M. & MEIBURG, E. 2000 Miscible rectilinear displacements with gravity override. Part 1. Homogeneous porous medium. *J. Fluid Mech.* **420**, 225.
- RUMYNIN, V. G., KONOSAVSKY, P. K. & HOEHN, E. 2005 Experimental and modeling study of adsorption-desorption processes with application to a deep-well injection radioactive waste disposal site. *J. Contam. Hydrol.* **76** (1-2), 19–46.
- SAFFMAN, P. G. & TAYLOR, G. I. 1958 The penetration of a fluid into a porous medium or hele-shaw cell containing a more viscous fluid. *Proc. R. Soc. London Ser. A* **245**, 312–329.
- SARIPALLI, K. P., SHARMA, M. M. & BRYANT, S. L. 2000 Modeling injection well performance during deep-well injection of liquid wastes. *J. Hydrol.* **227** (1-4), 41–55.
- SILIN, D., PATZECK, T. W. & BENSON, S. M. 2006 Exact solutions in a model of vertical gas migration. SPE 103145, San Antonio, TX.
- STEVENS, S. H., KUUSKRA, V. A., GALE, J. & BEECY, D. 2001 CO<sub>2</sub> injection and sequestration in depleted oil and gas fields and deep coal seams: worldwide potential and costs. *Environmental Geosciences* **8** (3), 200–209.
- STRAUSS, W. A. 1992 *Partial Differential Equations, an introduction*. John Wiley & Sons.

- TAN, C. T. & HOMSY, G. M. 1987 Stability of miscible displacements in porous media: radial source flow. *Phys. Fluids* **30** (5), 1239.
- TAN, C. T. & HOMSY, G. M. 1988 Simulation of nonlinear viscous fingering in miscible displacement. *Phys. Fluids* **31** (6), 1330.
- TTCHELEPI, H. A. 1994 Viscous fingering, gravity segregation and permeability heterogeneity in two dimensional and three dimensional flows. PhD thesis, Department of Petroleum Engineering, School of Earth Sciences, Stanford University.
- TTCHELEPI, H. A. & F. M. ORR JR. 1994 Interaction of viscous fingering, permeability inhomogeneity and gravity segregation in three dimensions. *SPE Res. Engng.* p. 266.
- TTCHELEPI, H. A., F. M. ORR JR., RAKOTOMALALA, N., SALIN, D. & WOUMENI, R. 1993 Dispersion, permeability heterogeneity and viscous fingering: acoustic experimental observations and particle tracking simulations. *Phys. Fluids* **5** (7), 1558.
- TORP, T. A. & GALE, J. 2004 Demonstrating storage of CO<sub>2</sub> in geological reservoirs: the Sleipner and SACS projects. *Energy* **29**, 13611369.
- TROTTENBERG, U., OOSTERLEE, C. W. & SCHÜLLER, A. 2001 *Multigrid*. Academic Press.
- UNION OF CONCERNED SCIENTISTS 2001 Policy context of geologic carbon sequestration. *Tech. Rep.*.
- VELLA, D. & HUPPERT, H. E. 2006 Gravity currents in a porous medium at an inclined plane. *J. Fluid Mech.* **555**, 353–362.
- VOSS, C. I. & SOUSA, W. R. 1987 Variable density flow and solute transport simulation of regional aquifers containing a narrow freshwater-saltwater transition zone. *Water Resour. Res.* **28**, 1851.
- WOODS, A. W. 2002 *Gravity Driven Flows in Porous Rocks: Effects of layering, reaction, boiling and double diffusion*, *Transport phenomena in porous media*, vol. 2. Pergamon.

- WU, X. H., EFENDIEV, Y. & HOU, T. Y. 2002 Analysis of upscaling absolute permeability. *Discrete Contin. Dyn. Syst.* **2** (2), 185–204.
- XU, T., APPS, J. A. & PRUESS, K. 2003 Reactive geochemical transport simulation to study mineral trapping for CO<sub>2</sub> disposal in deep arenaceous formations. *Journal of Geophysical Research* **108** (doi:10.1029/2002JB001979,).
- YANG, C. & GU, Y. 2006 Accelerated mass transfer of CO<sub>2</sub> in reservoir brine due to density-driven natural convection at high pressures and elevated temperatures. *Ind. Eng. Chem. Res.* **45**, 2430–2436.
- YORTSOS, Y. C. 1995 A theoretical analysis of vertical flow equilibrium. *Transport Porous Med.* **18**, 107–129.
- YORTSOS, Y. C. & HICKERNELL, F. J. 1989 Linear stability of immiscible displacement in porous media. *SIAM J. Appl. Math.* **49** (3), 730–748.
- YORTSOS, Y. C. & ZEYBEK, M. 1988 Dispersion driven instability in miscible displacement in porous media. *Phys. Fluids* **31** (12), 3511.
- ZHANG, Y. Q., OLDENBURG, C. M. & BENSON, S. M. 2005 Vadose zone remediation of carbon dioxide leakage from geologic carbon dioxide sequestration sites. *Vadose Zone J.* **3** (3), 858–866.
- ZHOU, H. & TCHELEPI, H. A. 2008 Operator based multiscale method for compressible flow. *Soc. Petrol. Eng. J.* (June), pp. 1–7.
- ZHOU, Q. L., BEAR, J. & BENSABAT, J. 2003 Saltwater upconing and decay beneath a well pumping above an interface zone. *Transport Porous Med* **61** (3), 337–363.
- ZIMMERMAN, W. B. & HOMSY, G. M. 1992 Viscous fingering in miscible displacements: Unification of effects of viscosity contrast, anisotropic dispersion and velocity dependence of dispersion on nonlinear finger propagation. *Phys. Fluids* **4** (11), 2348.